PhD Thesis

Optimising the Laser Powder Bed Fusion Process for the Manufacture of a Nickel Superalloy

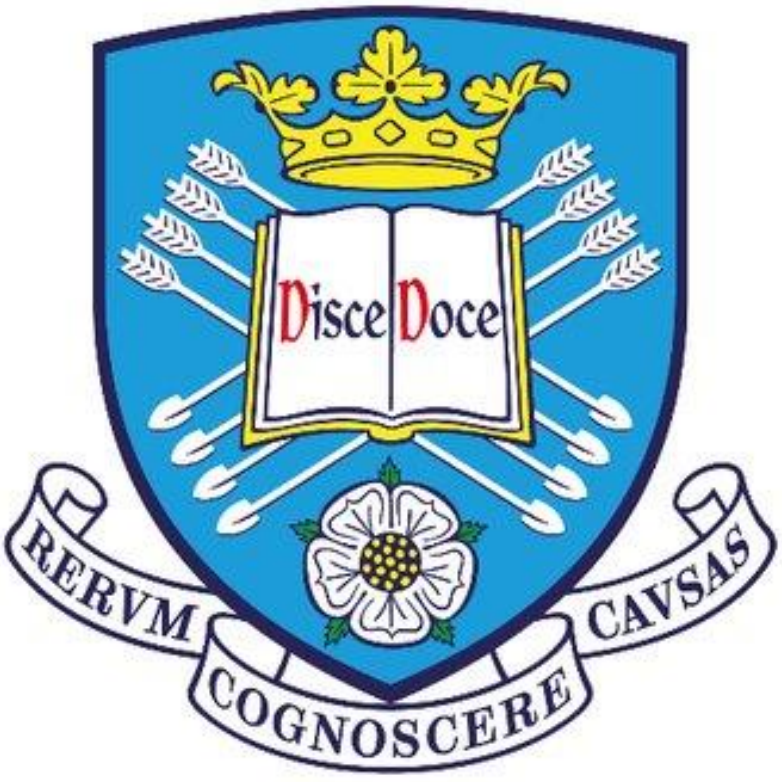

Alistair Lyle

Department of Materials Science

September 2017 – December 2021

EPSRC Advanced Metallic Systems CDT

Yet such is oft the course of deeds that move the wheels of the world: small hands do them because they must, while the eyes of the great are elsewhere.

— Elrond

Acknowledgements

It is customary to thank everyone from your partner down to your first pet… And I shall be no different for everyone has helped in their own way. A few people, though, deserve to be singled out by name. I want to thank everyone who helped me along the way to somehow submitting this thesis. It would not have been possible without so many people. To paraphrase, “It takes a village to submit a thesis”.

First and foremost, I would like to thank my wonderful research group, who have been there throughout the whole adventure. Felicity, Lova, George and Jiawei deserve special mention. At home, Caitlin has been a constant foundation of support. Obviously, I need to thank the rest of my family, who provide a sounding board for endless, very tortured analogies in order to understand it in my own head, John and Jan for providing a family support network in Sheffield and endless Sunday roasts. To Iain, who provided ideas and challenged my assumptions along the way, thank you. GKN Aerospace for providing the funding, support and a reason for this research. Lastly, to Kathy, who helped so much in writing and fine-tuning the endgame of this project.

Thank you from the bottom of my heart.

P.S. Since writing this, I have been joined by two new companions who have both helped and hindered me in their own special ways. Reggie, without you, I would not have got out of the house half as often, and my feet would have been much colder at night. Jesse, you truly are a gift, one that I treasure more with every day that passes

Abstract

Laser Powder bed Fusion as a form of additive manufacturing is a potentially desirable method of manufacture for aircraft parts that use nickel superalloys. One of the barriers to greater adoption is the uncertainty in mechanical properties build quality and microstructure that can arise from the LPBF process. This project explores how this uncertainty can be reduced or eliminated. Different methods achieve this reduction in uncertainty. A method for characterising both the laser and scanner system is outlined and tested. The different melting modes that can occur between the laser and the material are investigated. A closed-loop control system that included a machine learning algorithm was successfully implemented. This control had a statistically significant effect on reducing the variation in thermal emissivities. Constraints found from experimental observations and fundamental physics were imposed to reduce the creation of defects. The mechanical performance of Haynes 282 was benchmarked against other manufacturing methods and other alloys to find that test samples built using LPBF performed as well as wrought or cast samples in elevated stress rupture testing. In order to improve mechanical properties such as high temperature stress rupture resistance, the susceptibility of Haynes 282 to different cracking mechanisms was investigated. This susceptibility was tested through models and analysis of the microstructure and cracks themselves. The susceptibility was tested at different beam velocities, and it was found that the thermal front velocity was found to be critical in influencing the likelihood of crack formation. When the results of these experiments are combined, it suggests parameter ranges that suit both the alloy and the machine, whilst the closed-loop control can stay within these ranges even when the geometry or process conditions vary.

This project was funded by GKN Aerospace in conjunction with the Engineering and Physical Sciences Research Council (EPSRC).

Contents

List of Figures

List of Tables

List of Equations

Glossary

Symbol	Description	Units
A	Absorbtivity Coefficient	
a_0	Lattice Parameter	m
AM	Additive manufacturing	
B	Banded Cells Solidification Front	
C	Larson Miller Material Constant	
c	Specific Heat Capacity	J/mol
C_L	Liquid Composition	
C_L^*	Velocity-Dependent Liquid Composition	
CLC	Closed-Loop Control	
C_p	Specific Heat Capacity	J/mol
C_s	Solid Composition	
d	Characteristic Length	m
DAS	Dendrite Arm Spacing	m
DED	Direct Energy Deposition	
D_i	Diffusion in liquid coefficient	m^2/s
DLD	Direct Laser Deposition	
DoE	Design of Experiments	
D_s	Dendritic Solidification Front	
D_s	Diffusion Coefficient	
E	Energy Input	J
EBSD	Electron Back Scatter Diffraction	
EDM	Electrical Discharge Machining	
EDS	Energy Dispersive X-ray Spectroscopy	
EDX	Energy Dispersive X-ray Spectroscopy	
FPGA	Field Gate Programmable Array	
G	Thermal Gradient	K/m
h	Hatch Spacing	m
h*	Normalised Hatch Spacing	
HAZ	Heat Affected Zone	

HCS	Hot Crack Sensitivity	
h_s	Enthalpy of Melting	
$Iv(Pe)$	Ivantsov Solution	
k	Velocity Dependent Partition Coefficient	
k_e	Equilibrium Partition Coefficient	
LMP	Larson Miller Parameter	
LoF	Lack of Fusion	
LPBF	Laser Powder Bed Fusion	
m	Mass	*kg*
MBRL	Model-Based Reinforcement Learning	
MLA	Machine learning algorithm	
P	Planar Solidification Front	
P	Power	*W*
PDAS	Primary Dendrite Arm Spacing	*m*
Pe	Peclet Number	
PETS	Probabilistic Entropy Targeting System	
PMZ	Partially Melted Zone	
PNN	Probabilistic Neural Networks	
PSD	Particle Size Distribution	
q	Power	*W*
r_B	Beam Radius	*m*
RMSE	Root Mean Squared Error	
RS	Rapid Solidification	
SAC	Strain Age Cracking	
SEM	Scanning Electron Microscope	
SLM	Selective Laser Melting	
SROS	Surface Response Optimised Solution	
T	Temperature	*K*
t	Time	*S*
T_0	Initial Temperature	*K*
TDOS	Training Data Optimised Solution	
TEM	Transmission Electron Microscope	
t_f	Solidification Time	*S*

T_L	Liquidus Temperature	*K*
T_m	Melting temperature	*K*
T_P	Superheat Temperature	*K*
u	Velocity	m/s
UTS	Ultimate Tensile Strength	*Pa*
V	Thermal Velocity	m/s
v	Beam Velocity	m/s
V_c	Velocity of Sound	m/s
v_T	Beam Velocity	m/s
α	Radius of the meltpool	*M*
α	Thermal diffusivity	m^2/s
α_s	Fourier Number	
β	Shrinkage Factor	
δ	Interface Width	*M*
ΔH	Specific Enthalpy	
Δp_c	change in cavitation pressure	*Pa*
ΔT	Change in Temperature	*K*
$\dot{\varepsilon}_{p\,max}$	maximum deformation rate	
λ	(Primary) Dendrite arm spacing	*M*
λ_2	secondary dendrite arm spacing	*M*
μ	Viscosity of liquid	*Pa.s*
σ	Beam Diameter	*M*

1. Literature Review

1.1 Nickel Superalloys

Nickel superalloys are the focus of this research, and they are closely aligned with the jet engine and gas turbines. They have grown in prominence since the beginning of the jet age (from 1937 onwards). Research at that point focussed on alloy development and what additions to the superalloy composition would be advantageous. C. T. Sims *et al.* [1] gave a concise history of superalloys up to the 1980s. Sims *et al.* [1] outlined how the study of nickel superalloys exploded after the second world war in response to the need for new alloys for civilian jet engines. This period was characterised by the need to understand the effect of adding certain elements to enhance or acquire certain properties. These will be discussed in more depth in Sections 1.2, 1.8, and 1.11. However, after the 1970s, advances in processing reduced the need for some of these additions, so the compositions were simplified. A chart showing the progression of nickel superalloy development is shown in Figure 1-1

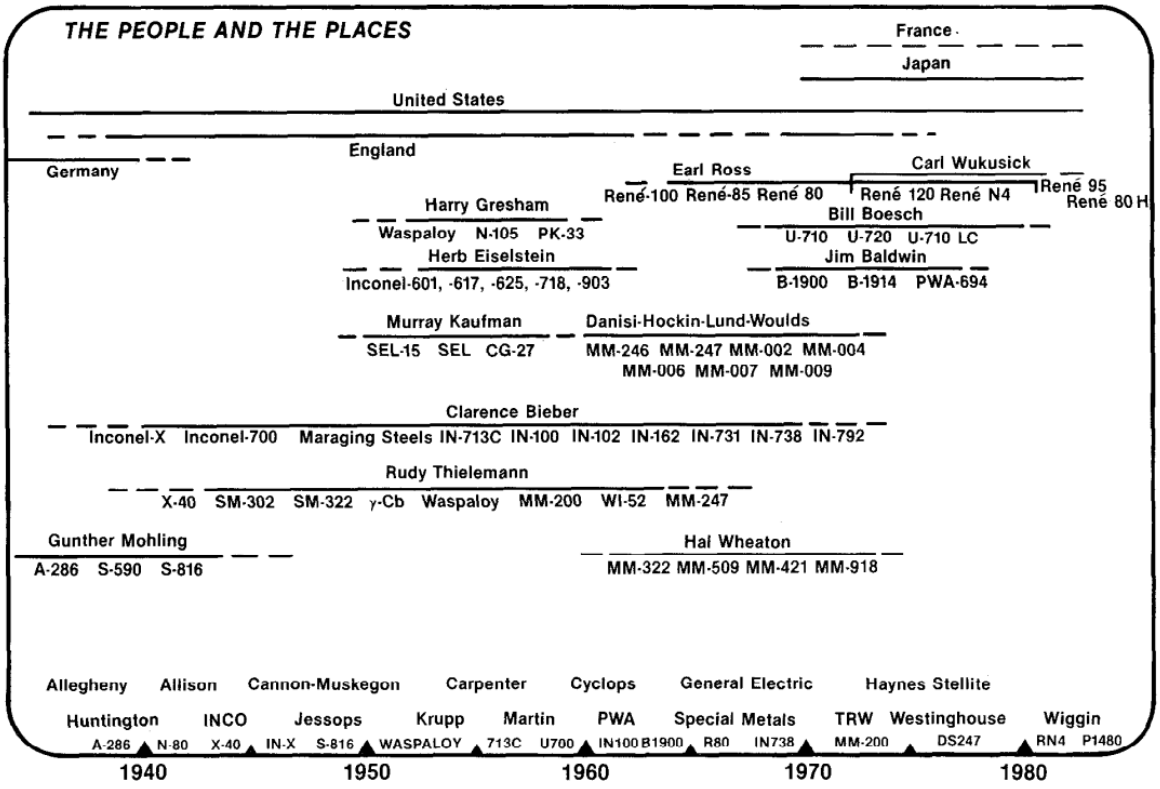

Figure 1-1 - Diagram showing the development of nickel superalloys up until 1980. This diagram shows several alloys still in use and candidate alloys for AM, such as Inconel 718 and 625 [1].

After the publishing of the document, the alloys have again increased in complexity due to increased demands placed upon them. Another type of material, High Entropy Alloys (HEAs), are the natural result of this but are beyond this project's scope. Today many highly utilised nickel superalloys have alloy additions to achieve specific purposes. Inconel 718 (IN718) is a highly utilised alloy in cast form and candidate for LPBF production.

1.1.1 Nickel Superalloys in Additive Manufacturing

Y. J. Liu *et al.* [2] goes into depth about the testing and characterisation of IN718 as an alloy for LPBF and outlines why LPBF and AM in general would be preferable for the production of IN718 and nickel superalloys compared to conventional casting, forging and machining. The property whereby nickel superalloys retain much of their strength at high temperatures leads to more significant tool wear when they need to be extensively machined. Thus, AM would be an ideal production method due to the reduced need for machining. Liu *et al.* [2] also review the testing and characterisation of IN718 when manufactured using LPBF. Useful guidance on what properties to measure is provided and what properties unique to LPBF, such as microstructural properties, might be imbued, for example, high-temperature oxidation resistance. However, the parts produced in the work of Liu *et al.* [2] do not reach the densification rates that are now required of LPBF parts. It reaches 98.4% dense. This project aims to reach much higher densification rates, as high as 99.9% or more. Studies into other well-established casting alloys with high strength due to their high γ' content currently used for turbine blade manufacture have been conducted. Wang *et al.* [3] conducted tests on CM247LC. It was found that the mechanical properties were on average similar to those achieved by forged once the sample had been heat-treated. The variation in results was significant. It was found that the strain was 9%±3% which would be unacceptable in safety-critical applications. One of the aims of this project will be to reduce this variation and allow the use within these safety-critical components. Another alloy that has been studied for use in LPBF is IN738. Engeli *et al.* [4] found that the Hot Crack Sensitivity was different depending on the batches of powder and that there were different amounts of cracking and porosity visible in the micrographs. These cracks and pores will significantly reduce mechanical strength, particularly in dynamic tests. This project will also focus on a more recent alloy Haynes 282, the background of which will be discussed in Section 1.2.

1.1.2 Haynes 282

Haynes 282 is a relatively new alloy. It was first developed in 2006 [5]. It is particularly noted for its resistance to degradation of properties as a result of long term exposure to high temperatures [6]. The composition of Haynes 282 is shown in Table 1-1

Table 1-1 - Composition of Haynes 282 alloy. This table shows the composition range of Haynes 282 in weight % [5].

Element	Weight %
Nickel	57 (Balance)
Chromium	20
Cobalt	10
Molybdenum	8.5
Titanium	2.1
Aluminium	1.5
Iron	1.5 max
Manganese	0.3 max
Silicon	0.15 max
Carbon	0.06
Boron	0.005

S. K. Srivastava, J. L. Caron, and L. M. Pike outlined the development of Haynes 282 in two publications at the seminal conferences on superalloys [7][8]. L. M. Pike described both the initial development of the alloy as well as the ongoing research developments into the alloy. It was developed as a γ' strengthened alloy with good fabricability, allowing for favourable property comparisons to solid solution strengthened alloys [7]. The main strengthening alloying element is molybdenum, a solid solution strengthening element [9]. It, therefore, ends up in the middle when it comes to properties, especially strength. It has superior strength to solid solution strengthened alloys but is inferior to alloys with increased precipitation such as Inconel 718 and CM247 [10][11]. It is hoped that due to its good weldability that it will suit LPBF. The use case investigated for this project is turbine blades and the combustion chamber in aircraft jet engines. The long-term heat exposure resistance is, therefore, a critical property. The part is designed for use between 750°C and 815°C, so falls within the temperature range

of the alloy of up to 900°C. Finally, Haynes 282 does not form Topologically Close-Packed (TCP) phases. These phases such as μ, σ and η, amongst others. Investigations to find these phases have not found these phases. Kruger *et al.* [12] did not observe any σ phase but suggested further microscopic techniques to determine this particularly in the interdendritic region. This project will look to replicate or improve on the stress rupture properties of cast & wrought Haynes 282 with the parts built using LPBF, it will also look to keep the advantageous features and conclusively find whether there are any TCP phases present.

Wang *et al.* [13] studied cast Haynes 282. In their work, they aimed to understand why cast Haynes 282 has comparable creep performance to wrought Haynes 282, but the tensile strength and ductility are lower. This project will use the result from the creep rupture to compare against results from within this project and other studies.

Osoba *et al.* [14], [15] studied the welding of Haynes 282. They created weld tracks at various speeds and analysed the microstructure achieved in these welds. Their work will act as a benchmark for crack formation. In their studies, they observe liquation cracking but no hot cracking. These will be used to conclude if hot cracking should occur in the samples within this work. The appearance of liquation cracking will be used to verify a liquation cracking method based on the soliduses of the meltpool and bulk. These results will give context to those from this project within broader rapid solidification metallurgy and help validate the methods of crack investigation.

1.1.3 Haynes 282 in Additive Manufacturing

Haynes 282 has been studied within additive manufacturing. Kirka *et al.* [16] studied Haynes 282 within the EBM process as a technical document and subsequent paper [17]. This initial study tried to find parameters that led to minimised porosity. Kirka *et al.* [16] found these parameters (but have not stated exact values), observed carbides within the material, and found them to be of the MC type (See Section 1.2.3). As well as carbides, the γ' phase was evenly distributed within the sample. The precipitate morphology changed from cuboidal at the bottom of the build to spherical at the top (See Section 1.2.2). The strength was tested against heat-treated pate, and the results showed a consistently lower yield and ultimate tensile strength (UTS) over all the temperatures tested from room temperature to 1000°C. There were also differences between the longitudinal; where the samples are tested parallel to the build direction and transverse tests; where the samples are tested perpendicular to the

build direction. The perpendicular tests show higher tensile strength properties. Ramakrishnan and Dinda [18] performed a similar experiment using the DLD process. They found that the as-deposited condition had higher mechanical strength than as-cast. They performed a heat treatment to improve these properties further. This heat treatment increased hardness from 294HV to 410HV, and yield strength increased from 633MPa to 894MPa however, elongation decreased from 31.5% to 18%. This result aligns with other alloys' testing and their as-cast counterparts' performance (see later sections). Finally, Otto *et al.* [19] used Haynes 282 in LPBF. They performed a parametric study to determine ideal properties based on full density and quantity of cracks. They found that full density was achieved by using an energy density of 95-100J/mm^3. They also found that with increased energy density the number of cracks increased.

Ramakrishnan *et al.* [18] used DLD to process Haynes 282. They characterised the built samples, including the microstructure and mechanical performance. The microstructural results will be used as they identified the dendrite arm spacing as well as give the parameters necessary to achieve this result. The values will be inputted into a model, and the output will be compared to the results from this current work in order to observe the broader trend in the relationship between DAS, thermal gradient and beam velocity. From this work, a characteristic gradient can be drawn that is unique to Haynes 282. Using these calculated values, the Hot Crack Sensitivity (HCS) can be found. This will be compared to other Haynes 282 HCS values and give context to the results obtained in this project.

Shaikh *et al.* [20] studied the manufacture of Haynes 282 parts using LPBF. They built stress rupture samples and tested them at elevated temperatures to observe how they perform. Within their experiment, they heat treat the sample using the Haynes recommended heat treatment and examine the resultant microstructure. The results from the stress rupture tests will be compared to other results from this study and other authors. The results will be compared to those with a different heat treatment tailored to LPBF to see if the different heat treatments cause the samples to have different stress rupture properties.

Christofidou *et al.* [21] tested the stress rupture properties of different proposed heat treatments. The paper found that existing heat treatments did not recrystallize the microstructure, and so a heat treatment that did result in recrystallisation was proposed. The results from the stress rupture tests performed on the heat-treated samples will be compared to both the Haynes heat-treated and as-built samples to heck if there is a significant difference in properties. The heat treatment proposed by Christofidou will be used on the stress rupture samples within this project.

Boswell *et al.* [22] performed a similar analysis to Shaikh but used Christofidou's heat treatment and measured DAS. The elevated temperature stress rupture results will be compared to those from the current work and values obtained from other sources. This may prove if the new heat treatment leads to a significant change in stress rupture results when compared to the Haynes heat treatment. The DAS will be used to calculate HCS and the relationship between DAS and thermal gradient and beam velocity. This analysis will validate the results from the current work as they will occupy the same region on the graph. The values, along with those from other studies, will allow a characteristic gradient unique to Haynes 282 to be found.

1.2 Haynes 282 Microstructure

1.2.1 Solid Solution Strengthening

Solid-solution strengthening is one of the two main mechanisms of a nickel superalloy gaining its properties. J. N. DuPont *et al.* [9] detailed much of the theory of welding of nickel superalloys. Table 1-2 outlines which elements contribute to which strengthening mechanism.

Table 1-2 - This shows which elements contribute to which strengthening mechanism. It shows the role that some elements have in multiple mechanisms [9].

Effect	Element
Solid Solution Strengthener	Co, Cr, Fe, Mo, W, Ta
γ'-$Ni_3(Al,Ti)$ Former	Al, Ti
Solid Solution Strengthening of γ'	Cr, Mo, Ti, Si, Nb
γ''-Ni_3Nb Former	Nb
Carbide Formers:	
MC and M(C,N)	W, Ta, Ti, Mo, Nb
M_7C_3	Cr
$M_{23}C_6$	Cr, Mo, W
M_6C	Mo, W
TCP Phase (σ, P, μ, Laves)	Ti, V, Zr, Nb, Ta, Al, Si
Surface Oxide (Cr_2O_3/Al_2O_3) Fromer	Cr, Al

As can be seen, Co, Cr, and Mo all contribute solid solution strengthening, and these are elements which Haynes 282 is rich in, having approximate 10, 20, and 8.5 wt. % of each respectively. Solid solution strengthening occurs when an element of different size is substituted into the matrix, hindering the movement of dislocations through the structure. Figure 1-2is a schematic diagram showing how it occurs.

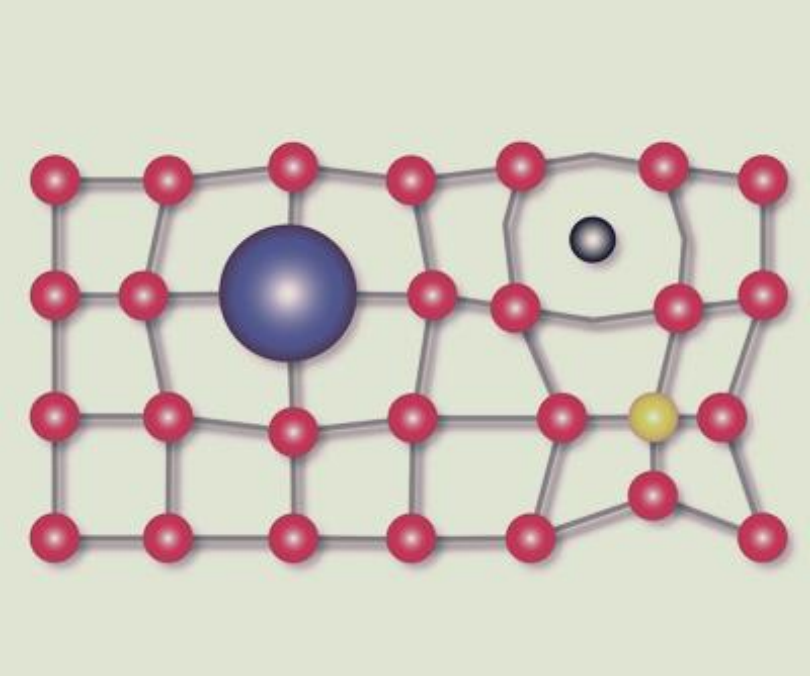

Figure 1-2 - This schematically shows how a mismatch in atomic sizes can create a blockade to dislocation motion. It shows how they can be both substitutional as well as interstitial [23].

From the diagram, the atom's irregular size, when compared to the rest of the matrix, hinders the propagation of defects and, as a result, strengthens the material. Various studies have investigated this phenomenon. Y. Mishima *et al.* [24] observed the effect different alloying elements have on Young's modulus and flow stress. It was found that the elements with a greater size mismatch gave a greater effect on properties than elements with a size closer to the main constituent. For this reason, molybdenum was used as this is a refractory metal with a high atomic mismatch compared to nickel. The study found that atomic size was of greater importance than modulus when considering an addition's effect on mechanical properties. This phenomenon explains several additions, such as large amounts of molybdenum to the composition of Haynes 282 and why it was suggested as a candidate for AM.

1.2.2 Precipitation Strengthening

The other mechanism by which nickel superalloys gain their mechanical properties is the precipitation of a favourable phase. Within nickel alloys, this is either through the formation of γ' or γ''. From Table 1-2, both titanium and aluminium contribute to the formation of γ'. The formation of the γ'' phase relies on significant additions of niobium, and as such, no γ'' forms in

Haynes 282. E. Nembach and G. Neite [25] detail the fundamental physics and mechanism behind precipitation strengthening or hardening. They also outlined how the volume fraction of γ' has changed as new nickel alloys have been created. Precipitation hardening works by resisting the glide of dislocations in the matrix. By forming within the γ matrix, γ' acts as a blockade to dislocation motion and strengthens the material. The size and ratio of precipitates compared to matrix differs depending on the alloy but can be anything upwards of 0.5. As the level of precipitation increases, the alloy must be treated more like a composite. For Haynes 282, the volume fraction of γ' is around 19%. Dislocations halted by the precipitates build up and form networks around the precipitate, causing the increase in strength. γ', unlike γ, does not have an FCC structure. The nickel atoms make up the faces of the unit cell, but the corners are either titanium or aluminium. This arrangement is shown below in Figure 1-3, where the nickel γ phase unit cell is compared to the γ' unit cell.

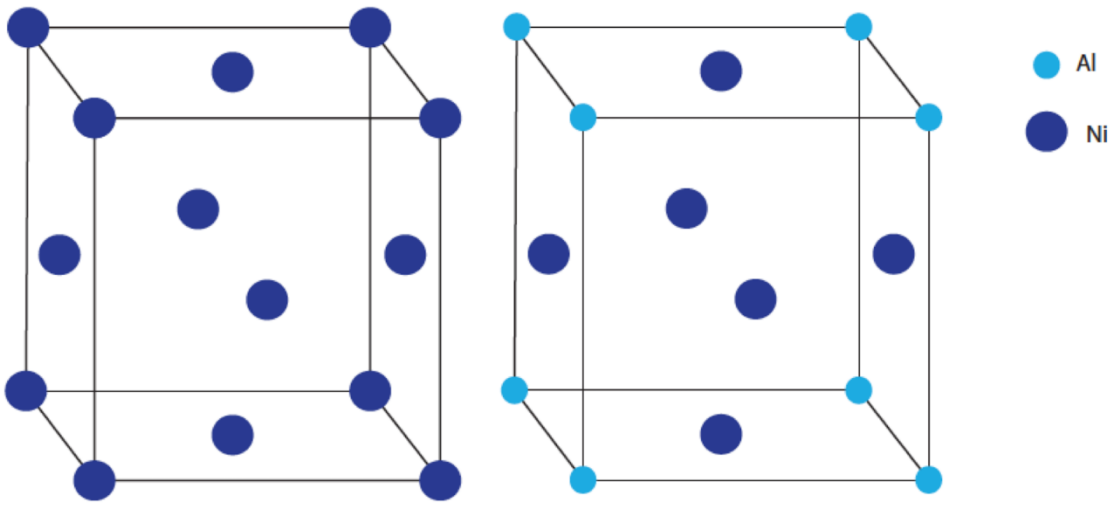

Figure 1-3 - This schematic diagram shows the difference in structure between the γ phase and the γ' precipitate. The γ phase is an FCC structure with nickel atoms at the faces and the corners, γ' has nickel at the faces but either aluminium or titanium at the corners.

Also, γ', unlike γ, is long-range ordered, meaning that it repeats its order over larger distances (Figure 1-4).

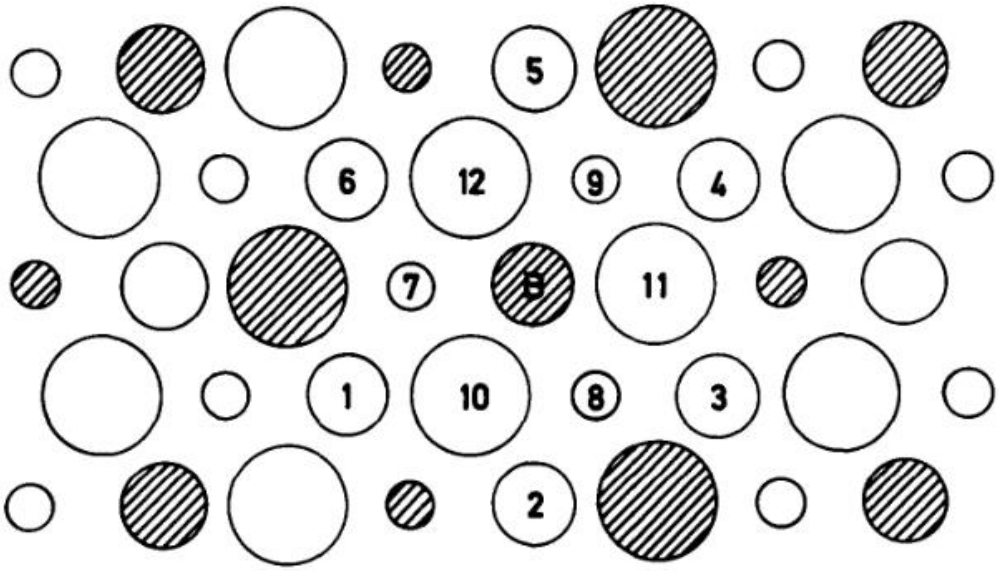

Figure 1-4 - This schematically shows the repetition of the γ' precipitate in a cross-section. The hatched circles are the addition (either Ti or Al), and the blank circles are nickel. The volume fraction of γ' depends on the Al/Ti content, whereas the thermal exposure of the material determines the size of the precipitates as this causes the γ' to grow [25].

The pattern does repeat itself. The schematic diagram shows the composition of γ' with the general chemical formula A_3B where A refers to nickel and B refers to either aluminium or titanium. On the schematic, the nickel (with blank centres) forms around the aluminium or titanium (with hatched centres) to form the γ'. The morphology of the γ' can take two forms. The spherical form is seen in Figure 1-5 or the cube shape seen in Figure 1-6. The cube shape comes about due to the γ' being less coherent with the matrix.

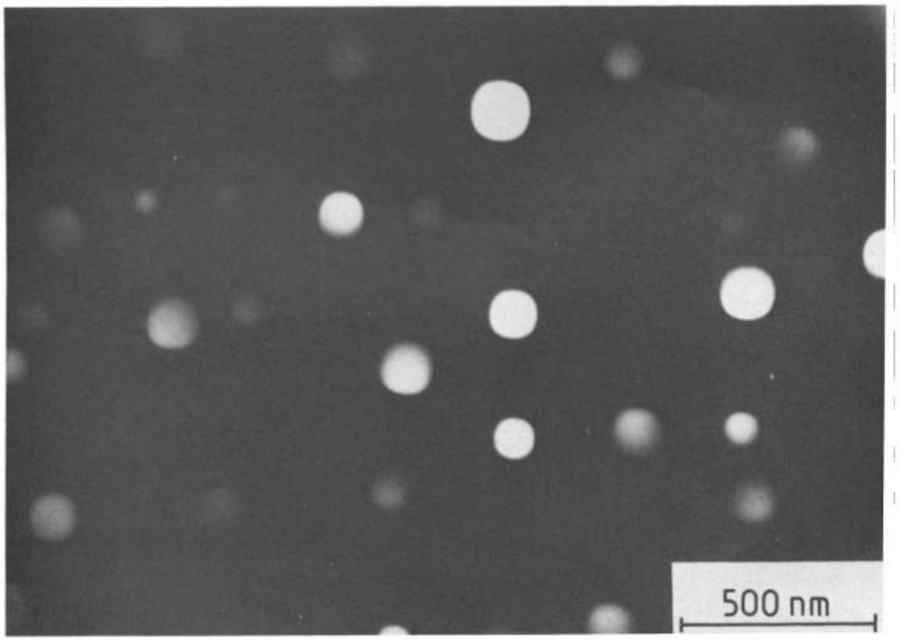

Figure 1-5 - These are the spherical morphology of the γ' precipitate in the alloy NIMONIC P16. The precipitates are more coherent with the γ matrix in as-built nickel superalloys. The precipitate is often on the scale of 10s of nanometres. As a result of heat treatments, these grow to the point where they are similar to the as-cast material[25].

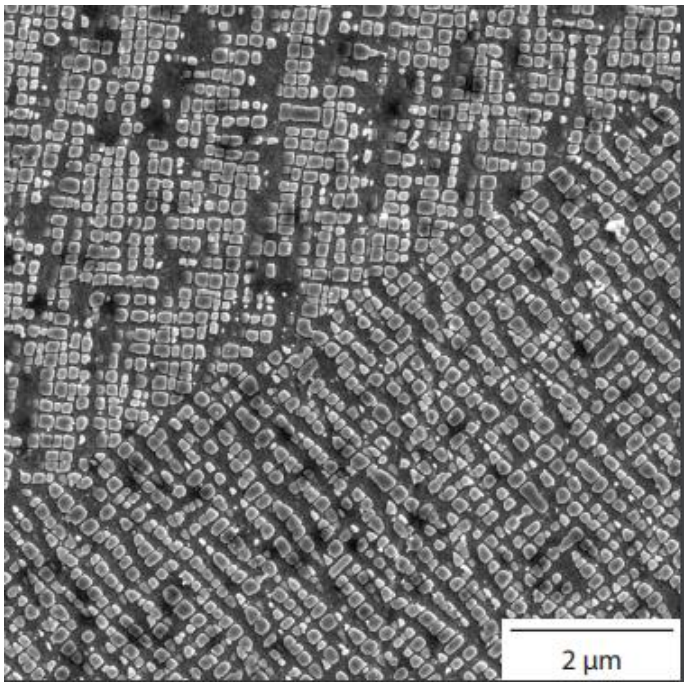

Figure 1-6 - This cuboidal network of precipitates is less coherent than the spherical form. However, in AM, the difference in misorientation is small, around 1°. Along with the main γ' precipitate, there is supplementary γ' around the precipitates in an octahedral morphology. The alloy shown is a model Ni-Co-Al-Ti-Cr superalloy. Reproduced with permission from K.A. Christofidou

With AM γ' precipitates out in the spherical form B. Dubiel and J. Sieniawski [26] used Inconel 625 to show the formation of γ' in the as-built condition Figure 1-7 shows how it is on the nanoscale.

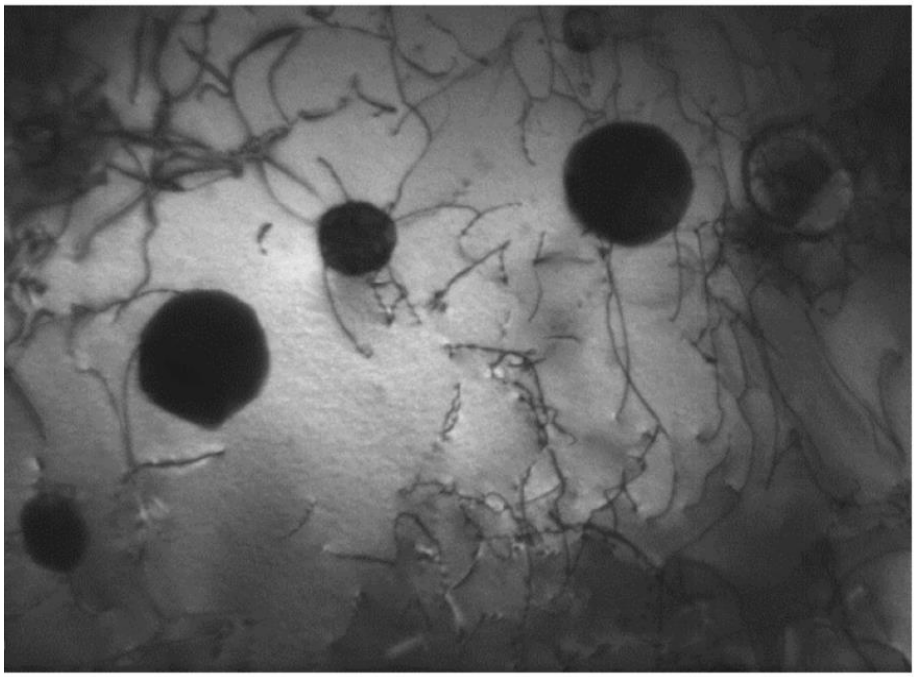

Figure 1-7 - This micrograph of IN625 shows how the precipitate works to strengthen the material. A dislocation network is forming around the precipitates. This network impedes their motion and other subsequent dislocations strengthening the material [26].

The dislocation networks surrounding the precipitate can also be seen. B. Dubiel and J. Sieniawski [26] did not heat treat the sample or grow the precipitate to create favourable properties. Separately, G. Marchese *et al.* [27] attempted the heat treatment. This heat treatment was done by solutionising at 1150°C for 2 hours then ageing the alloy at 700°C for 24 hours. The spherical γ' can be seen in Figure 1-8.

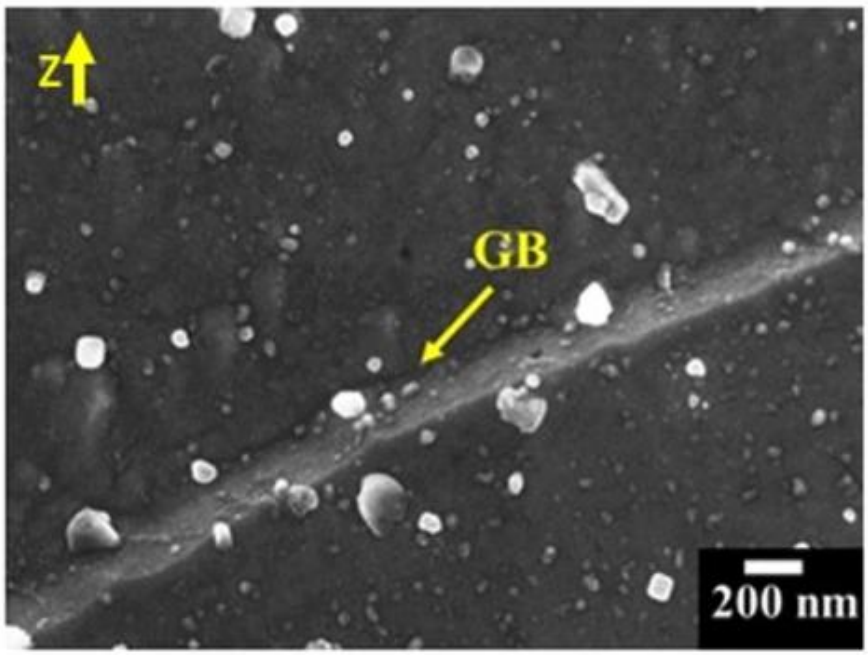

Figure 1-8 - This micrograph shows the formation of spherical precipitates in IN625 after heat treatment. The precipitate that forms is called secondary γ', and smaller particles can be seen surrounding it. These are tertiary γ' [27].

The smaller particles close to the grain boundary are tertiary γ' these aid in promoting good creep properties as without them, a/2<110> dislocations can easily glide.

This project will aim to precipitate out γ' to influence the properties favourably. A.J. Goodfellow *et al.* [28] investigated the growth of secondary γ' these are the form of γ' most commonly seen in AM alloys as these are in the sub-micron range. Figure 1-9 shows that cuboidal precipitates are commonly found after heat treatment.

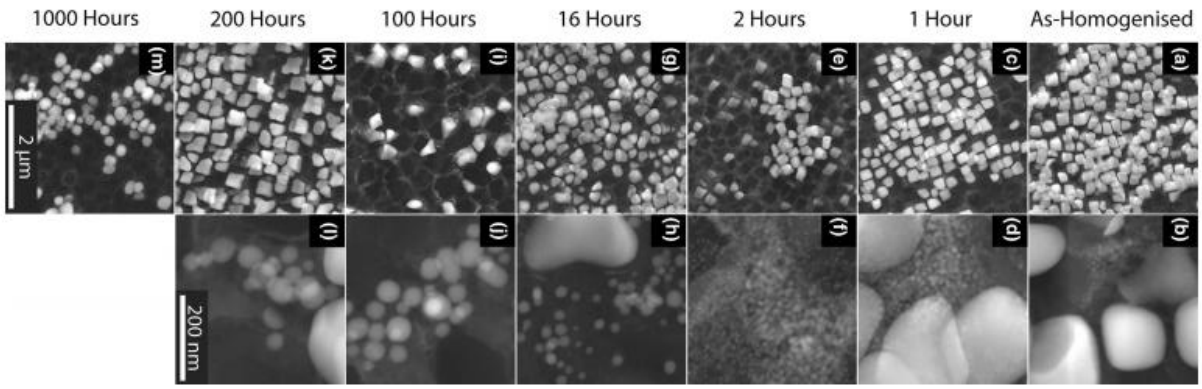

Figure 1-9 These micrographs show the evolution in morphology and size of secondary and tertiary γ' in a model nickel superalloy [28].

This study shows how precipitates change when exposed to elevated temperatures in-service. The secondary γ' changes form from cuboidal after homogenisation to octahedral after 1000 hours of heat treatment at 760 °C. This study also investigated tertiary γ;' and how it disappears after a long time in service. This project will build upon this work and investigate these microstructures in Haynes 282 built using LPBF instead of a model nickel superalloy. It will also investigate the effect of different processing parameters on the precipitation of γ'. Furthermore, studies of how heat treatments affect the formation of other strengthening mechanisms such as carbide formation and whether these precipitates ultimately have a beneficial effect on the mechanical properties of the final part will be performed.

1.2.3 Precipitate Evolution

The morphology and size of the γ' precipitate is affected by the cooling rate of the material. Fan *et al*. [29] studied this evolution in a powder metallurgy superalloy. By varying the cooling rate from 600°C/min to 2°C/min different morphologies of precipitate were found to evolve. At the fastest cooling rate, a spherical morphology is observed, as the cooling rate is slowed the morphology changed from square to octet to dendrite. This change is seen in Figure 1-10.

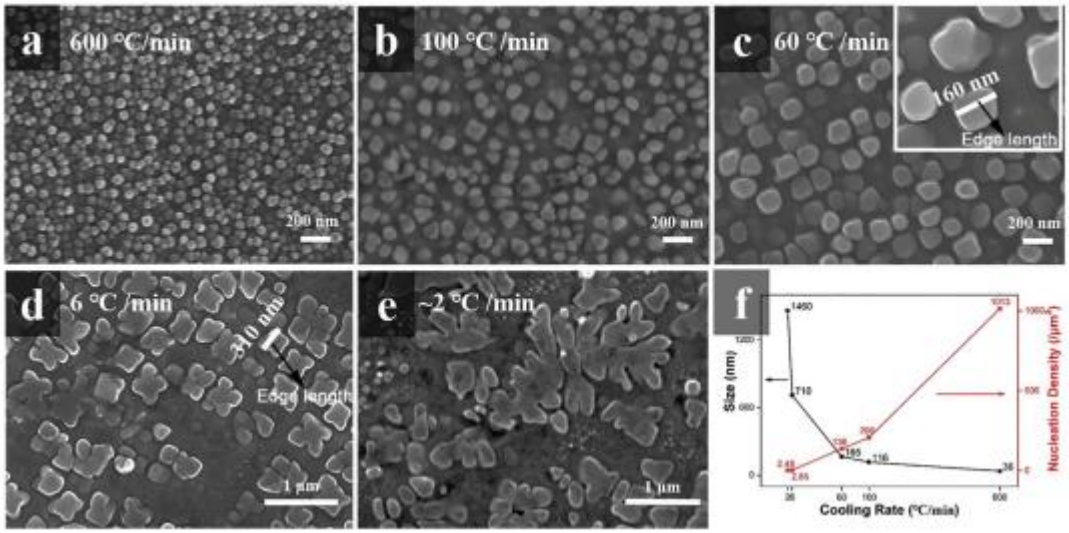

Figure 1-10 - These micrographs show the precipitate evolution in a model nickel superalloy (Ni-23.4Co-4.7Cr-4Al-4.3Ti) at different cooling rates. (a-e) show the morphology change as the cooling rate slows. (f) is a graph showing how the size of the precipitate decreases with increasing cooling rate [29].

Figure 1-10 shows that as the cooling rate increases the size of the precipitate decreases and the nucleation density increases. This observation is crucial for this current work as rapid solidification causes the cooling rate to be on the order of 10^7K/s this will lead to very small precipitates in the as-built condition. It will be necessary to use TEM to view the precipitates as they will be on the scale of nanometers. TEM will be used as part of this work to observe the precipitates within the microstructure.

1.2.4 Carbide Formation

Referring to Table 1-2, some elements promote carbide formation. Within Haynes 282, these are chromium, molybdenum, and titanium. G. P. Sabol and R. Stickler [30] describe the microstructural features of nickel superalloys. They describe MC based carbides as the most common carbide. These can be formed by the M representing titanium or molybdenum. These will, therefore, be expected to be found in the alloy, and it will constitute an aim of this project to observe the carbides present in LPBF Haynes 282. The book describes how MC carbides are unaffected by heat treatments as they are stable up to temperatures close to the fusion temperature. It describes how, as is the case with LPBF, the morphology and position of the carbides might change with high cooling rates. In this scenario, the carbides are found in the interdendritic region. As a result, carbides found in the middle of grains with a suitable composition will be MC carbides. This book explains how under load for long durations, the

MC carbides decompose into $M_{23}C_6$ and γ' that deleteriously affects the mechanical properties, which lead to failure. When the samples are investigated post-mortem, the phases surrounding the crack will be investigated in this work. $M_{23}C_6$ can also be formed directly due to chromium and molybdenum being present. It is also the most common carbide found in heat-treated samples formed due to exposure to a carbide stabilisation between 843°C and 1066°C. $M_{23}C_6$ can be observed in two different morphologies. The first is discrete secondary particles along the grain boundary. This microstructure maximises creep resistance and ductility. Examples are shown in Figure 1-11[30].

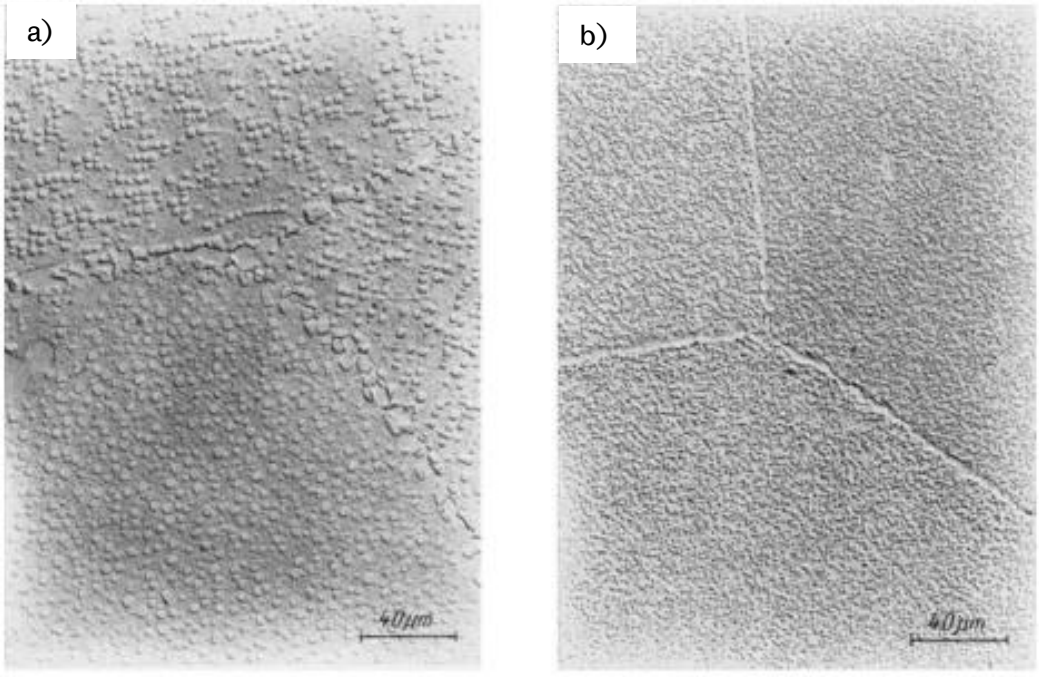

Figure 1-11 - These micrographs show the different manners in which $M_{23}C_6$ carbides can be precipitated out for Udimet 710. In a) (on the left), carbides are distributed as cuboidal particles at the grain boundary. In contrast, b) (to the right) has needle-like carbides forming on the grain boundaries. [30].

The second is as extensive grain-boundary platelets or sheets. This microstructure has been shown to have an embrittling effect, particularly reducing creep ductility. In a majority of nickel superalloys, $M_{23}C_6$ forms between 760°C and 980°C and is in solution between 1010°C and 1040°C [30]. $M_{23}C_6$ precipitates out in the advantageous state of discrete particles when the material is aged between 760°C and 871°C. Higher temperatures out of this range can lead to a cellular morphology that has been shown to reduce ductility. When lower ageing temperatures were used, $M_{23}C_6$ was shown to have precipitated with an acicular morphology

intragranuarly. It is also formed when a drastic quench from the solution temperature has been employed. This carbide formation is significant to LPBF as the cooling rates are high.

The final carbide to be discussed will be the M_6C. This carbide is more stable than $M_{23}C_6$ but less stable than MC. It is found in alloys with high refractory and transition metal contents such as Haynes 282 (which has a molybdenum content of 8.5% and a cobalt content of 10%). It has been found that with alloys with molybdenum content higher than 6%, it becomes more common than $M_{23}C_6$. It can be hard to distinguish between the two carbides as they have similar crystal structures and similar morphologies and can be found to precipitate in similar regions. They can be differentiated using specific etchants and TEM. As part of this project, the presence and morphology of carbides will be investigated and their effect on the mechanical properties determined. It is the hope that by characterising the carbides and controlling where they form in an LPBF part, the macro mechanical properties can be controlled and optimised.

1.2.5 Twinning

Twinning is one of the methods by which alloys can deform [31]. Along with dislocations, these can account for strain seen in metal as it is deformed. Dislocations are discussed, and their effects on cracking are discussed in Section 1.8.

The geometrical aspects of twinning can be shown by using a unit sphere, as shown in Figure 1-12. This figure shows how the twinning plane k_1 intersects the plane of the page in the shear direction η_1.

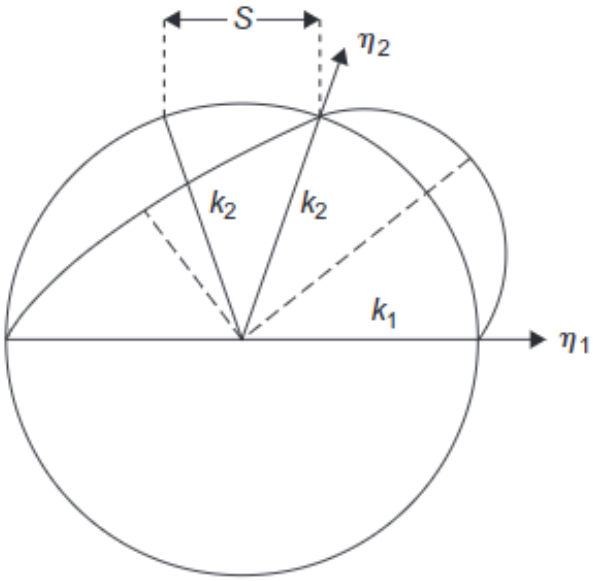

Figure 1-12 – This unit sphere shows how twinning affects the unit sphere. Whilst the plane k_1 which intersects the plane shown in the 2D drawing, all others are shifted, so the sphere becomes an ellipsoid of equal volume shifted by distance S, k_2 is shifted, and the direction η_2 is also shifted. [31]

The unit sphere is distorted to an ellipsoid of the same volume upon twinning. The shear plane k_1 is unchanged during twinning, but all the others are tilted as a result.

Twinning occurs in metals with a low stacking fault energy as the dislocations dissociate to become stacking faults. These impede the motion of further dislocations. When dislocations of similar orientation combine, they form dislocation locks that can be hard for further dislocations to overcome directly, so other movement methods must be used. Due to this, twinning is the preferred mode of deformation to overcome these locks [32]. There are two types of twinning deformation twinning, which is more common in Hexagonally Close Packed crystal structures and annealing twins seen in Haynes 282 [33]. Annealing twins are formed due to a stacking sequence disruption as new layers form the sequence continues until the original sequence is reinstated. As annealing twins only need to reduce interfacial energy [34], they can stop in the middle of the grain. Previous studies into Haynes 282 found that annealing twins could be found in the microstructure. Rozman [33] showed that as well as micro-twinning occurring in the precipitate, as shown in Figure 1-13, annealing twins could be found after standard heat treatment.

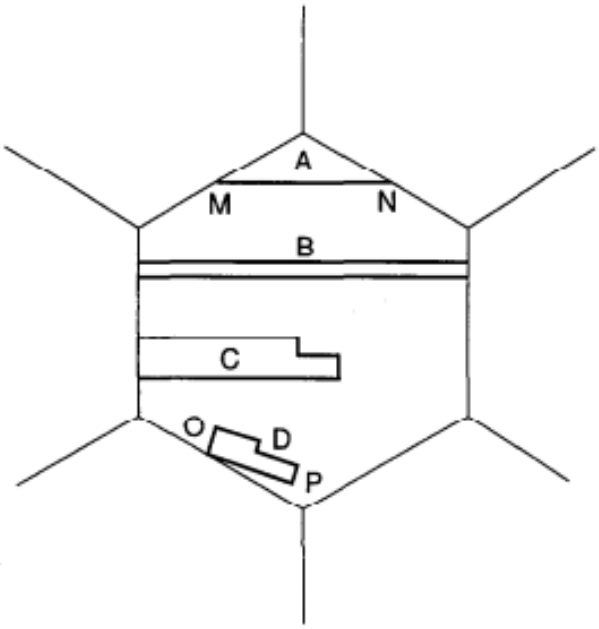

Figure 1-13 – This diagram schematically shows different annealing twin morphologies, the thin feature running up the middle of the micrograph. Twinning occurs as the dislocations dissociate due to the low stacking fault energy. As a result, the only way these locks can be overcome is by twinning. This mechanism can aid in strengthening a material, particularly at high temperatures. Twinning is characterised by parallel fault lines. [33]

One reason for including the elements seen in the composition of Haynes 282 is for its ability to deform through twinning and therefore withstand higher loads even at high temperatures.

1.2.6 Solidification

Cooling and solidifying the liquid meltpool into the bulk solid is critical for the LPBF process. Solidification can be thought of as two distinct phases nucleation and growth [35]. In summary, nucleation occurs as the molten metal reaches the solidification temperature. As it does this, small changes in the local composition cause the solidification temperature to rise, so a nucleation point is created. These can form anywhere in the melt but are significantly more likely to form near the boundary, which is cooler and heterogeneous. Figure 1-14 below [51] shows that the activation energy would be lower, and the number of nucleation sites would increase considerably.

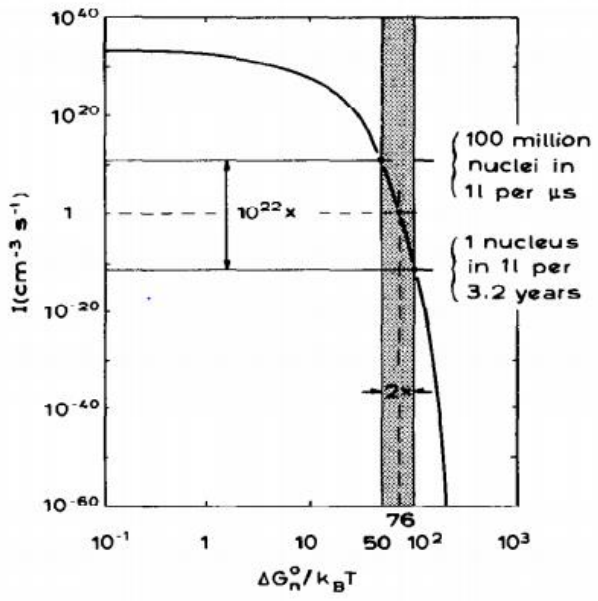

Figure 1-14 shows the number of nuclei nucleated at a specific activation energy. Activation energy is dependent on temperature and that number of nuclei is significantly dependent on activation energy. [36]

For this project, the focus will be on growth and controlling it. The growth of the solid phase can be categorised into five distinct types depending on the cooling rate. Askeland *et al.* [37] describe how at slow cooling rates, also called equilibrium cooling, the solidification front advances at a slow rate that allows the latent heat of fusion to be conducted away by the bulk solid. If there is a small protuberance surrounded by liquid, the growth stops until the rest of the interface catches up. Dendritic growth occurs when fewer nucleation sites are present, and as such, the liquid must be undercooled before the solid forms. This undercooling causes a solid protuberance called a dendrite at the solid-liquid interface. It is encouraged to grow into the undercooled liquid. As the dendrite grows, the latent heat of fusion is conducted into the undercooled liquid raising its temperature. If needed, secondary and tertiary dendrites form to increase the surface area and aid the raising of the temperature of the liquid. Once the undercooled liquid rises above the freezing range, the remaining liquid solidifies due to planar growth. In summary, the difference is that in planar growth, the bulk or container must be the heat sink, whereas, in dendritic growth, the undercooled liquid absorbs it.

Between these two is cellular growth, where there are not enough nucleation sites, or the cooling is too rapid to allow planar growth. However, the undercooling of the liquid is low enough for primary dendrites to be enough to warm the liquid, termed cellular growth. In standard solidification cases, these states would be enough. However, in LPBF and welding before it, this is rapid solidification.

Rapid solidification can be separated into three different length scales whose conditions were outlined by Kurz *et al.* [38]. Boig [39] outlined these conditions as:

1) The diffusion field becomes shorter than the microstructural scale when the Peclet number (Pe = ud/2α where u is thermal front velocity, d is characteristic length scale, e.g. tip radius, and α is thermal diffusivity) becomes larger than unity. This condition occurs when the interface velocity is of the order of centimetres per second. (At interface velocities below RS conditions, the microstructure follows the relationship $d^2u = const.$*)*
2) The diffusion distance becomes comparable with the interface width, and local non-equilibrium is established, leading to solute trapping. This condition occurs when the velocity of the interface, given by the ratio of diffusion coefficient to interface width, is of the order of metres per second.
3) The interface movement driven by atom attachment reaches the velocity of sound (V_c) *and cannot move faster. This condition occurs when the interface velocity is on the order of kilometres per second.*
[39]

As a result, the thermal gradients are much higher, and the morphology of the dendrites and cells are determined by how fast the cooling rate is and how fast the laser moves. Figure 1-15 shows how depending on the cooling rate dendritic (D_s), banded cellular (B) and Planar (P) solidification fronts are possible.

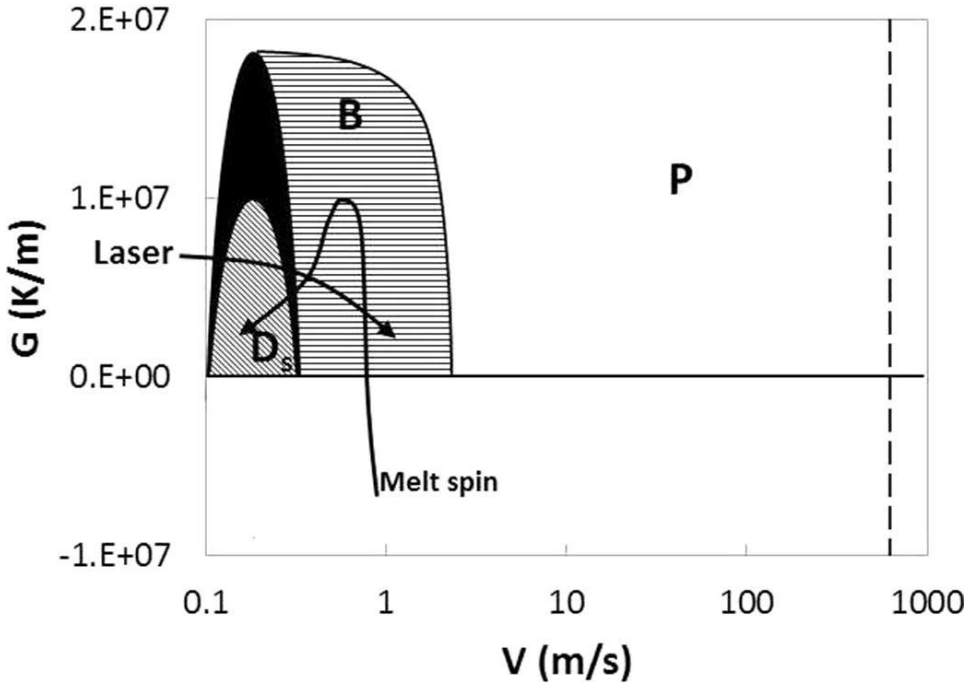

Figure 1-15 – This graph shows the thermal front velocities and gradients that result in different microstructures being formed from dendrites (D_s) to planar (P) with banded cells (B) in between. [40]

Harrison *et al.* [40] found thermal gradients to be higher than expected, giving rise to the cellular morphology that was found in their samples. The thermal gradients seen in LPBF are in the region of 1.2×10^7 K/m and velocity upwards of 2m/s [41]. From Figure 1-15, this should lead to equiaxed planar growth. However, this is not the case. This growth can be explained through the multiple passes that the laser makes in LPBF, which cause a thermal front to be created perpendicular to the laser direction. Subsequently, layers also cause a vertical thermal front to be created. Prior experiments with single rapid cooling regimes found that equiaxed grains were formed. Hayzelden *et al.* [42] found that segregation free equiaxed fine microstructure formed. However, they note that this structure can evolve into epitaxial growth in the direction of the heat source due to recoalescence. Harrison *et al.* observed this epitaxial growth, shown in Figure 1-16.

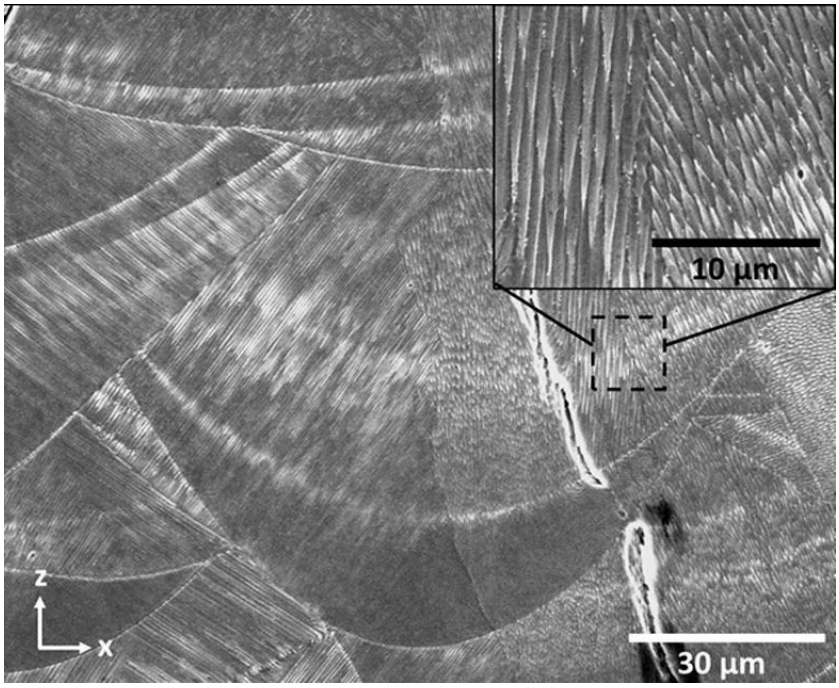

Figure 1-16 – The epitaxial cells can be seen as well as the individual meltpools in which they were formed for Hastelloy X. The epitaxial cells are formed at the meltpool boundary as predicted by the nucleation theory and grow perpendicular to the boundary. [40]

There is a tendency for the cells to be elongated in the direction of the heat source (the z-direction). As such, large regions of equiaxed cells are difficult to achieve through LPBF. Heat treatments such as homogenisation can eliminate this epitaxial growth but enlarge the cells (See Section 1.12).

Kurz-Fisher analysed the dendrite tip radius [36]. It was found that as the dendrite tip radius is small, only small perturbations are possible in the undercooling and segregation, leading to local undercooling being dominant. This undercooling would allow for segregation to only occur on a local level which is why the precipitates are so small.

Micro segregation is an issue that is also linked to the cooling rate. A micro-segregation free structure was formed in rapid cooling scenarios such as those presented by Hayzelden *et al.* [55]. However, Tao *et al.* [41] found that microsegregation can be found in LPBF samples investigated using Transmission Electron Microscopy (TEM). This segregation can be explained by solute trapping [43]. Solute trapping is where during rapid solidification, solute may be incorporated into the solid phase at concentrations significantly different than predicted under equilibrium conditions. Solute trapping occurs as the speed at which the melt freezes is quicker than the diffusion velocities of the alloy's constituent elements [44]. This fast cooling causes elements to be trapped on the grain boundaries or in the matrix. The fast cooling will cause some regions to be depleted in certain elements and may cause detrimental

properties such as increased susceptibility to corrosion due to chromium-lean regions. It may also cause detrimental phases to form (See previous sections). These phases and segregation may be small in the as-cast form but can grow under service life conditions (See Section 1.2.6). A homogenisation will alleviate this issue but must be controlled to grow the microstructure adversely (See Section 1.12).

Cell size or primary dendrite arm spacing is a signifier of mechanical strength and can be related to temperature gradient by Equation 1-1[45].

$$\lambda_1 = 97 \pm 5 \left(\frac{\delta T}{\delta t}\right)^{-0.36 \pm 0.01}$$

Equation 1-1

It may be possible to impart different mechanical properties by controlling the temperature gradient. The effect of gradient control will be investigated in this project by using different parameters to induce different cooling rates to see if different cracking mechanisms are more prevalent.

1.3 Powder Feedstock

Metal powder can be manufactured in numerous different ways both mechanically and chemically [46] this work will focus on outlining mechanical manufacturing methods as these are used to create alloy powders whereas chemical methods are used to extract pure metals.

Initially mechanical milling was the most widely used method for powder manufacture. There are three types of milling, grinding, crushing and attrition. Mechanical alloying is a powder processing technique that uses high energy mills to weld fracture and reweld fragments to create a powder. The advantage of this method and why mechanical milling was so popular initially was that it allowed for the use of different raw materials such as pure elements, sponges, fibres, ores or even waste products of machining including shavings. However, this method creates a powder that is non spherical as shown in Figure 1-17.

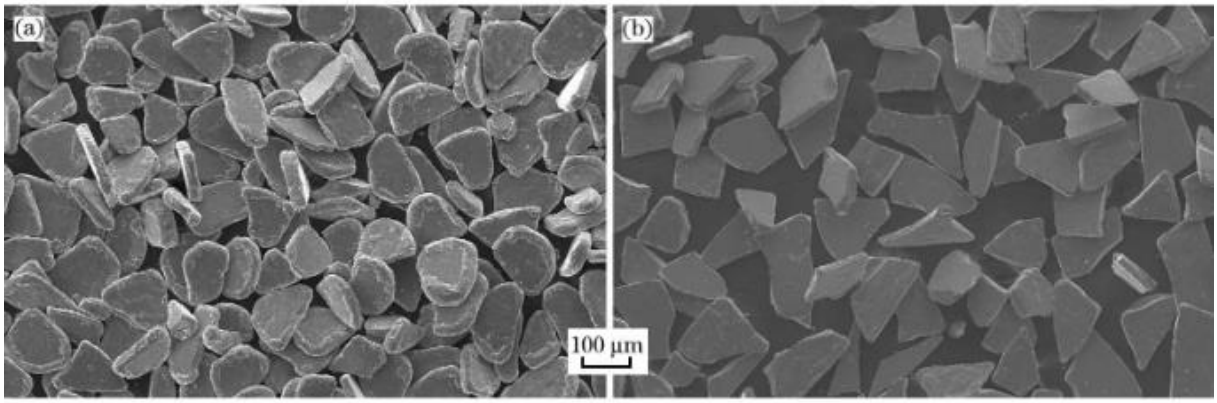

Figure 1-17 - Micrographs of FeCuNbSiB showing the morphology of (a) crushed and (b) ball-milled powder[47].

Both the crushed Figure 1-17a and ball milled Figure 1-17b powders are non-spherical with the crushed having more rounded edges but the ball milled having pronounced angular edges. As a result, a different method was needed that could create spherical powder. This family of methods is called atomisation and it is the dominant method for powder manufacture at present [46].

Among the atomisation methods available, the method that was used to manufacture the powder in the current study was gas atomisation. This involves a billet being suspended above a stream of inert gas (usually argon), usually within a vacuum, the bottom of the billet is heated until molten metal starts to drip off. These drops fall into the stream and a fine spray of particles is created. These then solidify as individual powder particles and a powder is thus created. The advantage of gas atomisation is that it creates spherical, high cleanliness, fine and homogenous powder particles due to the rapid solidification.

A more recent atomisation method is plasma atomisation. This involves a wire feedstock being melted and the drops being dispersed into a powder by a plasma torch. The use of a hot atomising gas means that the powder droplets are prevented from freezing into irregular non spheroidal shapes as would be the case with a cold stream. Figure 1-18 shows a powder manufactured using gas atomisation under SEM.

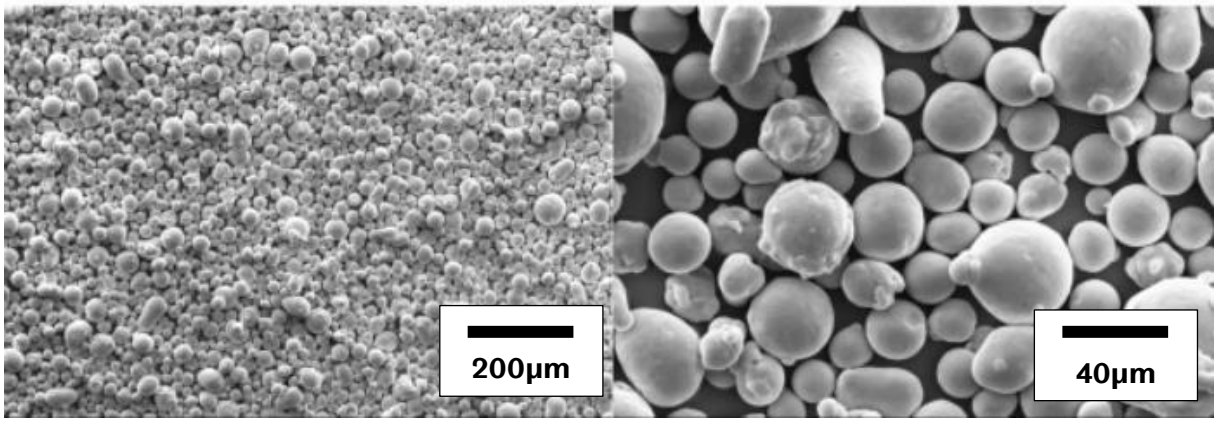

Figure 1-18 - Micrograph of the gas atomised AlSi10Mg powder. Satellites can be seen on the powder and some of the particles are non-spheroidal [48].

Whilst the particles are predominantly spherical, there are non-spherical particles as well as satellites on the spherical particles. Some of the particles also have a rougher surface than others due to the gas atomisation process. When powder manufactured using plasma atomisation was imaged under SEM it was found to be more spherical as shown in Figure 1-19.

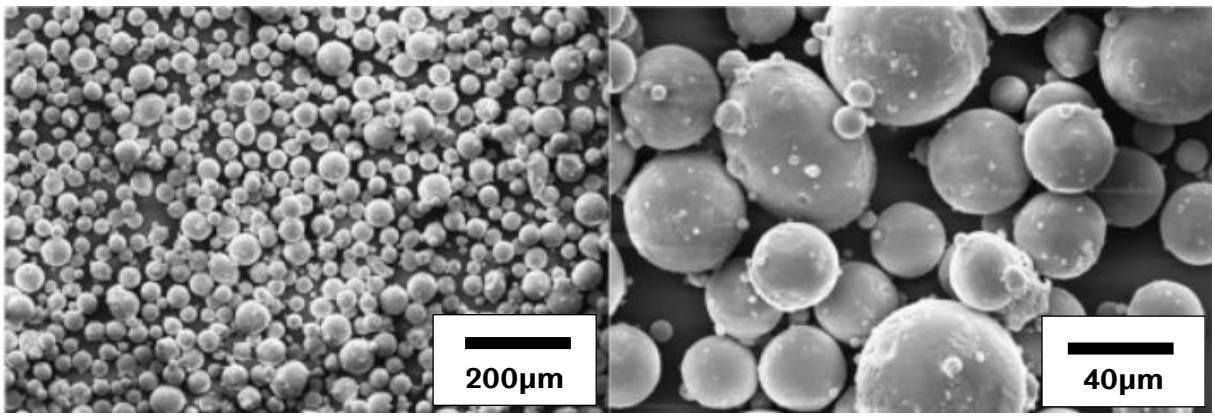

Figure 1-19 - Micrograph of the plasma atomised AlSi10Mg powder. There are still satellites on the powder but it is more spheroidal and the surface is smoother [48].

As well as being more spherical the surfaces of the powder particles are smoother. There are still satellite particles.

Riener *et al.* [48] studied the different properties of AlSi10Mg powder manufactured using gas and plasma atomisation. It was found that the aspect ratio of the powder was much higher as shown in Figure 1-20.

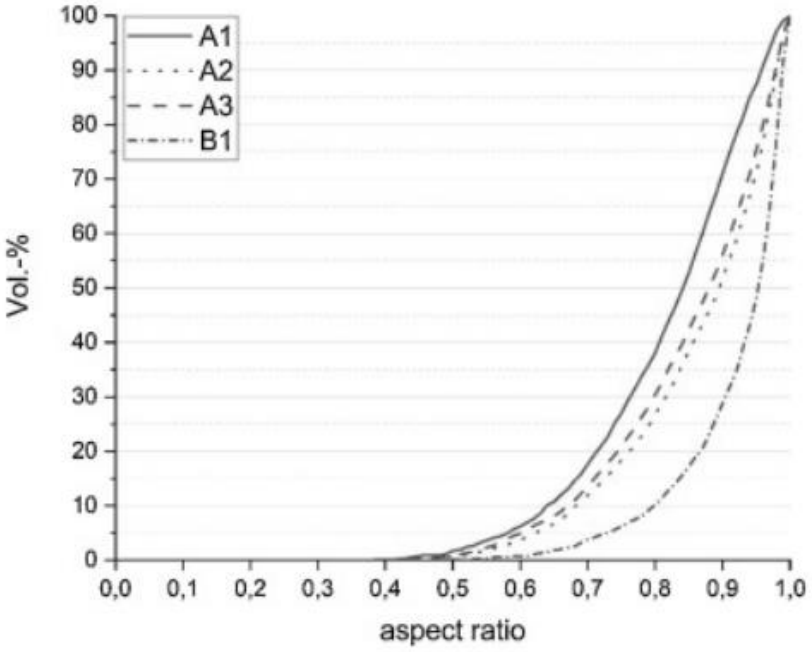

Figure 1-20 - Graph showing the aspect ratio distribution for AlSi10Mg powder manufactured using gas atomisation (A1-A3) and plasma atomisation (B1). B1 shows a significantly higher aspect ratio distribution [48].

From the figure, B1 represent the plasma atomised powder whilst A1-3 represent different batches of gas atomised powder. The steep gradient of the line for B1 shows that the powder is significantly more spheroidal than the other tested powder. This is further proved when looking at the flowability. The avalanche angle was tested for all four batches. The results are shown in Figure 1-21.

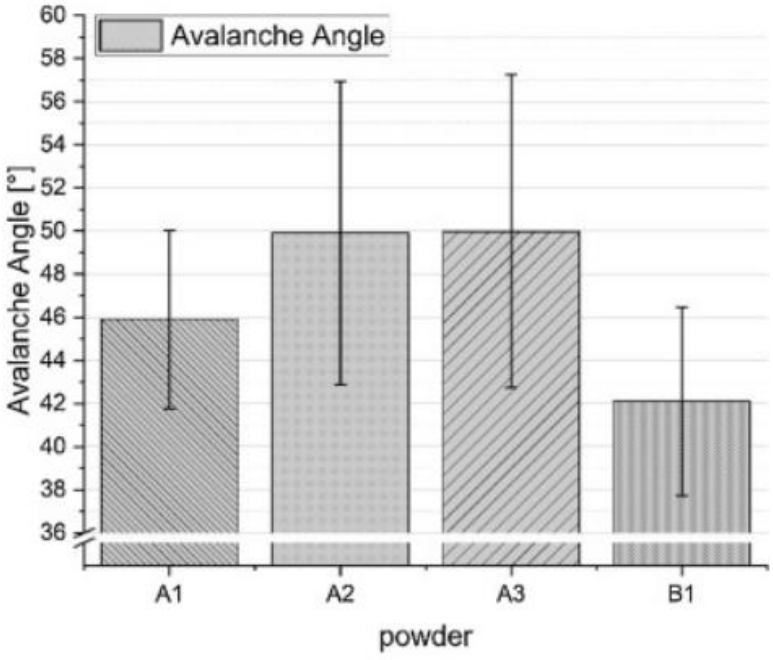

Figure 1-21 - Comparison of the flowability of the different batches of AlSi10Mg powder, manufactured using gas atomisation (A1-A3) and plasma atomisation (B1)[48].

B1 has a lower avalanche angle than the three other batches which shows that plasma atomisation can achieve a powder with a higher flowability. This is a key characteristic for powders in LPBF as the powder needs to be able to be spread across the whole buildplate. The powder morphology not only affects its flowability, but it also affects the absorptivity when exposed to the laser. Figure 1-22 shows the absorptivity for the different batches

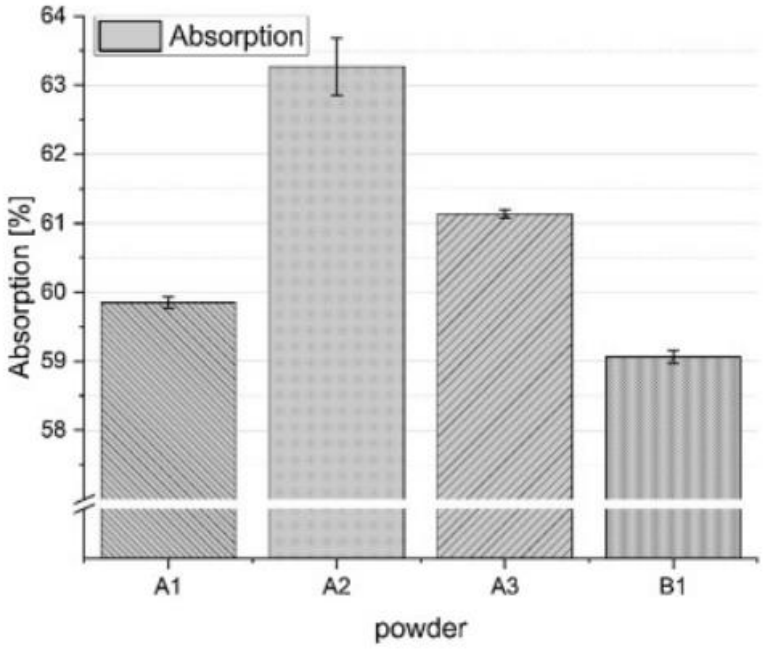

Figure 1-22 - Graph shows the absorptivity of the different batches of AlSi10Mg powder. The batches were manufactured using gas atomisation (A1-A3) and plasma atomisation (B1)[48].

It shows that there is a negative correlation between absorptivity and flowability. This is due to the additional satellites and non-spherical shape trapping more of the laser when its initially reflected off the surface of a powder particle.

The morphology of the powder has an effect on the final density of the part. This is shown in Figure 1-23 below.

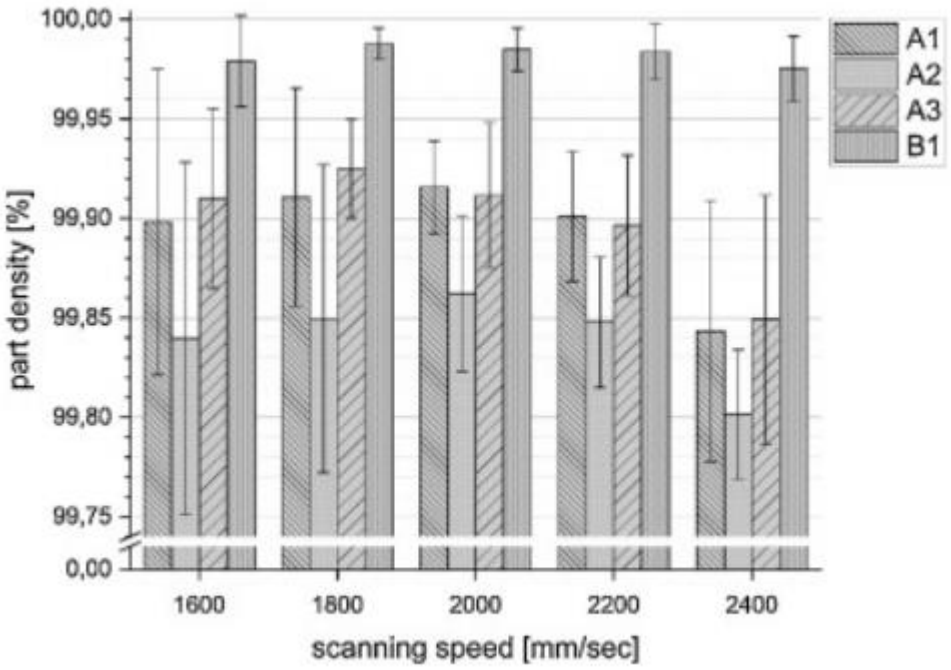

Figure 1-23 - Comparison of the achieved part densities at different scanning speeds for the different batches of AlSi10Mg. A1-A3 represent batches of gas-atomised powder, B1 represents plasma atomised powder [48].

From the figure it can be seen that the plasma atomisation powder resulted in the highest part density. This was explained through the good flowability of the powder. This would allow the powder to create a higher density layer of powder before melting. this would then lead to a higher density part as it started from a higher base level. This increase in density then translates to a higher UTS as shown in Figure 1-24 below.

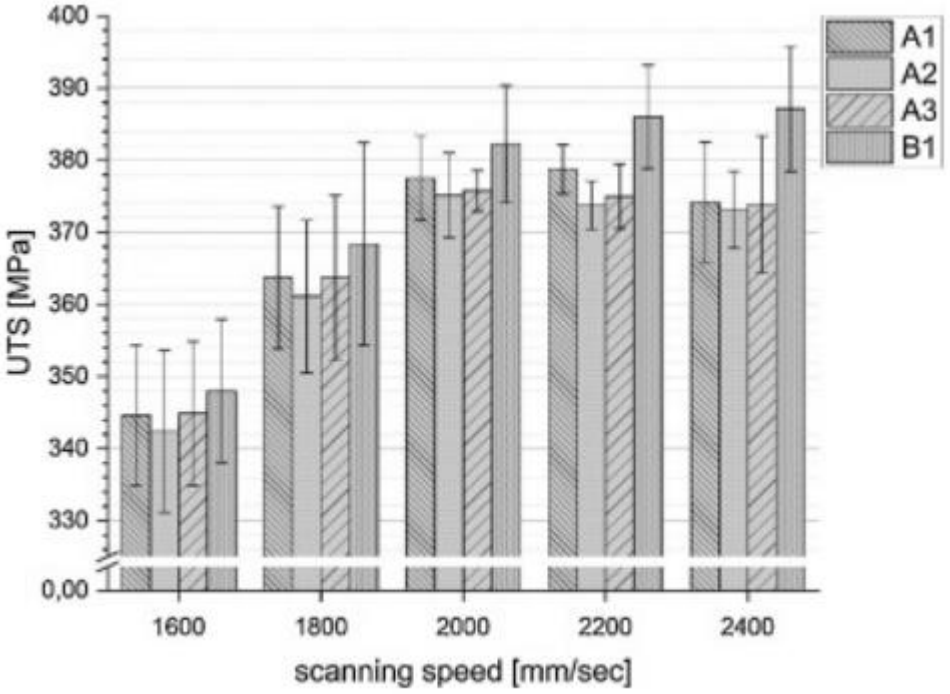

Figure 1-24 - Graph comparing the UTS achieved by parts built at different scanning speeds and using different powders. A1-A3 are batches of gas atomised powder, and B1 is plasma atomised [48].

This improvement in UTS was explained through the improved relative density for the plasma atomised powder, even at the higher velocities when the other batches' UTS stagnated or dropped the high relative density resulted in a high UTS. Finally, the plasma atomised powder resulted in improved elongation to failure, as shown in Figure 1-25.

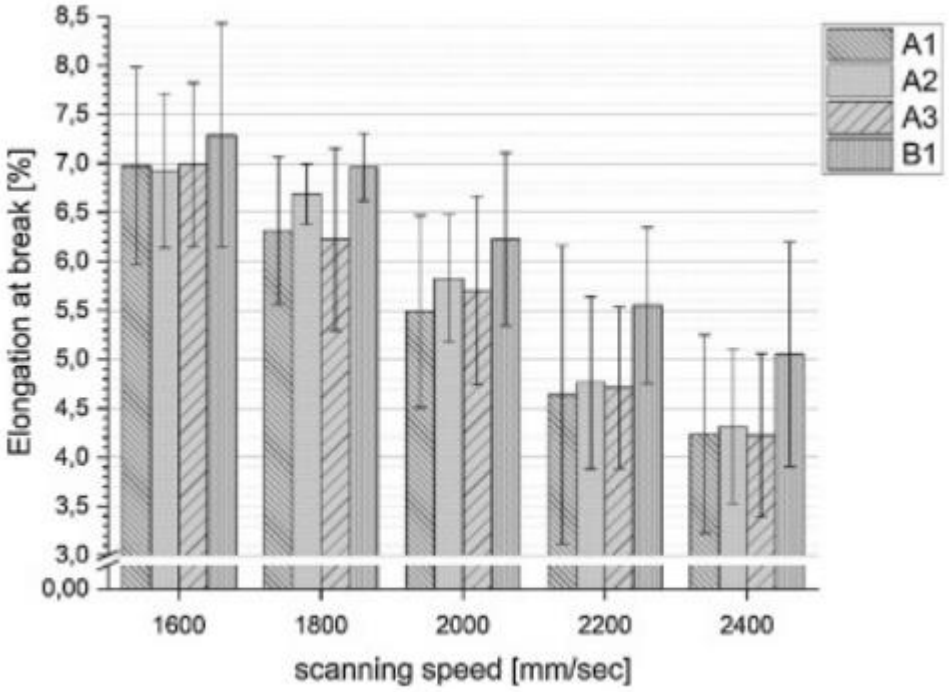

Figure 1-25 - Graph comparing the elongation to failure achieved by parts built at different scanning speeds and using different powders. A1-A3 are batches of gas atomised powder, and B1 is plasma atomised [48].

It had consistently the highest elongation to failure of all the batches. However, the properties did degrade as the scanning speed increased. These results show the need for powder analysis before part manufacture in order to understand the quality of the powder and hence how it will perform. This study will investigate the powder under SEM to see if the particles are spherical and if they have satellites.

1.3.1 Powder Recycling

One of the proposed benefits of LPBF and AM in general is that the final component weight is a much higher percentage of the raw material input (around 90%) than other manufacturing techniques. Ardila *et al.* [49] conducted a study on IN718 and the effect that recycling has on the powder distribution powder internal porosity and final mechanical properties. When a particle size distribution (PSD) analysis was conducted it was found that after 7 uses there was no change in the distribution as shown in Figure 1-26Figure 1-1 below.

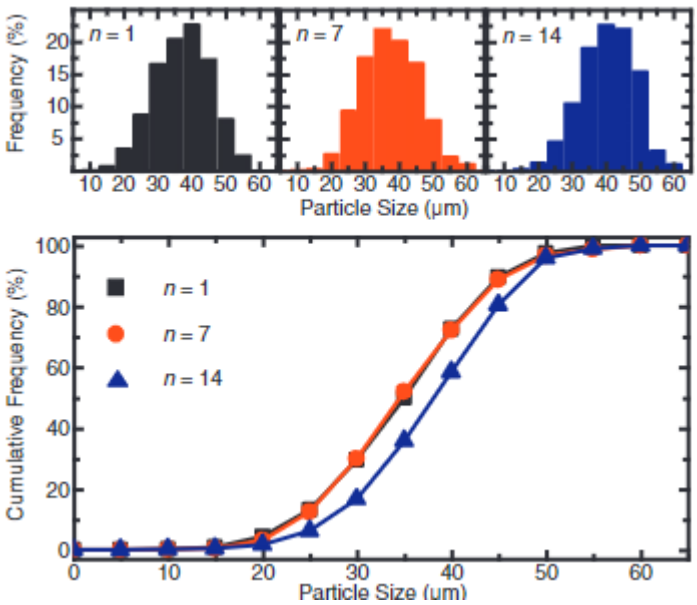

Figure 1-26 - Graph showing the different particle size distributions for powder samples after being used 1 7 and 14 times. The feedstock powder is IN718 [49].

After 14 times there was a slight change in PSD. There were fewer smaller particles and more larger particles as particles started to stick together. However, the variation with respect to nominal values was only 10%, which was small enough to not significantly impact porosity or mechanical properties as will be shown later. The porosity was investigated through taking a cross section of the powder and measuring the internal porosity. This showed that there was no change in internal porosity (Figure 1-27).

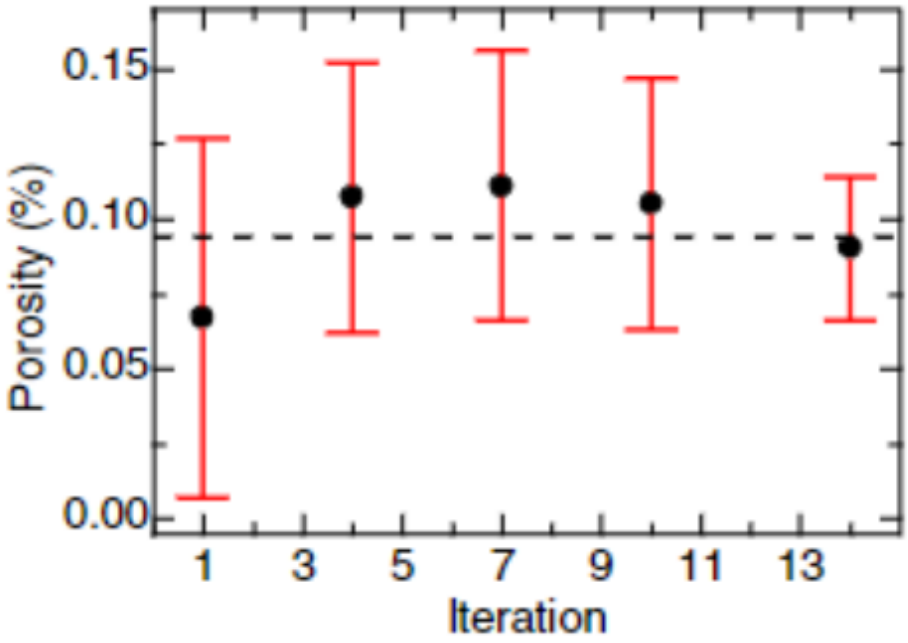

Figure 1-27 - Graph showing the porosity found in powder samples taken after a certain number of uses. IN718 was used as the feedstock powder [49].

Across all iterations the average observed porosity was below 0.12% it was also independent of the iteration number which showed the possibility for recycling. The Charpy test results reinforce this conclusion as shown in Figure 1-28.

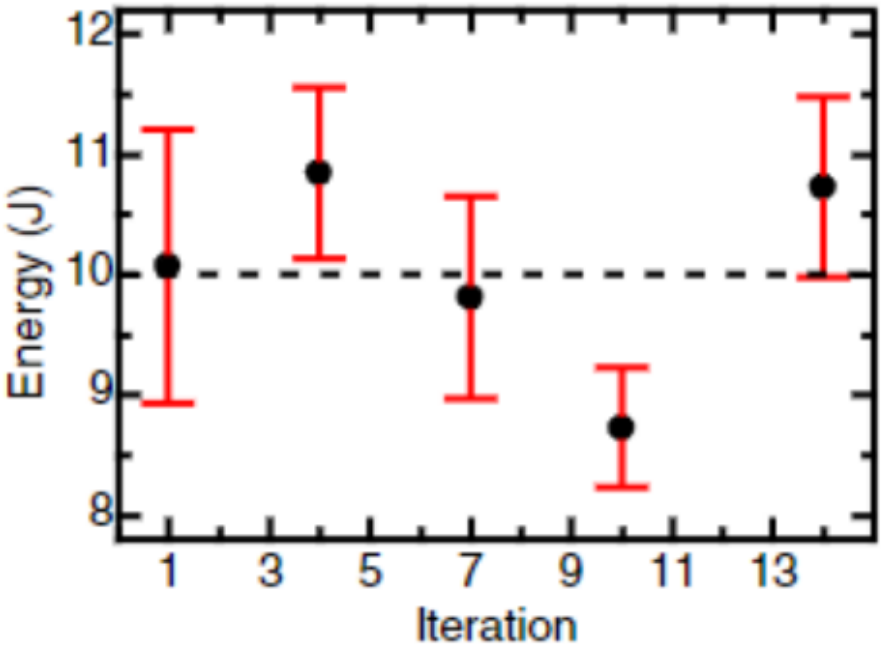

Figure 1-28 - Graph comparing energy required to fracture a Charpy test sample with how many times the IN718 powder had been recycled [49].

The results show no correlation between required energy to cause fracture and the number of times the powder had been used. In this study the powder will be reused multiple times. The quality of the powder will be investigated by monitoring the chemistry of the powder instead of conducting mechanical tests. This along with SEM imaging of the powder particles and a PSD analysis will inform us if there is a degradation of the powder after multiple uses.

1.4 Hot Isostatic Pressing (HIP)

Hot Isostatic Pressing (HIP) is a method of near net shape manufacturing where the simultaneous application of high pressures and temperatures are used to consolidate the material into a fully dense workpiece [50]. Powder is usually used as a feedstock, the process results in high density, highly complex and homogenous microstructure. It can also be used to heal castings where porosity is present. The layout of a HIP system is given in Figure 1-29.

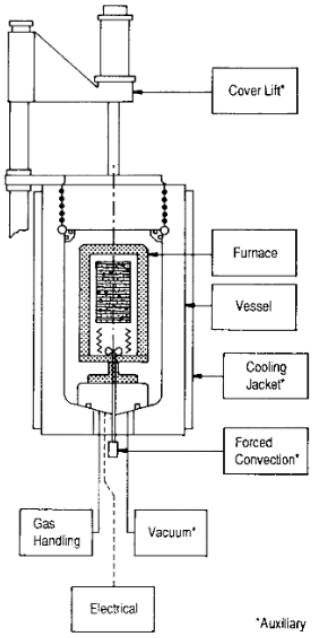

Figure 1-29 – A representative drawing of the layout of a HIP system [50]

HIP is sometimes used as a post processing stage for AM parts. It is used to reduce porosity and improve consolidation [51] where the density was increased to 99.98% relative density. In this study, the objective is to achieve a fully dense part without the need for HIP. The microstructure will also be evaluated to find the degree to which epitaxial growth has occurred as HIP is associated with homogenous equiaxed grain structure.

1.5 Additive Manufacturing

Additive manufacturing (AM) is a family of alternative processing techniques that promise to increase flexibility in the manufacturing process. AM works through selective addition of material in areas where it is needed until the part is formed. This method differs from most current manufacturing methods classed as subtractive as the initial input material is gradually cut away where necessary until the desired part geometry has been achieved. Initially patented in 1984 [52], AM was developed for plastics where the polymer was cured to a specific cross-section using UV light [53]. In the mid-1990s, the first metals were printed [51]. With AM in general, there is much promise as a manufacturing process as it allows for complex geometries that would not otherwise be possible [54]. These geometries can be designed to better account for the stresses experienced by a part in service or calculated through modelling. By reducing material where stresses are lowest and increasing material in regions of high stress [55], a more efficient part is made that could produce weight savings on a traditionally manufactured part whilst withstanding greater forces. AM reduces the amount of input material significantly; it is estimated that compared to traditional manufacturing methods. AM can result in an 80% reduction in material usage [56], allow the use of many more expensive or exotic alloys as the input costs would be significantly reduced, and help reduce the environmental impact of a part's manufacture. The environmental impact of manufacture is becoming an increasingly more significant concern as all industries seek to reduce their carbon footprint. Multiple parts of an assembly can be combined into one part; this reduces the amount of input material required, reduces the cost of manufacture, and reduces the manufacturing process's environmental impact [57]. A reduction in the cost of tooling is another reason why many manufacturers are developing parts using AM [58].

In general, AM machines are expensive. As a result, the parts manufactured using this process are of high value. The medical and aerospace sectors are two industries in which high-quality parts are crucial. These two industries have invested heavily in AM as it suits their requirements. For aerospace, AM's weight savings and geometrical freedom are critical. In contrast, the ability to create growth-promoting lattices for medical applications and build fully personalised prosthetics and implants is revolutionary. Another advantage of AM that makes it particularly desirable for these two industries is the cost for small batches. This method means a small number of parts can be created without a cost penalty [58]. The

machining cost of going from the forged part to the finished part is high for many metallic parts. With AM, this cost is reduced as the part requires less finishing than traditionally manufactured parts as it is closer to the final geometry.

These benefits have yet to be fully realised due to the reduced knowledge associated with AM part performance and the reduced control over microstructure that is currently available using AM [59]. This work will address some of these concerns by characterising Haynes 282 which due to its weldability is suited to AM [60]. This alloy is designed for gas turbines in the energy sector and turbine blades and combustion chambers in the aerospace sector. These environments require a material that can withstand high temperatures and stresses. The alloy is designed to operate at temperatures ranging from 600°C to 900°Cand has better creep resistance than any comparable alloys tested [5]. AM is preferable for turbine blades as weight is crucial in determining an engine's performance. By understanding the effect that different steps within the AM process have on the part, better design decisions can be made. These decisions will be more informed about how changing a particular AM parameter or set of parameters might have on part quality and crucially whether a part can be used in-service. This work will increase the trust in this alloy to be used successfully and safely.

The lack of certainty of mechanical properties is one of the significant drawbacks and hindrances to the more widespread adoption of AM as a manufacturing technique [63]. This uncertainty results from the complex interactions between the heat source and the feedstock and the rapid solidification of the material. This causes complex microstructural features. It means that it is less likely to be used in safety-critical parts, an area where it would be most suited due to weight savings. Also, to date, the dynamic properties of alloys manufactured using AM are much lower than those of forged parts. In their review of AM, Vaezi *et al.* [61] highlight fatigue performance as a reason that AM has not seen wider adoption. This work seeks to address this by optimising the Laser Powder Bed Fusion (LPBF) processing to obtain the best mechanical properties. It will also look to reduce the variation in part performance between different builds, as Lewandowski *et al.* [62] have highlighted this as a necessary research topic for future work.

1.5.1 Laser Powder Bed Fusion

Laser Powder Bed Fusion (LPBF) is a technology within AM. It is a process through which a part is built incrementally. Initially, a Computer-Aided Design (CAD) file of the desired part is

generated. This file is split into layers of cross-sections. Inside the machine, a layer of powder is swept across a build area. The cross-section of the part is then melted using a laser, and then the build area is dropped. The process is repeated until the part has been made. Figure 1-30 shows schematically how this process works.

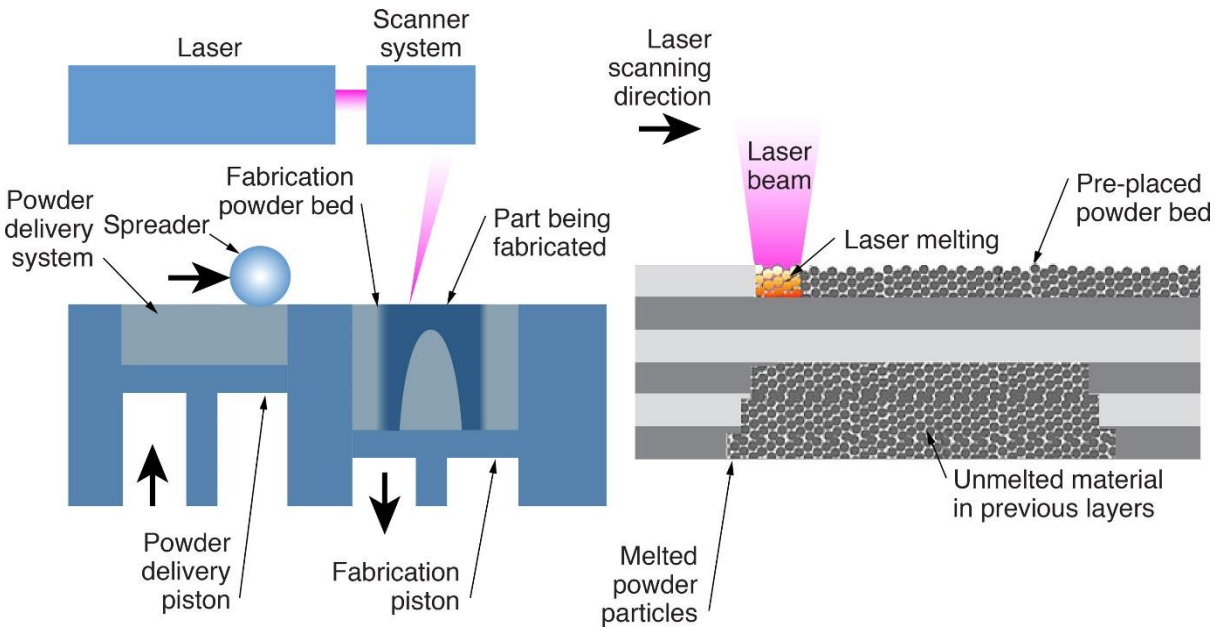

Figure 1-30 - A schematic diagram showing how a typical Laser Powder Bed Fusion (LPBF) machine works. [63]

It is one of the most widely used AM technologies for printing metals. LPBF [63] is widely regarded as having a better surface finish and resolution than other technologies. It creates a part that has excellent fidelity to the original CAD and allows for the printing of small features. This sacrifices speed and size of the built part as the build chambers are smaller than other technologies. The speed of the laser melting the powder reduces the productivity significantly compared to other techniques.

C. Y. Yap *et al.* [64] gave a good overview of the background to LPBF or Selective Laser Melting (SLM) (SLM is a proprietary technology, but the two terms are used interchangeably). Yap describes the phenomena that are present and need to be considered when investigating LPBF. These include absorptivity of the powder material to laser irradiation balling that disrupts the creation of continuous melts, thermal fluctuations that lead to crack formation and part failure. These are problems that need addressing. All these issues will be further elaborated on in later sections, as well as detailed uses of LPBF in the industry for metallic parts and the properties of LPBF samples, including relative density, static material properties

and surface roughness. This project will discuss the relative density and static and dynamic mechanical properties concerning nickel superalloys and Haynes 282. Balling, one of the issues presented by Yap, occurs due to incorrect processing parameters and was investigated by N. T. Aboulkhair *et al.* [65]. They showed a different more time and energy-efficient manner to reduce balling where the speed is increased instead of decreased. However, this increased speed still led to the formation of large depth melt tracks and thus increased the likelihood of keyholing. Keyholing is another type of defect often found in AM parts and will be discussed in more depth in Section 1.8. This project will build on T. Qi *et al.* [66], which, although on aluminium, has many applicable conclusions to the work undertaken in this project, whilst also detailing strategies of avoiding keyholing and working solely in the "conduction" mode.

In addition, W. E. King *et al.* [63] outlined some of the future challenges that face LPBF before it becomes a widely adopted building method. This work provided a sound basis to find some of the research avenues on which to venture to maximise the utility of this project. Furthermore, King *et al.* [63] have provided good state of the art and guidance on how some of these challenges may be approached and overcome. Qualification of parts for use in service is considered one of the significant hurdles for adopting AM by manufacturers, 47% of which identified this as a barrier. King *et al.* [63] states that understanding the physical mechanisms behind the LPBF process is necessary to achieve this goal. This review also evaluates computational and modelling techniques that can be used to model the physical processes, which are the same as described by Yap *et al.* [64].

1.5.2 Other Additive Manufacturing Techniques

1.5.1.1 Direct Energy Deposition

Direct Energy Deposition (DED) is an AM technology that uses metal wire or powder deposited onto a substrate coupled with a simultaneous melting to form a part. A part can be created by rotating the substrate in 3D space and moving the feedstock and heat source. Thompson *et al.* [67] outlined the history of DED as well as its uses, advantages and limitations. A schematic diagram for the process is given in Figure 1-31 below.

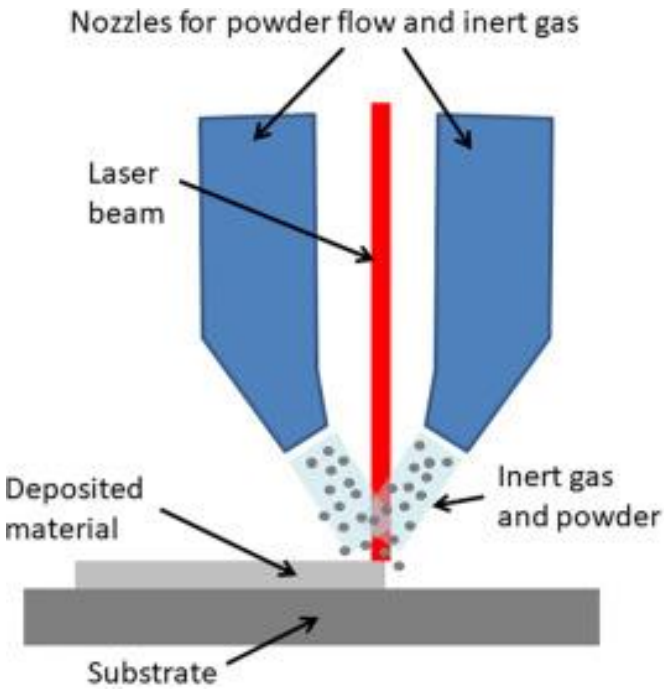

Figure 1-31 - Schematic drawing of the DLD process [68].

Of the available types of DED, Direct Laser Deposition (DLD) is the most used. In this technique, the powder is blown onto the substrate whilst being melted by a high-powered laser. DLD is very flexible in the types of geometry that can be produced, particularly when the substrate can move on its axes. It is especially suited to create thin-walled sections. Compared to other AM processes, it can repair damaged components by directly printing onto the surface that needs to be repaired [69]. Another benefit of DLD is that different powders can be mixed *in situ* to create a functionally graded component [70]. However, there are issues with DLD that need to be resolved before it achieves wider usage. Control of the meltpool and thermal history is one. Due to the high power of the laser and the constant movement of the powder during the process, the meltpool and thermal history can be hard to control and must be understood before this technique is used in-service [71].

1.5.1.2 Electron Beam Melting

Electron Beam Melting (EBM) is a powder bed technology that uses an electron beam to melt the powder to a specific cross-section. The bed is then dropped, a new layer is swept across, and the process is repeated. A schematic diagram of the EBM process is given in Figure 1-32 below.

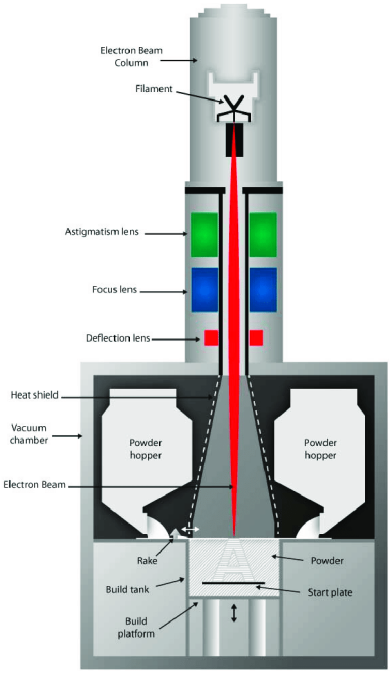

Figure 1-32 - Schematic drawing of the EBM process [72].

Compared to other AM techniques, it is relatively fast. This speed is due to the large powder size (45µm-150µm), allowing for a thicker layer size and higher production rates [73]. The electron beam is guided around the cross-section by magnets. Therefore, a high scanning rate can be used as a preheating step and reduces residual stress in the component. Due to the nature of the electron beam and its control using magnets, only certain alloys can be used, i.e. those that are not affected by a magnetic field. In addition, the surface roughness is higher due to the large layer sizes compared to other AM processes. Finally, there is a high tendency for epitaxial growth due to the large layer sizes and the preheating step. This epitaxial growth can cause a high degree of anisotropy [74].

1.6 Machine Capability

1.6.1 Machine Characterisation and Calibration

Machine characterisation is essential to achieving the desired end microstructures and mechanical properties. Knowing how the machine will behave during the printing process and what parameters are achievable makes it easier to understand what the inputted processing parameters will do in terms of laser behaviour, movement, size, and accuracy. Standard builds, called artefacts used to calibrate machines, have been developed. One of the most extensive is the NIST sample build. Moylan *et al.* [75] compared existing artefacts and their features to develop their own. The diagram of this build is shown below in Figure 1-33.

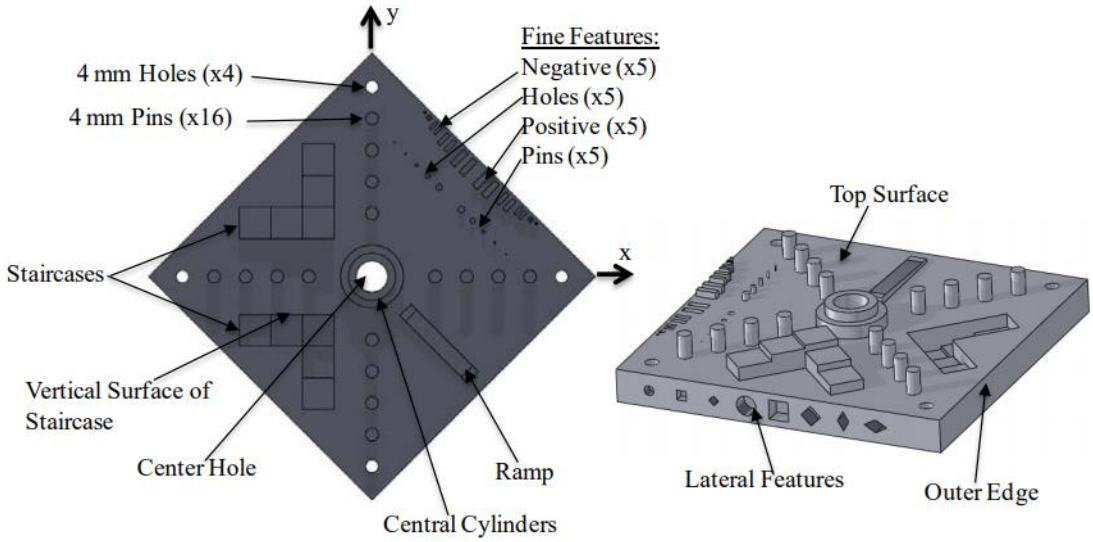

Figure 1-33 – A diagram showing the NIST calibration build to test capability and accuracy. This build has representative geometries of different features and means that the results of different machines can be compared to one another [75].

This artefact includes many features to test how the laser and machine produce parts and specific geometric features (such as holes of a certain diameter) to a given CAD specification. While this achieves the goal on a macro scale, the features can be measured and compared to those of a different machine, it has drawbacks. The powder is a factor in this test, as different powder batches and size distributions will give different results. This artefact is costly and time consuming to make. This part is 17mm tall and has a volume of 101000 mm^3. This artefact will determine if the parameters chosen will work on that material in that machine. In this study, this calibration process will be simplified to be quicker and cheaper to perform, thus enabling it to be performed on multiple machines. It will also focus on the laser and its interaction with

a given known material (such as 316L stainless steel plate). Its accuracy and path will be determined. These can then be combined with modelling work (see Section 1.7.5) to calibrate machines to perform how they are expected to perform. The result of these tests will still be able to be compared across machines, but it should also work across materials and types of laser (see Section 1.6.2).

1.6.2 Laser Characteristics

1.6.1.1 Laser Wavelength

Laser wavelength affects absorptivity, i.e. how much of the energy from the laser is absorbed or reflected by the powder. Different materials will have different absorptivity at different wavelengths. Kruth *et al.* [76], in their review paper, found that Nd: YAG lasers were more applicable than traditional CO_2 lasers for SLM applications due to the better absorption at 1060nm wavelength compared to 600nm for the CO_2 laser Figure 1-34 show the absorptivity of different materials at different wavelengths.

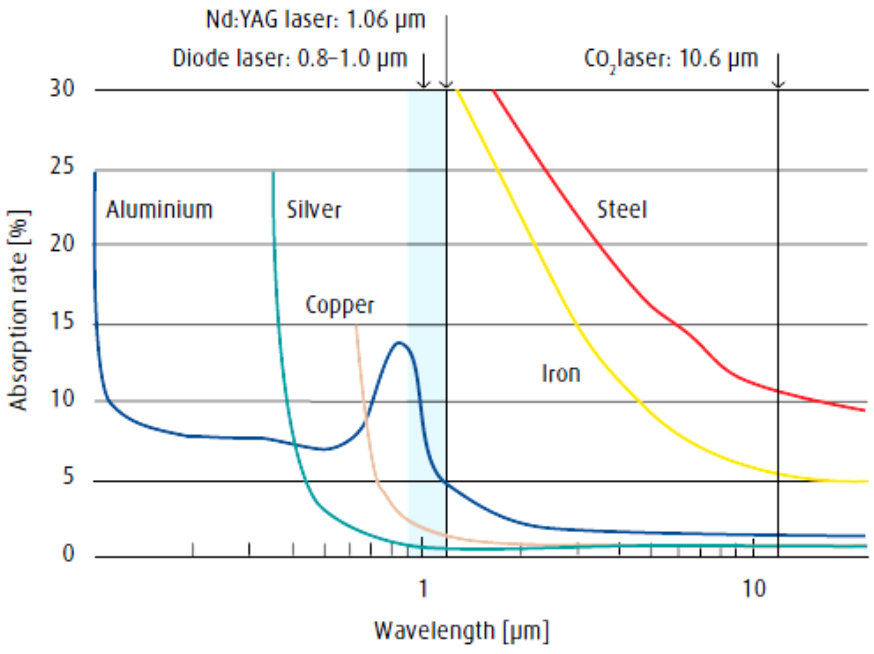

Figure 1-34 – The absorptivities of different metals using different laser wavelengths are shown. The versatility of the 1060nm laser is shown as it is absorbed by aluminium, steel, and iron [77].

The absorptivity of aluminium is crucially higher at around 5% compared to 1% for the CO_2 laser. This absorptivity is essential as aluminium in the alloys needs to be melted.

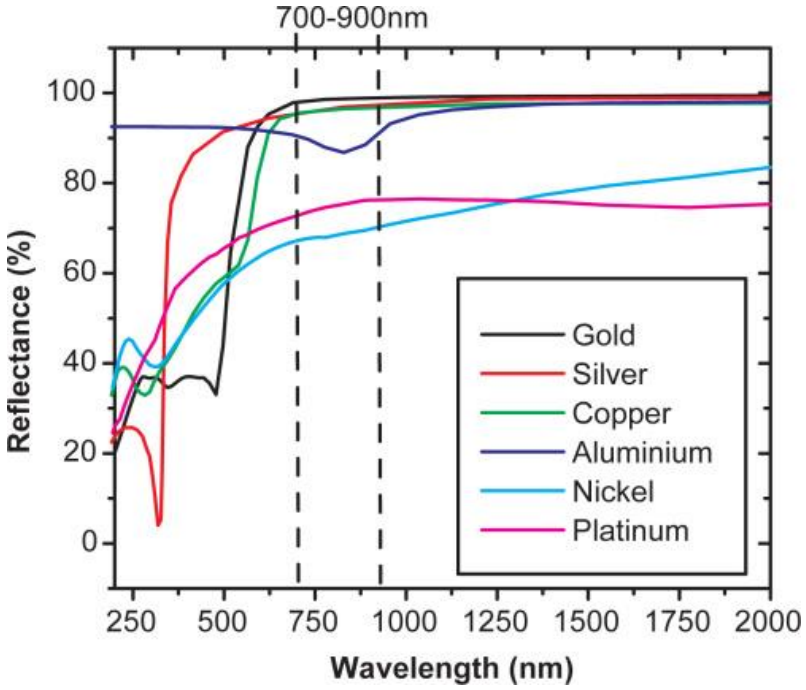

Figure 1-35 – The reflectance (reciprocal of the absorptivity) is shown for different metals, including nickel, which has a reflectance of 70% at the 1060nm wavelength. This reflectance will allow for the complete melting of the alloy [78].

Reflectance is the reciprocal of absorptivity. Figure 1-35 [78] shows how the absorptivity is around 0.25 for Nickel at 1060nm. Absorptivity is lower than steel and iron but higher than aluminium and copper, with absorptivities of 0.05 and 0.02, respectively. A lower wavelength laser is not used as there is only a small amount of aluminium, and an absorptivity of 0.25 is acceptable. Smaller wavelength lasers are also more expensive, which is a factor that must be considered. The absorptivity will be considered in Section 1.7, where there is an absorptivity coefficient.

1.6.1.2 Pulsed and Continuous Wave Laser

Within LPBF, there are different ways the laser can move to melt the part. These are used by different manufacturers and are often patented as a result. They can be broadly separated into two categories pulsed and continuous. The methods by which these lasers move with respect to time are outlined in Figure 1-36.

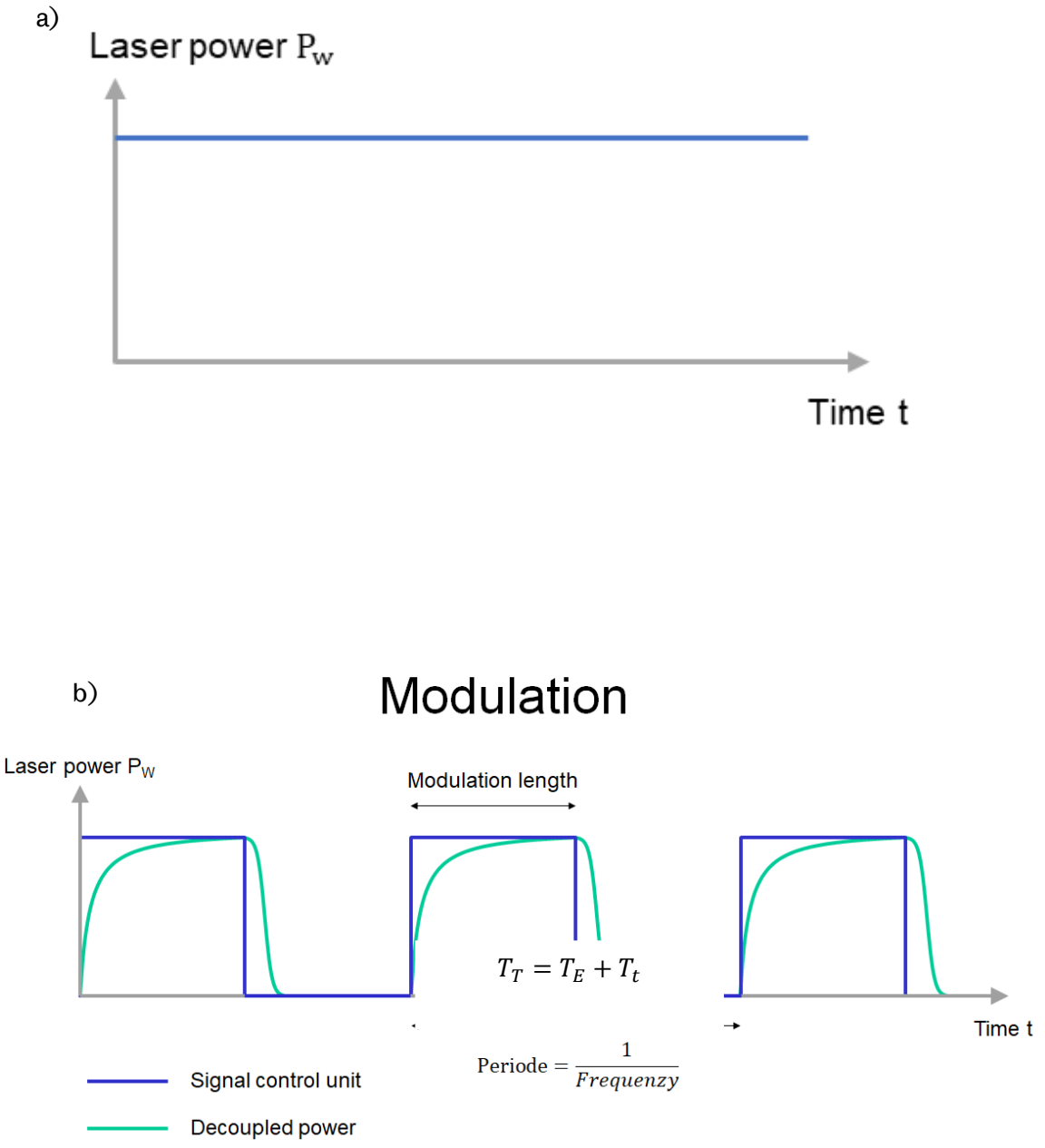

Figure 1-36 –Schematic graphs show how power changes with time for continuous (a) and pulsed (b) lasers. There is a ramp-up stage for the pulsed laser while the laser gets to full power. Accompanying this is the time taken for the laser to travel to the new position T_t.

For continuous wave, the power is constant with respect to time, and the velocity is constant across the hatch length. With pulsed lasers, the power oscillates between on and off modes. Thus, the total time T_T is equal to the exposure time T_E and travel time T_t. Between pulsed modes, some machines stop when the laser is on (stationary pulsed) and those that continue moving at a steady velocity whether the laser is on or off (constant velocity pulsed). Caprio *et al.* [79] discuss the duty cycle, which is the ratio of the laser being on to the total time. In this project, the effect of the duty cycle will be explored. Additionally, Caprio *et al.* [79] do not

mention that the laser takes time to ramp up to full power (this can be seen in Figure 1-36 by the green curve). This ramp-up will be investigated in this study. The study does mention that there are advantages to both modes. The continuous mode is useful for bulk sections due to its efficiency, whereas the pulsed mode is suitable for fine features. The machine that Caprio *et al.* [79] use is a constant velocity pulsed mode machine. For this study, obtaining finer features and greater fidelity to the CAD input is not an objective. Instead, the ability to translate from one machine to another will be investigated. This translation is crucial to the industrial partner as currently, as part of the qualification process, the part is tied to the machine. If it can be shown that similar microstructures can be achieved using stationary pulsed mode and continuous mode lasers, this will enable the decoupling of part and machine. Freeman [80] found that continuous and stationary pulsed velocity can be made equivalent to Equation 1-2 when the point distance is small.

$$V = \frac{D_{PD}}{T_E + \frac{D_{PD}}{V_T}}$$

Equation 1-2

Where D_{PD} is the point distance and V_T is the laser travel velocity between exposures. In Freeman's study, the aim is to create large thermal strains brought about by large energy densities. As such, there is a significant overlap of the meltpools. This overlap can be seen in Figure 1-37

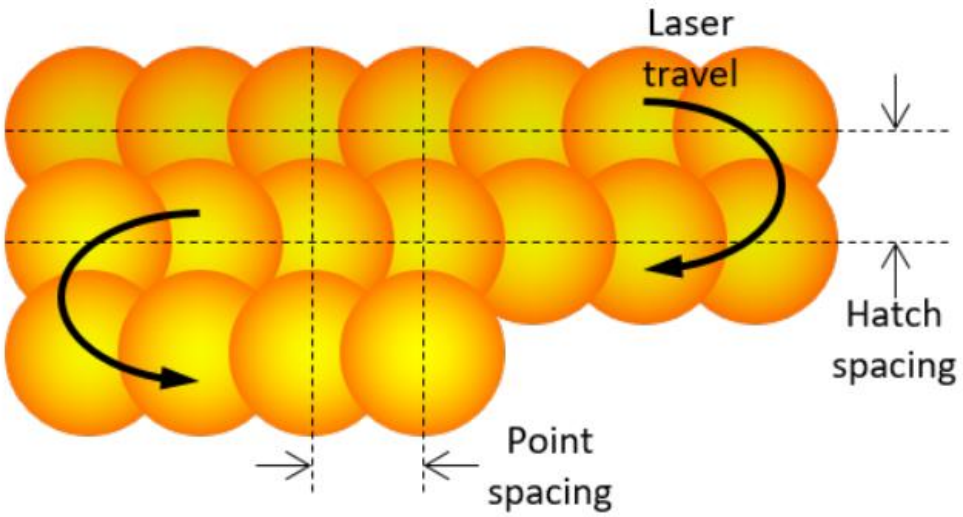

Figure 1-37 – Schematic to show how the laser moves in a stationary pulsed machine and the different parameters. The melt pools must overlap to create a fully dense part. [80].

In this work, the gap between the meltpools will be increased in subsequent tests to speed up the process. There is only a short time between the laser being turned off after melting one region and being turned on in an adjacent region. It is hoped that the two meltpools will form a continuous meltpool. This melting would require short exposure times and medium distances (around one beam diameter). Initial studies using this type of laser have opted for long exposures and large distances. Demir *et al.* [81] were limited in their velocity as they opted for large overlap and long exposures. Stwora *et al.* [82] encountered a similar problem with the parameters used, tabulated in Table 1-3 below.

Table 1-3- The parameters investigated by Stwora et al. [82] *in their work on a stationary pulsed laser. When looking at the exposures and point distances and comparing them to Equation 1-2, velocities range from 0.5 – 1 m/s. This velocity is slower than the 2m/s, creating fully dense parts using a continuous laser* [82].

Investigated parameters of SLS process		
Laser power	(P)	200-400 [W]
Scanning Speed	(SP)	100-130 [mm/s]
Exposure Time	(ET)	75-100 [μs]
Point Distance	(PD)	45-75 [μm]

From this table, the speeds achieved using the pulsed mode (exposure time and point distance) are between approximately $0.5 - 1\ m/s$ this contrasts with other studies which have used continuous-wave to achieve speeds up $2\ m/s$. This study by Koutiri *et al.* [83] uses parameters up to $2\ m/s$ to achieve near fully dense parts. This would be impossible with the overlapping of meltpools as currently practiced in stationary pulsed mode machines.

1.7 Process Parameters

1.7.1 Parameter Selection

Powder Bed Fusion is a well-researched AM technology where much research has gone into relating processing parameters to build quality. Multiple papers looked at microstructure and how this can be optimised by choosing processing parameters. Aritsoy *et al.* [84] looked at how build parameters affected microstructure, grain size and growth direction. They went into detail about how the microstructure and the cells are affected by changing parameters. The study uses image recognition to identify cells and their growth direction. In this project, similar techniques will be used to identify cell size. However, this project will use EBSD to identify growth direction and grain orientation. Though this is a slower technique, it is widely used and the results more reliable. This project will also utilise a more straightforward surface response design of experiments (DoE) as the results can be more easily interpreted.

Original surface response DoE looked at single tracks and were material specific. "Ideal" parameters were found by inspecting the melt track that parameters left. Kruth *et al.* [85] produced one of the first studies into parameter selection. They conducted their studies and categorised their results into balling, smooth and no connection where a medium power and velocity lead to the best outcome (Figure 1-38).

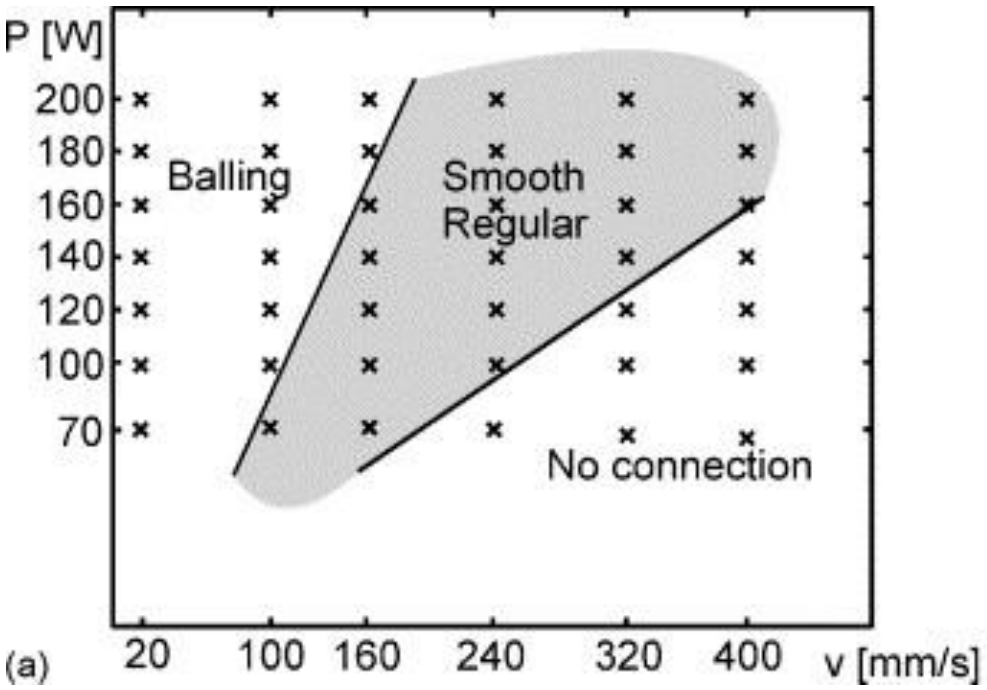

Figure 1-38 - The effects of parameter sets on the appearance of weld tracks. There is a region of smooth tracks that can lead to good build quality [85].

The boundaries of the acceptable parameter space are the solid black lines. Kruth *et al.* [85] found that if parameters were kept within these lines, that would create consistent melt tracks. This work does not consider hatch spacing and layer thickness that also contribute to build quality and reduce porosity.

This work was expanded and generalised to account for different materials and AM techniques by Thomas *et al.* [86]. They summarised multiple different AM technologies as well as different materials to see if there is a commonality in energy input when material properties are taken into account, producing the map shown in Figure 1-39.

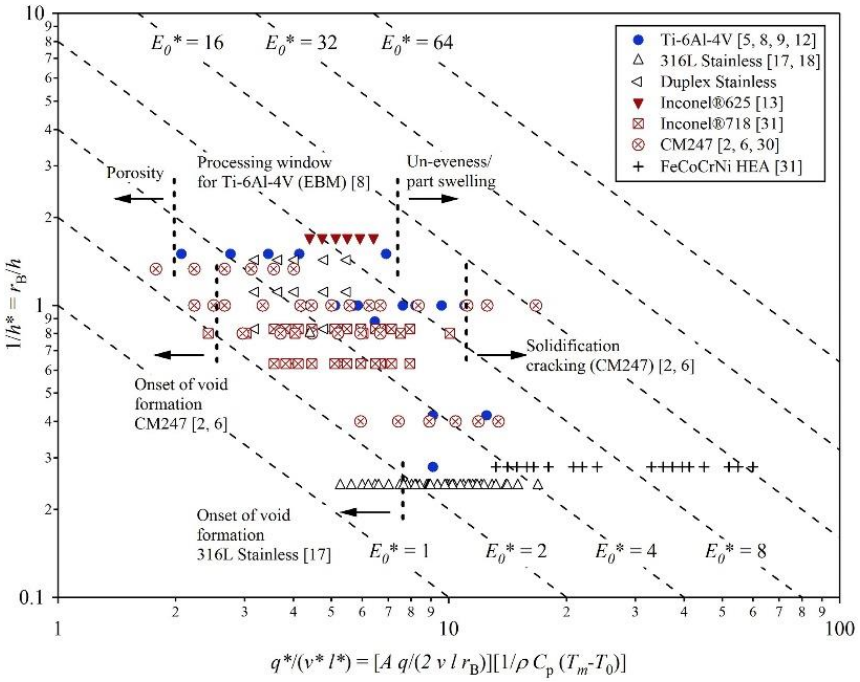

Figure 1-39 - This normalised map shows the results of parameter studies for different experiments that looked at different technologies, not just LPBF [86].

The x-axis of this chart is given by the normalised energy, which has the equation:

$$E = \frac{Aq}{2vlr_B\rho C_p(T_m - T_0)}$$

Equation 1-3

Where E is the energy imparted into the material, A is the absorptivity coefficient (See Section 1.6.1.1), q is the power of the laser, v is the velocity, l is the layer height, r_B is the beam radius, ρ is the density, C_p is the specific heat capacity, T_m is the melting temperature and T_0 the initial temperature.

The y-axis is the normalised reciprocal of the hatch spacing obtained using the equation:

$$\frac{1}{h^*} = \frac{r_B}{h}$$

Equation 1-4

Where h is the hatch spacing and r_B is the beam radius. From Figure 1-39, there is a region where the best build quality is to be found. An initial set of starting parameters can be determined using this chart. The parameter space boundaries can be estimated by limiting the parameters to the dotted lines. A drawback of this diagram is that whilst it can give a good

first estimate, it cannot precisely guide. Both the scales are logarithmic, so the range of values for both the normalised energy (x-axis) and normalised hatch (y-axis) are large.

1.7.2 Laser Parameter Effects

How the laser is used to build the part can affect the part density, the microstructure and the part mechanical properties. Hilaire *et al.* [87] investigated the effect of changing parameters on porosity, microstructure and high temperature mechanical properties of LPBF IN718. It was found that decreasing the hatch overlap resulted in denser samples, this was explained by better overlap between the meltpools. The results of the analysis are shown in Figure 1-40 below.

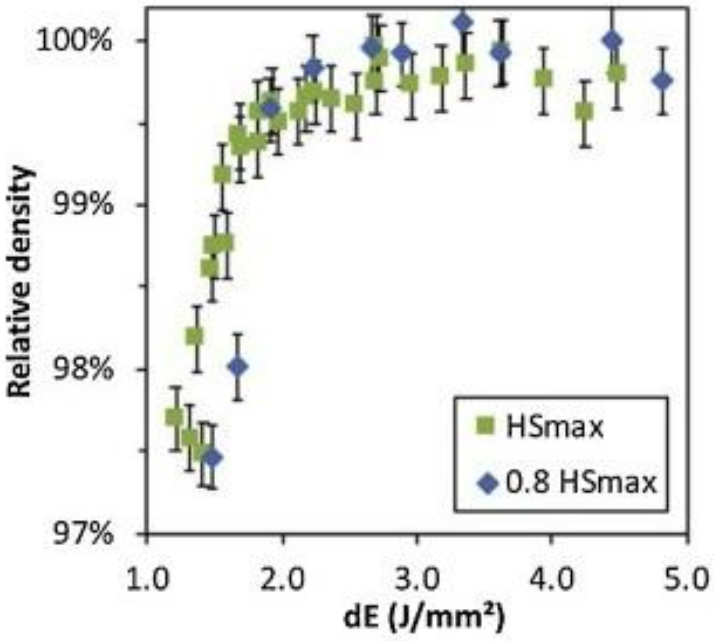

Figure 1-40 - Graph showing the effect on the relative density of built IN718 of increasing input energy at two different hatch spacings [87].

The results show that for a given energy input, a lower hatch spacing results in a higher relative density. A similar experiment was conducted at two different power levels where the scanning speed was varied. This is shown in Figure 1-41.

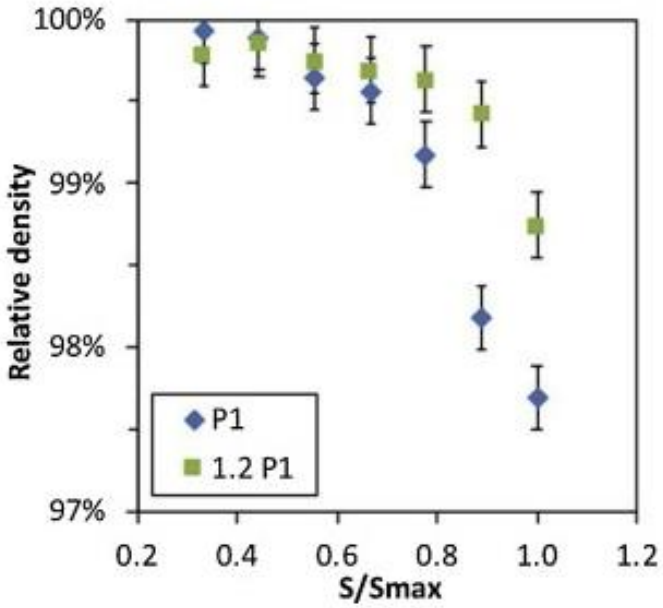

Figure 1-41 - Graph showing the effect of reducing scanning speed on the relative density of built IN718. Two different power levels are shown on this figure [87].

The higher power results in a higher relative density at each scan speed except the two lowest scan speeds. This was attributed to the onset of keyhole defect formation. Defect formation will be discussed in Section 1.8.1. In this project parameters will be adjusted to achieve a fully dense part. A surface response DoE will be performed as well as using a closed loop control and a machine learning algorithm to reduce porosity.

The effect of the process parameters on meltpool geometry and morphology was investigated. It was found that equivalent energy densities achieved through different process parameters resulted in different meltpool shapes. There was an increase in the depth of the meltpool with increased power whilst experiencing a stabilisation in the melt width. The change in melting mode is discussed further in Section 1.8.2.

It was found that processing parameters affected mechanical properties by Hilaire *et al.* [87] and Hilal *et al*. [88] found a correlation between process parameters and mechanical properties. Hilal *et al*. found the high-temperature creep performance improved if the process parameters were optimised such that there no defects present in the part. Defect effects on the part performance will be discussed further in Section 1.8.1.

1.7.3 Build Orientation

Due to the heat source building subsequent layers in the vertical direction parts built using LPBF exhibit epitaxial growth and anisotropy in their mechanical performance.

In their study Hilal *et al.* [88] performed small punch creep testing on builds in two different orientations. They tested at 90° to the buildplate (i.e parallel to the build direction) and at 30° to the buildplate, using the same parameters for both orientations. Figure 1-42 shows the results of these tests.

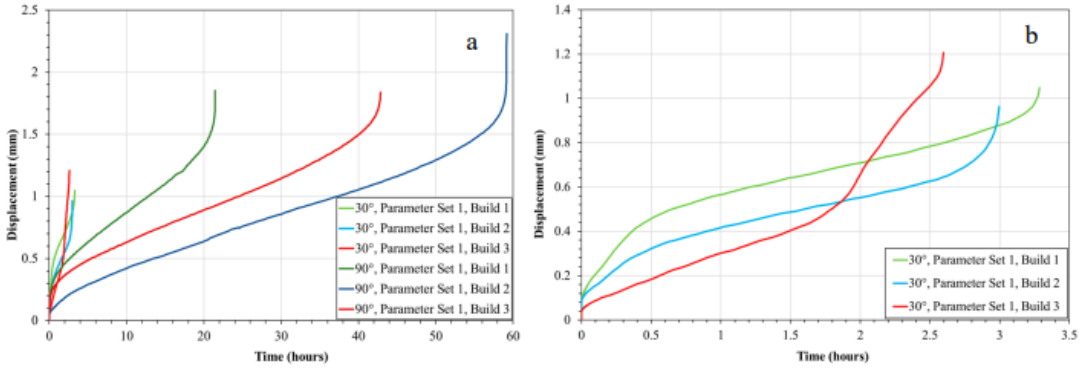

Figure 1-42 - These show the small punch creep test results in the 90° orientation and in the 30° orientation for CM247LC. (b) is an enlarged view of the 30° as the times to failure were much shorter [88].

Figure 1-42a shows how the 90° orientation results in much longer time to failure than the 30° orientation (Figure 1-42b). This was explained through the different grain sizes in the tested directions. The 90° sample had larger elongated grains in the test direction. When measured the 90° sample had an average grain size of 20.4µm after heat treatment whereas the 30° sample had a grain size of 9.9µm. The increased number of grain boundaries caused the drop in creep performance. The equiaxed grain structure in the tested direction resulted in brittle fracture for the 30° orientation. Figure 1-43a shows the starfish fracture pattern along the grain boundaries.

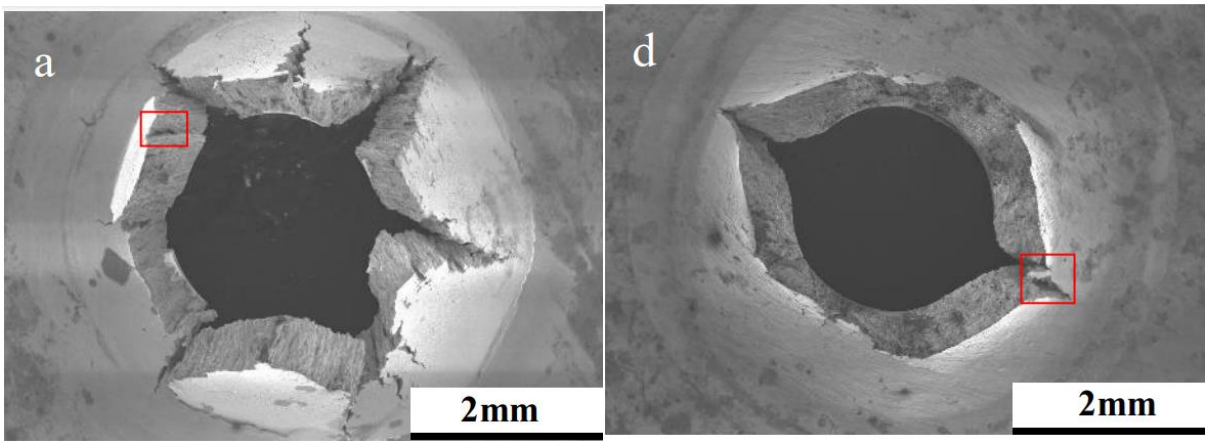

Figure 1-43 - Micrographs of the fracture surface for the small punch creep tests on the CM247LC. (a) shows the result for the 30° orientation and (b) displays the result for the 90° orientation [88].

This is in contrast to Figure 1-43b where ductile fracture has occurred, and the larger elongated grain have only allowed fracture in two directions. In the current study samples will be built to be tested in the vertical direction. Stress rupture samples that conform to ASTM3 will be used as this will reduce the effect that local variation in microstructure have on the results. The grain structure will be investigated in the XZ plane parallel to the build direction to see if different parameters sets create different grain sizes or aspect ratios.

In their study Hilaire *et al.* [87] investigated the difference between samples tested in the vertical and horizontal direction. They found that the yield strength was similar in both directions as shown in Figure 1-44.

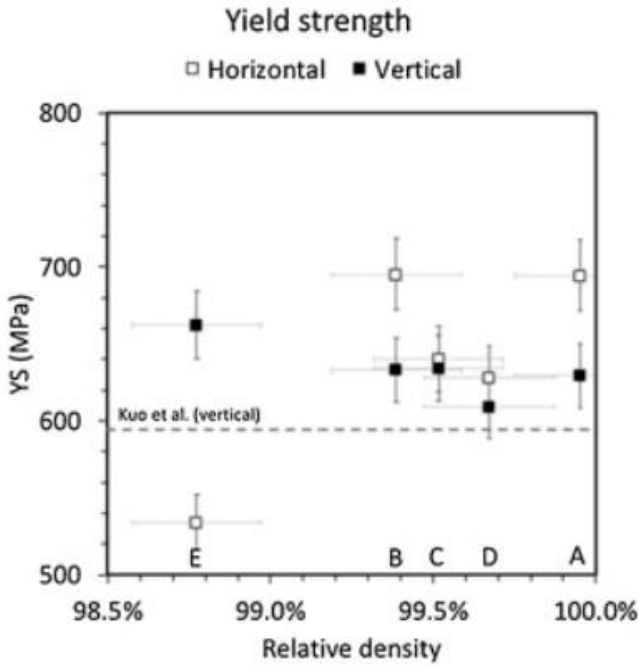

Figure 1-44 - This plot shows how relative density and porosity can affect yield strength in IN718. The effect is show for parts tested in both the horizontal and vertical directions [87].

Both orientations resulted in similar yield strength when the tested samples were fully dense but the horizontally tested sample had an approximately 100MPa drop in yield strength when the relative density fell below 99%. There was no such drop for the vertical sample.

The UTS was higher in the horizontal plane at higher densities as evidenced by Figure 1-45.

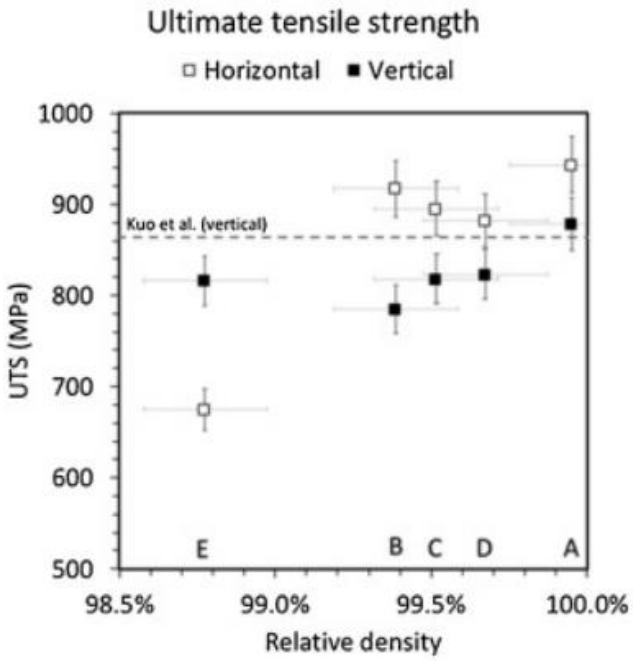

Figure 1-45 - This plot shows how relative density and porosity can affect UTS in IN718. The effect is show for parts tested in both the horizontal and vertical directions [87].

This is due to the larger amount of grains causing a strengthening effect once plastic deformation starts to occur. This higher UTS is not the case for the lowest relative density sample as the pores are present in such large quantities as to negate this effect. Elongation to failure was measured and it was found that for the least porous sample the elongation to failure was higher in the vertical direction (Figure 1-46) but this reduced significantly even with a small amount of porosity to below that of the horizontal sample which was much more tolerant to porosity.

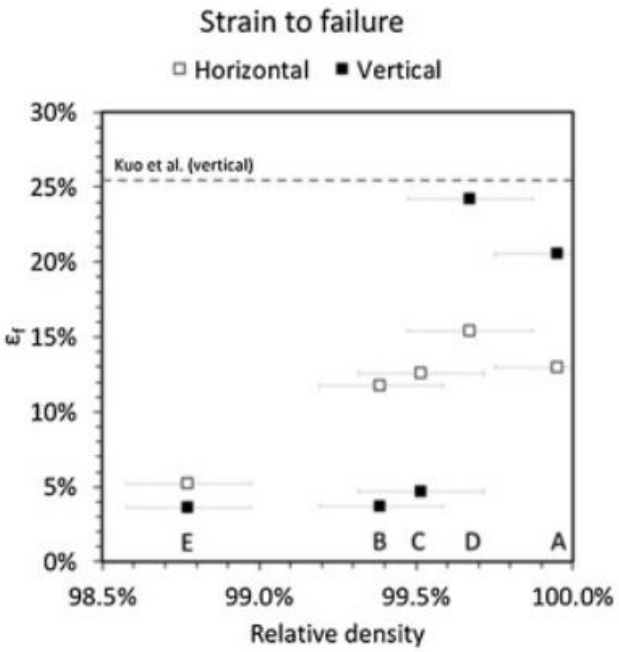

Figure 1-46 - This plot shows how relative density and porosity can affect strain to failure in IN718. The effect is show for parts tested in both the horizontal and vertical directions [87].

Both directions exhibit poor elongation to failure (around 5%) at high porosity as the large LoF defects significantly decreased the mechanical performance.

Finally, the fracture volume was investigated, and cracks were found to follow the geometry of the meltpool. Figure 1-47 shows the fracture surface and the meltpool is clearly visible.

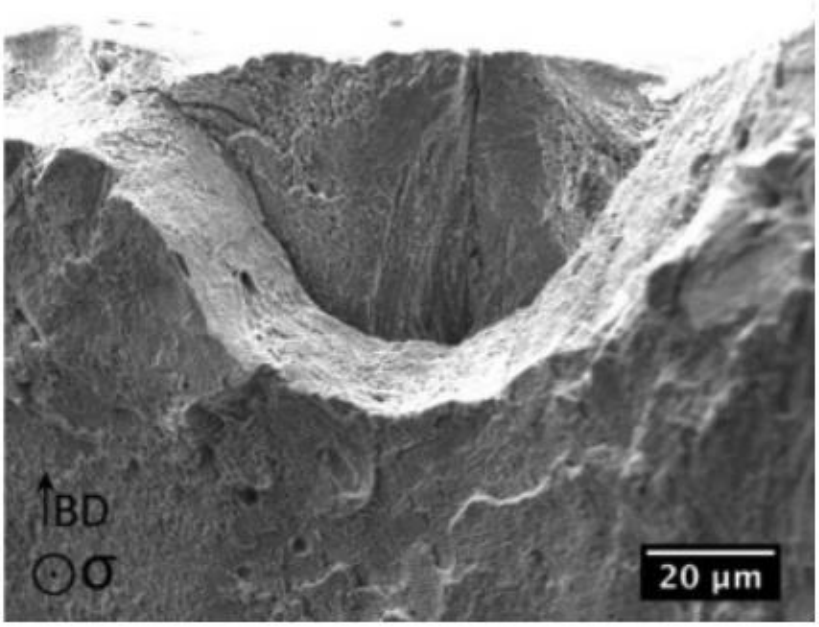

Figure 1-47 - A micrograph showing the fracture surface for the IN718 vertically tested sample. This shows the fracture along the bottom of a meltpool [87].

The fracture surface and volume will be investigated for the stress rupture tests carried out in this study to see if the same type of cracking is seen in this work as that seen both in the works by Hilal and Hilaire [87], [88].

1.7.4 Return Time

Return time is an important concept in LPBF. It can be defined as the time for the laser to return to a point adjacent to the initial spot. The cooling kinetics are altered depending on how long it takes for the laser to return. If the return time is large, then the bulk will have cooled more than if the return time is short, and so the bulk would have retained more heat. This variation will lead to different temperatures in the meltpool as if the initial temperature is higher. The same amount of energy will result in a higher meltpool temperature, which will affect the material in several ways. Firstly, in defect formation, King's equation (Equation 1-5) [89] shows that keyholes are more likely to form at high energy density inputs. As a result, if the energy input remains the same, a shorter return time will mean keyholes are more likely to form.

Conversely, shorter return times will result in lower thermal gradients and cooling rates meaning cracking is less likely to occur (see Section 1.8). Helmer *et al.* [90] have investigated return time in EBM for IN718. The results are shown below in Figure 1-48.

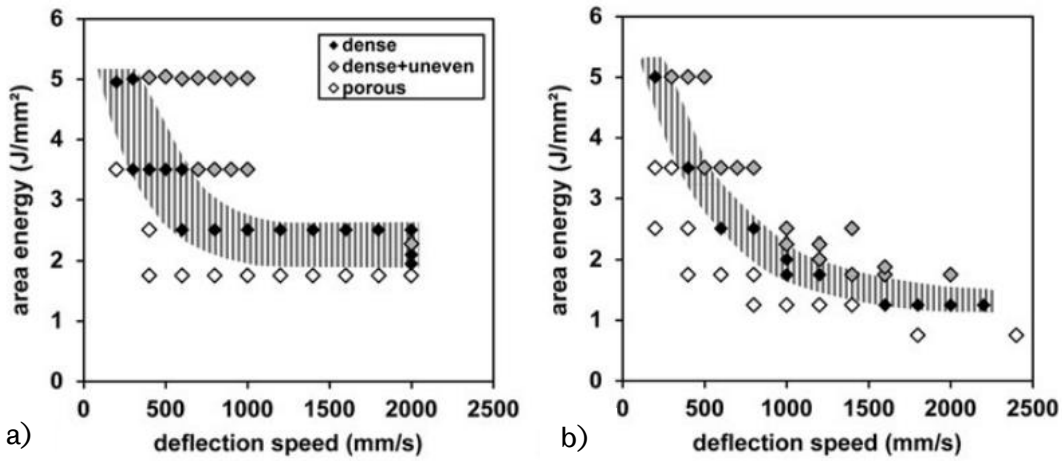

Figure 1-48 – These diagrams show the effect of return time on the build quality of IN718. From both a) focussed and b) unfocussed beam, at a faster return time, "beam deflection speed" (the energy required to create a fully dense part) decreases, especially for the unfocused beam [90].

If the geometry and hatch length is kept constant, a lower energy density or "Area Energy" is required to create a fully dense part with higher deflection speeds (velocities). This result is valid for both the defocused and focused beams ((a) and b)). Past a certain point, increasing the defection speed does not require reducing the area energy to create a fully dense part. This result can be explained as the build chamber is preheated to 900°C, so past a certain point, the bulk is not losing enough heat such that a shorter return time does not need less energy input. For the defocussed beam, this occurred at a lower deflection speed as the spot size was larger and therefore took less time to return.

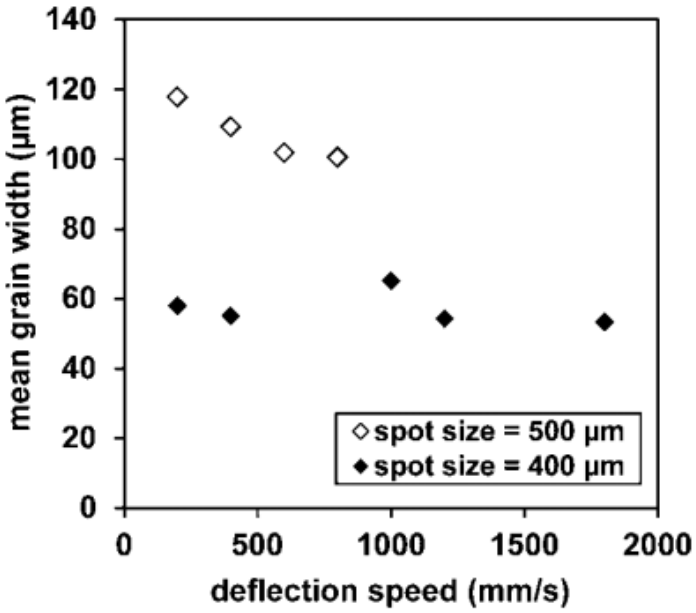

Figure 1-49 – Mean grain width dropping with increased deflection speeds for the unfocused beam. This drop was explained due to the higher thermal gradient created by the faster speeds [90].

Figure 1-49 shows how grain width is altered depending on the beam focus and deflection speed. The lower grain width at higher deflection speeds is explained as being a result of the higher temperature gradient achieved through higher speeds [90]. This conclusion is further reinforced because the focussed beam has a smaller grain width due to the higher thermal gradients. This smaller grain width is also explained as a result of higher temperature leading to greater undercooling. As well as this, the higher temperatures and higher thermal gradients cause dendrites to be broken off into the meltpool creating nucleation sites for new grains. Overall, there is minimal change in the grain width produced by the focussed beam over the range of deflection speeds. This minimal change could be explained by the higher thermal gradients parallel to the beam direction, with high beam speeds being counteracted by the lower thermal gradient perpendicular due to the lower return time.

In this project, return time will be investigated with respect to keeping the thermal history the same across the whole part. In Helmer *et al.* [90], the hatch-time is kept constant by making cubes where the laser path rotates 90° between layers. This scan pattern is shown in Figure 1-50 below.

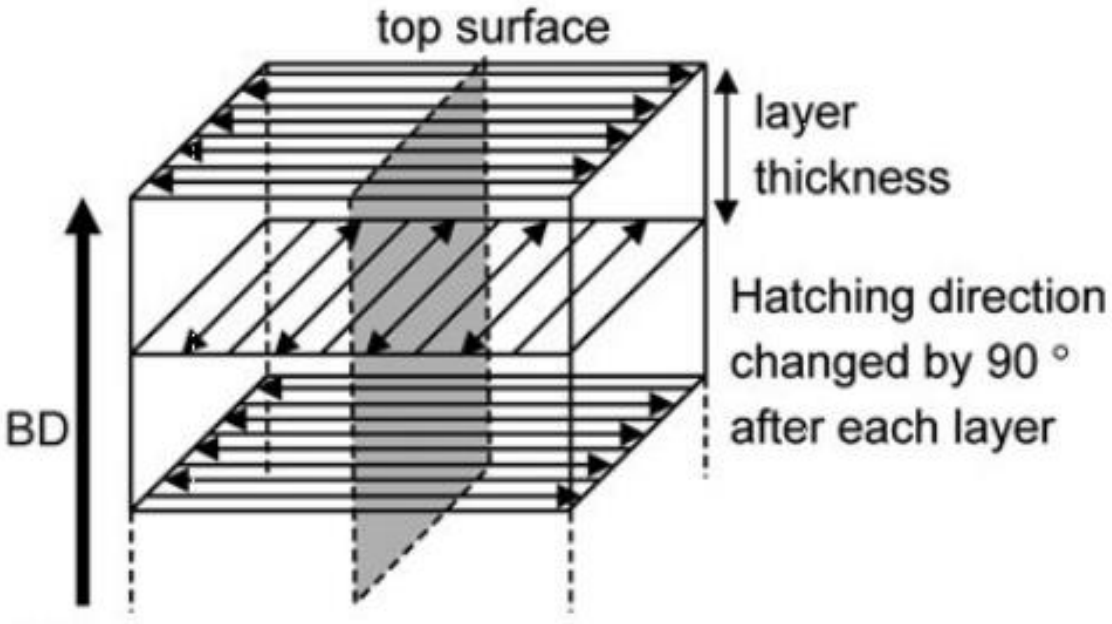

Figure 1-50 – This schematic shows how the laser path is rotated layer by layer. As a result, the return time is kept constant throughout the part. [90].

Other papers have used different angular offsets between layers, usually 90° at an initial 45° offset or 67° [91]–[94]. These will result in differing hatch lengths within layers (corners vs middle) and between layers. There will also be hatches of different lengths in irregularly shaped objects, i.e., not cubes.

1.7.5 Meltpool Models

Meltpools models can be a useful tool for parameter selection and building quality improvement by predicting meltpool geometry grain size and morphology and the likelihood of porosity. They offer a quicker route to parameter optimisation and reduce both the time and cost as fewer builds have to be built to optimise the parameters for a particular mechanical property [95].

Models, however, must be calibrated and verified to calculate their accuracy. This verification can be done experimentally, with initial experimental results informing future parameters and geometry selection. Once a model is calibrated and verified, a trade-off must be made. In general, the precision of a model means more computational time and power is needed. Conversely, a model that will take less time will not be as precise. As such, a compromise must be made between these two ends of the modelling spectrum.

In the model demonstrated and verified by Panwisawas *et al.* [96], the powder is modelled as individual powder particles of similar sizes. The model is a computational fluid dynamics-based model, and it considers all interfacial forces, including surface tension, Marangoni's flow, recoil pressure and drag force in the mushy zone. The energy dissipation in the mushy zone due to evaporation conduction convection and radiation has also been considered. Figure 1-51 shows the result of the simulation and calculating the temperature at the beam spot. Within the meltpool, the quantity size and possibility of keyhole formation (See Section 1.8) was calculated.

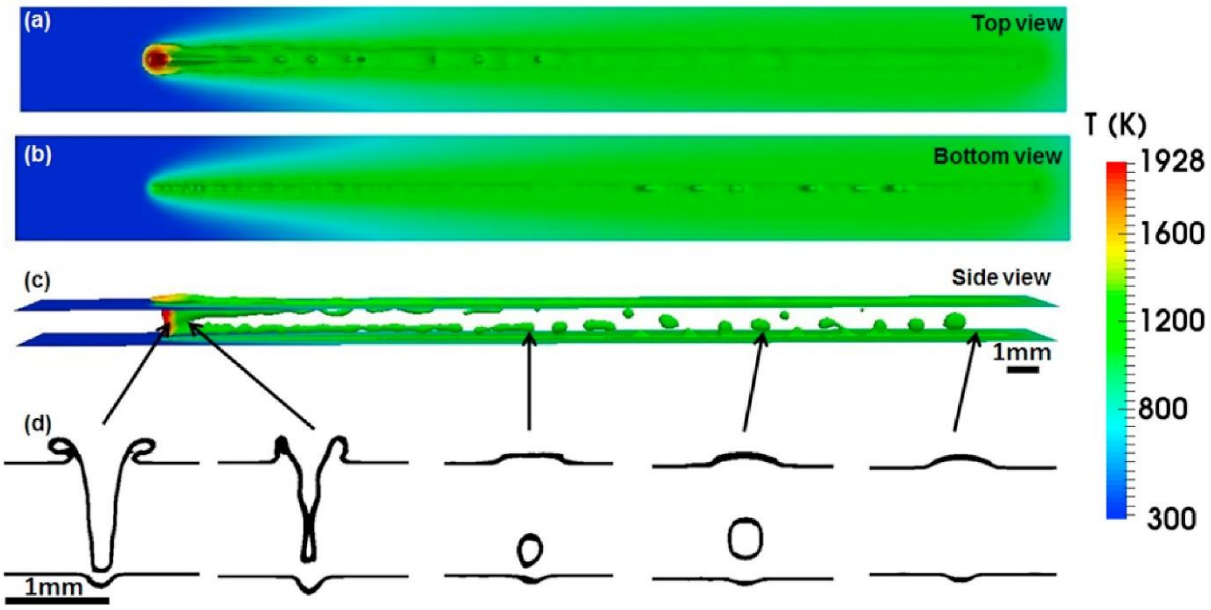

Figure 1-51 – These images show the results of a meltpool modelling experiment. a) shows what the meltpool would look like from above. b) shows the meltpool from below, c) shows the meltpool from the side and d) schematically shows the formation of a keyhole defect [96].

In their study, Panwisawas *et al.* [96] verified that the model accurately predicted the geometry of the meltpool and the formation of keyholes and other process-induced porosity. This verification was done experimentally by using X-ray computed tomography and optical microscopy. Even though this model was built to examine fusion welds, it has applicability in LPBF. It was used by Qiu *et al.* [97] when investigating meltpool dynamics for LPBF.

The model and the experimental aspect of this work demonstrate parameters that will lead to fully dense parts [96]. The model accurately predicted both the meltpool geometry and the selected parameters' defects. When an iteration of this model was used by Qiu *et al.* [97], it accurately predicted porosity formation due to increased velocity. However, the ability to predict keyholing in LPBF was not investigated.

On the other side of the spectrum, in her thesis Freeman [80] developed a model based on the Eagar-Tsai[98] model for travelling heat sources with a Gaussian distribution. Freeman modified the model to account for the pulsed nature of the laser (See Section 1.6.1.2) used for the experiments. This model will be used with both a continuous and quasi-continuous laser, with the way the laser moves will be adjusted, and a duty cycle applied to the quasi-continuous model. Only the bulk and the molten metal are modelled using this model, and the powder particles are not, significantly accelerating the calculation times. The meltpool size and shape is calculated. As with the Panwisawas *et al.* [96] model, keyholing is accounted for by calculating the amount of energy imparted over the boundary of keyholing found using the equation in King's paper [89], compensating for that with an increased depth of meltpool. Freeman's model calculates porosity, particularly lack of fusion porosity, by calculating the volume of unsintered powder and comparing that to the total volume of the reference volume. One aspect that this model considers that Panwisawas *et al.* [96] does not is return and multiple passes. This model allows for the input of the build size, so the last hatches next to the initial point are considered when the meltpool geometry is found. Additionally, previous layers are also considered.

Figure 1-52 shows the effect of taking previous hatches into account, with the meltpool being skewed in the direction of previous hatches. When more hatches are considered, the meltpool is more skewed. This skewing will affect the thermal gradients and cooling rates seen in the build. In turn, this will transfer into differing thermal histories within the cross-section. When investigating parameter sets and build conditions, multiple hatches must be considered as return time overall geometry and previous hatches significantly impact part properties.

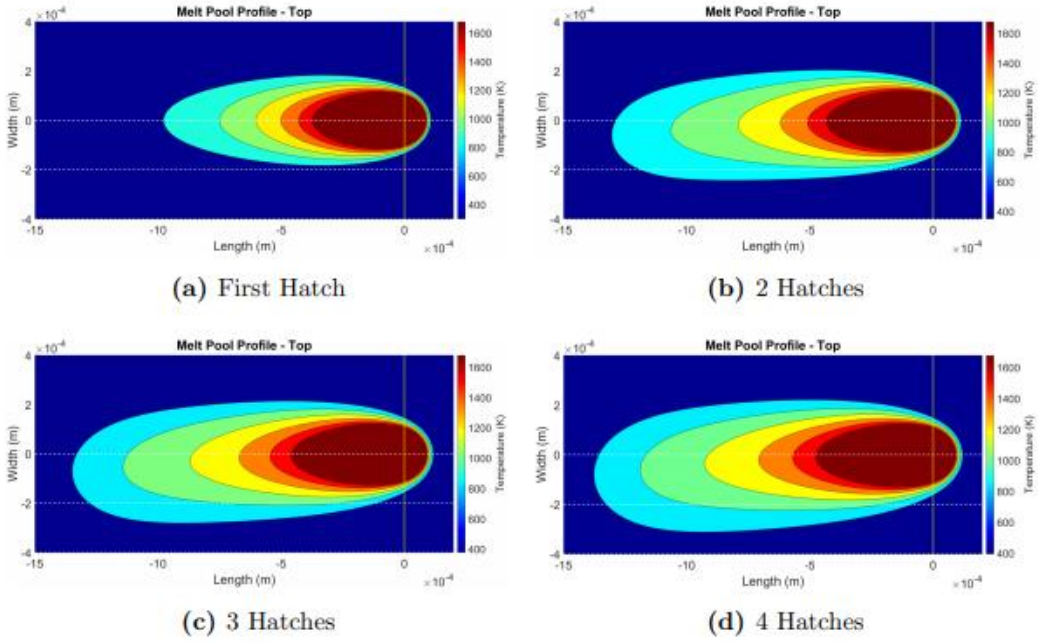

Figure 1-52 – These figures show how previous hatches are taken into account and show that for more hatches the meltpool shape when viewed from above starts to skew to the side where the previous hatches have come from [80].

Both models have their benefits and risks. The Freeman model will be verified and calibrated for this project for Haynes 282. The model will be used for both the quasi-continuous (pulsed) and continuous beams.

1.8 Defects

1.8.1 Defect Formation

Defects are crucial reasons AM and LPBF have yet to be used in safety-critical applications. Snell *et al.* [99] identify three types of defects or pores. These are; gas porosity, lack of fusion and keyhole defects. Gas porosity results from gas trapped inside the feedstock powder being transferred into the final built part. It is characterised by spherical pores of size ≈ 10 μm. The small pores are due to the porosity being encased in the powder before being processed in the machine. This porosity is alleviated by using powder with minimal pores and the proper processing parameters. Ng *et al.* [100] identified that with favourable processing parameters, the pores could float to the surface and be removed from the meltpool. Unfortunately, unlike Snell *et al.* [94], Ng *et al.* [100] did not distinguish between gas porosity and keyhole formation. Though these can look similar in morphology to gas pores using a cross-section in the XY plane, they are smaller than keyhole defects and are not tear-drop shaped, as is apparent when a cross-section in the XZ plane is taken. Snell *et al.* [94] identify these as the most prevalent defect in AM. This result is especially true when processing parameters to minimise the other two defect types have been used. Figure 1-53 shows both keyhole and gas porosity defects. The gas porosity defects have been circled. Figure 1-55 shows a keyhole defect in the XZ plane and its distinctive “teardrop” shape.

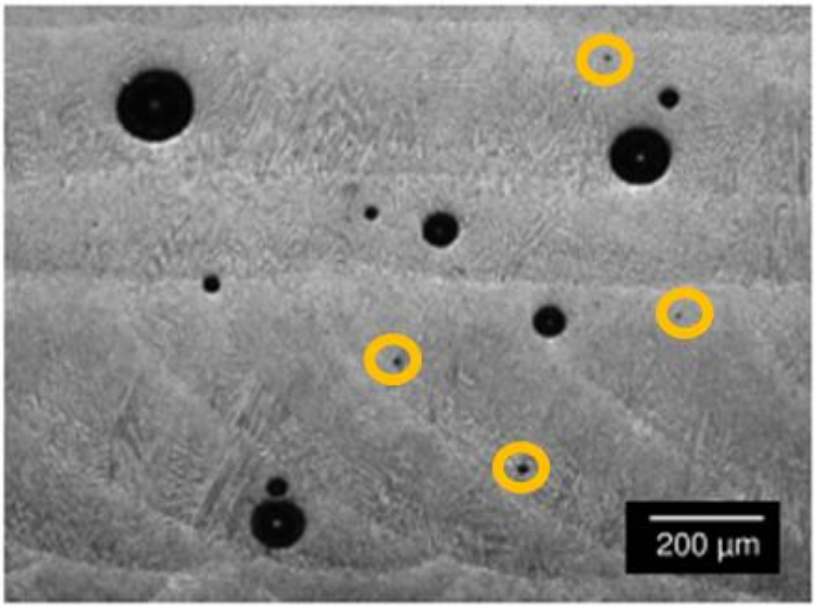

Figure 1-53 – A micrograph showing porosity within a cross-section of IN718. There are two types of porosity seen in this picture. The keyhole pores, the larger circles in the XY plane, appear as "teardrop" formed in the XZ plane (see Figure 1-55). The gas porosity, identified by the orange circles, are smaller in diameter and result from porosity already in the powder not being allowed to escape during the melting stage. This micrograph was taken in the XY plane. [100],

Keyhole defects occur in all processes where a heat source is melting feedstock. The physics behind keyhole formation are outlined by Liu *et al.* [2] and is shown in Figure 1-54.

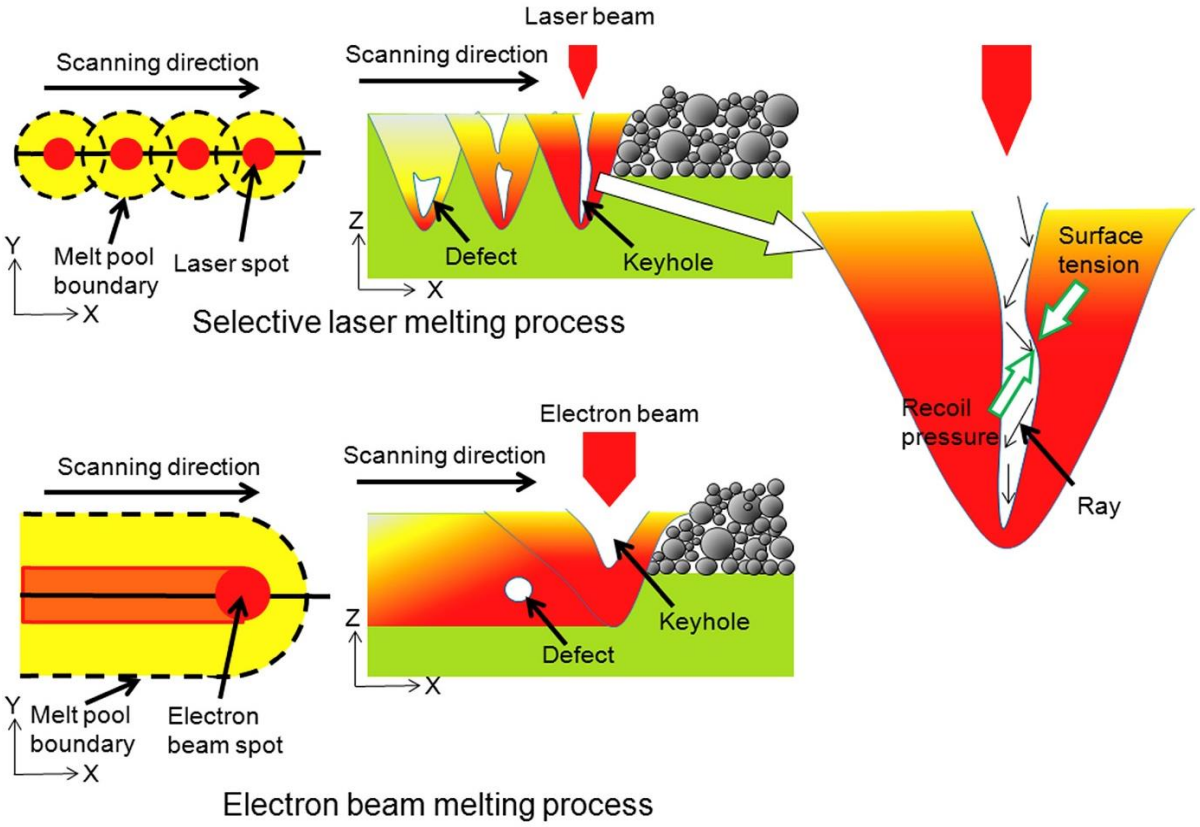

Figure 1-54 - The formation of keyhole defects in the LPBF and EBM processes is shown. In both cases, the defect arises from the beam creating a cavity that then reflects the beam and captures more of its energy. Once the force from the cavity being formed overcomes the force of the surrounding liquid, the cavity is preferentially driven downwards until it collapses and a defect is formed [2].

As the alloy is melted, a pore is formed where a gas bubble is trapped. The forces on the bubble prevent it from growing. In equilibrium, the recoil pressure from the trapped gas matches the surface tension from the surrounding liquid. In LPBF, the bubble can be exposed to the surface. If this occurs, then the laser may be reflected within the cavitation. If the surface tension matches this force, then the melting is in transition mode. Once the recoil pressure is greater, this causes the melt pool to preferentially drive downwards and create deep, narrow meltpools. As the surface tension increases due to the depth, the cavity collapses, trapping the pore. The teardrop shape can identify a keyhole defect that this collapse creates or by its presence at the bottom of a meltpool. King *et al.* [89] observed the formation of the keyhole as a result of laser melt tracks being performed on bulk material. Figure 1-55 shows the formation of keyhole defects

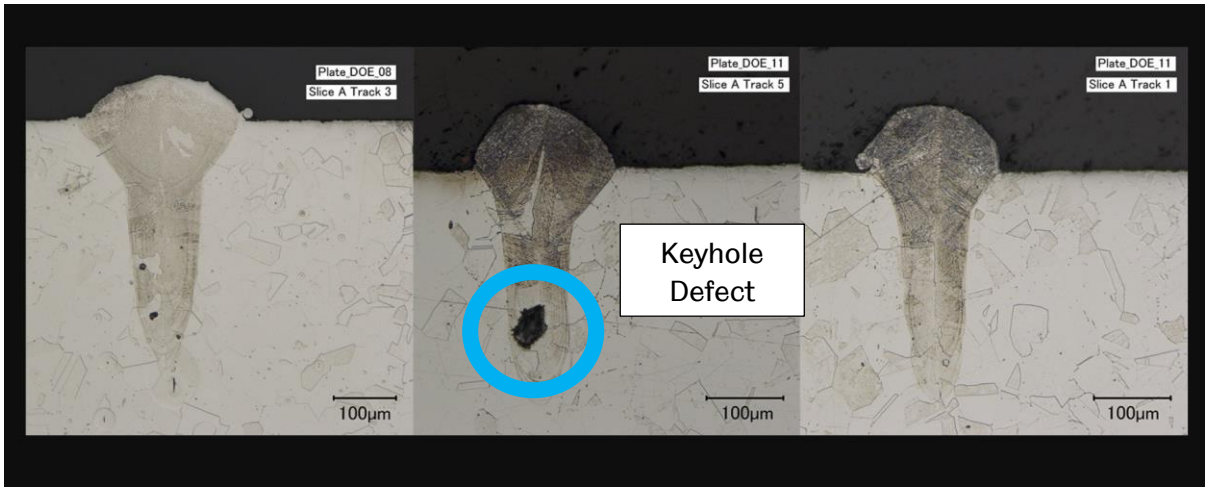

Figure 1-55 – These images show where in the meltpool a keyhole defect forms. It can be seen particularly from the middle image that the defect is near the bottom of the meltpool. All images show the presence of keyhole melting where the depth of the meltpool is much larger than the width [89].

The middle image shows a good example of a keyhole defect forming at the bottom of a meltpool. Keyholing occurs in higher energy density states, and for lower energy density states, the melting mode is called conduction mode. Conduction mode melting is shown in Figure 1-56 below.

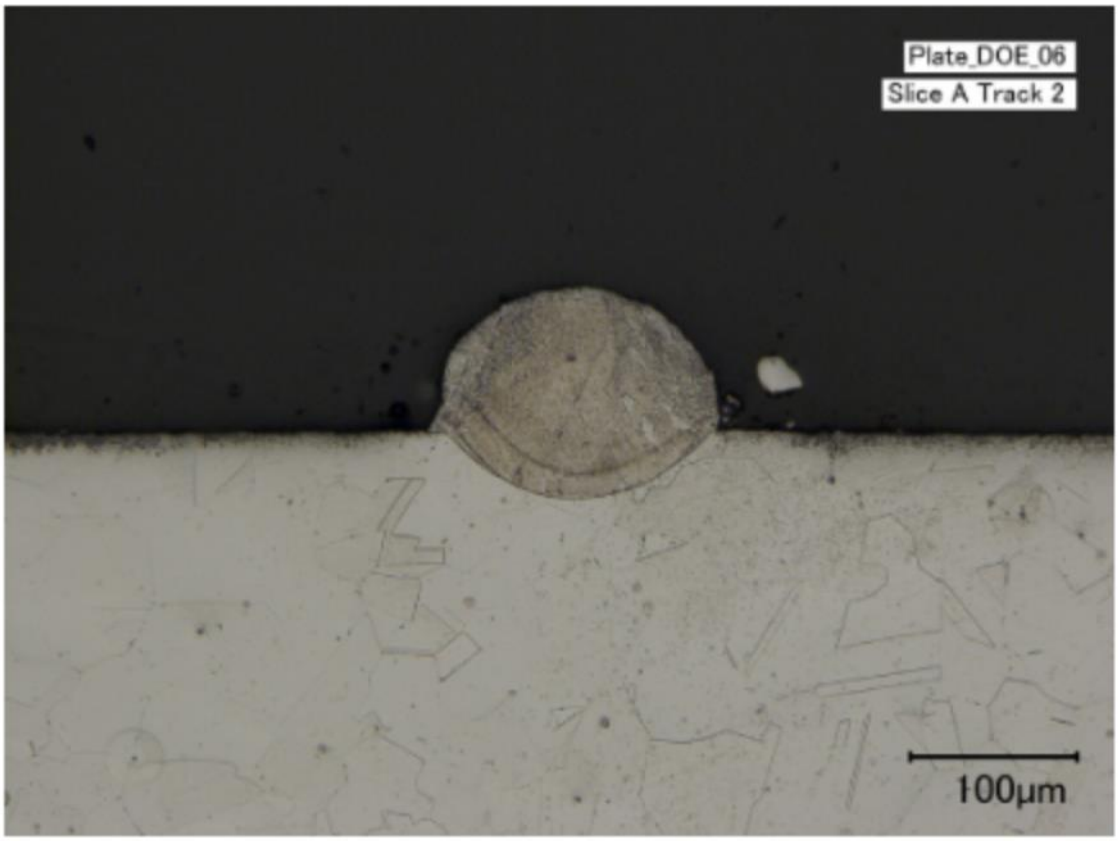

Figure 1-56 – This image shows conduction mode melting stainless steel 316L. A single weld track has been formed on a plate. The depth of the melt track is similar to that of its width [89].

The meltpool can be seen to be shallower and approximately the same depth as the meltpool width. Additionally, there are no defects at the bottom of this meltpool. This mode is the preferable mode in which to operate. The relatively simple geometry makes it easier to overlap and create processing parameters that minimise overlap. These two modes can be seen when the normalised melt depth σ/d where σ = beam diameter and d = melt depth is plotted against normalised energy density $\Delta H/h_s$ where ΔH = specific enthalpy and h_s = enthalpy at melting. Both modes are shown in Figure 1-57 below.

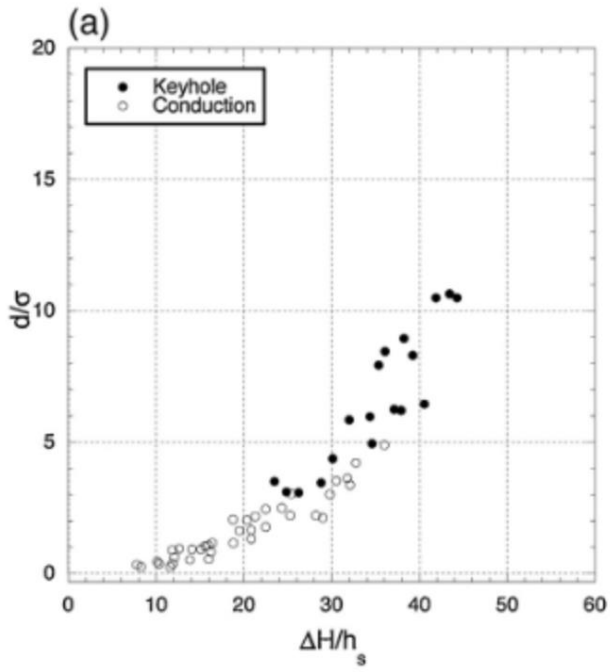

Figure 1-57 – This graph shows the effect on the melt depth of different parameter sets. It shows that the depth of the meltpool increases with increased energy density, and the gradient changes as the energy density increases [89].

The is a difference between the modes. In the middle of the modes is transition mode, discussed previously. Transition mode is where the extra energy exerted trying to melt the material is expended on keeping the cavity from collapsing under the pressure from the surrounding liquid. King [89] defines an equation that defines the origins of keyholing. This relationship is described in Equation 1-5 below.

$$\frac{\Delta H}{h_s} > \frac{T_b}{T_m} \approx 6$$

Equation 1-5

As this equation considers material parameters, it is alloy agnostic. This project aims to experimentally verify this equation and observe keyhole melting in Haynes 282. By doing this, the upper limit on energy density can be defined.

Theoretically, the lower limit can be found through physics by considering the necessary energy to raise the temperature of a given volume to above the material's melting point. A schematic diagram of this occurring is shown below in Figure 1-58

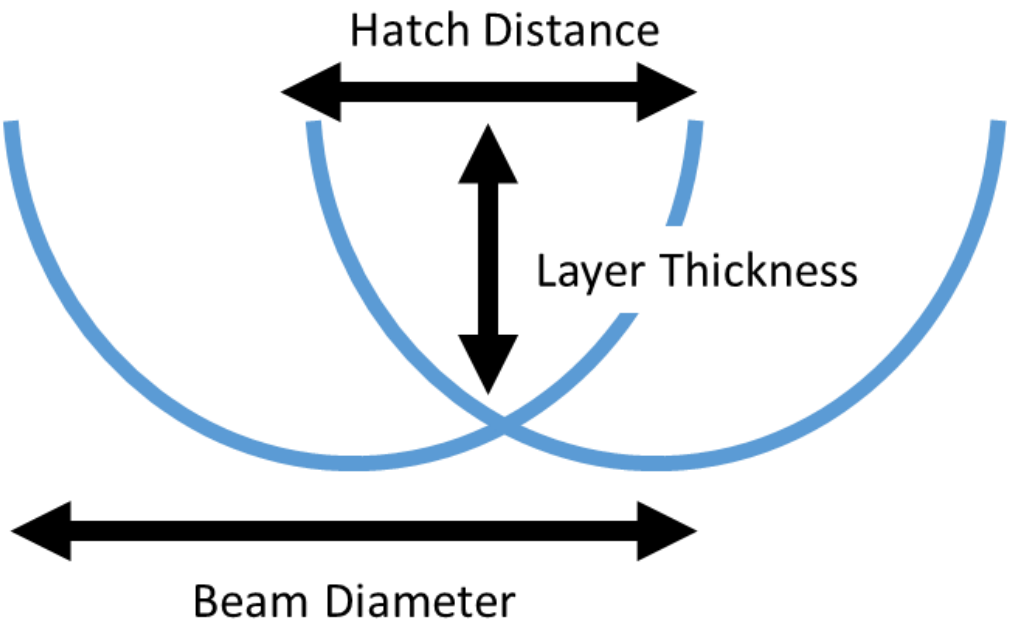

Figure 1-58 – This diagram shows the overlapping of two meltpools and what conditions must be met to melt all powder completely. The depth of the overlap between the two meltpools must be equal to or greater than the layer thickness.

At its most basic, the laser must melt the hemisphere of the beam diameter to above the melting point—this relationship is described in Equation 1-6 below.

$$AE = mC_p\Delta T$$

Equation 1-6

Where A is the Absorptivity (this is alloy, process and powder dependent), E is the energy required, m is mass, C_p is specific heat capacity and ΔT is temperature gain required. This equation can be further altered by defining $m = \rho V$ where ρ = density and V = Volume for a hemisphere $V = \frac{2\pi r^3}{3}$ where r = beam radius, $\frac{\sigma}{2}$, combining this results in:

$$E = \frac{\rho C_p \sigma^3 \Delta T}{12A}$$

Equation 1-7

This result will be lower than the actual value as this equation assumes a uniform heat throughout the hemisphere. This uniform heat is not the case as the temperature will be lower the further from the middle of the hemisphere. The heat will be conducted out by the material

bulk and radiated from the meltpool surface. One of the aims of this work is to experimentally find the lower limit before not all the material is melted.

When this occurs, lack of fusion (LoF) defects are observed. Snell *et al.* [94] define LoF as large, often the size of the meltpool, and irregularly shaped. They will often have powder in them that is unmelted or partially melted. This type of porosity is one of the simplest to manage as it just requires more energy to be input.

1.8.2 Keyhole Microstructure

When investigating the microstructure, the mode of melting can affect the cell orientation and growth. Wei *et al.* [101] investigated the cellular morphology achieved when keyhole melting occurs. This melting is more turbulent than conduction mode and so leads to different growth mechanics. Cells are liable to grow in more directions than with conduction mode melting, particularly from the meltpool walls. This leads to more elongated cells and curved cells. These are shown in Figure 1-59.

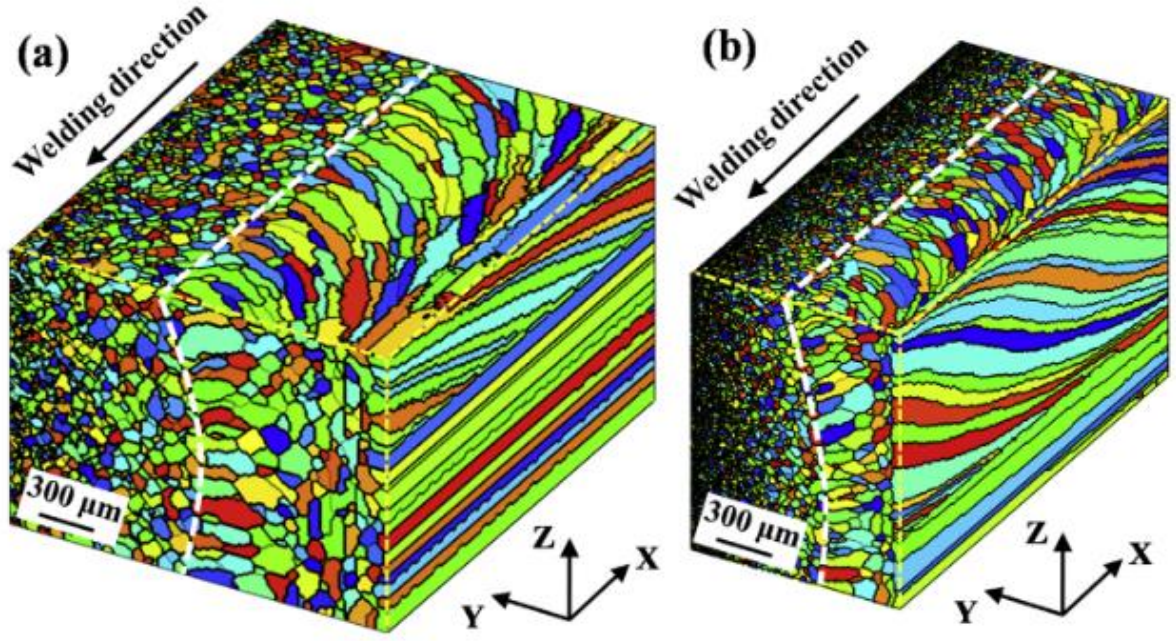

Figure 1-59 - EBSD maps in the different planes show the cellular structure and how it is influenced by the weld direction and speed and how close to the top of the weld that structure is observed. A) was formed at 1m/min, whereas b was formed at 8m/min. The cells are horizontal closer to the top surface at 1m/min, whist they are curved for the 8m/min condition. A finer cellular microstructure is achieved in the 8m/min HAZ [102].

From the EBSD maps, the different cellular growths can be seen. Below the weld top surface, there are horizontal cells, especially with the 1m/min (a). With the 8m/min, the cells are curved in the direction of the weld. There is a finer cellular structure in the HAZ of the faster weld. The different orientations will be observed in the XY though the measurements though an XZ cross-section would have been necessary to identify what morphology the cells have.

This work will use this knowledge to inform the analysis of the cellular structure visible in the cross-section. The cells will be of different orientations. And so, the relationship between thermal velocity and gradient and measured DAS will be different to that achieved in conduction mode.

1.8.3 Defect Effects on Mechanical Performance

Studies have been conducted [87], [88] that investigated the effect of sub optimal parameters on both the mechanical performance and fracture morphology of the tested samples. Hilaire compared the yield strength of sub optimal parameters and found that for the samples tested there was no relationship between defect population (porosity) and yield strength or ultimate tensile strength once a threshold of 99% relative density had been reached. This is shown in Figure 1-60 below.

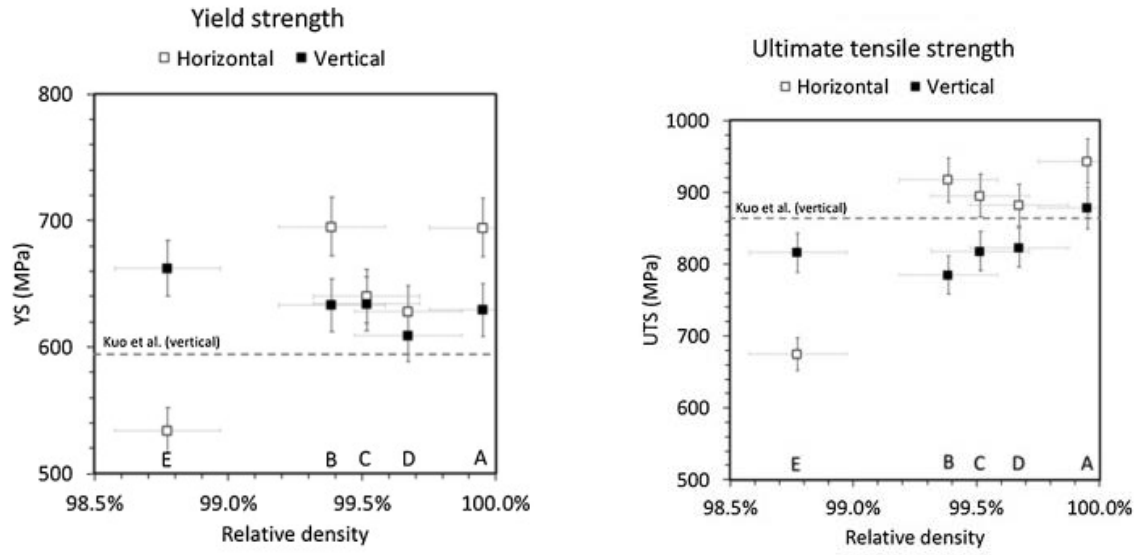

Figure 1-60 - These graphs show how porosity affects mechanical performance in both the horizontal and vertical directions. (a) shows the yield strength (b) UTS [87].

The figures show that above the threshold there is no additional increase in strength. Defects were shown however, to affect strain to failure significantly. Figure 1-61 shows the effect of porosity on strain to failure.

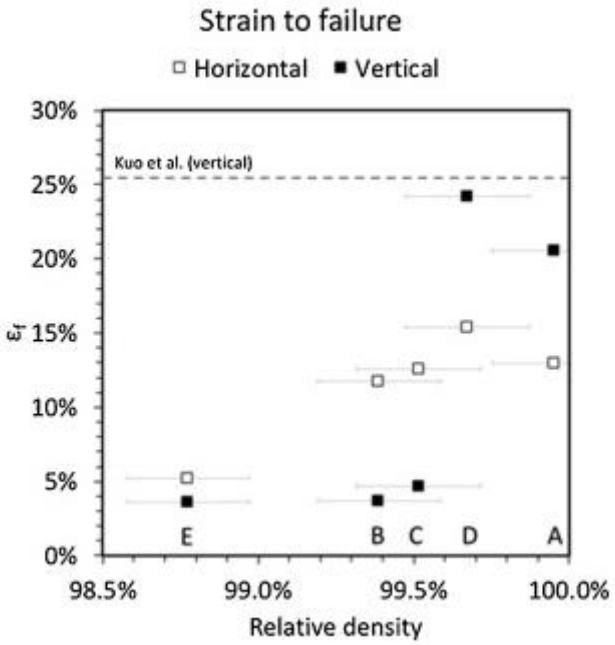

Figure 1-61 - This plot shows how porosity affects elongation to failure for both the horizontal and vertical build orientations [87].

Even a small amount of porosity causes the strain to failure to be significantly reduced. This is more the case in the vertical direction. In the horizontal direction the elongation to failure is less dependent on relative density. There is a drop in elongation to failure only when the relative density drops below 99%. This drop in elongation to failure is attributed to highly distributed pores within the material. When the fractures are observed they coincide with lack of fusion defects. The fracture surfaces are shown in Figure 1-62 below.

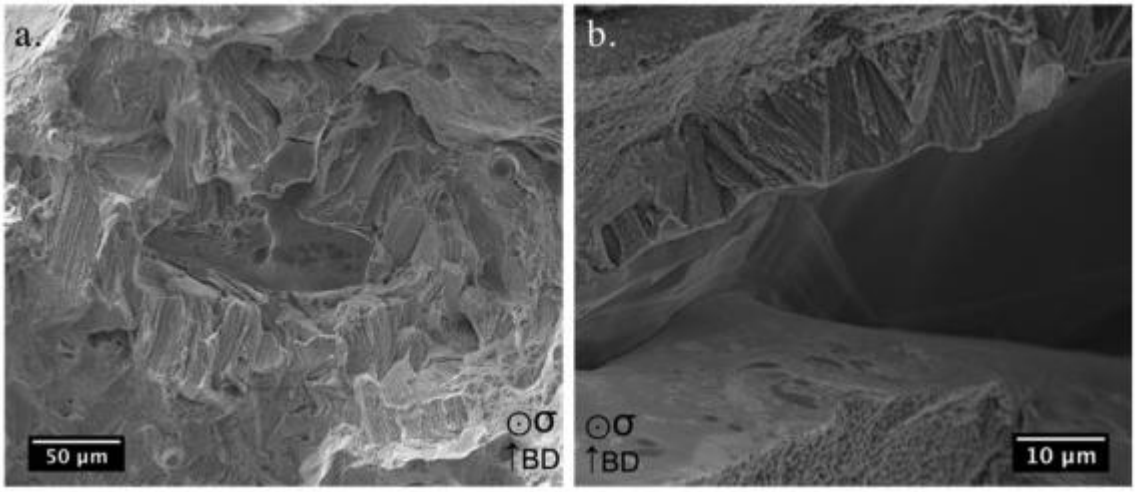

Figure 1-62 - Fracture surface for the tested IN718. The unmelted areas are visible indication lack of fusion defects are responsible for this fracture [87].

Lack of fusion defects have been observed and the shape of the defect has acted as a stress concentrator. As a result, inter-dendritic fracture has occurred. Not all pores act as stress concentrators. The microstructure surrounding internal gas pores was found to exhibit ductile fracture, as shown in Figure 1-63a.

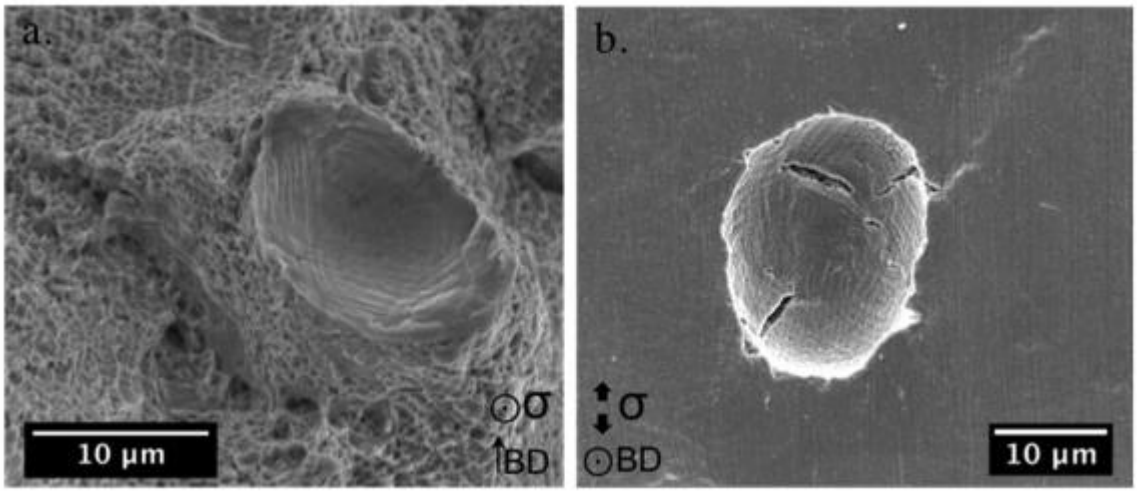

Figure 1-63 – These micrographs depict gas pores in IN718. (a) is an internal pore with a ductile fracture surface surrounding it. (b) is a surface pore and cracks can be seen initiating from it [87].

However, surface defects on the gauge as depicted by Figure 1-63b have caused intergranular fracture. Pre-existing cracks will also detrimentally affect the mechanical performance of the sample. In this study the fracture surface will be investigated such that the mode of failure can be identified. As well as this the fracture volume will be observed to see how and where cracks have been initiated.

The creep performance and its relationship with defects was studied by Hilal [88]. It was found that grain boundary cavitation can lead to a decrease in high temperature creep performance. The cavity can be seen in Figure 1-64 below.

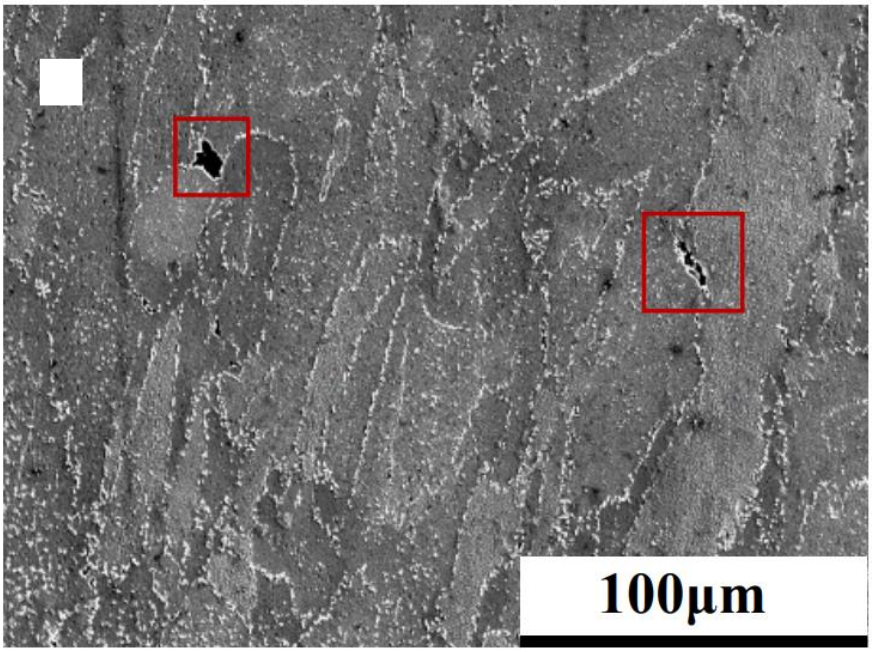

Figure 1-64 - Micrograph of the CM247LC microstructure. Cavities formed in the intergranular region by excess energy input are highlighted by the red boxes [88].

The cavities are identified by the red boxes. Associated with higher energy densities are intergranular cracks. These are shown in Figure 1-65

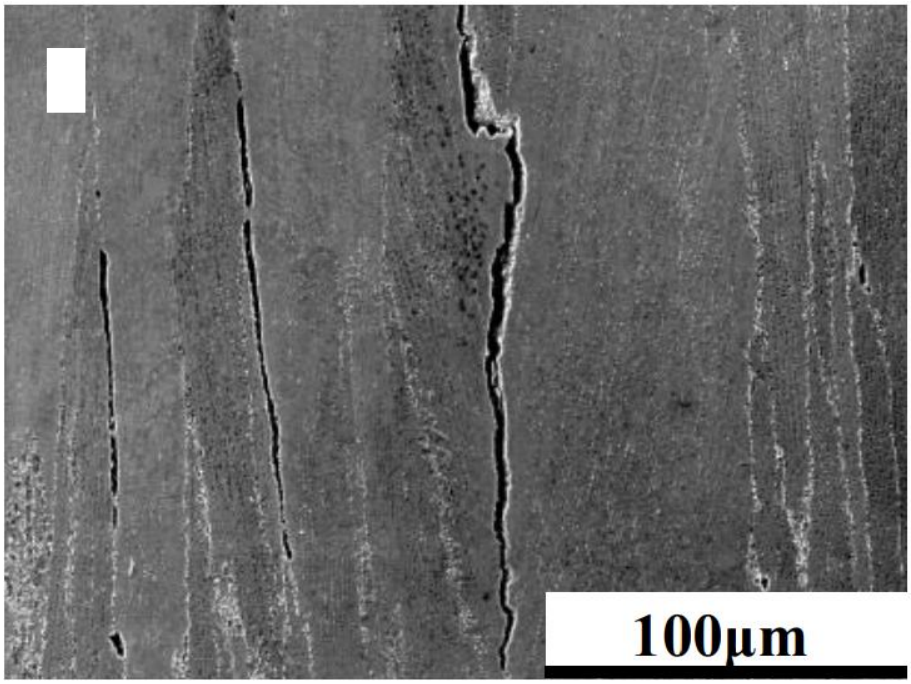

Figure 1-65 – Crack that has formed in the CM247LC microstructure. It has formed in the intergranular region as a result of high energy input [88].

The appearance of these cracks will cause the creep performance to drop and can be a cause of failure. In this study. The microstructure of samples that have undergone stress rupture testing will be observed. The location of the cracks will be studied as well as the chemical composition of the surrounding material to determine what kind of cracking has occurred. This study will only test optimal fully dense samples but will change process parameters to investigate parameters of similar energy density as defined by Thomas [86].

1.9 Cracking Mechanisms

An understanding of cracking mechanisms is essential in AM and traditionally manufactured parts, as cracking can lead to premature failure in static and dynamic loading conditions. Several types of cracking mechanisms occur, which are significant in different types of alloy, and, these are important in different processing conditions. A basic prediction of how likely a superalloy is to crack is through a weldability diagram (Figure 1-66). Alloys are plotted based on aluminium and titanium content, which determines the propensity to crack due to γ' formation. Although the figure has a distinct line around which an alloy is either weldable or not, the reality is a sliding scale. Haynes 282 lies in the weldable region with an aluminium content of 1.5% and a titanium content of 2.1%.

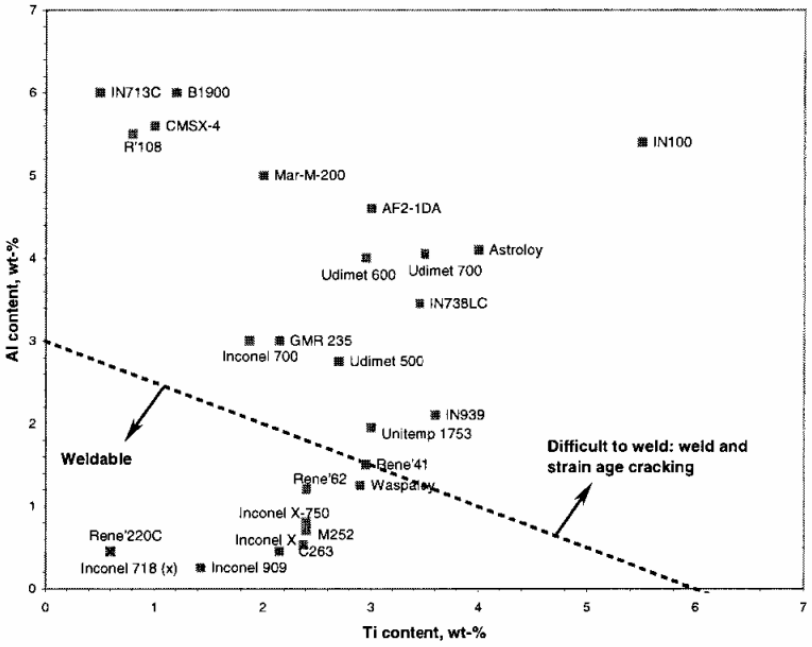

Figure 1-66 – The predicted weldability of different nickel superalloys is shown. This weldability is dependent on aluminium and titanium content. Aluminium contributes to a lack of weldability more than titanium [103].

1.9.1 Strain Age Cracking

Strain age cracking (SAC) occurs due to repeated reheating to near the solidus temperature. This cracking is prevalent in LPBF as the layer size tends to be small compared to the melt pool depth, resulting in multiple instances of reheating and melting the same layer. This study [104] characterised the different cracking mechanisms in LPBF nickel superalloys. SAC is found to occur on the grain boundary along with liquation cracking and ductility dip cracking. SAC

occurs due to the γ' precipitating out due to the post-weld/processing heat treatment. Whilst this does reduce residual stress, the harder γ' from the solid solution acts in tandem with the remaining residual stress to cause cracking. It forms on the grain boundary because it works with carbides that act as crack initiators. This project will aim to reduce this type of cracking by finding a suitable beam. Finding a suitable velocity and meltpool depth has been shown to reduce this type of cracking from the paper. Haynes 282 is slow to precipitate γ' due to its intentionally controlled content [105]. It was designed to have a γ' content low enough to have good fabricability but high enough to have good strength properties. As such, it has a higher γ' content than alloys such as 263 at 19% but lower than higher strength alloys such as R-41 and Waspalloy, which have γ' contents of 27% and 24%, respectively. This reduced γ' content also leads to its sluggish precipitation kinetics. The sluggish kinetics result from the precipitation mechanisms that mean that lower γ' contents lead to lower accelerations of γ' formation. γ' formation is calculated by [61] by measuring the hardness of the material after exposure to 704°C. The results of this are shown in Figure 1-67.

Nickel superalloys tend to form either μ or σ phase. Both these TCP phases are deleterious to the material's mechanical performance. σ phase is characterised by being hard and brittle at room temperature as the dislocations cannot move [106]. In this state, the phase is likely to form and then propagate cracks. As the phase is exposed to elevated temperatures, the phase becomes more ductile as the dislocations can slide. This behaviour at high temperatures means that this phase may not contribute to cracking. μ phase also forms after extended exposure to elevated temperatures [107]. It has been shown to precipitate faster under higher stresses. This reduces the mechanical performance by softening the matrix and causing hard and brittle μ phase to form on the grain boundary and initiate cracks. EDX maps of the cracks will be used to identify if these phases have formed and so contributed to the failure of the sample.

New PHACOMP[108] is a method of calculating the propensity of an alloy to form TCP phases such as μ and σ phase based on the alloy's composition. This prediction is based on an elements' electron valence, and the rule of mixtures is used to calculate the contribution of each element based on atomic weight %. The equation is shown in Equation 1-8 below:

$$\bar{M}d = \sum_{i=1}^{n} X_i (Md)_i$$

Equation 1-8

The Md values for each element are shown in

Table 1-4.

Table 1-4 - These are the Md values for each constituent element these are based on the electron valence and the $\bar{M}d$ is weighted based on the atomic weight % of each element.

Element	Md Level (eV)
Ti	2.271
Cr	1.142
Fe	0.858
Co	0.777
Ni	0.717
Mo	1.55
W	1.655
Al	1.9
Si	1.9

The overall $\bar{M}d$ values for the alloy will be calculated. If the value is above 0.915, then it is said to be likely to form μ phase. This value will also be compared to other alloys to observe how it performs relative to these. Different build conditions based on beam velocities and compositions found in the microstructure will be tested to see how these affect the $\bar{M}d$ value.

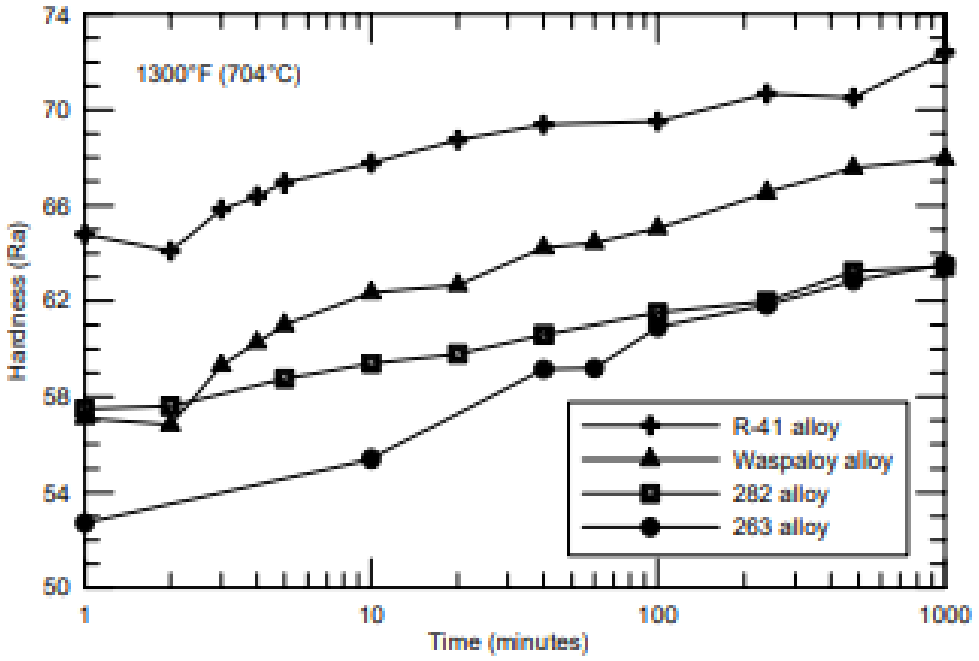

Figure 1-67 – The hardness of an alloy as it is heated is displayed on this graph. This hardness corresponds to the formation of γ'. Haynes 282's hardness increases the slowest of any of the tested alloys [105].

This graph shows how the hardness increases by a smaller amount than any other compared alloys. This comparison includes Haynes 263, which starts with a lower hardness but ends with an equal hardness to Haynes 282. In conclusion, this intentional reduction in the speed of γ' formation reduces the likelihood of SAC.

1.9.2 Liquation Cracking

Liquation cracking occurs away from the meltpool where the bulk material is rapidly heated. This heating causes some phases such as the γ-γ' eutectic present in high γ' fraction alloys to melt, forming a liquid film which combined with the lower melting point carbides and the residual stresses inherent in LPBF form cracks along the grain boundaries [104]. Cracking will be mitigated in Haynes 282 due to its lower γ' content and absence of eutectic formation. Haynes 282 does, however, form carbides easily as this is one of its main strengthening mechanisms. This mechanism was found in directionally solidified nickel superalloys by K. Zhao *et al.* [109]. Cao and Kou's[110] method for predicting liquation cracking will be employed. This method uses the relationship between the solidus of the weld filler material and the base material. It was found that if the solidus of the filler material was above that of the base, then

liquation cracking would occur (Figure 1-68b), whereas if the base material solidifies first (Figure 1-68a), then no cracking occurs.

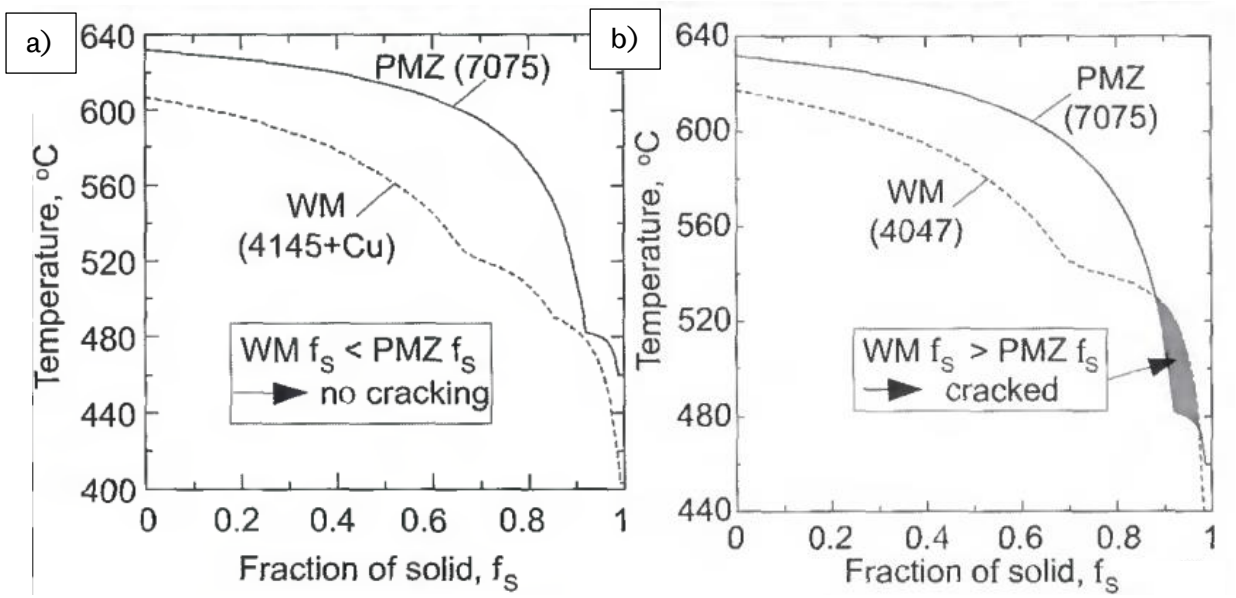

Figure 1-68 - Graph showing the propensity to crack a) will not crack as the filler material solidifies at lower temperatures than the base, whereas b) does crack as the solidus of the filler material is above the base and so exerts a strain on the base as it cools which the base cannot sustain [110].

Cracking occurs when the base material cannot support the strains put upon it. When the base is liquid, but the filler is solid, strain is exerted by the filler, which the base can't support due to it still being liquid. As such, cracking occurs. This method will be applied to LPBF, where the meltpool will be the filler material, and the bulk will be the base. Different velocities will be tested to observe if liquation cracking should occur.

1.9.3 Solidification Cracking (Hot Tearing)

Solidification cracking or hot tearing results from the dendrites that form as the material cools. The dendrites solidify and cause small pockets of liquid metal that shrinks as it cools. If the dendrites block the addition of more liquid from the remaining bulk, it will cause voids to form, which in turn, as the material cools, can cause cracks. Zhang and Singer [111] investigated the castability of different alloys and how adding certain elements caused a change in the propensity to "hot tear". It was found that titanium and hafnium additions caused the most significant decrease in castability. These increased the rate of change of liquid fraction as a function of temperature drop. They found that the steeper the drop in the critical temperature range just before it is 100% solid, the greater the likelihood that hot tears will be created. Figure 1-69 shows the difference in the drop between castable and non-castable alloys.

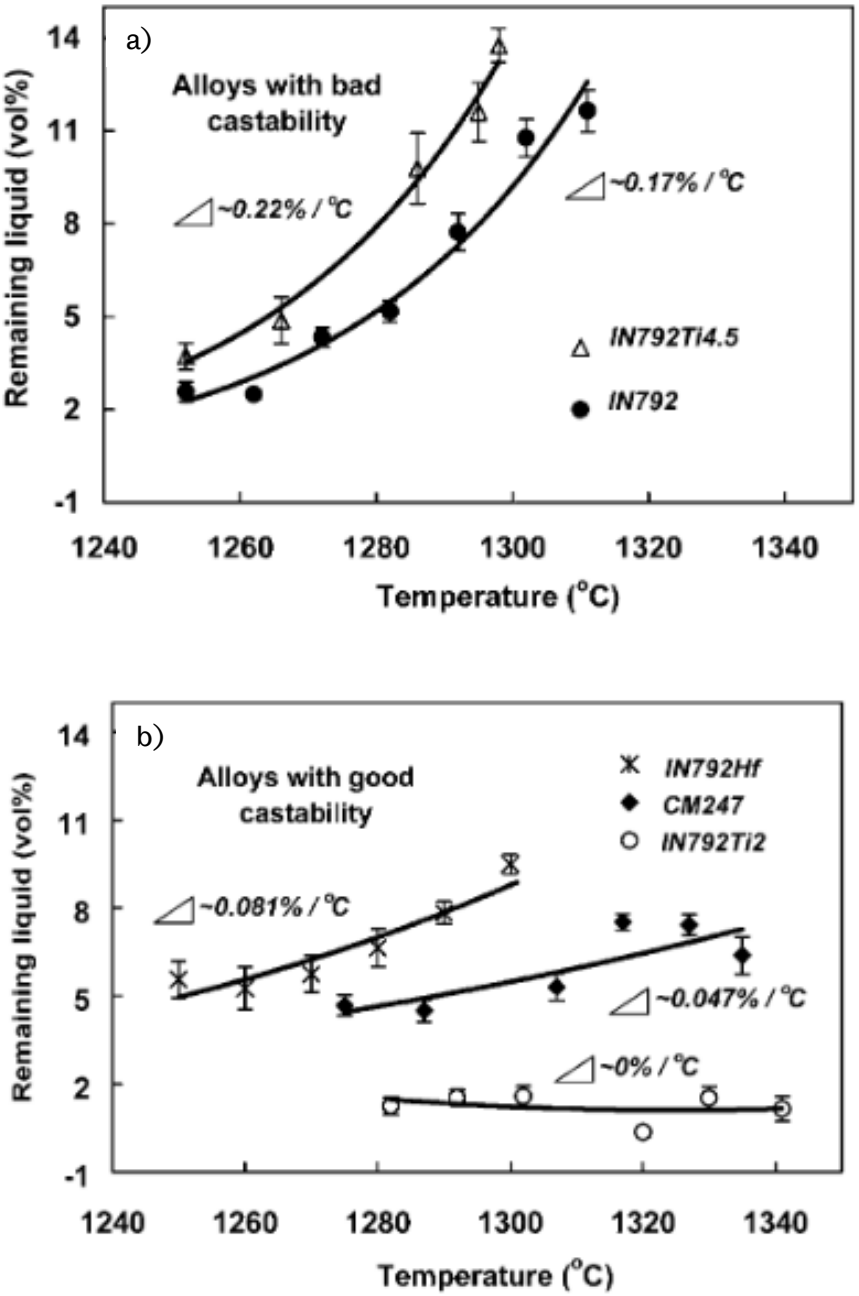

Figure 1-69 – These graphs show the reduction in liquid content between alloys with bad (a) and good (b) castability. The slope gradient of the castable alloys is significantly lower than that of the alloys with reduced castability [111].

The difference in gradient between the good castability and bad castability alloys is evident. This critical zone is crucial and usually defined as between 90% solid at the upper end and fully solid at the lower end. The longer the alloy can spend in this zone, the easier it will be for the remaining liquid to fill the voids as it solidifies. Fast cooling rates in LPBF cause the alloy to spend even less time in the critical zone than traditional manufacturing methods. Cooling mechanisms makes it important to choose alloys that have good weldability, as described in

the diagram in Figure 1-66. To assess more precisely how susceptible a given alloy will be to hot cracking, Rappaz, Drezet, and Gremaud [112] defined a hot-tearing criterion that took into account both processing parameters (through cooling rates) and material properties of hot-tear cracking occurring. This study will assess specific parameters to minimise this cracking by lowering the hot crack sensitivity (HCS). Carter *et al.* [104] presented Figure 1-70, showing which normalised parameters are more critical.

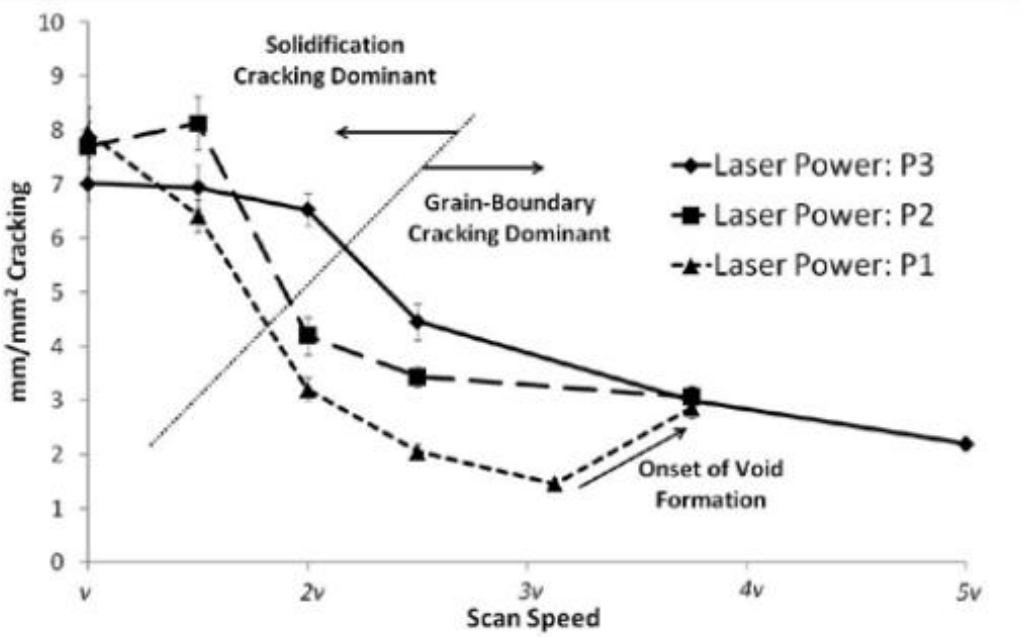

Figure 1-70 - This graph shows the dominant cracking types at different powers and velocities. Solidification cracking is more prevalent at high powers and low velocities, whereas at low powers and velocities, cracking at the grain boundary is more dominant. A minimum value for cracking can be seen at a medium speed and low velocity. Low velocities reduce cracking before the increase in velocity creates voids as the powder has not been completely melted [104].

This graph demonstrates that solidification cracking is the more important cracking mechanism to consider at high powers and low velocities. Cracking at the grain boundary is dominant at higher speeds or lower powers.

Haynes 282 has been designed to avoid these mechanisms or extend the period until they become prevalent. LPBF as a process can exacerbate these due to the high cooling rates and multiple passes over the same area observed in the process. As such, Haynes 282 seems an ideal candidate for use in LPBF compared to previously used alloys such as IN718.

1.10 Closed-loop Control

Closed-loop control is the overall mechanism whereby the control of parameters and necessary alterations is controlled automatically, and no human input is required for the build duration. This manual control contrasts with open-loop control, where a suggestion of the best parameters is made, and these can be accepted or rejected by the user. Closed-loop control is expensive to implement, so it is beneficial for complex and high-value applications, such as the case in AM and LPBF [113].

Closed-Loop Control is associated with electrical motors, and a proportional-integral controller is often used to control. Kin Sang-Hoon [114] outlines electrical motor control and how this can be achieved through closed-loop control. The Proportional-integral (PI) controller allows fast response and a zero steady-state error. This control method can be applied to other machinery and non-electrical systems. Sharma [113] described how closed-loop control could be applied to water heating. Figure 1-71 shows schematically how this is achieved.

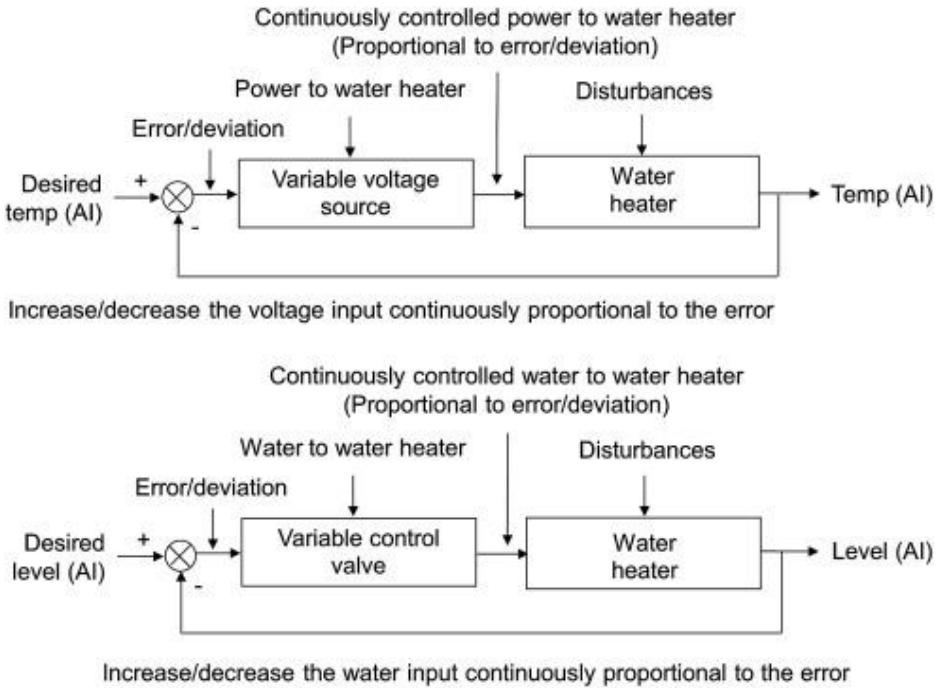

Figure 1-71 – A schematic to show an example of closed-loop control, in this case, for the temperature and volume of hot water from a hot water boiler system. It shows how control can be exerted either through the power to the water heater (top) or through the volume of water supplied to it (bottom). When control is exerted in a system to achieve a certain target without the input of an external user, it is termed a closed loop. [113]

This shows that control can be exerted either by increasing power to the water heater or through water flow control. This theory can be applied to LPBF by controlling power and

speed, with the output being surface temperature. This project will look at implementing closed-loop control to the LPBF process. A method for computing the best alterations to the parameters to match the necessary output will be needed. Rather than a PI controller, a machine learning algorithm (MLA) will be used. This MLA is discussed in Section 1.10.1. The monitoring device that will measure the temperature will be a pyrometer. It can do this with a high resolution and be implemented in-line with the laser so the meltpool can be observed as it is being formed no matter where it is on the build platform. This measurement is discussed in greater depth in Section 1.10.2.

1.10.1 Machine Learning

Machine learning (ML), like AM, is an emerging technology that promises to revolutionise how parts are built-in LPBF as well as other AM methods. There are different methods of ML as well as different methods for implementing ML within the LPBF process. Machine learning aims as a subject area were outlined as early as 1983 by Carbonell *et al.* [115]. Li [116] gives a good overview of ML, both the different levels of supervision as well as the different approaches to learning that have been applied. Li [116] also outlines some use cases for ML, including what learning methods might be applicable.

Li [116] states that generally, in supervised learning, there are labelled data; in unsupervised learning, there are no labelled data; and in reinforcement learning, there are evaluative feedbacks but no supervised signals. In unsupervised learning, the lack of labelled data leads to clustering and density evaluation. From this, trends and relationships can be found that would otherwise go unnoticed. With both supervised and unsupervised learning, there must be an instant "reward," i.e. the goal must be met immediately after one try. Reinforcement learning allows for cumulative rewards and multiple attempts that bring the output closer to the desired goal. Deep learning is a machine learning scheme that approximates a function that includes multiple inputs into one output. Deep learning is also known as a deep neural network.

Algorithms in ML are composed of four elements. The four elements were described by Goodfellow *et al.* [117] - Firstly, the data-set; this is all data collected in experiments so far. A cost or loss function, a procedure for optimisation and finally, a model. The data set must be split into segregated parts. There is the training dataset through which the specific function is developed. Then there is the verification set in which the algorithm's accuracy is tested—finally, a testing dataset to see if the algorithm accurately follows these trends. The cost/loss

function measures the performance of the model. It achieves this by measuring the error or variability away from a central trend. Training error is the error between the training data and the prediction. Test error is when this prediction is tested with unseen data. Models are described as under-fitting if the error in the training data is large and over-fitting if there is a discrepancy between training and test error.

Deep learning is defined as having multiple "layers" in which the input to the next layer is a weighted sum of units from the previous layer. A nonlinear transformation such as the sigmoid or tanh function is used before the next node is "activated". Once the output has been found, the error can be derived from working backwards from the output through the hidden layers to the input. As a result, the algorithm can be optimised to reduce this error.

Thus far, applications of ML to LPBF have been either ex-situ (analysing the data after the build) to determine what steps can be taken to optimise the output, or the methods have been applied theoretically to systems to propose an optimised feedback set-up to control the build quality.

This project aims to be the first that will use *in situ* monitoring and feedback control to apply an ML method to improve the quality of the build through proof of concept where a basic ML method and a single measured input will be combined to give an optimised set of parameters. The ML methods that will be used are Probabilistic neural networks and Cross-sample Entropy (these are further discussed in Sections 1.10.1.1 and 1.10.1.2)

This project is a metallurgy-based project. As such, a thorough investigation of the benefits of specific ML methods as well as developing new approaches are beyond the scope of this project. However, it is useful to understand how an ML algorithm functions and is created to understand if it will serve the application into LPBF. In the following sections, the exact method applied by another researcher is outlined.

1.10.1.1 Probabilistic Neural Networks

Probabilistic neural networks (PNN) are deep learning (or neural networks) methods with exponential functions rather than single activation functions, as discussed in Section 2.8.1.1. Specht [118] wrote the first paper to define this term. Using PNN, functions can be altered in real-time as new data is acquired, and thus the algorithm can be modified. Previous algorithm

optimisation methods were much slower, with PNN offering speed increases of up to 200,000 times. PNN was compared to backpropagation, where the algorithm is analysed using the underlying class statistics. Minor modifications are then made that incrementally improve performance. Figure 1-72 shows the overall schematic layout of a PNN. There are multiple inputs that contribute to multiple pattern units or hidden units, which are then combined into summation units. These are then combined into a final output.

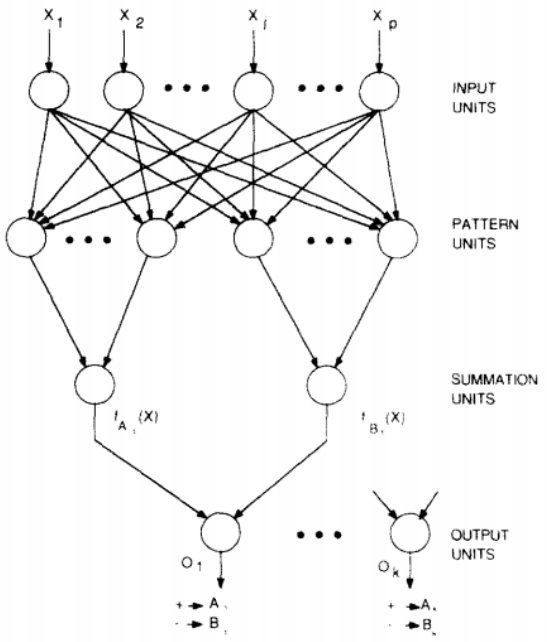

Figure 1-72 – This shows schematically how a PNN works. Multiple inputs are combined then output in different layers and groups until the result is output. This result can be a weighted summation of all of the layers previously, and any error estimation can be done by working backwards through the algorithm [118].

Figure 1-72 focuses on the pattern unit. The activation equation is nonlinear. In this case of the form seen in Figure 1-73, where.

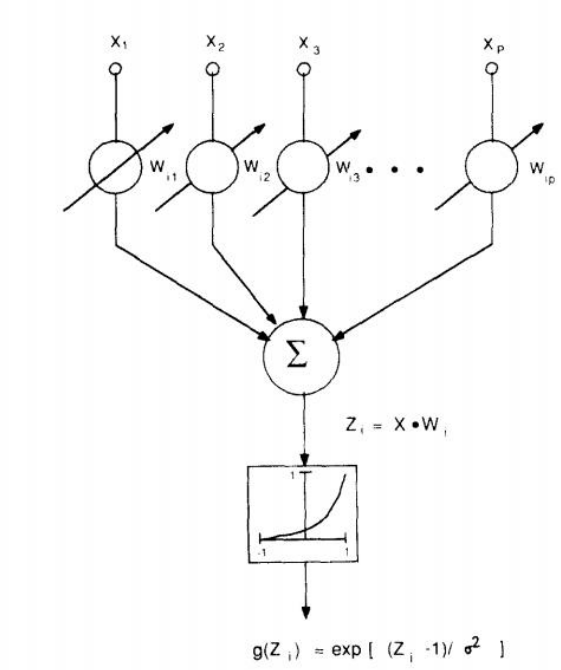

Figure 1-73 – This shows the activation function. The distinguishing feature of a PNN is that it includes a probabilistic function that can have values from between -1 and 1 rather than just the extremes. This function enables a degree of uncertainty to be integrated and creates a more accurate algorithm [118].

$$g(Z_i) \approx \exp\left[{Z_i - 1}/{\sigma^2}\right]$$

Equation 1-9

Where $g(Z_i)$ is the activation function, Z_i is the dot product of the pattern unit X and a weight vector W, σ is the "smoothing parameter".

In summary, PNNs offer a flexible framework for building an algorithm. This algorithm can be as complex or simple as necessary to allow computation and implementation time to be short enough to allow for "on the fly" parameter alterations.

As stated before, this algorithm will be created and implemented by another researcher. This project will focus on analysing the results and how effective it is at achieving the goal to minimise the variation from a target value of the measured value from the pyrometer.

1.10.1.2 Cross-Sample Entropy Method

Cross-sample entropy (SampEn) was first devised by Richman and Moorman [119] in their work, where SampEn was compared to existing methods using approximate entropy (ApEn). As it relates to ML, entropy is the rate at which information is produced. The example and

initial use case is given in the paper [119] was clinical data that was often noisy. It also tended to have small data sets as large data sets can be hard to obtain. ApEn was found to be biased as it counted sequences that matched themselves. This counting was done to avoid the case of ln (0), for which the value is undefined. This bias causes ApEn to be dependent on the dataset size. The regularity and unpredictability measured by ApEn were also consistently lower than expected. Finally, it lacked self-consistency. These limitations were addressed in SampEn as it did not need to count self matches. Crucially the calculation time was faster with SampEn. They found that SampEn matched the overall trends much better and was largely independent of record length and showed self-consistency.

1.10.2 Pyrometry

Pyrometry measures the surface temperature by measuring the radiation flux or emissivity from the surface. Lovegrove and Stein [120], in their book on the concentration of solar power, define pyrometry and state its advantages, highlighting its usefulness as an alternative to contact methods, especially at high temperatures. High temperatures are found in LPBF, where the temperatures in the meltpool exceed 1600°C and contact methods would not be feasible. The surface emissivity coefficient of the material also has to be considered, as stated by Lovegrove and Stein [120]. Infra-red pyrometry can measure the substrate directly. Wright *et al.* [121] found that a gallium-arsenide pyrometer was necessary for high-temperature applications, such as monitoring grain growth. This limited the use case to above 500°C but meant that much higher temperatures could be accurately measured. This range suits the application as temperature monitoring below this threshold is unnecessary due to the few to no microstructural changes observed below 500°C. Another advantage of pyrometry is that high-resolution data can be collected. The pyrometer used in this project measures every 6µs [122]. Despite this the data file is relatively small when compared to other monitoring techniques, it produces data files that are hundreds of megabytes per build as opposed to hundreds of gigabytes for techniques such as thermal imaging.

Pyrometers can be calibrated, though, in their paper, Wright *et al.* [121] found that these readings changed over time as a coating appeared on the viewport. Figure 1-74 shows how the emissivity at a specific temperature changes as the coating on the viewport ages.

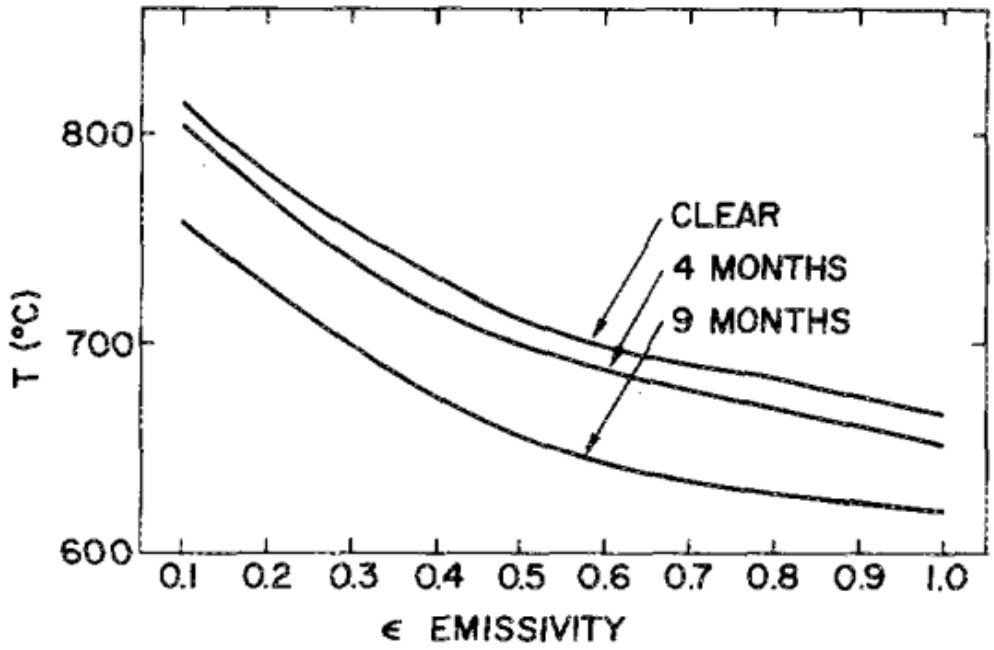

Figure 1-74 – This graph shows the degradation of the viewport of a high-temperature pyrometer. Over time the calibration must be altered to account for this. This problem can be overcome by using the relative change of emissivity reading rather than absolute as this will change less [121].

Another consideration that must be made when measuring the meltpool is that the emissivity changes significantly between the liquid and solid phases. Watanabe *et al.* [123][124] found that its emissivity changes as the metal cools from liquid to solid. This can be seen in Figure 1-75, which depicts how the measured output voltage from the pyrometer drops as copper solidifies.

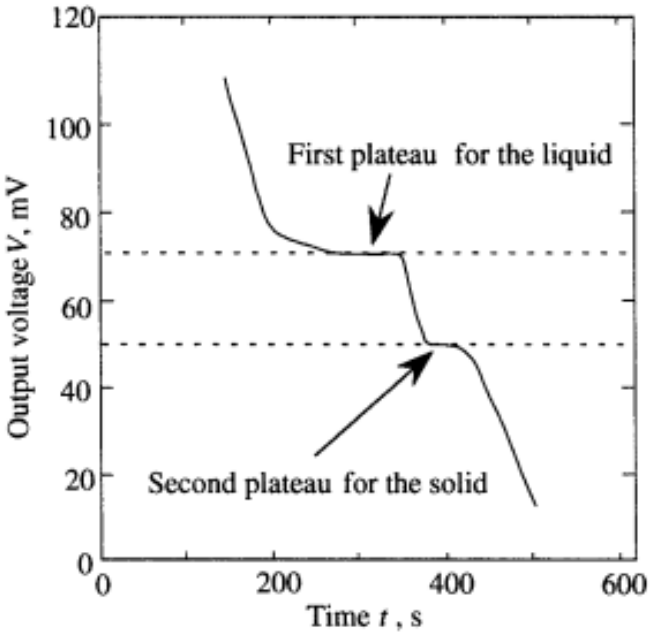

Figure 1-75 - This graph shows how emissivity drops from the liquid to the solid phase. This drop will make accurate temperature measurements from pyrometer readings challenging. As such, a relative change in readings will be used to mitigate the uncertainty surrounding measuring both solid and liquid phases [123].

Figure 1-76 shows how the emissivity changes in nickel around the melting point and how the emissivity is higher in the infra-red spectrum than visible. This result proves that infra-red is better for measuring emissivity.

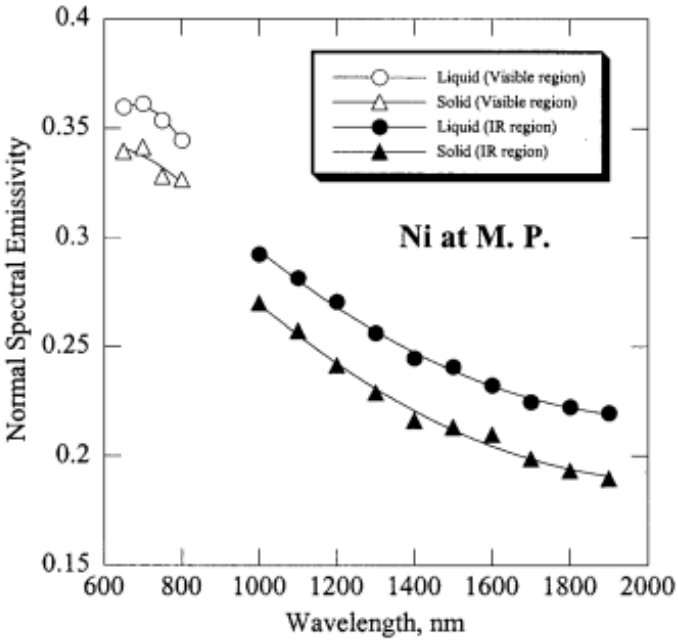

Figure 1-76 - This graph shows the different spectral emissivities for nickel at the melting point at different wavelengths. The difference that can be seen between the solid and liquid phases is significant [124].

This phenomenon of the changing rate of changing emissivity with respect to temperature will make determining an accurate temperature measurement difficult. This accurate measurement would be possible with a two-colour pyrometer as the emissivities could be compared. However, this would have been more expensive. However, accurate temperature measurements are unnecessary as the temperature that would have been observed would have been the long-range temperature. The pyrometer beam radius is 1mm [122]. The meltpool is only 100µm in size. This difference means that the pyrometer is reading the temperature of the meltpool and the surrounding bulk. Instead, the relative change in emissivity will be considered and compared to different builds, such that higher emissivity readings will mean hotter builds. The pyrometer reading being kept more constant will also mean more consistent builds. Due to one alloy being considered in this project, Haynes 282. Observing the relative change in "temperature" will meet the objective of using the pyrometer for this project.

1.11 Damage Mechanisms

1.11.1 Creep

Creep is the time-dependent plastic flow of material under conditions of constant load or stress [125] It takes place over a long duration of exposure to high stress but below yield stress. It is most commonly found at temperatures near melting point. The temperature range at which creep can occur is around 40% of the alloy melting point.

There are three stages of creep, primary, secondary, and tertiary. In primary creep the strain rate is relatively high. However, as time increases the strain rate decreases due to work hardening. Eventually this strain rate reaches a minimum and becomes almost constant. This near-constant strain rate is secondary creep. During this stage there is a balance between work hardening and thermal softening. Finally, tertiary creep occurs when the strain rate increases exponentially due to necking.

These stages can be seen in Figure 1-77, which shows the creep curves for Haynes 282.

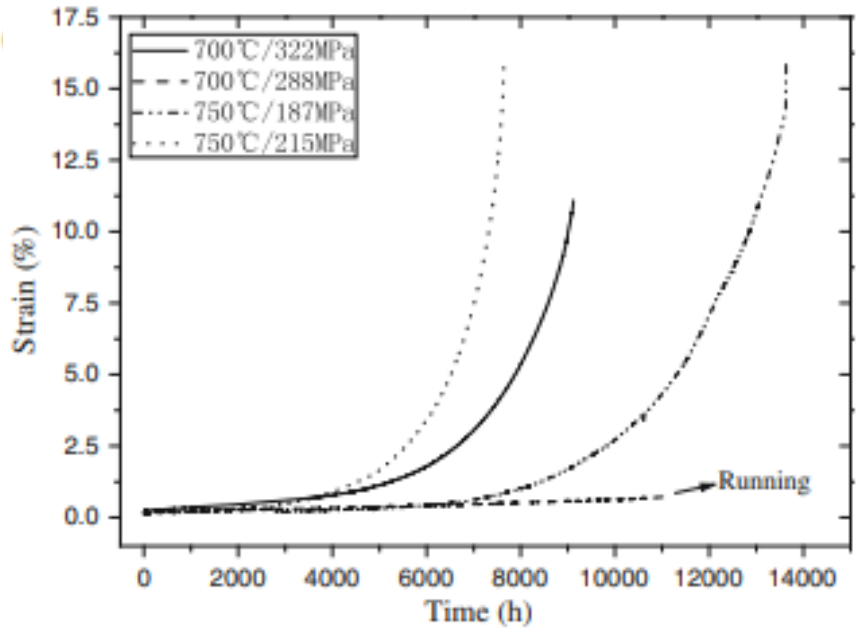

Figure 1-77 – This graph shows the creep rupture data at different temperatures and applied loads for Haynes 282 [126].

The primary stage is very short and then the secondary stage is characterised by the constant shallow gradient. For test at 750°C the gradient was steeper than for 700°C and a higher

applied stress results in a shorter time spent in the secondary stage. The tertiary stage is characterised by the gradient increasing exponentially until failure.

Haynes 282 exhibits good creep resistance properties [126] when compared to N263 and Inconel 740. This is due to the γ' behaviour within Haynes 282. The γ' has slow growth kinetics [105] which means that the γ' coarsens at a slower rate. This coarsening occurs due to the lattice misfit and the difference between the elastic modulus of the matrix and the precipitates.

When investigating the fracture volume of the samples that had been tested. The samples have failed by intergranular fracture. Dislocations piled up at the carbide matrix interface. These were relieved by cracking of the carbides or decohesion of interfaces.

Figure 1-78 shows the fracture volume for Haynes 282 with an applied stress of 322MPa at 700°C.

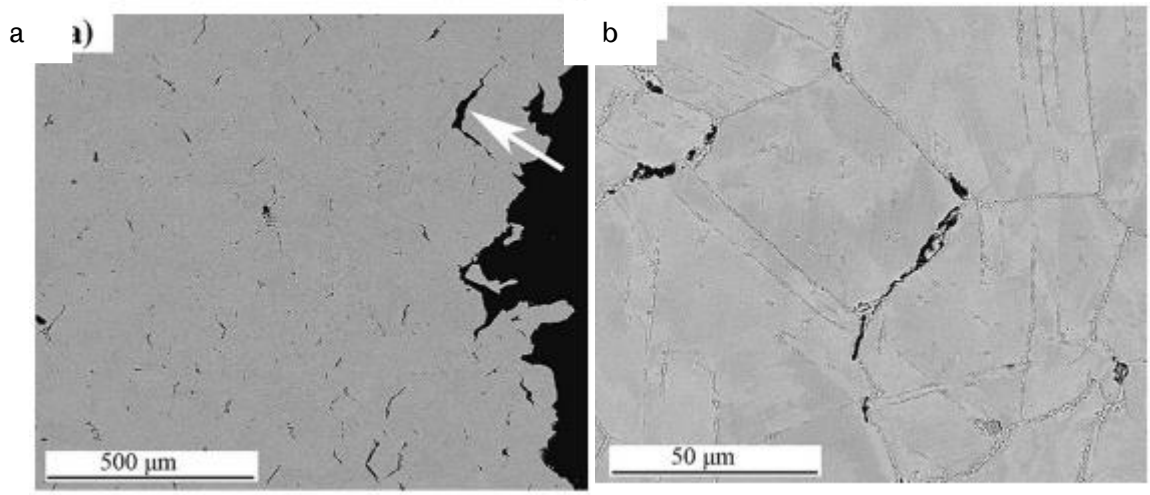

Figure 1-78 – Micrographs of the fracture volume showing cracks appearing at the bottom of meltpools (shown in (a) by the arrow), and at the grain boundary (b) [126].

Decohesion between grains is observed in both images. In this project the fracture volumes of samples that have undergone stress rupture testing will be evaluated. The positioning of the cracking will be noted to find if it is in the same position for samples built using LPBF as for traditionally manufactured parts. This will suggest that the material is behaving in the same way.

1.11.2 Stress Rupture and Larson Miller Parameter

Stress rupture and creep life are important considerations when evaluating material for use in-service. For AM and LPBF, this is especially important as whilst the static mechanical properties of an LPBF part are comparable to a traditional forged part, X. Wang *et al.* [3] showed that the LPBF mechanical strength could be better than as cast. However, Wang *et al.* [3] also showed that elongation to failure is significantly reduced in AM parts. It is the aim of this thesis to get comparable overall properties to as-cast material for the Haynes 282 parts that are made using LPBF. Porosity must be minimised, as small porosity can lead to large drops in elongation to failure. Significant drops in ductility occur mainly in the transverse direction. Due to the porosity morphology and typical processing parameters, the porosity leads to a hybrid ductile-brittle fracture and a drop in ductility. This type of fracture was found by Z. Chen *et al.* [127]. Defects are discussed more in Section 1.8. That study found that the anisotropy was limited when it came to other properties that were tested in the mechanical tests performed, namely ultimate tensile strength (UTS) and yield strength. This anisotropy, however, was found to be present by K. Kunze *et al.* [128], who, amongst other properties, investigated creep. When the transverse direction was tested, Kunze *et al.* [72] found a drop in creep life. It was concluded that the difference in creep life was due to the difference in texture between the vertical and transverse directions, which was observed in EBSD maps. One of the objectives of this project is to reduce this anisotropy of properties through a suitable heat treatment.

Further studies have compared the dynamic properties, particularly creep, to traditionally manufactured parts. This study by V. A. Popovich *et al.* [129] looked at the creep life of LPBF parts. It compared them to wrought. The test was carried out at 650°C with 690MPa of stress. The LPBF parts compared unfavourably to wrought with all parameters leading to reduced creep life and one case, unable to reach test conditions before failing. The study found the best time to failure to still be ≈5% of the wrought condition. This project aims to reach close to the creep life of the traditionally manufactured part. An elevated temperature stress rupture test will be employed to reduce cost and the time requirement to perform creep tests. This test applies a given stress at a given temperature until the sample fails. However, unlike a creep test, it does not measure the elongation during the test, only after the sample has failed. This cost reduction is required as multiple samples will be needed in multiple conditions to map the properties in the parameter space. This campaign will include different parameter sets, heat treatments, and different orientations of samples (vertical and transverse) and repeats

to get statistically significant data. When comparing test results to others found in the literature, it will be necessary to compare tests done at different temperatures and stresses. This comparison is achieved using the Larson-Miller parameter, and Equation 1-10 is shown below.

$$LMP = T(C + \log(t))$$

Equation 1-10

The Larson Miller equation compares different temperature and stress states within a material and between different materials. F. T. Furillo *et al.* [130] outline how the basic equation is flawed and that the parameter needs to be adjusted in line with material parameters. Haynes has done this analysis in their brochure [5]. Figure 1-79 shows how the LMP changes over stress states and how the LMP for Haynes 282 compares to other similar materials.

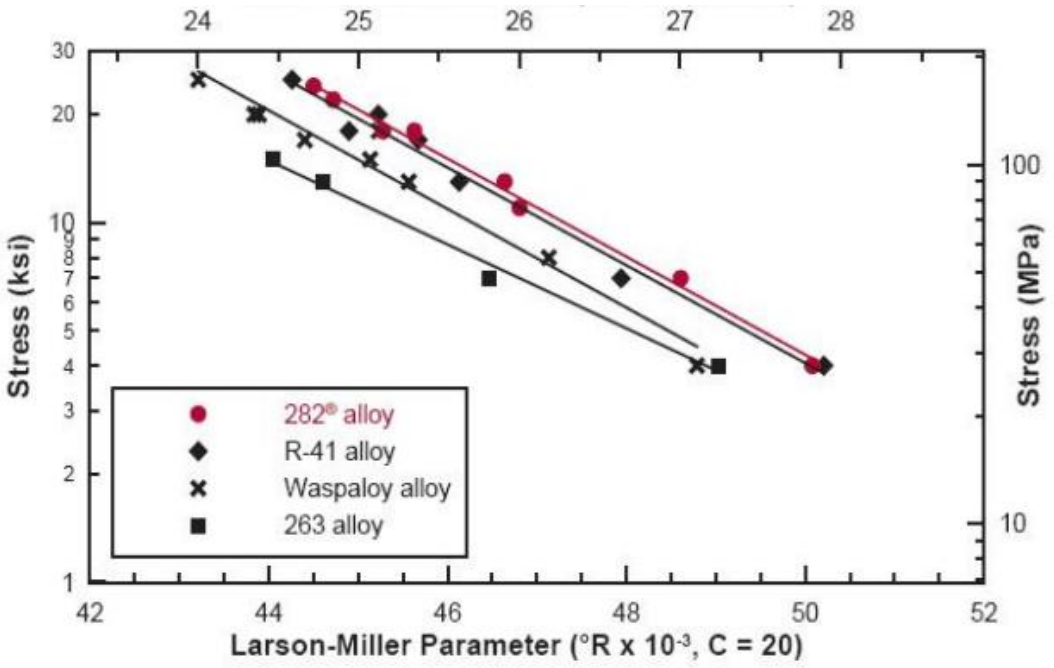

Figure 1-79 - This graph shows how Haynes 282 performs in long term exposure scenarios. A line further to the right represents better long-term exposure resistance. This graph must be read carefully as a small difference in LMP can lead to a large change in service life, particularly at stresses well below the yield strength [5].

This graph shows how the LMP for Haynes 282 is higher than alloys in its class. The graph must be read carefully as a different LMP can lead to significant changes in stress rupture life.

1.12 Heat Treatments

Heat treatments are an essential post-processing step to achieving desired microstructure and mechanical properties. Vrancken *et al.* [131] studied heat treatments in Ti–6Al–4V and compared the effect of optimised LPBF heat treatments to those of heat treatments for traditional forged parts. It was found that some of the microstructural features present in the as-built state are maintained into the post-heat-treated state. It was also found that while the SLM part could reach the ASTM standard, a different heat treatment was required, and different mechanical properties would be achieved due to the growth mechanics from the as-built microstructure heavily influencing the microstructure post heat treatment.

In nickel superalloys, initial experiments into potential heat treatments started with the standard heat treatments for as-cast. These improved mechanical properties such as UTS, but ductility was maintained compared to cast and heat-treated [132], [133]. Deng *et al.* [132] performed the individual steps in the standard IN718 heat treatment. The results showed an increase in the yield strength and UTS compared to as-built and were the same as as-cast and heat-treated [134]. The yield strength rose from 800MPa for as-built to 1400MPa for heat-treated, similar to the strength of 1395MPa obtained from conventionally processed and heat-treated samples reported by Raghaven *et al.* [134]. However, the ductility decreased from as-built to heat treated and was similar to cast and heat treated. As-built had a ductility of around 34%, which dropped to around 22% for the fully heat-treated sample. This ductility is similar to the 20% reported in [134]. The full results are shown in Figure 1-80.

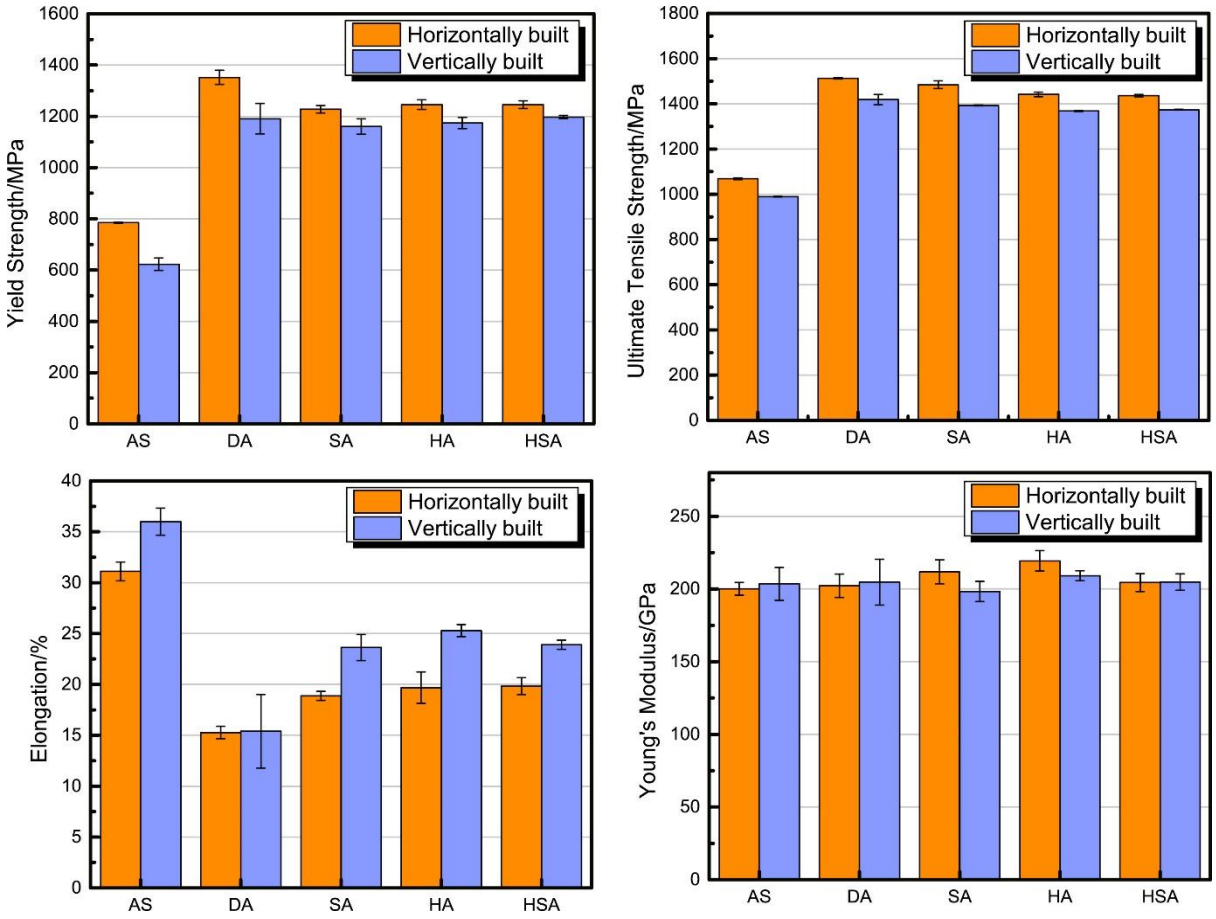

Figure 1-80 – These graphs show the changes in mechanical properties for a sample of IN718 tested in both the horizontal and vertical directions. The effect of heat treatment can be seen to increase yield strength (top left) and UTS (top right), decrease ductility (bottom left) and have little effect on Young's modulus (bottom right). AS refers to as-cast, DA – direct ageing, SA – Solution treatment and Aged, HA – Homogenised and Aged, and HSA – Homogenised, Solution Treated and Aged [132].

Anisotropy between horizontally and vertically built samples is reduced but still present in Figure 1-80 when yield strength and UTS are investigated. This anisotropy can be explained as the initial microstructure is present after heat treatment. This microstructure can be seen in Figure 1-81 and Figure 1-83. In Figure 1-81, the cellular structure is still visible along with the precipitated γ' (the white dots within the grains). The δ phase, which forms due to the niobium content of IN718, has been identified. This forms due to exposure to high temperatures for an extended period. The increase in mechanical strength due to the reduced grain size will be mitigated by the increase in deleterious phase formation (δ phase) on the grain boundary keeping the mechanical properties (yield strength and UTS) the same

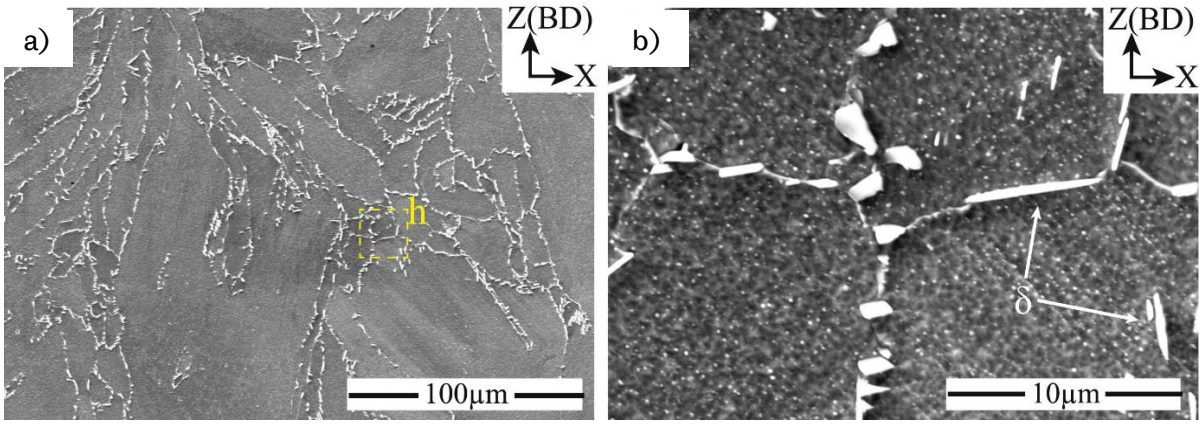

Figure 1-81 – These micrographs show the grain and cellular microstructure still present even after heat treatment for IN718. They also show the different phases being precipitated out mainly on the grain boundaries [132].

However, both orientations have tensile strengths over the ASTM standard for IN718. Raghavan *et al.* [134] also obtained EBSD maps in the build direction after heat treatment, and these are shown in Figure 1-82. The texture is still seen even after the 1200°C heat treatment, and the maps show that a more extensive heat treatment is needed.

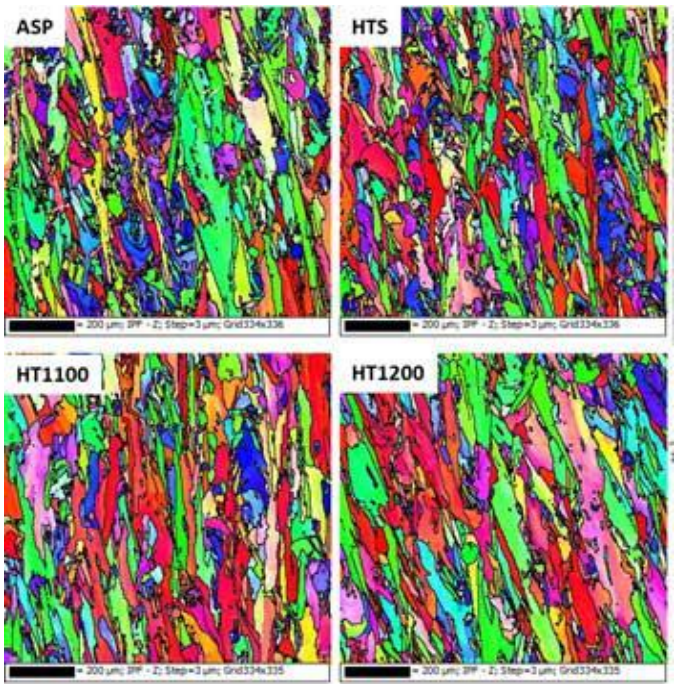

Figure 1-82 – These EBSD maps show the grain morphology perpendicular to the build direction. At higher heat treatment temperatures, there is a grain coarsening effect. Despite this, the initial texture remains, suggesting a different heat treatment is needed to eliminate this [134].

Deng *et al.* [132] obtained an EBSD map in the build direction for the as-built condition for IN718. This is shown in Figure 1-83 below.

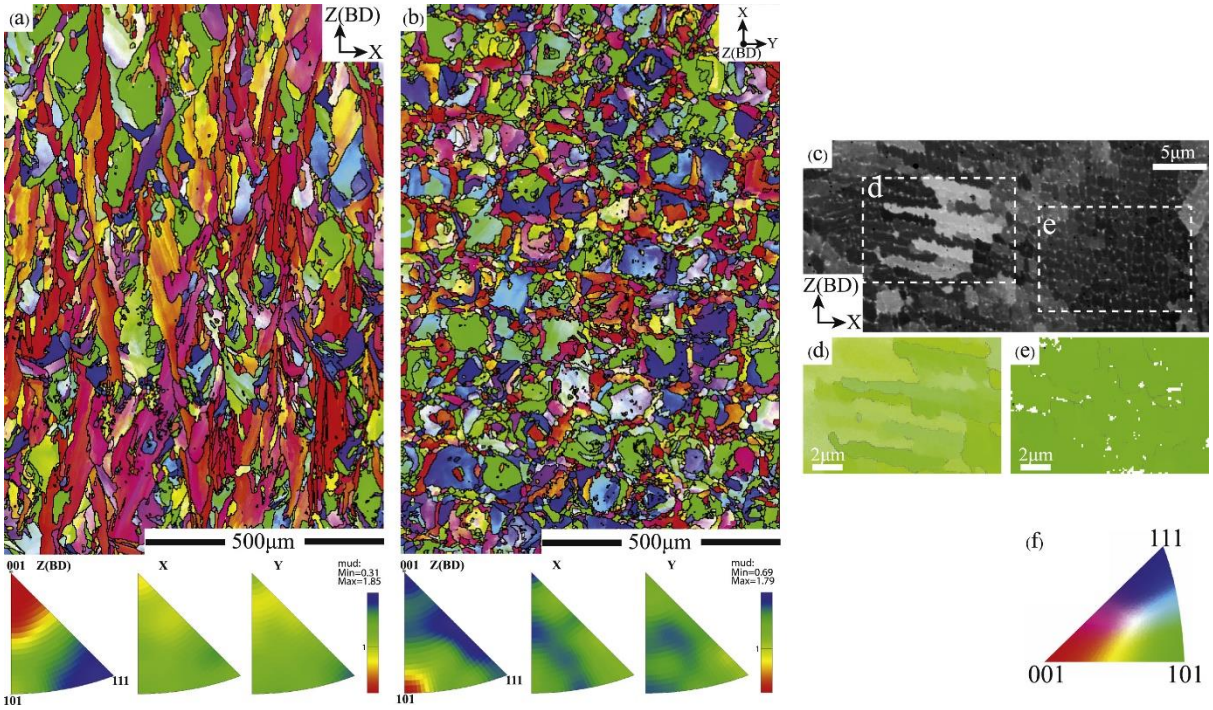

Figure 1-83 - These figures show the extent to which the texture is still seen even after heat treatment for IN718 (a) and b)) and the cellular structure (c). The predominant direction is along the [001] (z) direction [132].

The texture can be seen in a) where the inverse pole figure shows a large concentration in the [001] direction (i.e. build direction). When the build plane is investigated, a much lower fraction of anisotropy is observed, and hence the grain structure in this plane is more equiaxed. Heat treatments that do not homogenise the microstructure can be seen in Figure 1-84 below. The melt tracks are visible, both the width and depth.

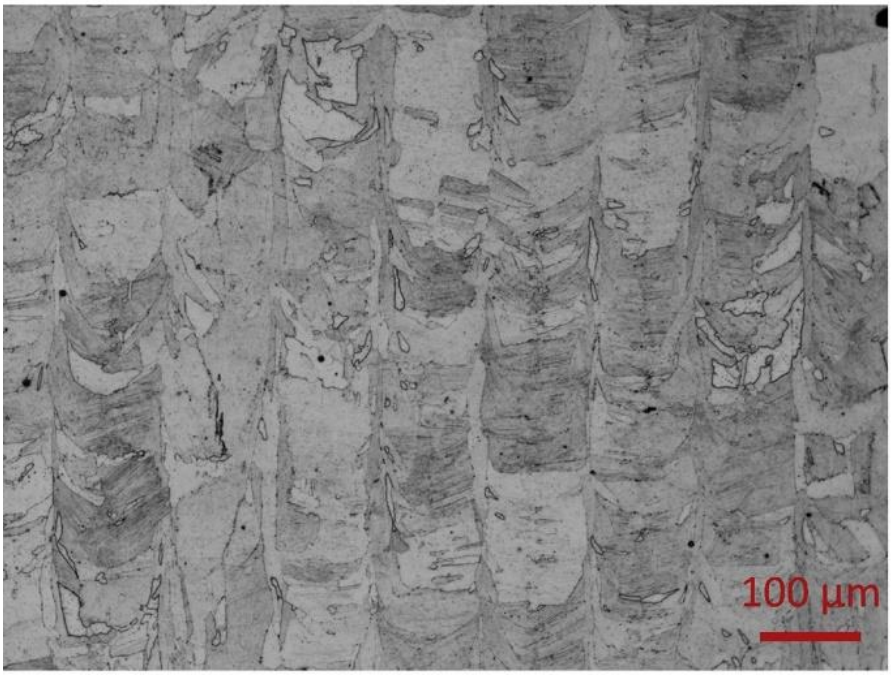

Figure 1-84 – In this micrograph, the melt tracks can still be seen in the z-direction. This micrograph is post heat treatment of IN718 [132].

Schneider *et al.* [133] used IN718, increasing the solution treatment temperature to 1163°C for 1 hour and including a HIP treatment at the same temperature for 3 hours. The complete heat treatment also includes a stress relief of 1066°C for 1.5 hours and ageing steps of 954°C for 1 hour 720°C for 8 hours and 620°C. This heat treatment produced the best mechanical strength, equal to the wrought properties and had a higher elongation to failure of 22%. The microstructure achieved through this treatment created an equiaxed microstructure, as shown in Figure 1-85. Although both a) and b) have an equiaxed microstructure, b) is finer due to the post heat treatment quench.

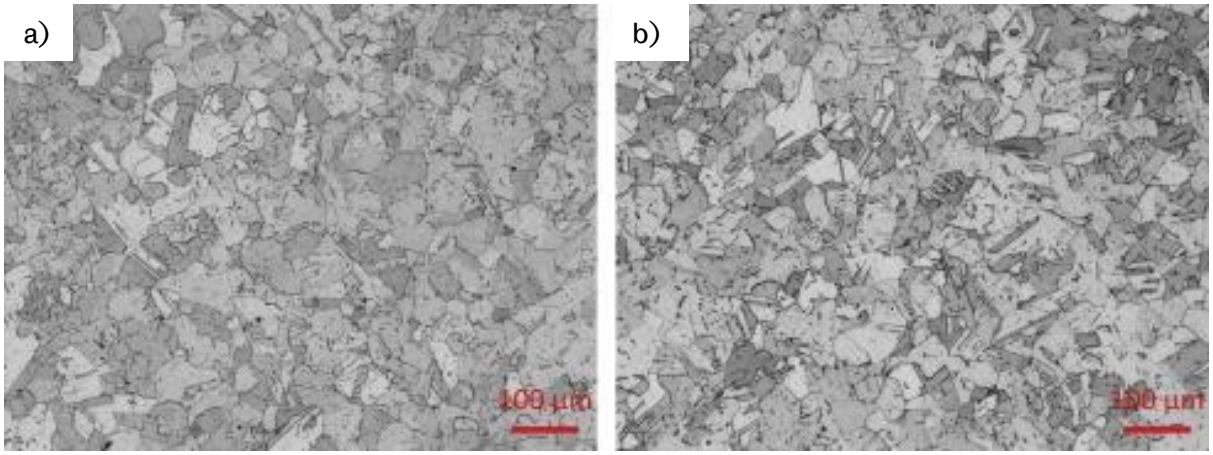

Figure 1-85– The microstructure of IN718 after heat treatment can be seen in these two micrographs. Due to the quench, the microstructure of b) is more refined than that of a), which has not been quenched. As a result, the finer microstructure is maintained from the as-built samples. [133]

Raghaven *et al.* [134] included a higher solution treatment (up to 1200°C) in their heat treatment. This reduced yield strength (1200MPa to 800 MPa) and UTS (1400MPa down to 1100MPa). However, elongation to failure was increased from 18% to 21%. The complete set of results are shown in Figure 1-86.

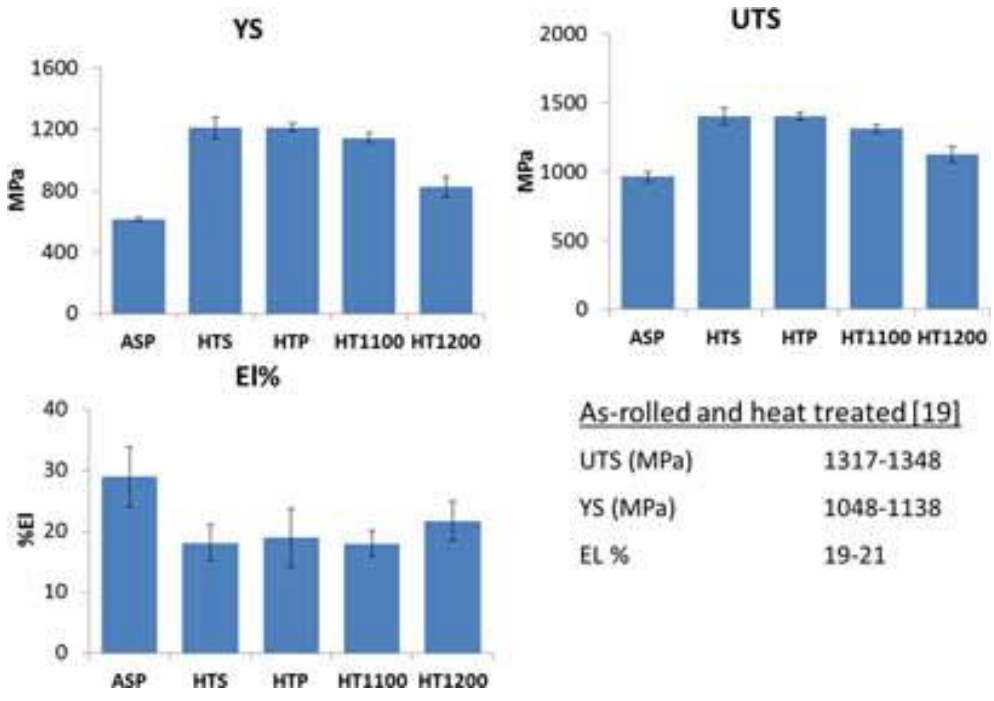

Figure 1-86 - These graphs show how higher temperature heat treatments can result in different properties for IN718 [134].

Comparing the results of Raghaven [134] and Schneider [133], it can be seen that a higher solutionising temperature does not lead to higher yield or ultimate tensile strength. A more

nuanced approach is needed to consider more heat treatments between the two states tested by Raghaven [134].

Haynes themselves suggest an age hardening heat treatment for Haynes 282 [5] that involves heating to 1010°C for 2 hours followed by an ageing treatment of 788°C for 8 hours. Joseph *et al*, [135] investigated the effect of this heat treatment on the microstructure and the mechanical properties of Haynes 282. In the study Joseph took micrographs of the un-heat-treated microstructure. Figure 1-87 shows the grain growth as a result of the heat treatment.

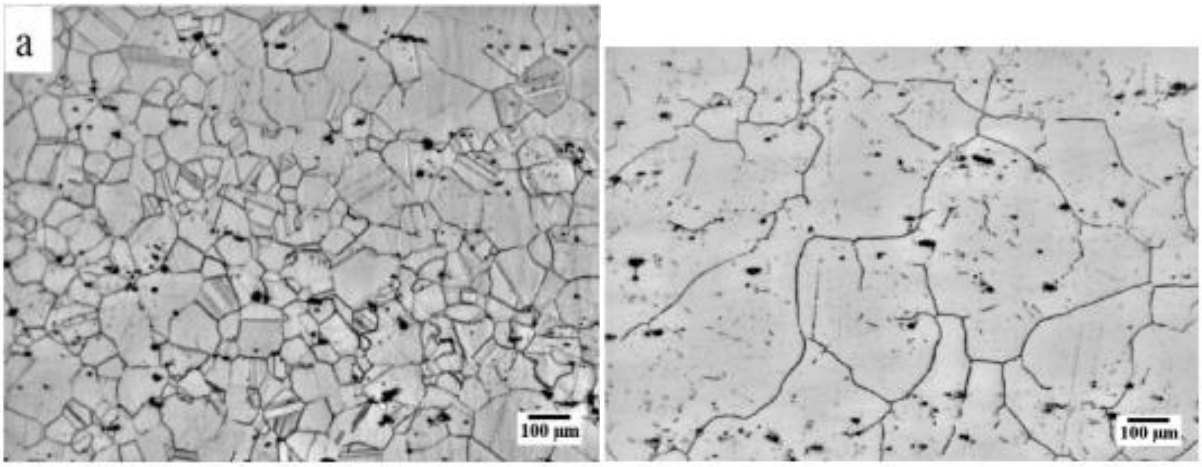

Figure 1-87 – Comparison of the grain structure from the un-heat treated (a) to the heat treated (b) state for Haynes 282. Grain growth can be seen to occur between the un-heat treated to heat treated condition [135].

The grains were observed to have grown from 100µm to 200µm. This change in the microstructure had a corresponding change in the mechanical properties. There is an increase in the hardness from 212HV to 310HV. The heat treatment results in a dispersion of γ' precipitates intragranuarly. In this project the γ' distribution was examined to see if the γ' distribution was the same when the heat treatment was applied to the LPBF manufactured part.

Boswell *et al*. [22] investigated the effect of Christofidou *et al*.'s [21] proposed heat treatment on LPBF Haynes 282. It was found to result in recrystallisation of the microstructure. This is evidenced by the comparison of the pole figures for the as-built and the heat-treated microstructures shown in Figure 1-88.

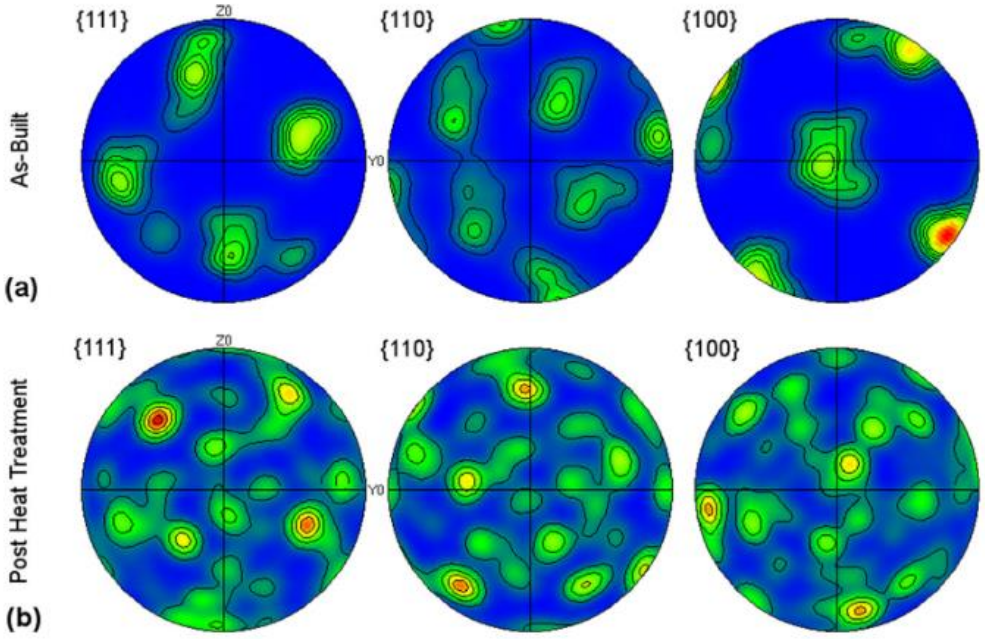

Figure 1-88 – Pole figures of the microstructure for LPBF Haynes 282. The strong texture seen in the as-built state (a) has been removed after heat treatment (b) [22].

The change in texture can be seen between a and b the strength in the 100 direction has been dissipated by the full recrystallisation of the microstructure. This is also seen in the creep rupture performance when tested in the direction parallel to the build direction and perpendicular. Figure 1-89 shows that the properties are isotropic.

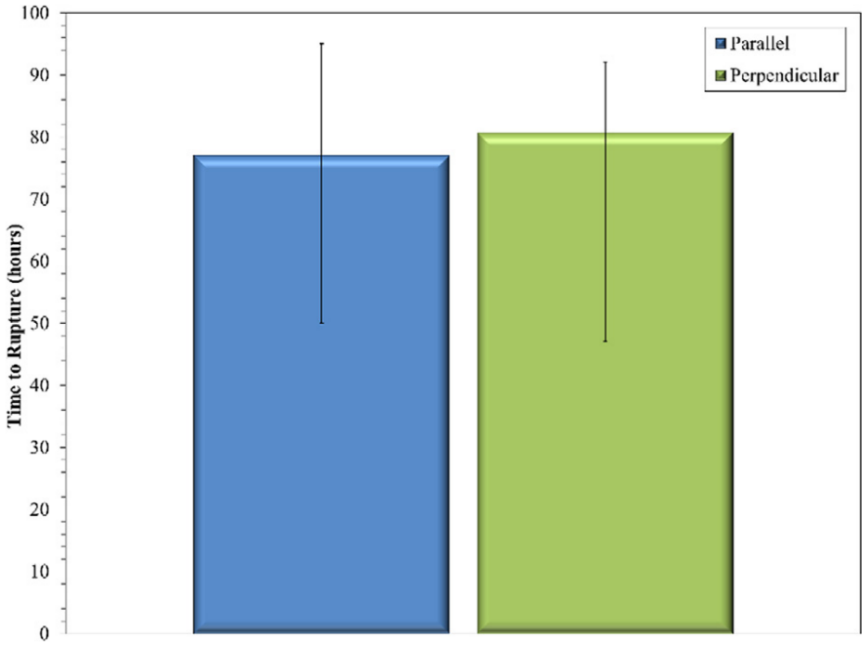

Figure 1-89 – Stress rupture test results for Haynes 282 in the different orientations. The anisotropy has been reduced by the heat treatment [22].

The time to rupture is the same in both directions due to the microstructure being recrystallised.

Variations in the heat treatment and its effect of the size and morphology of γ' precipitates were investigated by Ghiaasiaan *et al.* [136] This study showed how different heat treatments with temperatures below that suggested by Haynes effect the precipitates. Figure 1-90 shows these heat treatments and their effects.

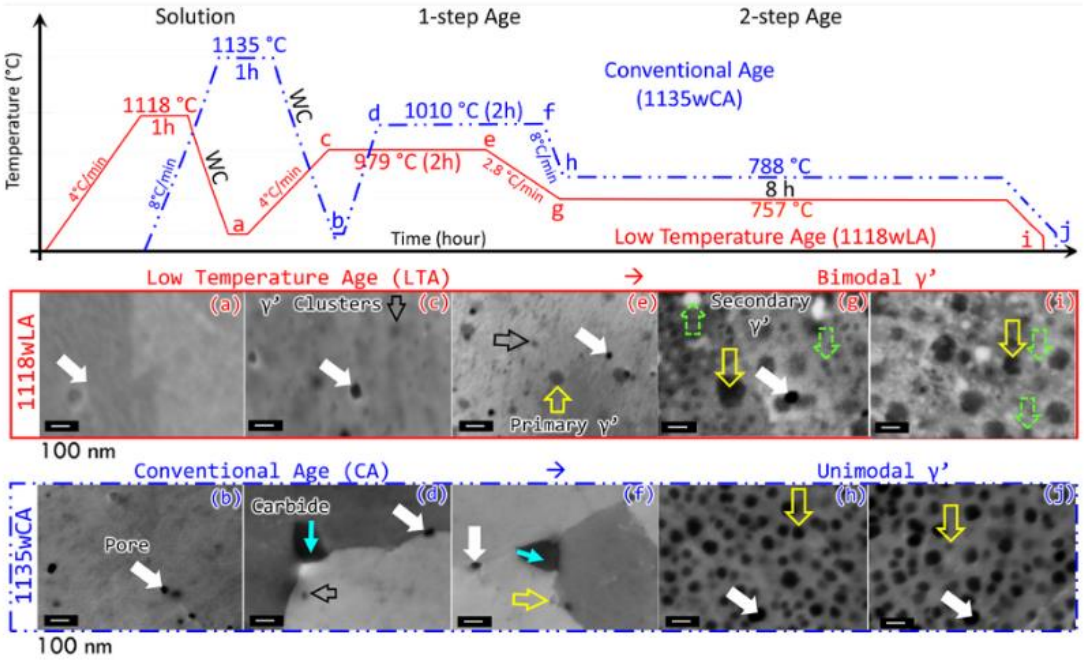

Figure 1-90 – Micrographs showing the precipitate evolution over the course of two heat treatments (a),(c),(e),(g) and (i) show the evolution as a result of a low temperature ageing, whereas (b), (d), (f), (h) and (j) shows the evolution for a conventional ageing [136].

The low temperature ageing results in a bimodal precipitate structure in contrast to the unimodal distribution for the conventional ageing treatment. The change in precipitate size distribution results in similar mechanical performance because the finer precipitates provide additional strengthening when the larger precipitates coarsen. This behaviour means that reductions in the heat treatment temperature due to larger component size does not lead to significant penalties in the mechanical properties of LPBF Haynes 282.

In this project, the aim is to use and analyse the heat treatments proposed by Christofidou *et al.* [21] and by Haynes [5]. The properties will be tested after heat treatment in the horizontal and vertical build directions to investigate whether anisotropy remains after the heat treatment. In terms of analysis, SEM images of the etched microstructure and EBSD maps will

be taken. These will be performed both in the build plane and direction. If the heat treatment is successful, there will be equiaxed grains in both directions.

2. Aims and Objectives

2.1 Background

This project arose out of the need from the sponsor to create lighter, more fuel-efficient engines. LPBF was chosen by the sponsor as the AM technique that would achieve this need, as it could produce topology optimised components that were lighter. Other candidate nickel superalloys such as Inconel 718 and CM247 were deemed unsuitable due to cracks and other defects in LPBF parts produced using these alloys. As such, there was a need for a new alloy to be used. Haynes 282 was an existing nickel superalloy chosen due to its excellent weldability and high-temperature performance.

2.2 Aims

- To ascertain whether Haynes 282 is suitable for this application by comparing mechanical properties achieved with other alloys.
- Compare the mechanical performance to existing literature both for LPBF and wrought alloys.
- Characterise the microstructure to identify features and how altering parameters affect these features.
- Investigate the susceptibility of Haynes 282 to cracking and which mechanisms are dominant.
- Analyse the effect that changing parameters has on cracking.
- Characterise machines and laser systems to optimise their performance.
- Find a method of translating parameter sets between machines and laser types.
- Control parameters during the build process to improve part quality.
- Analyse the effect of control on measured emissivity.
- Improve the parameter selection process by picking a target.

2.3 Objectives

- Samples will be built to ASTM standards, tested and compared to other LPBF Haynes 282 studies, and wrought and cast test results.
- The samples will be analysed using different techniques to identify present microstructural features and explain the mechanical properties observed.
- Alter parameters within the parameter space to observe if they result in a change in microstructure.
- Use existing models and equations to determine the susceptibility to cracking of Haynes 282.
- Analyse the phase composition around cracks to determine if certain phases are found around these cracks.
- Use velocity-dependent partition coefficient as well as thermal gradient models to determine how parameter changes affect crack susceptibility.
- Identify what standard heat treatments do to the microstructure and mechanical properties of LPBF parts.
- Identify and implement a heat treatment optimised for use with LPBF parts.
- Find a more generalised and efficient way to characterise an LPBF machine.
- Gain the ability to transfer parameters between different types of LPBF machines.
- Use a combination of different traditional approaches to minimise the time taken to find optimal processing parameters.
- Use Closed-Loop Control “on the fly” to monitor and suggest optimal parameters.
- Find if the control makes a statistically significant impact on the measured emissivity by conducting a Kruskal-Wallis analysis.
- Use Closed-Loop Control to reduce variation in thermal history within the part.
- Reduce location and geometrically based differences in thermal history.

3. Methods

3.1 Machine Operation

3.1.1 Renishaw SLM125

Figure 3-1 - Renishaw SLM125

The Renishaw SLM125 is a quasi-continuous laser powder bed fusion machine (LPBF). It has a 200W laser which operates with a wavelength of 1070nm. This laser is above the build chamber. Build files were prepared using the Netfabb software package. These files were then transferred to Renishaw. Once the parameters had been checked, the powder was poured into the build chamber hopper. The square baseplate (125mm width) was secured on top of the build platform and lowered, so it was flush with the build chamber. The build was then started.

The wiper blade causes the hopper to dispense powder which is then swept across the platform and collects in the powder reservoir below. Builds that are in progress can be viewed through the glass window. There are gloves so that easily combustible alloys can be worked on safely whilst the door is still closed.

Once the build had finished, the chamber was opened. The excess powder was removed from the build chamber, and the build plate with the builds attached was removed from the machine for post-processing.

The excess powder was transferred to the powder reservoir for recycling. The rest of the machine was then cleaned of any powder that might contaminate the next build.

3.1.2 AconityMini

Figure 3-2 - AconityMini machine set-up.

The AconityMini is a continuous laser system. The laser used has a wavelength of 1070nm and has a maximum power of 200W. The laser and scanner system are housed above the build chamber.

Build files were prepared using the Netfabb software package. These files were then transferred to the computer attached to the AconityMini. When the parameters had been checked, the powder was poured into the powder supply chamber within the machine to give a sufficient supply factor of powder (ratio of the depth of supply chamber/ height of build). The baseplate (140mm diameter) was secured on top of the build platform and lowered, so it was flush with the build chamber. Argon was then pumped into the sealed chamber until it reached below 1000ppm; the recirculation pump was then started. When the oxygen level had stabilised, the laser was turned on, and the build started.

Once the build had finished, the argon was turned off, and the chamber opened. The excess powder was removed from the build chamber, and the build plate with the builds attached was removed from the machine for post-processing.

The excess powder was transferred to the powder reservoir for recycling. The rest of the machine was then cleaned of any powder that might contaminate the next build.

The circular build platform has a diameter of 140mm. The build platform is fed by a second chamber whose base rises as the build platform lowers. The revealed powder is then swept across the platform by a wiper blade. There is a powder reservoir that can be emptied at the back of the machine. The whole build chamber is separate from the optics and can be moved in and out of position as required.

3.1.3 AconityLab

Figure 3-3 - Photo of the AconityLab

The AconityLab is a continuous laser machine with a wavelength of 1070nm and a maximum power of 400W. The laser and scanner system are housed above the build chamber.

Build files were prepared using the Netfabb software package. These files were then transferred to the computer attached to the AconityLab. When the parameters had been checked, the powder was poured into the hopper behind the machine. The baseplate (170mm

diameter) was secured on top of the build platform and lowered, so it was flush with the build chamber. Argon was then pumped into the sealed chamber until it had reached below 1000ppm, and then the recirculation pump was started. When the oxygen level had stabilised, the laser was turned on, and the build started.

Once the build had finished, the argon was turned off, and the chamber opened. The excess powder was removed from the build chamber, and the build plate with the builds attached was removed from the machine for post-processing.

The excess powder was transferred to the powder reservoir for recycling. The rest of the machine was then cleaned of any powder that might contaminate the next build.

Due to valves, the powder hopper and reservoir can be isolated from the build chamber and refilled or emptied as required whilst the build continues.

3.2 Powder Analysis

The powder used for all the experiments and builds within this work was manufactured by Praxair. The powder was manufactured using the gas atomisation method. Before the powder was used it was analysed using different methods. The elemental chemistry was found for the virgin powder using Inductively Coupled Plasma – Optical Emission Spectrometry method. The results of this are shown in Table 3-1. The chemistry is within the bounds of those specified by Haynes.

Table 3-1 – Table showing a comparison of the composition of the virgin powder received with the elemental composition and ranges stated by Haynes.

	Virgin Powder (%)	**Haynes Specification** [5]
Aluminium	1.6	1.5
Cobalt	10.25	10
Chromium	19.5	20
Iron	0.09	1.5 Max
Molybdenum	8.99	8.5
Nickel	57.38	57 (Balance)
Silicon	0.03	0.15 Max
Titanium	2.16	2.1

The virgin powder was put under the Inspect F50. The morphology was inspected for satellites. This is shown in Figure 3-4.

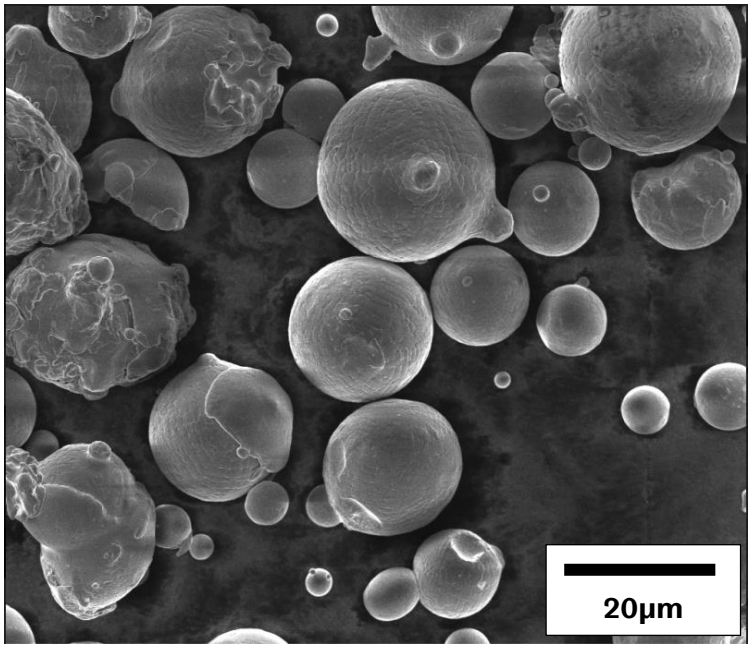

Figure 3-4 – Micrograph showing the virgin powder particles. The particles have varying surface finishes and morphologies but are close to spherical with small satellites. This is characteristic of gas atomised powder.

Satellites can be seen; this is a feature of gas atomised powder manufacture. They also affect flowability. A large quantity of satellites causes the flowability to reduce and can lead to the baseplate not being covered and powder building up in certain regions creating an uneven layer. The surface roughness is variables across the particles with the particles on the left having a very rough surface. However, the particles on the right have a significantly smoother surface. The satellites seen will allow the powder to cover the baseplate fully with a single layer of powder.

A powder size distribution study was conducted using a Mastersizer 3000. Virgin powder was placed in the machine having been sieved and the sizes of all the particles was measured. Figure 3-5 shows this distribution.

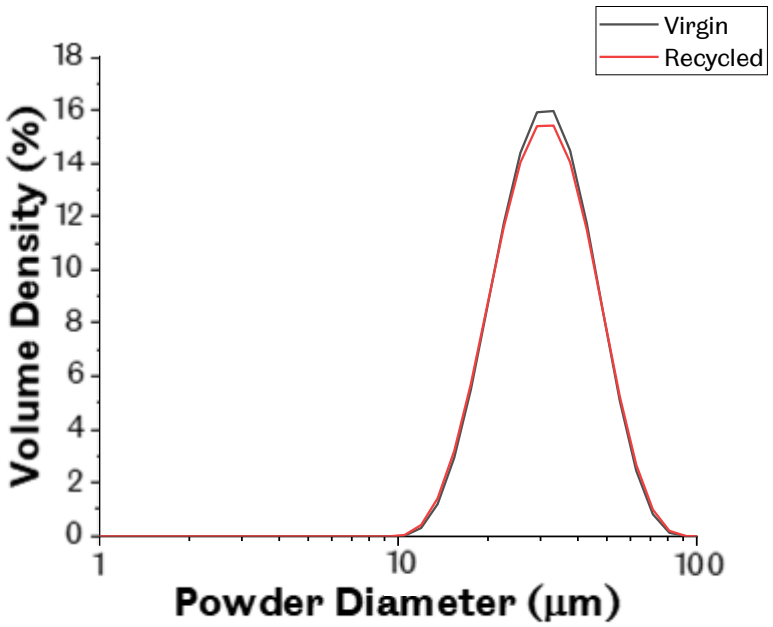

Figure 3-5 – Graph showing the PSD for the virgin powder and powder which has been recycled 8 times. There is a similar PSD across both powder sets with peaks within the nominal 15-45µm distribution.

It also shows the PSD for the powder after being recycled 8 times. The nominal distribution is 15-45µm and the peak can be seen between these values for both PSDs. Table 3-2 shows the D10, D50 and D90 values for the powders.

Table 3-2 – Table showing the D10, D50, D90 values for the virgin and recycled powder. The results for both samples are equivalent, showing the validity of recycling the powder.

	Virgin Powder		**Recycled 8 Times**	
	Mean PSD	**Standard Deviation**	**Mean PSD**	**Standard Deviation**
Dx (10) (µm)	19.1	0.151	19.3	0.259
Dx (50) (µm)	31	0.227	30.9	0.341
Dx (90) (µm)	50.4	0.806	49.1	0.498

Powder degradation was monitored as the powder was recycled. As powder was used it was stored in a separate container. Once all the powder had been used this waste powder was recycled by sieving out all the oversize particles and oxidised particles. The chemistry and

morphology were monitored as well as the PSD as the powder was recycled. Table 3-3 shows the chemistry for the different number of times the powder was recycled.

Table 3-3 - Comparison of the chemical compositions of the powder after being recycled. There is no trend for changing composition after being recycled.

	Recycled # Times								
	0 (Virgin Powder)	**1**	**2**	**3**	**4**	**5**	**6**	**7**	**8**
Aluminium (%)	1.6	1.61	1.6	1.58	1.59	1.59	1.59	1.56	1.58
Cobalt (%)	10.25	9.99	9.95	9.89	9.73	9.88	9.91	9.82	9.92
Chromium (%)	19.5	19.25	19.25	19.08	19.31	19.21	19	18.82	19.02
Iron (%)	0.09	0.09	0.1	0.09	0.09	0.09	0.08	0.08	0.09
Molybdenum (%)	8.99	9.2	9.16	9.03	8.87	8.96	8.93	8.78	8.88
Nickel (%)	57.38	57.64	57.73	58.16	58.21	58.11	58.34	58.78	58.26
Silicon (%)	0.03	0.04	0.04	0.03	0.03	0.03	0.03	0.05	0.07
Titanium (%)	2.16	2.18	2.17	2.14	2.12	2.13	2.13	2.11	2.14

From the table there is little change in the chemical composition after any of the times it was recycled. This validates the use of the powder multiple times as the composition. SEM micrographs of the powder were also examined. Figure 3-6 shows the micrograph for the last time it was recycled.

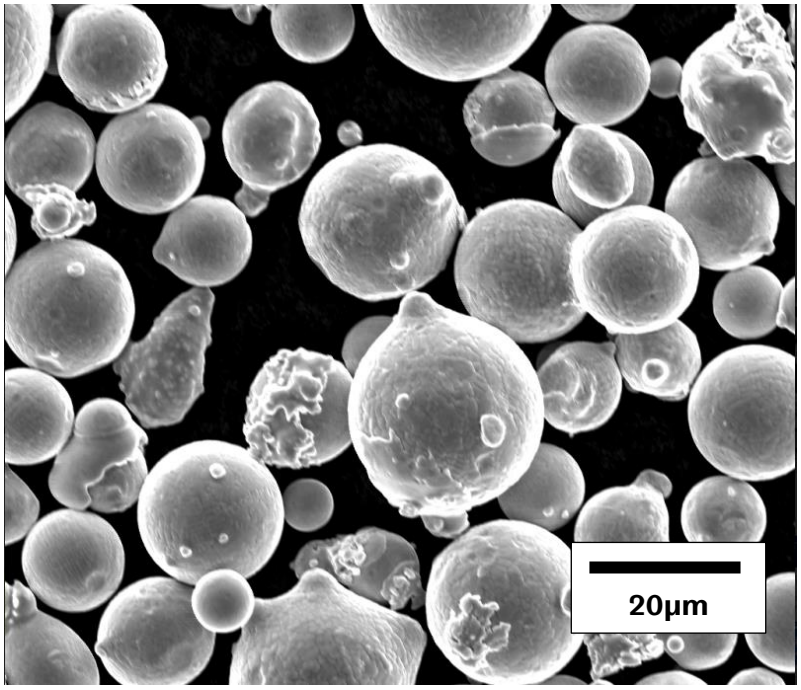

Figure 3-6 – Micrograph of the powder having been recycled 8 times. The particles have a similar morphology, size distribution and variation in surface finish as the virgin powder.

From the micrograph similar morphology as for the virgin powder is observed. There are satellites on the larger particles. This again validates the use of recycled powder. As a result of this analysis the results of experiments where the powder was virgin can be directly compared with those where the powder was recycled eight times. Overall the quality of the powder is governed by the initial manufacturing method and not the number of times it has been used. Gas atomised has been used for all builds due to availability. Future builds could look at using plasma atomised powder to see the effect on mechanical performance.

3.3 Methods for Part Manufacture

This work's parts were manufactured on three separate machines; Renishaw SLM125, an AconityMini and an AconityLab. Three different machines were used in order to explore different laser types; pulsed (Renishaw) and continuous (Aconity). The AconityLab was also required to explore higher powers due to its 400W laser. The AconityMini on the other hand had in-situ measurement equipment which enabled emissivity measurements of the meltpool to be taken. As such, all three machines were necessary.

The microstructure was examined for parts from all machines with attention to the primary dendrite arm spacing (PDAS). These PDAS were then plotted against a thermal gradient and thermal velocity function and compared to results from other laser powder bed fusion (LPBF) experiments with Haynes 282 and welding experiments with Haynes 282.

3.3.1 Renishaw

Cubes were built on a Renishaw SLM125 (SLM125). These 1cm cubes were designed using MTT software. The experiment included five cubes at three different energy levels; the exact parameters are given in Table 3-4 below. These parameters were based on consultations with another researcher [137].

Table 3-4 – Table shows the input parameters used for this initial experiment. The parameters were decided as a result of a consultation with another researcher.

Parameter	High Energy (HE)	Medium Energy (ME)	Low Energy (LE)
Power (W)	200	200	200
Hatch Distance (µm)	35	35	35
Point Distance (µm)	40	50	60
Exposure Time (µs)	80	80	80
Layer Thickness (µm)	30	30	30

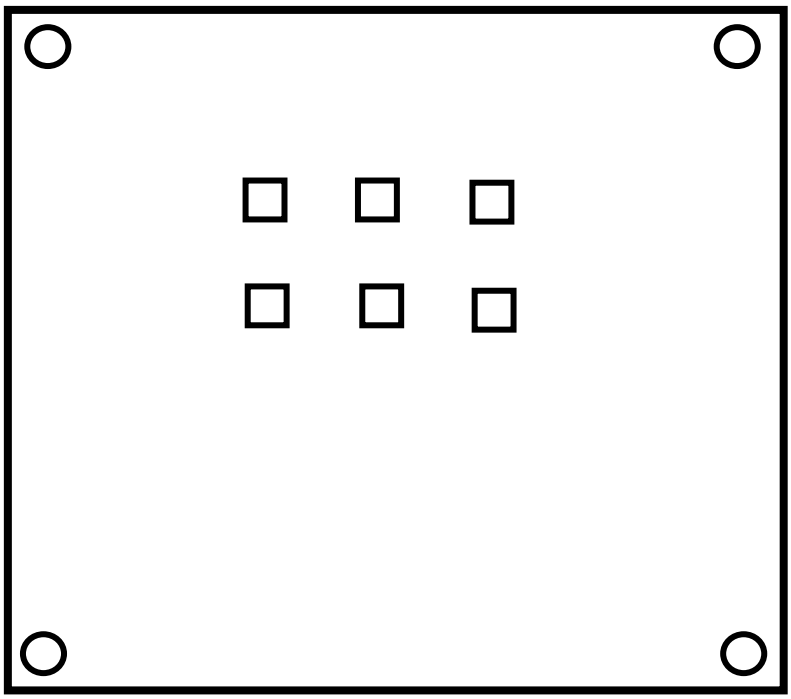

Figure 3-7- Schematic drawing of how the samples were arranged within the Renishaw. The left column was low energy, the middle column was middle energy, and the right was high energy.

The cubes were arranged on the build plate, as shown in Figure 3-7 above. The left column had low energy, the middle column had medium energy, and the right column had high energy. The samples were built on a stainless-steel baseplate and then were cut off using Electrical Discharge Machining (EDM).

3.3.2 AconityMini

The builds from AconityMini were done as part of a surface response design of experiments. To pick the central point, the Normalised Processing Map was used[86]. This map provided both the central and axis points for the DoE. The axis points were the onset of lack of fusion defects and the onset of keyholing (Figure 3-8). Schematically, the centre point (yellow) and range (red) are shown.

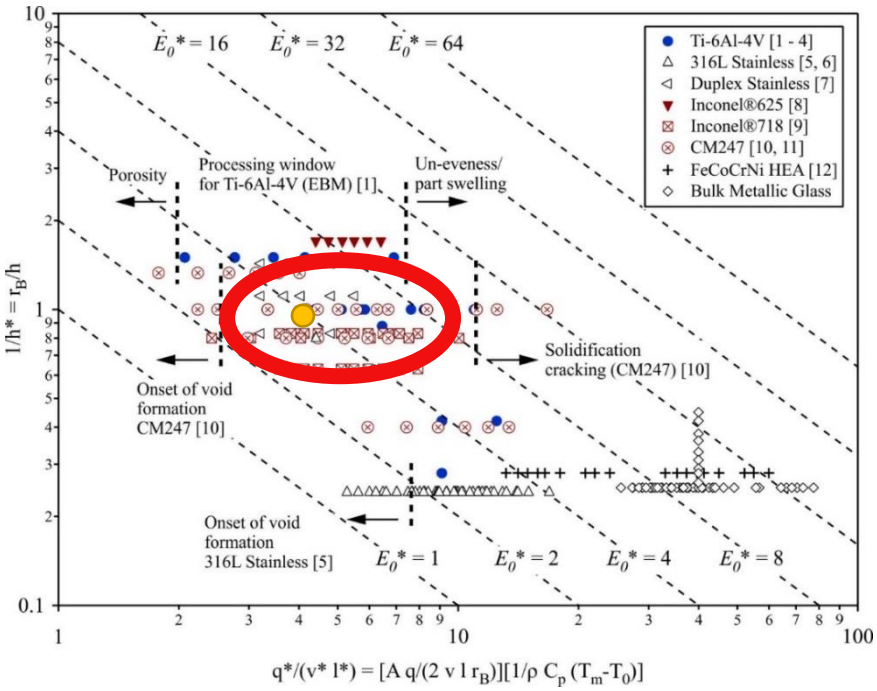

Figure 3-8 - The processing window explored in the surface response DoE. The yellow point was the centre point with the processing window shown schematically by the red ellipse. The response spanned the onset of lack of fusion to the onset of keyholing.

The exact parameters used for each parameter's low and high axial points are given in Table 3-5. These were used to build 1cm cubes.

Table 3-5 - These were the parameters used as the axial points for the surface response DoE. A total of 21 cubes were made for this DoE, including six central points to measure the potential error in readings.

	Low	**High**
Power (W)	90	130
Velocity (m/s)	0.75	1.5
Hatch Spacing (µm)	25	45

As with the Renishaw, the layer thickness was constant at 30µm. As the build progressed, any build that was swelling and in danger of causing the whole build to fail was prematurely stopped. The layout of the buildplate is shown in Figure 3-9. Rows that were immediately behind one another were offset to minimise the chase of failure in one part affecting another part.

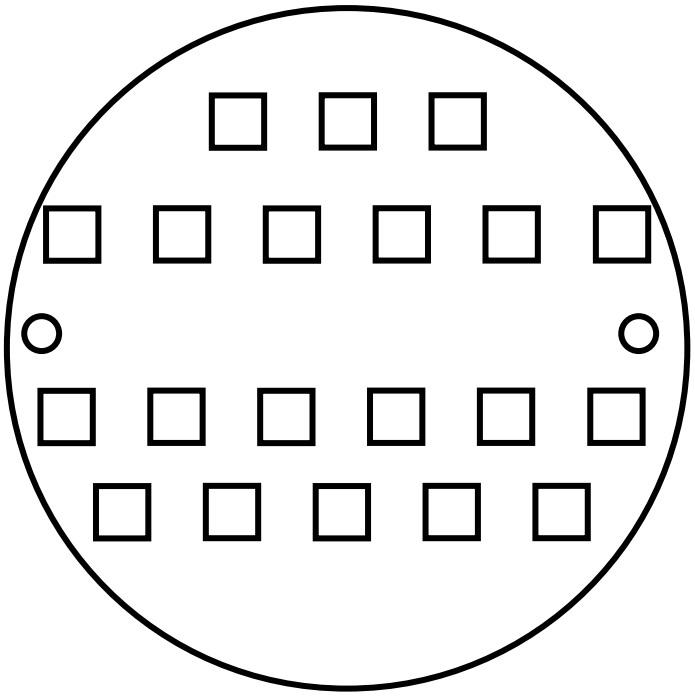

Figure 3-9 - Buildplate layout for the surface response DoE performed on the AconityMini. The 1cm cubes were built with a layer height of 30µm. Rows directly next to one another were offset in order to reduce the chance that a failure in one part could cause surrounding parts to fail.

The samples that were successfully built were examined (Table 3-6).

Table 3-6 - These are the parameters that were successfully built. Parameter sets from the surface response that were swelling were suppressed to protect both the wiper blade and other parts in the build. These successful builds were then analysed after being built.

Specimen ID	Velocity (mm/s)	Hatch Distance (µm)	Power (W)
SR12	1500	35	90
SR17	1500	45	90
SR16	1125	35	76.36
SR7	1760	35	110
SR5	1125	35	110
SR1	1125	45	110
SR14	1125	51.8	110
SR10	1125	25	143.64
SR15	750	45	130
SR3	750	35	130
SR2	490	35	110

Once the samples had been built, they were cut from the plate using EDM.

3.3.3 AconityLab

These builds were completed to investigate the effect of similar energy densities but with varying parameters on the microstructure and mechanical properties. The parameters spanned the optimal parameters found from the surface response DoE on the AconityMini and the recommended nickel parameters on the EOS M290; these are highlighted in green and blue, respectively (Table 3-7).

Table 3-7 - These are the parameters used in the similar energy build on the AconityLab. As these had similar input energies, parameter sets were used and tested that were interpolated between them and extrapolated to the bounds of what the machine could build in terms of enough power in the laser to cause fusion to occur and the maximum power possible with the laser on the upper end.

Specimen ID	Power	Speed	Hatch	Energy
ED1	75	1.17	22.7	94
ED2	110	1.125	35	93.1
ED3	145	1.08	47.6	94
ED4	180	1.035	61.7	94
ED5	215	0.99	77.0	94
ED6	250	0.945	93.8	94
ED7	285	0.9	110	94.3
ED8	320	0.855	132.7	94
ED9	355	0.81	155.4	94

Beyond these points, the parameters were extrapolated to span the entire range of powers possible using the AconityLab's laser system. The lowest value was set at 75W as below this, the power within the laser would not be enough to melt the powder. The highest value was set at 355W, which was the highest value that the machine could reach.

As with the other builds, 1cm cubes were built with a layer thickness of 30µm. Figure 3-10 shows the buildplate layout for the AconityLab. The samples were rotated 20° in order to reduce the load on the wiper as it encounters the parts.

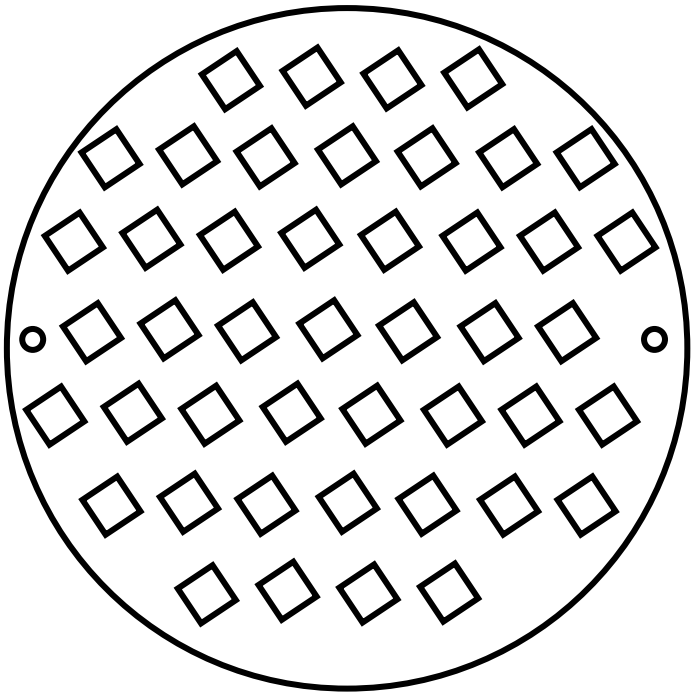

Figure 3-10 - Build plate of AconityLab experiment five 1cm cubes for the nine parameter sets. The energies were kept the same, but the powers and hatches were altered.

Once built, the cubes were cut from the baseplate using EDM before examination.

3.4 Microscopy

All samples were then sectioned in the XY plane using a SECOTOM. The samples were mounted in Bakelite, then ground and polished using the method in Methods 0. Once a mirror finish had been achieved, they were etched using glyceregia and the method in Methods 3.6.2. The surfaces were checked using an optical microscope to ensure that the cellular microstructure had been revealed.

The samples were imaged using an Inspect F50 scanning electron microscope (SEM). Using the SEM, the centre of a meltpool caused by the laser was found. The cells were then observed at the micron scale. Multiple images of each sample were then taken at different sites. These images were then processed using the CLEMEX image analysis software. The software identified each cell using colour differentiation, measured its length, and recorded it. All cells' average and standard deviation from a particular data set were found.

3.5 Stress Rupture Specimens

Stress rupture specimens were built to test the stress rupture properties of the built samples. The stress samples were built on the AconityLab. Samples were built in the vertical direction. This was done to compare more easily with results obtained by other continuous beam laser experiments.

Three heat treatment conditions were tested during the stress rupture experiments. These were no heat treatment, the heat treatment developed by Haynes themselves (Table 3-8) and the heat treatment devised by Christofidou (Table 3-9).

Table 3-8 - This table details the heat treatment steps suggested by Haynes. This heat treatment was designed for cast or wrought alloys and not those made using LPBF.

Temperature	Time
1150°C	1 Hour
1150°C→1010°C	Furnace Cooled
1010°C	2 Hours
1010°C → 788°C	Air Cooled
788°C	8 hours
788°C → Room Temperature	Air Cooled

Table 3-9 - The heat treatment steps suggested by Christofidou. This heat treatment has a higher solutionising temperature.

Temperature	Time
1250°C	1 Hour
1250°C→788°C	Furnace Cooled
788°C	8 Hours
788°C → Room Temperature	Gas Furnace Quenched

Having been heat treated in an argon environment the samples were then machined.

The samples were built to ASTM3 standard as this was the largest size that could be built due to the constraint of the size of the build plate. A diagram of the form of the sample is given in Figure 3-11 below.

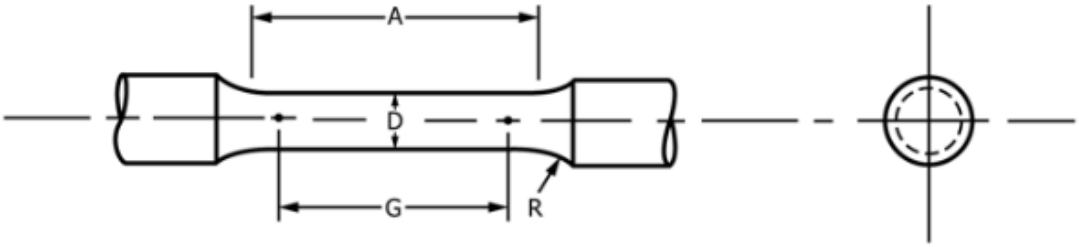

Figure 3-11 – Diagram of the stress rupture sample. All the key dimensions are labelled with definitions given in Table 3-10.

Below in Table 3-10 are the dimensions for the ASTM 3 standard.

Table 3-10 – Dimensions for the ASTM3 sample used for stress rupture testing.

Gauge Length (mm)	24±0.1
Diameter (mm)	6±0.1
Radius of Fillet min (mm)	6
Length of reduced parallel section min (mm)	30

The samples were machined on a Hardings GS 42 CNC machine to the ASTM standard and then tested on a Moyes tensile test machine with a furnace attachment to achieve the elevated temperature for the stress rupture.

3.6 Sample Preparation

3.6.1 Sectioning

Samples were cut using the SECOTOM 50 table top cut-off machine, then mounted and clamped in place. The cutting disc used had a diameter of 200mm and a thickness of 0.5mm.

The exact setting used were as follows:

Table 3-11 - Settings for the SECOTOM cutting process.

Rotation speed (rpm)	2200
Feed Rate (mm/s)	0.05

The disc was raised above the sample to ensure that it cut at an angle and reduced the disc motor's load. The settings were adjusted if the motor load reached above 20%, at which point the feed rate was reduced.

3.6.2 Grinding/Polishing

Grinding and polishing were performed predominantly using a Struers Automet 250. The following grinding papers and polishing cloths were used in the order presented by

Table 3-12.

Table 3-12 - Steps of the grinding and polishing method for Haynes 282.

Grit # / Cloth Name	# of Repeats	Polishing Solution Used?	Water Used	Platten Speed (Head Speed) (rpm)	Force (N)	Time
400 Grit	4	No	Yes	180 (59)	30	90 seconds
600 Grit	4	No	Yes	180 (59)	30	90 seconds
800 Grit	4	No	Yes	180 (59)	30	90 seconds
1200 Grit	4	No	Yes	180 (59)	30	90 seconds
MD Largo	1	9µm Diamond Suspension	No	150 (51)	25	15 minutes
MD Dac	1	1µm Diamond Suspension	No	150 (51)	15	12 minutes
MD Chem	1	50% Water / 50% OPS colloidal Silica	Dripping	120 (41)	10	5 minutes

The samples and the machine were thoroughly cleaned between each stage to ensure no contamination between stages. The diluted silica and water from the tap were allowed to drip at the same rate onto the pad. This rate was approximately one drip per rotation of the pad. After the silica step, the water flowrate was immediately turned up, and the platform flooded to remove as much silica from the surface as possible. This flooding was done for approximately 2 minutes. After this, the samples were rinsed with tap water and then sprayed with isopropanol and dried with compressed air.

3.6.3 Etching

Etching was performed using a modified glyceregia etchant (with composition in Table 3-13) within a fume cupboard.

Table 3-13 - Composition of the modified glyceregia etchant used.

Hydrochloric Acid	25 ml
Glycerol	15 ml
Nitric Acid	15 ml

The glycerol was added to the hydrochloric acid. Once these were mixed thoroughly using a glass rod, the nitric acid was added and mixed in thoroughly. Once the etchant has been made, it must be used immediately.

A freshly polished surface was immersed in the etchant for 10-20 seconds until the surface was dulled. Once this occurred, the sample was placed in water and the etchant removed. After washing the sample and then drying it with isopropanol, the sample was checked under an optical microscope to ensure that the etching had been successful.

3.7 Image Analysis

Images of the cells taken using the Inspect F50 SEM were analysed using a routine on the CLEMEX software.

- An SEM image of the cellular microstructure is taken (Figure 3-12a)
- A delineation operation is applied to make the difference between the cells more significant, allowing the cells to be measured more easily.
- A threshold was applied to the image where pixels of a similar colour are grouped in order to identify the cells (Figure 3-12b).
- the cells were identified,
- Each cell's primary diameter and sphericity were measured. These results were transferred to a table for further analysis.
- From the results table, the cells can be identified on the original image.
- The lowest diameter that measures a whole cell is taken as the lower limit, and all cell diameters lower than that are not counted towards the average cell size.
- Similarly, the largest value that measures a single cell and not two cells (due to pixel bleed) is taken as the upper limit, and all values greater than that are not counted.
- The last condition that must be met for a cell to be counted is that the sphericity is below the value representing either a mismeasurement of a cell or that the measurement represents two cells.
- Cells that satisfy these conditions are coloured green in Figure 3-12c. Those with sphericity that is too low are coloured pink, and those measuring multiple cells are coloured teal.
- These conditions are applied to the image through the routine, and the mean of the remaining cells is taken, as well as the standard deviation and number of cells counted.
- These values are used to plot the cell size and the error.

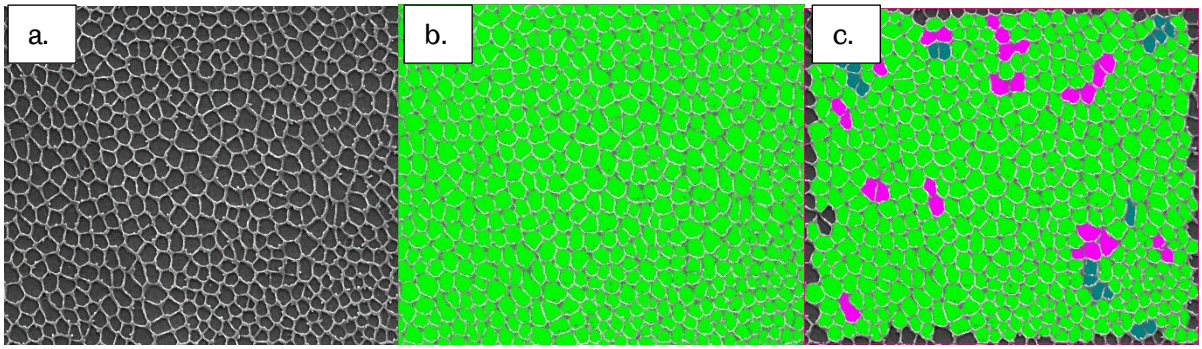

Figure 3-12 - These images show the original SEM image (a), the image after thresholding (green denotes the cells to be measured), (b) and the regions that do not satisfy the criteria are coloured pink and teal (c).

Whilst this method allows the measurement of hundreds of cells simultaneously, it has accuracy issues. There has to be a clear boundary of a different colour between two adjacent cells for the threshold to pick up the two cells' size accurately. There cannot be too much of a change in colour within each cell, or it will treat the cell as two separate cells. Thresholding minimises both inaccuracies. However, these errors may still be recorded, especially if the micrograph quality is low. The removal of data that does not meet the conditions reduces the error, but there are still measured values that are not of a single cell, be it a measurement of part of a cell or two cells.

The mean cell diameter, as well as standard deviation, could then be extracted from the data. The cell diameter is underestimated using this method as there is often no clear boundary to the cell, so the gaps between cells are not counted.

3.7.1 Image Error Calculation

An investigation into the effect of removing those measured values on the mean and standard deviation was conducted. The mean, standard deviation and standard deviation before and after the conditions were imposed. Table 3-14 displays the results.

Table 3-14 - Results of the investigation into the effects of imposing the conditions. In all cases, the standard deviation has been reduced, and the mean has been altered.

Sample		Mean	Standard Deviation
1	**Whole Data**	0.54	0.28
	Conditions Imposed	0.65	0.14
2	**Whole Data**	0.39	0.62
	Conditions Imposed	0.45	0.11
3	**Whole Data**	0.67	0.68
	Conditions Imposed	0.57	0.14
4	**Whole Data**	0.19	0.22
	Conditions Imposed	0.16	0.03
5	**Whole Data**	0.77	0.44
	Conditions Imposed	0.7	0.13
6	**Whole Data**	0.18	0.3
	Conditions Imposed	0.52	0.14
7	**Whole Data**	0.62	0.27
	Conditions Imposed	0.61	0.15

From the table, the standard deviation has been reduced by imposing the conditions. In addition, the mean has been altered. In some cases, it has been increased, whilst it has been reduced in others.

The effect of imposing the conditions can also be seen in the effect that altering the imposed threshold has on the mean and standard deviation. The threshold is based on the pixel intensity and is on a scale of 0-255. The threshold that best creates defined cells can be hard to specify. This can be a significant cause of error. The effect of altering the threshold value upwards and downward by five was observed when the conditions were imposed. The results are shown in Table 3-15

Table 3-15 - Results of a study into the effects of altering the threshold value. There is no significant effect of changing the threshold on standard deviation from the table, and there is a small effect on the mean value in Sample 2 but not in Sample 1.

Sample	Pixel Intensity	Mean	Standard Deviation
1	150	0.65	0.14
	155	0.65	0.14
	160	0.66	0.14
2	129	0.17	0.03
	134	0.16	0.03
	139	0.19	0.04

The effect of a change in the threshold has been shown to be minimal in changing the standard deviation and only has a small effect on the mean value for Sample 2. This has reduced the potential chance for a measurement error to be introduced.

3.8 Density measurement

3.8.1 Archimedes Method

The Archimedes density measurement method was employed to quickly measure the built samples' density.

A Mettler Toledo digital balance was used with the attached density kit, as shown in Figure 3-13 below.

Figure 3-13 - The Mettler Toledo digital scale with density kit attachment. Samples were weighed in dry air on the arms (circled in red) and then placed in the basket immersed in the water (circled in blue) to be measured again.

The sample was first placed on one of the protruding arms (circled red), and its mass was measured. The sample was then immersed in the water, placed in the basket, and measured again. The machine calculated the sample volume based on the buoyancy force exerted by the water. The density of the sample was found using Equation 3-1

$$\rho = \frac{m}{v}$$

Equation 3-1

Where m is the mass of the sample in dry air and v is the volume of the sample.

This measurement is a quick method for gauging how dense a sample is compared to others in the same build. The accuracy is lower than that of the image analysis and pycnometer because the result is affected by surface roughness. This roughness can trap air bubbles which results in lower densities being recorded.

3.8.2 Relative Density – Image Analysis

The porosity of the samples was measured using a polished cross-section of the part. This cross-section was imaged using the CLEMEX optical microscope. A mosaic was made for all surface porosity measurements that imaged the whole cross-sectional area at 100x magnification. This mosaic was then analysed using ImageJ software. The cross-section was selected from within the image, and a threshold was taken. The threshold separates and measures the number of pixels with an intensity above and below a specific value. Using the fact that pores appear dark on optical micrographs, the threshold can measure the porosity present.

This method requires a high contrast between the pores and the bulk material and a polished surface. The accuracy limit of this measurement is the pixel size of the image, and that this is only taking a cross-section and not measuring the whole volume.

3.8.3 Density Pycnometer

For more accurate density measurements, the Accupyc 2 pycnometer was used.

Figure 3-14 - Accupyc 2 pycnometer

This method used smaller samples as the cylindrical chamber was 1cm³. The samples were weighed using digital scales and then placed in the chamber. The pycnometer calculates the volume taken up by the sample within the known chamber and the mass.

This method is accurate but more time consuming than the Archimedes test. The samples need to be small enough to fit into the chamber and so sometimes must be cut up. This would not be suitable for larger parts where the whole density must be calculated.

3.9. Error Bars

Standard error is used to draw the error bars within this current work. Standard error shows the range that the mean value of a set of results could be, and it is found through Equation 3-2.

$$Standard\ Error = \frac{\sigma}{\sqrt{n}}$$

Equation 3-2

From the equation, measuring a large population results in a low standard error. This is particularly important for the cell measurements where the large number of readings from the images result in low standard errors.

4. Stress Rupture Sample Analysis

4.1 Introduction

This chapter will analyse the results of stress rupture tests performed at elevated temperatures with those from other studies[5], [13], [20]–[22]. These studies will include those performed on LPBF Haynes 282, incorporating cast and wrought samples. The results from the studies will be compared using the Larson-Miller Parameter[130]. The effect of different heat treatments on the properties will be examined. These heat treatments are proposed by Christofidou *et al.* and Haynes themselves[5], [21]. Haynes 282 will be compared to other similar alloys to see how well Haynes 282 performs. Measurements of the grain size and orientation will be made from parts with different parameter sets to see how the parameter sets affect these characteristics and how these characteristics may explain the mechanical behaviour.

The AconityLab was used to manufacture the stress rupture test samples. These were tested both before and after heat treatment. After testing the samples were placed under an SEM and the fracture surfaces were examined. The samples were then sectioned perpendicular to the fracture surface to investigate the volume behind the surface and how cracks have formed. The results of the stress rupture tests were compared to studies on LPBF Haynes 282 with different heat treatments. In addition, results were compared to cast and wrought samples. The overall results for Haynes 282 were then plotted along with those for similar alloys to see how Haynes 282 performs.

4.2 Method

In this experiment, results for stress rupture tests from different sources [5], [20],[13], [21], [22], as well as ones for this current work, were compared. All samples were built to the exact specification, and this specification was 11mmx11mm x100mm. The samples were built in the vertical orientation on the base plate. The parameter set used from this work is given Table 4-1 below:

Table 4-1 - This table details the parameters used to build the stress rupture samples for this work. These were chosen as they were the ones EOS recommended for nickel superalloys.

Power (W)	285
Velocity (m/s)	0.9
Hatch Spacing (µm)	110
Layer Height (µm)	30

To compare the results across the different pieces of work, the Larson Miller Parameter will be used. This parameter relates time to failure results at different temperatures using the equation:

$$LMP = \frac{T}{1000}(C + \log(t))$$

Equation 4-1

The plot of LMP against Stress will be populated from results quoted in the Haynes brochure [5] for an age-hardened plate. The exponential line of best fit will predict the stress rupture time at the test conditions. The experimental results from the stress rupture tests will be compared to this value to see if the results were an improvement.

In addition, the benchmark set by the sponsoring company will be used both for time to failure and elongation to failure. As the benchmark stress and test conditions are different from those used in the current work, the LMP will compare the results in the current work to the benchmark.

The effect of two different heat treatments on the stress rupture results will be examined. The reason for choosing these two heat treatments is that one was designed for wrought Haynes 282 whereas the Christofidou heat treatment was developed specifically for LPBF Haynes 282. It will therefore be useful to examine the differing effects that the two heat treatments have

and compare them to the as-built condition. The heat treatment proposed by Christofidou [21] is outlined in Table 4-2 and the Haynes treatment in [5](Table 4-3). The results will be used to understand if the heat treatments have had the desired effect of increasing ductility whilst maintaining time to failure.

Table 4-2 - The heat treatment steps suggested by Christofidou. This heat treatment has a higher solutionising temperature.

Temperature	Time
1250°C	1 Hour
1250°C→788°C	Furnace Cooled
788°C	8 Hours
788°C → Room Temperature	Gas Furnace Quenched

Table 4-3 - This table details the heat treatment steps suggested by Haynes. This heat treatment was designed for cast or wrought alloys and not those made using LPBF.

Temperature	Time
1150°C	1 Hour
1150°C→1010°C	Furnace Cooled
1010°C	2 Hours
1010°C → 788°C	Air Cooled
788°C	8 hours
788°C → Room Temperature	Air Cooled

The results from the current work and the work done by the sponsoring company and Shaikh *et al.* [3] will then be plotted on an LMP Stress plot to visually compare the results to those found by Haynes [5]. Plotting these data points will give a more accessible visual representation of the results and fit into the overall trend.

The overall results, as well as the spread of data, will be recorded. The gradient for Haynes 282 will be compared to similar alloys to observe how it performs relative to these alloys.

4.2.1 Fracture Surface and Volume Investigation

The fracture surfaces of the tested samples were then preserved. The samples were cut parallel to the fracture surface so they could be mounted inside the Inspect F50 SEM. Micrographs were then taken of the fracture surface for analysis. After this had been conducted, the sample was then cut perpendicular to the fracture surface and then mounted in conductive Bakelite. The fracture volume was then imaged using the CLEMEX microscope to observe the location and morphology of the cracks. Finally, the sample was placed under SEM and EDS was performed so that the chemistry of the region surrounding the cracks could be investigated.

4.2.2 Grain Size and orientation

EBSD maps were taken of sample ED1 and ED9 from the AconityLab similar energies build (Table 3-7) The average grain size and aspect ratio were found using the Channel 5 software. The measurements were compared to see if the change in normalised enthalpy corresponded to a change in grain structure.

4.3 Results

Stress rupture tests conducted as part of this work and other pieces of work[5], [20] have been combined to more fully characterise the stress rupture performance of Haynes 282 built using LPBF in both the as-built and heat-treated condition.

A comparison between the stress rupture results at both the 340MPa and 310MPa stress levels compared to expected times to failure from the brochure is possible using the Larson-Miller Parameter (LMP). This parameter predicts the time to failure based on the stress and temperature at which the test occurs. The equation is shown as Equation 4-2 below.

$$LMP = \frac{T}{1000}(C + \log(t))$$

Equation 4-2

Results from the brochure for age-hardened plate Haynes 282[5]at various temperatures can be plotted (Figure 4-1). Haynes quoted the stress required at specific temperatures to cause rupture at 100, 1000 and 10000 hours.

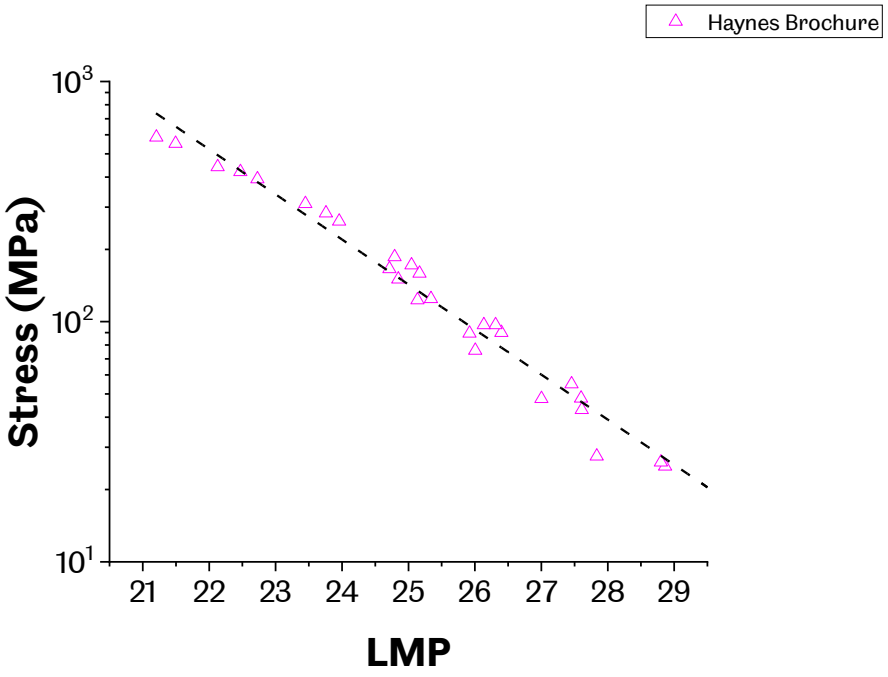

Figure 4-1 - The quoted stresses that cause rupture at 100, 1000, and 10000 hours for different temperatures were plotted on this graph. Haynes quoted the values in the Haynes 282 brochure.

The Y-axis is the stress and is a logarithmic plot to accommodate the range of stresses required to cause rupture. On the x-axis is the Larson Miller Parameter. An exponential line of best fit can be drawn that encompasses all the points from the brochure. This line then gives

a relationship between stress and LMP. The LMP associated with 340 MPa and 310 MPa can be found. The expected time to rupture can be found in the LMP equation. This time can then be compared to the experimentally found values. Values from literature and testing by the sponsoring company can be compared to the experiments to verify the results and give more certainty to the conclusions.

Figure 4-2 shows the LMP vs stress plot with the addition of the data points from this current work and those found from other studies [13], [20]–[22]

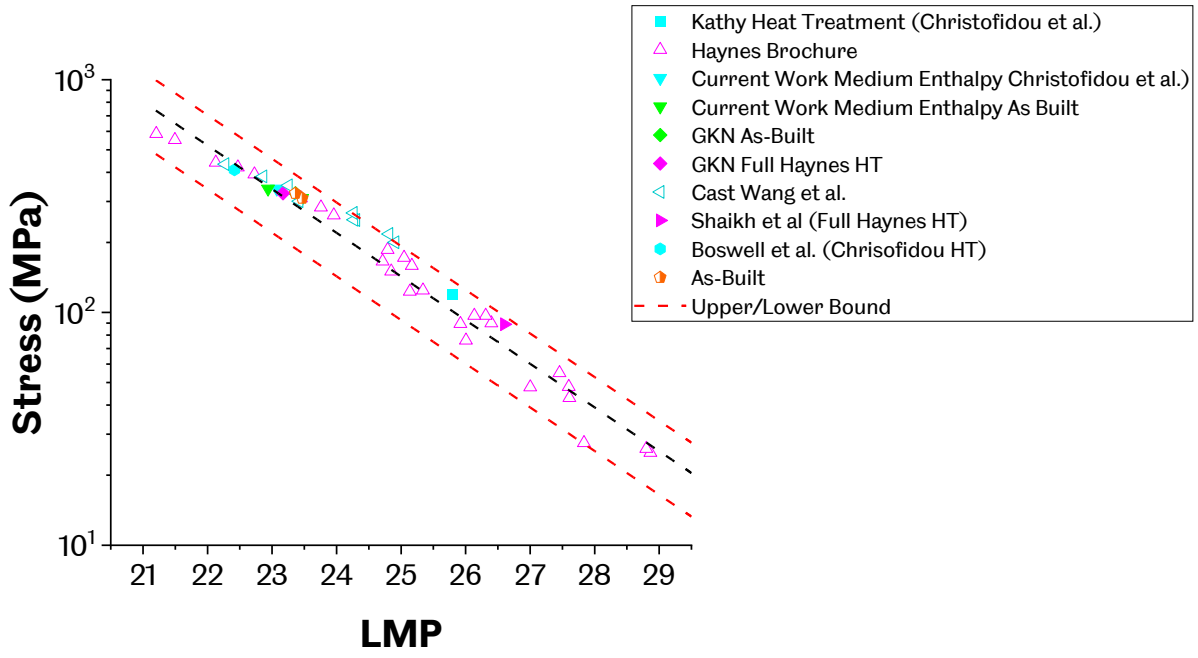

Figure 4-2 - This plot of LMP against stress includes data from different sources. Data from LPBF builds has been plotted with cast and wrought samples. A single line of best fit has been drawn through all the data as it forms a continuum. The effect of the heat treatment has not been statistically proven. Upper and lower bounds for the best fit line encapsulating all the data have been drawn.

These include LPBF tests with[5], [20]–[22], [138] and without heat treatment[13], [139]. The two different heat treatments from Haynes and Christofidou [5], [21] are shown. The LPBF points are in a continuum with the original points from the Haynes Brochure. The upper and lower bound of all data points has been drawn by taking the gradient of the line of best fit and intercepting it with the point that is furthest to the bottom left and also to the top right. The point to the bottom left comes from the Haynes brochure and is for a plate material. All the results from this study and others on LPBF material lie between this point and the high point which came from a study on cast material. This shows that the results agree with existing literature and existing manufacturing processes. As such the error seen within the stress rupture tests conducted in this study is acceptable.

The effect of the heat treatments on the time to rupture is unclear as there is no apparent difference between the two heat treatments or with them and the as-built samples. Whilst this is the case in the vertical (build) direction, this may not be the case in the horizontal direction. EBSD maps were made using the Inspect F50, which show the grain size and orientation (Figure 4-3). shows the maps for the ED9 and ED1 samples (Table 3-7).

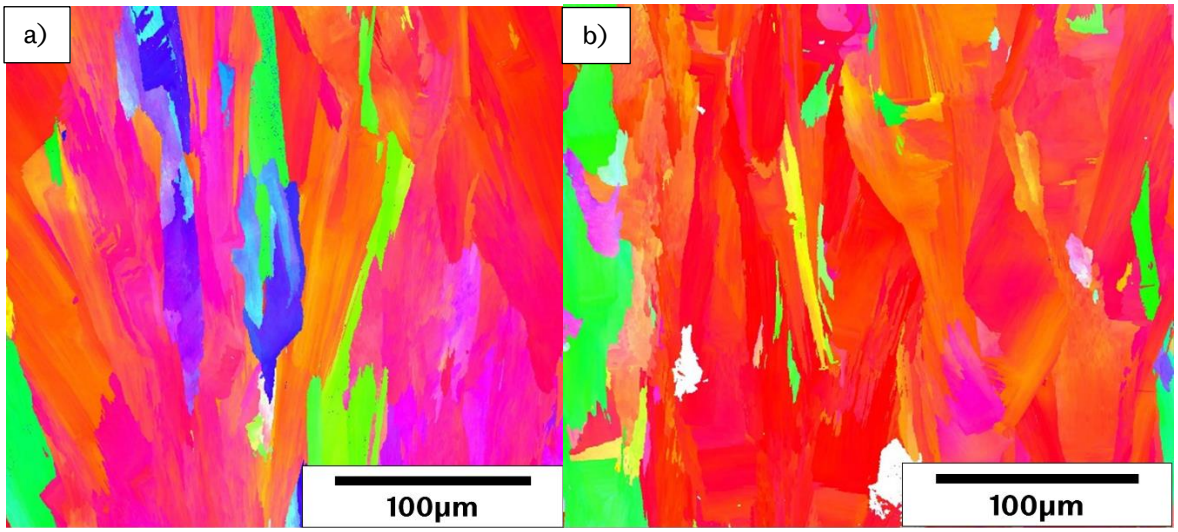

Figure 4-3 - EBSD maps of the as-built microstructure with the lowest enthalpy a) and highest enthalpy b) parameter sets. The maps are taken in the XZ direction. The columnar grains can be seen in both maps.,

The EBSD maps show epitaxial growth occurring in the build direction. When comparing the maps from the two samples, there is no difference in the grain size or aspect ratio (Figure 4-4).

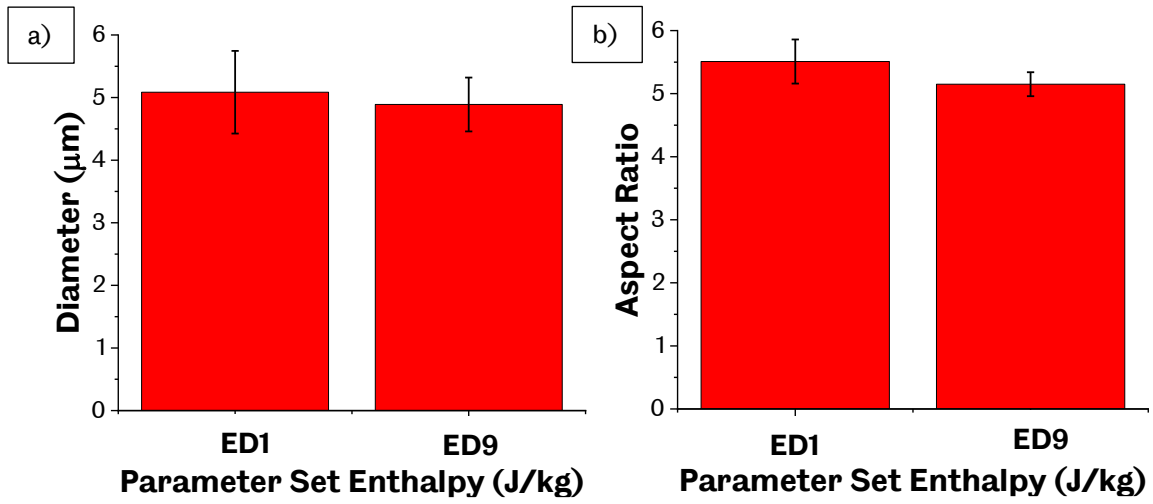

Figure 4-4 - The results of the image analysis for the two enthalpy levels. These different laser parameters show no difference in grain size (a) or aspect ratio (b).

From the graphs, there is no statistically significant change in either metric. The enthalpy has been significantly altered between the two-parameter sets; the layer height has remained the same. This consistent parameter has allowed grains to grow in the build direction as each subsequent layer has been built. The grain structure is no different between the two parameter sets, and there are no differences between the two-parameter sets on this length scale. In Section 5.7, the differences in what crack mechanisms these two parameter sets may be susceptible. When the pole figures are analysed (Figure 4-5a and b), a strong texture in the 100 direction correlates with the grain morphology seen in the EBSD maps.

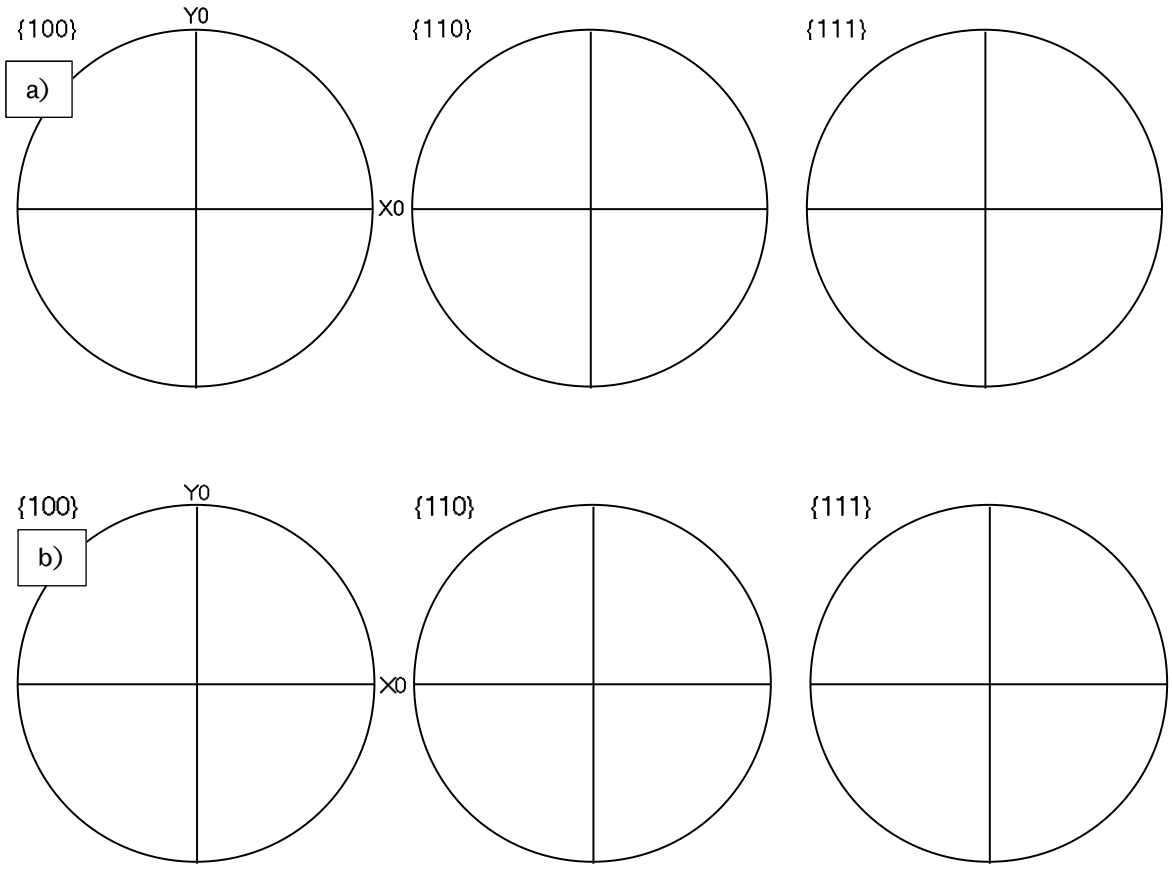

Figure 4-5 - Pole figures for the different parameter sets. a) is for ED1, b) is ED9. Both parameters sets result in a strong texture in the 100 direction. This texture correlates with the map, which saw elongated grains in the build direction.

Having established why the built LPBF as-built samples perform as well as the wrought parts from Haynes. The next step is to analyse if the heat treatment has the desired effect of recrystalising the microstructure and creating a more equiaxed microstructure. The results of the two heat treatments are shown in Figure 4-6 below.

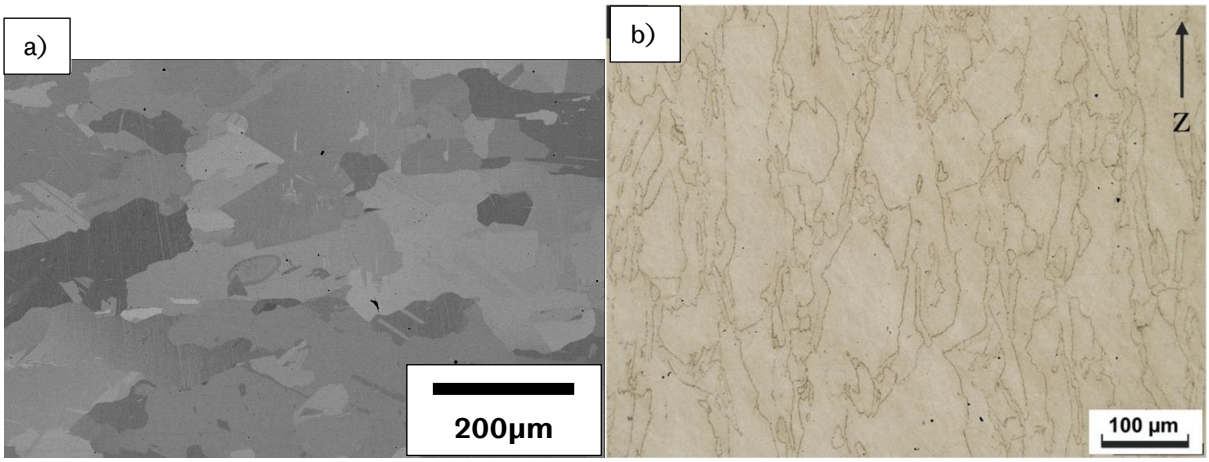

Figure 4-6 - The micrograph on the left a) and the micrograph on the right b) show the effects of the heat treatments. They are both taken in the XZ plane. The treatment by Christofidou[21] *has resulted in recrystallisation and an equiaxed microstructure. The Haynes heat treatment*[5] *has retained the elongated columnar grains present before the heat treatment.*

Both images are taken in the XZ plane. For the Haynes heat treatment, the micrograph on the right shows that there is still a columnar grain structure present, meaning that no recrystallisation has taken place. This microstructure contrasts the microstructure achieved by Christofidou, the micrograph of which is shown on the left. The micrograph shows an equiaxed grain structure. The heat treatment developed by Christofidou has a higher solutionising temperature which overcomes the additional energy required to achieve recrystallisation in LPBF [21]. The lower temperature designated in the Haynes heat treatment [5] does not achieve this required additional energy.

The recrystallisation should have had the effect of reducing the time to rupture in the vertical direction as there are more grain boundaries in the direction of applied stress. This reduction in time to rupture does not occur according to the results. More testing is required to validate this. This result suggests that other factors affect the mechanical properties, such as cracking mechanisms. These will be discussed further in Section 5.7.

Taking the results from all sources for Haynes 282 together, a characteristic line of best fit for Haynes 282 can be drawn (Figure 4-2).

The upper and lower bound encompassing all the data points have been drawn. The bounds show a variation of $\pm$30%, and this deviation shows how much variation there is in stress rupture. The test results can be heavily affected by minor differences in the microstructure,

such as cracks that may have formed during the build process or defects found within the part due to lack of fusion or keyhole defects.

Taking the line of best fit, this can be compared to those from other alloys to observe how Haynes 282 performs compared to similar alloys. This comparison is shown in Figure 4-7 below:

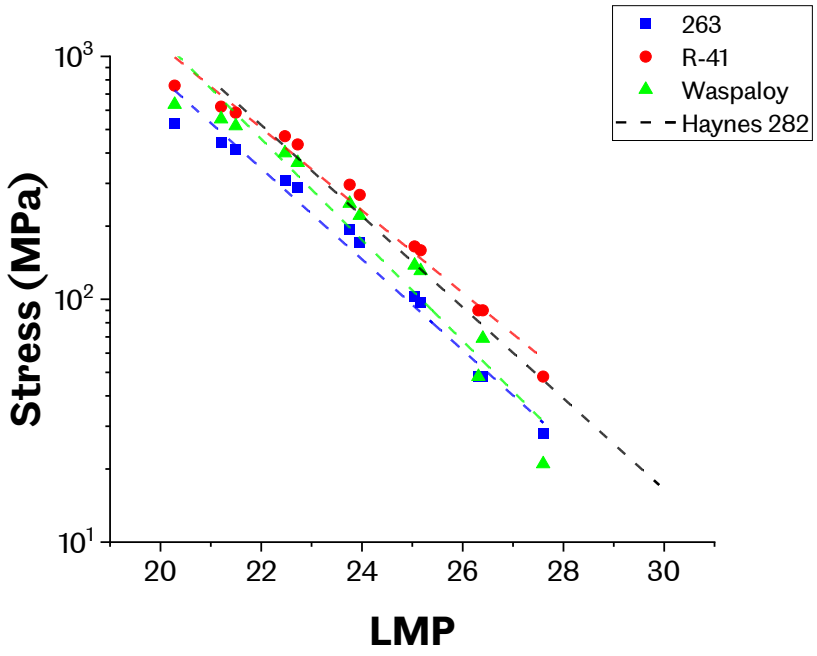

Figure 4-7 – Comparison of the different LMP vs stress plots for equivalent nickel superalloys. Haynes achieves a better LMP parameter than either Waspalloy or 263 within the tested regions but is below R-41.

The plot shows that Haynes 282's stress rupture performance within the tested region is lasts longer than Waspalloy and 263 whilst its time to rupture is below R-41. More testing is needed to verify if this is still the case when more data points are available. Further comparisons between these alloys will be made in section 5.7.5.1 when their susceptibility to strain age cracking will be plotted.

Looking further at the fracture surface it can be seen that all samples fractured in a ductile manner. This is backed up by the elongation to failure results which are shown in Table 4-4.

Table 4-4 – Results of the stress rupture testing. The elongation to failure for different heat treatment conditions is shown.

Specimen ID	Heat Treatment	Elongation to Failure (%)
ABED7	**As-Built**	16.6±2.3
HED7	**Haynes Heat Treatment**	13.1±1.9
CED7	**Christofidou Heat Treatment**	17±2.6

The table shows the results from the stress rupture have achieved elongation to failure in excess of 10% this was the benchmark set by GKN to identify whether the sample had fractured in a ductile or brittle manner. It can be seen that the heat treatments have had contrasting effects on the elongation to failure. The Haynes heat treatment has reduced the elongation from the as-built state whereas the Christofidou heat treatment has increased the elongation to failure slightly. This decrease in ductility has come due to the strengthening effect that the heat treatment has on the microstructure The Christofidou heat treatment causes recrystallisation as shown in Figure 4-6. This will reduce the anisotropy that is exhibited in the as-built sample (See Figure 4-3) and thus the elongation to failure will increase. Looking at the fracture surface will inform us as to what type of fracture has occurred. This is shown in Figure 4-8a which depicts the fracture surface of HED7.

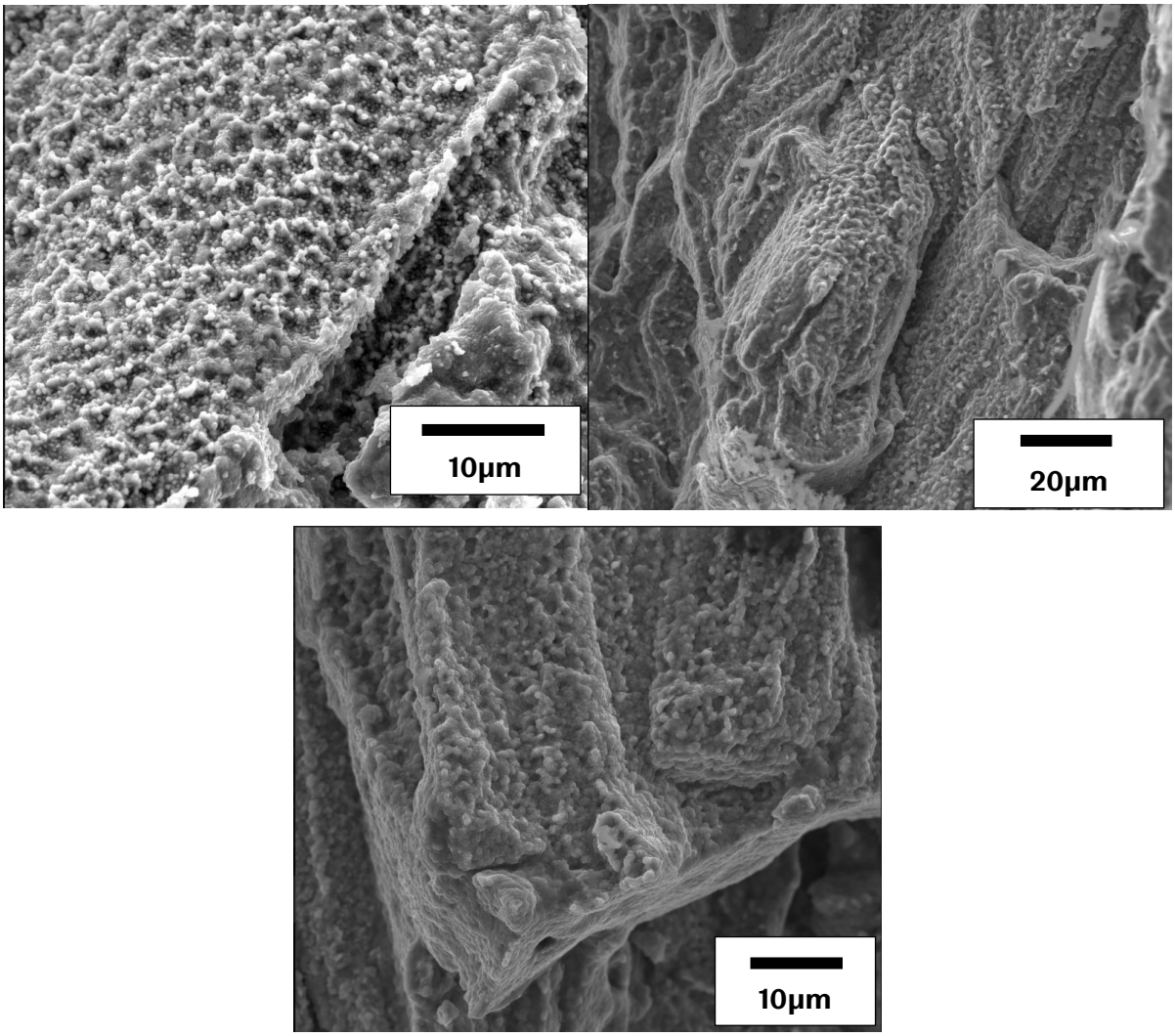

Figure 4-8 - Micrographs showing the fracture surfaces of the stress rupture tests. (a)HED7, (b) ABED7 (c) CED7. All samples display ductile fracture, characterised by the appearance of dimples.

The fracture surface has many dimples on it. This is indicative of ductile fracture. Looking at the other surfaces, they too have dimples which would suggest that ductile fracture has occurred. By looking at the fracture volumes the location of where the cracks have formed can be identified. Figure 4-9a shows ABED7.

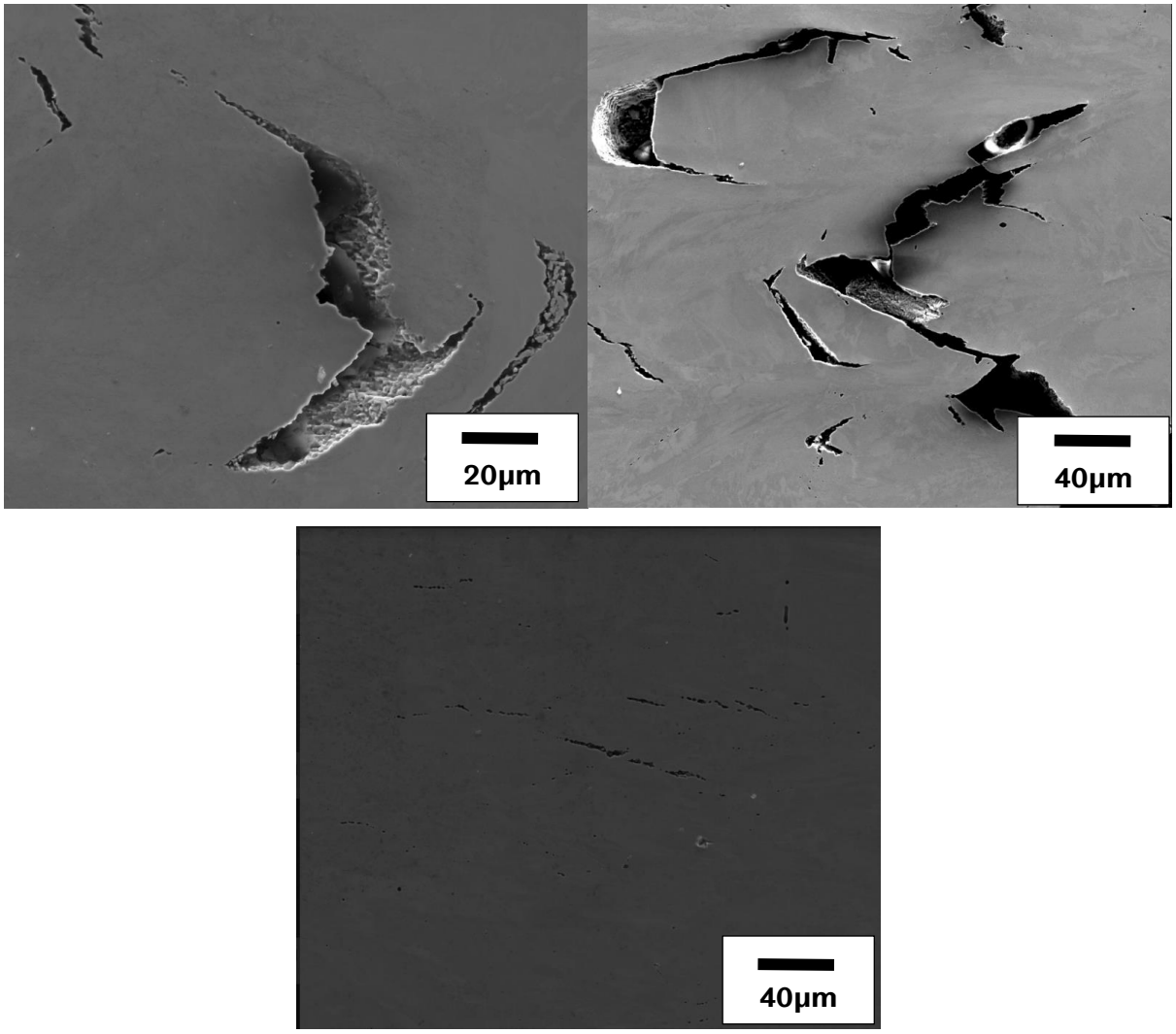

Figure 4-9 – Micrographs showing the fracture volume for (a) ABED7, (b) HED7, (c) CED7. Decohesion and cracks at the bottom of meltpools can be seen in (a) and (b), (c) shows cracking in the intergranular region.

The u-shape of the cracks point to the fact that the cracks have formed intergranularly and at the bottom of the meltpool causing decohesion between neighbouring meltpools. This is the case with HED7 as well. Even though the sample has undergone a heat treatment due to the lack of recrystallisation there are still the same grain structure present and so it will fracture in the same place. This was observed by Hilal [88] in their work as well. The only sample that didn't exhibit u-shaped cracks was that of CED7. The cracks appear straight; this is due to the recrystallisation that will have eliminated the as-built microstructure. As such the microstructure will be more equiaxed and similar to that found by Christofidou in Figure 4-6

[21]. The cracks will have still formed in the intergranular region as precipitates and phases that can act as crack initiators are known to form in this region. Cracking mechanisms will be discussed further in Section 5.7.

4.4 Conclusion

Stress rupture results from this work were combined and compared with those from other sources both within LPBF and cast and wrought samples to investigate how the samples perform compared to traditional manufacturing methods. It was found that they performed just as well as traditional methods, and a characteristic line of best fit could be drawn through the data points from all sources. No statistically significant difference was found in the stress rupture performance of the Christofidou heat treatment compared to the Haynes heat treatment. More tests will need to be carried out to find if there is a difference. Tests in the horizontal direction will be needed for a complete picture of the mechanical performance. The crack surfaces and volumes were observed and it was confirmed that ductile fracture had taken place. In addition, the shape of the cracks was investigated in the fracture volume. Two samples ABED7 and HED7 were found to fracture intergranuarly at the bottom of meltpools whereas CED7 still cracked intergranuarly but the recrystallized microstructure meant that the crack morphology was different.

5. Understanding Cracking Mechanisms to Improve Mechanical Properties

5.1 Introduction

One of the barriers to the broader adoption of laser powder bed fusion (LPBF) as a method of manufacture is that the solidification mechanics and crack mechanisms that are most prominent are sometimes unknown. A previous study by Carter *et al.* [104] outlined the causes of cracking within nickel superalloys built using LPBF. Understanding the cracking mechanisms within Haynes 282 and particularly those that may arise when processed in LPBF is crucial to increase confidence in its implementation in structurally critical components.

An investigation into the primary dendrite arm spacing (PDAS) will be conducted. The PDAS is a crucial characteristic of the solidification process. By measuring the PDAS for the builds from the different machines and using different parameter sets, this will give the ability to compare Haynes 282 and whether it follows the same behaviour as that of other alloys. As well as the results from this study, the results from other studies that have looked at PDAS of Haynes 282 [18], [22], [140], both using LPBF and welding, will help achieve a better overall view of its performance.

The three main types of cracking mechanisms that affect mechanical properties (hot cracking, liquation cracking and strain age cracking) will be investigated. This study will use a hot crack susceptibility (HCS) equation [112] to assess how likely parts built using certain parameter sets are to exhibit hot cracking. Parameter sets from this current work and those from other studies will be compared to explore the propensity towards hot cracking.

Segregation analysis of the as-built microstructure will be performed using both SEM and TEM methods to investigate different length scales. This analysis is necessary because the rapid cooling inherent with LPBF causes the dendrite tips to be small and segregated over short distances as local undercooling dominates [36].

An investigation into the partitioning of elements will establish what effect the changing chemistry has on the liquidus and solidus and if this is the sole reason for the change in solidus and liquidus or if velocity effects impact the freezing range.

Liquation cracking will be examined primarily using Scheil cooling curves. Curves will be calculated for bulk material composition and the meltpool. The solidus temperature for the

meltpool and the bulk will be compared using Cao and Kou's [110] method. This method states that if the solidus of the filler material of a weld falls below that of the base material, then liquation cracking may occur as the bulk cannot sustain the additional stresses placed on it as the filler material cools. Wei *et al.* have applied this method to AM in general[102]. The validity of whether this method can be applied to the case of LPBF will be assessed through how well it predicts liquation cracking in other parameter sets or alloys where liquation cracking has been reported. Osoba's [140] study into the welding of Haynes 282 will be used, and CM247LC, which is known to be prone to liquation cracking.

Strain age cracking will be investigated as the last primary cracking mechanism. This mechanism occurs due to the volumetric difference between the precipitates and the bulk [141]. Strain age cracking, as the name suggests, can become an issue after prolonged exposure to elevated temperatures, as will be the case when this alloy is used in service. This work will use Thermocalc calculations to build upon the analysis by Pike [6] in their initial development and characterisation of Haynes 282 compared to other alloys.

New PHACOMP [108] will be used to examine which phases are likely to occur. This method uses the electron valence of the constituent elements to predict whether the alloy will form either μ or σ phase. This analysis will help understand the microstructure and how it will perform mechanically.

The cracks will be imaged using EDX, and the phases surrounding the cracks will be identified through their composition. This analysis of phase formation will be used to identify the causes of failure within the observed test samples and if strain-age cracking contributes as a mechanism to the initiation and propagation of cracks within the microstructure.

All these analysis methods will be combined to give a comprehensive view of the solidification and cracking behaviour of Haynes 282 in LPBF compared to other methods of manufacturing using Haynes 282 and other alloys that have been used for similar applications in the past.

5.2 Dendrite Arm Spacing Investigation

The etched cross-sections of the samples revealed the meltpools at low magnification.

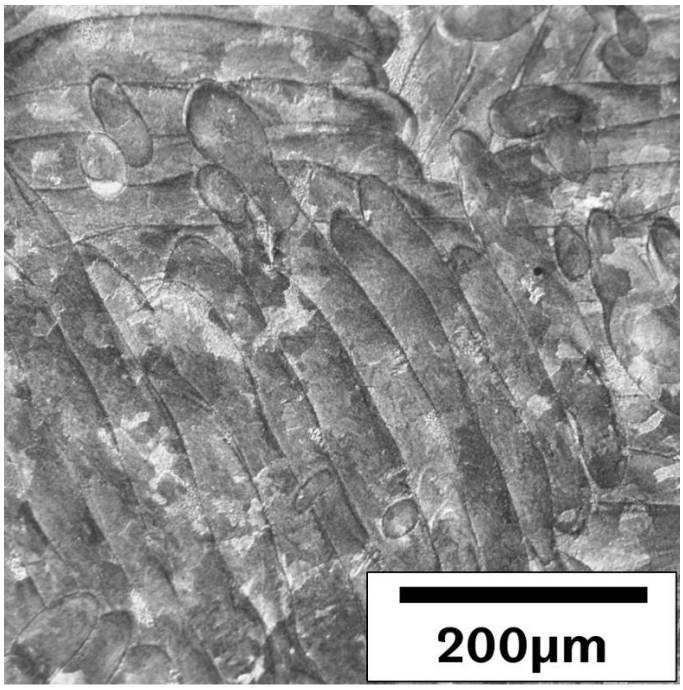

Figure 5-1 - A micrograph taken in the XY plane of the etched cross-section from a surface response DoE sample. The long meltpools can be seen, and the layer beneath is at a 67° angle. The visible long meltpools result from the continuous beam, which means fewer discrete meltpools.

From Figure 5-1, the long meltpools associated with a continuous beam are observed. The 67° rotation between layers is shown with the tracks in the top left that are orientated differently. As well as the long tracks, there are separate short discontinuous meltpools that arise when the turbulent flow of the meltpool causes molten material to be ejected from the meltpool and solidify in a separate location.

The quasi-continuous laser creates more of these distinct meltpools, as seen in Figure 5-2 below.

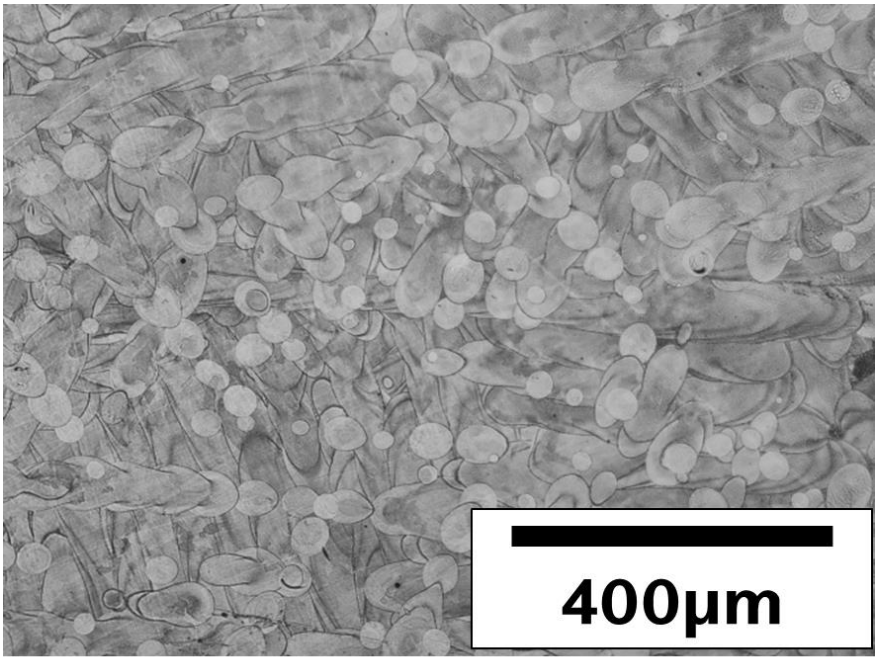

Figure 5-2 - This micrograph shows the meltpools created during the build process on the Renishaw. It is taken in the XY plane. The quasi-continuous nature of the laser creates discrete meltpools. In addition, molten particles ejected from the meltpool can solidify elsewhere and create these meltpools.

The pulsed nature of the laser creates the condition for more molten material to be ejected from the meltpool and solidify elsewhere.

The etched microstructure was then placed under an SEM, and the cellular structure was investigated. In the centre of the meltpools, the cells appeared to be equiaxed in the XY plane (Figure 5-3).

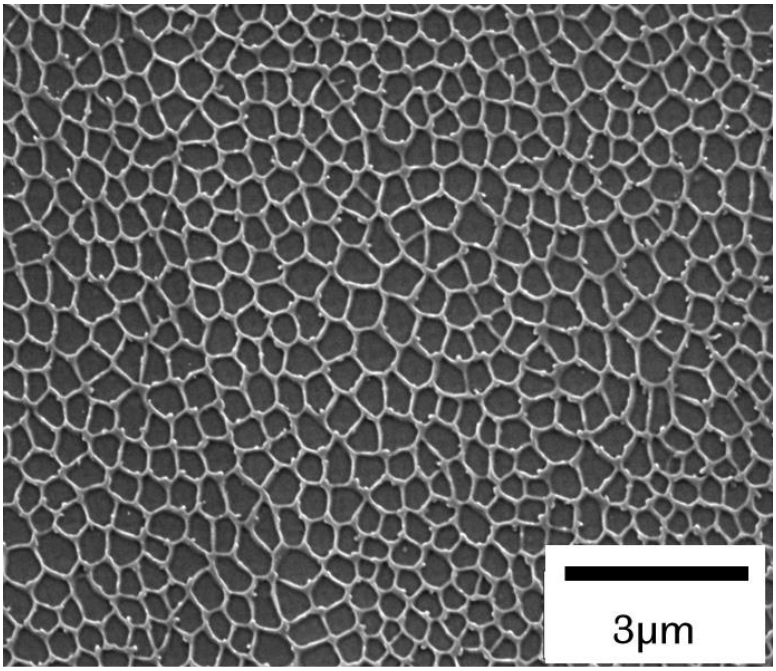

Figure 5-3 - This SEM micrograph shows the etched microstructure. This shows the middle of a meltpool and was taken in the XY plane. The cells can be seen, and in this region and from viewed from this plane, they are equiaxed.

In the centre of the meltpool, the solidification conditions and thermal gradient create the environment for cells to be formed. This cellular structure demonstrates that rapid solidification is occurring. In addition, the process conditions satisfy either condition one or two of the three conditions for rapid solidification as outlined by Kurz and Trivedi[38] the condition that:

1) The diffusion field becomes shorter than the microstructural scale when the Peclet number (Pe = ud/2α where d is characteristic length scale, e.g. tip radius) becomes larger than unity. This condition occurs when the interface velocity is of the order of centimetres per second. (At interface velocities below RS conditions, the microstructure follows the relationship $d^2u = const.$*)*

2) The diffusion distance becomes comparable with the interface width, and local non-equilibrium is established, leading to solute trapping. This condition occurs when the velocity of the interface, given by the ratio of diffusion coefficient to interface width, is of the order of metres per second.

3) The interface movement driven by atom attachment reaches the velocity of sound (V_c) *and cannot move faster. This condition occurs when the interface velocity is on the order of kilometres per second.*

[39]

The thermal gradients and cooling rates within this work lie between conditions one and two. The onset of solute trapping is discussed further in section 5.7.2.

Cells grow towards the edge of the meltpool as this is the direction of the thermal gradient. This thermal gradient causes the cells to be elongated near the edge of the meltpool (Figure 5-4).

Figure 5-4 shows both equiaxed cells (at the top and bottom of the micrograph) and elongated cells (in the centre of the micrograph). This change could be the transition point between the two cell types; however, this image is from only one plane. Another image in the XZ direction would be required to confirm if this is a columnar to equiaxed transition.

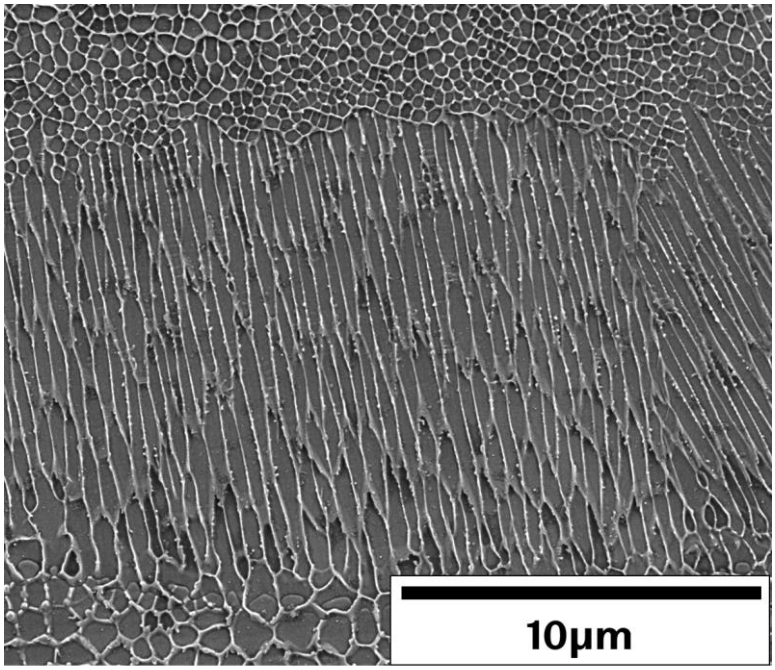

Figure 5-4 - This micrograph shows equiaxed and elongated cells. It was taken at the edge of a meltpool in the XY plane. Viewed from this plane, this change could be the columnar to equiaxed transition, but cross-sections in different planes must be taken to confirm this.

For this experiment, only the size of the central-most cells were considered. This constraint was imposed to create a fair comparison between the parameter sets.

5.3 Calculating Thermal Gradient G

The thermal gradient needed to be calculated for all the parameter sets. This calculation was done by applying two versions of the Eagar model [98], a stationary pulsed version for the quasi-continuous laser and a moving continuous heat source for the continuous beam laser. These models were tested on previously found meltpool depths from the top layer in the XZ direction of some built parts. The meltpool depth of five different meltpools within the top layer were measured, and then an average was found. These measurements were performed on a sample from the Renishaw and AconityMini.

The parameters and conditions were then inputted into the model using Freeman's Code [80]. The measured meltpool was then compared with the estimated to observe how they compare (Table 5-1).

Table 5-1 - Details of the parameters and the comparison of the model with the measured meltpool depth. The Renishaw speed is equivalent as it stops to perform each pulse and then moves between the points. The equation for this velocity is given in Equation 1-2

	Power (W)	**Velocity (m/s)**	**Hatch Spacing (µm)**	**Layer Height (µm)**	**Estimated Meltpool Depth (µm)**	**Actual Meltpool Depth (µm)**
AconityMini	110	1.125	35	30	45.6	47.2
Renishaw	200	0.45*	35	30	187	184.3

The Renishaw's velocity is equivalent as it is stationary whilst the laser turns on for each pulse and then moves between the points when the laser is turned off.

The estimated depth is close to the actual depth measured for both versions. This result validates this model for use in the following experiments. One output from the program is the thermal gradient. This value can be used to plot parameter sets against the DAS to find the characteristic gradient for a material (See Section 5.5.4). It can also be used for HCS analysis which will be carried out in section 5.6.

5.4 Enthalpy and the Onset of Keyholing

When comparing microstructures, it is essential to ensure that the melting mode is constant across the machines. As such, the normalised enthalpy for each parameter set was found (Equation 5-1) by using,

$$\frac{\Delta H}{h_s} = \frac{AP}{h_s\sqrt{\pi D u \sigma^3}}$$

Equation 5-1

Where ΔH is specific enthalpy, h_s is the enthalpy of melting, A is the absorptivity coefficient, P is power,α is thermal diffusivity, u is velocity, and σ is the beam diameter.
The values for the normalised enthalpy for all builds are given in Table 5-2 below.

Table 5-2 - This table shows the input parameters for the builds. The normalised enthalpy is recorded for each set of parameters. If the value exceeds six, then keyhole melting is said to occur. The Renishaw's speed is equivalent as it is stationary whilst the laser is turned on and only moves when it is turned off between points.

Reference	Specimen ID	Power (W)	Velocity (m/s)	Normalised Enthalpy
[14]		2000	0.0167	26.73
[14]		2000	0.0333	18.93
[140]		2000	0.025	21.85
[22]		170	0.95	7.56
[22]		240	0.95	10.67
[22]		285	0.95	12.67
[22]		355	0.95	15.79
[18]		750	0.012	11.82
Current Work (Renishaw)	HE	200	0.45*	9.51
	ME	200	0.54*	10.42
	LE	200	0.63*	11.65

Current Work (AconityMini)	SR12	90	1.5	3.18
	SR17	90	1.5	3.18
	SR16	76.36	1.125	3.12
	SR7	110	1.76	3.60
	SR5	110	1.125	4.49
	SR1	110	1.125	4.49
	SR14	110	1.125	4.49
	SR10	143.64	1.125	5.87
Current Work (AconityMini)	SR15	130	0.75	6.51
	SR3	130	0.75	6.51
	SR2	110	0.49	6.78
Current Work (AconityLab)	ED1	75	1.17	3.01
	ED2	110	1.125	4.49
Current Work (AconityLab)	ED3	145	1.08	6.05
	ED4	180	1.035	7.67
	ED5	215	0.99	9.37
	ED6	250	0.945	11.15
	ED7	285	0.9	13.02
	ED8	320	0.855	15.00
	ED9	355	0.81	17.10

Using the Eagar models developed into a MATLAB code by Freeman, the gradient (G) was found, and the parameters were plotted on the graph of DAS against $G^{-\frac{1}{2}}V^{-\frac{1}{4}}$.

All enthalpy values greater than six will be considered from the table as this includes most of the data. All the points for that machine will be considered to observe if the different melting modes affect the DAS.

Keyhole mode melting causes different solidification conditions than conduction mode melting, and these conditions are explained through modelling by Wei *et al.* [101]. The geometry of the meltpool causes changes to heat flow and the thermal gradients are seen. This change in geometry can be caused by either the keyhole causing changes in the shape of the meltpool wall. Alternatively, the turbulent nature of keyhole melting leads to changes in meltpool geometry.

Curved columnar grains on the meltpool boundary coexist with straight axial columnar grains in the middle of the meltpool. Depending on their orientation, they can appear as columnar or equiaxed grains. These would cause errors when measuring the cells in a plane, as was done in this experiment. The grains change size depending on how far the grains are from the top surface due to changes in the thermal gradient. These factors combine to make comparing the two modes of melting impossible in the meltpool.

Figure 5-5 shows the grain growth in welds at different speeds viewed from different angles.

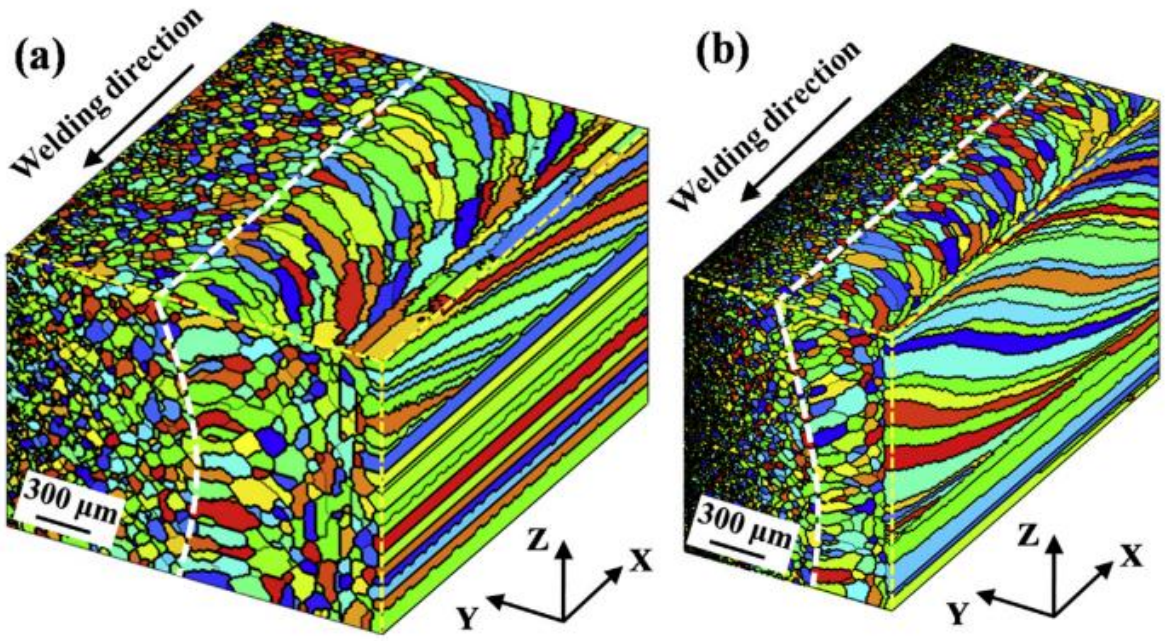

Figure 5-5 – These figures show the simulated grain growth in welds at different beam velocities a) was performed at 1m/min, resulting in larger grains. For b), the 8m/min velocity creates smaller grains due to the faster cooling rates and curved grains in the weld direction [102].

Figure 5-5a shows larger grains and a larger meltpool than Figure 5-5b, performed at 8m/min. It also shows how grains change away from the top of the meltpool and away from the centre. The grains can be seen to be more curved in the direction of the weld. The grains in the HAZ for the higher velocity weld are smaller due to the faster cooling rates experienced. Another

difference due to the different velocities is that the height of the region composed of axial grains is reduced. These changes in grain growth between high and low-velocity laser passes will cause differences in measured DAS, especially as the cross-section is taken in the XY plane. These issues with keyholing affecting DAS are compounded in LPBF. The built parts comprise many overlapping welds that interact with one another and cause more complex thermal gradients and so more varied DAS than would be expected from the theory.

5.5 Transition Builds

Two of the builds included both parameters that result in keyhole melting and conduction mode. These are highlighted in Table 5-2. This next section will investigate the difference between the two melting modes on the dendrite arm spacing.

5.5.1 AconityMini

Three parameter sets for the surface response DoE resulted in an enthalpy greater than six, indicating keyhole mode melting (Figure 5-6). The onset of keyholing has been marked.

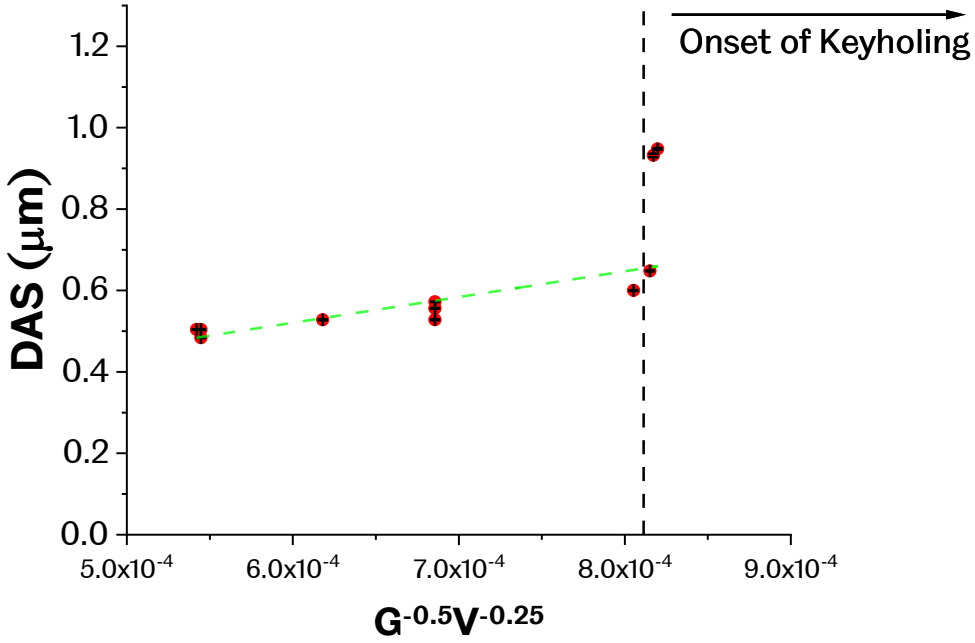

Figure 5-6 - Plot for the Aconity Mini the onset of keyholing has been noted. A marked difference in DAS values on either side of the line suggests a fundamental difference in how solidification occurs.

The sudden change in DAS readings and deviation from the line of best fit suggests a fundamental change in the type of solidification occurring. When in conduction mode, the trend line passes close to each point; this suggests a more consistent process occurs again, suggesting that conduction mode melting occurs. This transition between conduction and keyhole mode melting and its effect on DAS must be investigated further.

5.5.2 AconityLab

Below is Figure 5-2; a plot of DAS against $G^{-\frac{1}{2}}V^{-\frac{1}{4}}$. As with the AconityMini experiment, this also spans both conduction and keyhole mode melting.

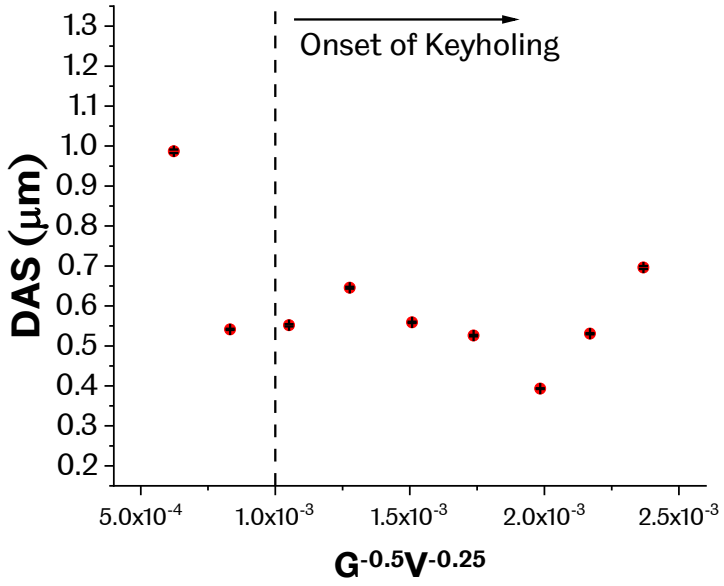

Figure 5-7 - This graph shows how the DAS is affected by changes in the thermal gradient and velocity. There is less of a clear relationship compared to the results for the other machines. This lack of relationship may be due to the onset of keyholing. Keyhole melting creates a different kind of solidification regime resulting in different morphologies of cells.

To the left of the line are two points. The first point has a much higher DAS than would be expected. More testing is needed to see if there is a difference in DAS between the two melting modes. There is not a significant rise in the DAS over the observed range. This observation is due to the uncertainty in readings of the DAS.

Due to differences in solidification, points within the keyhole region will be compared to results from the literature. These lie within the keyhole region.

5.5.3 Renishaw

Figure 5-8 shows the DAS against $G^{-\frac{1}{2}}V^{-\frac{1}{4}}$ for the Renishaw build. The range of DAS observed can be seen.

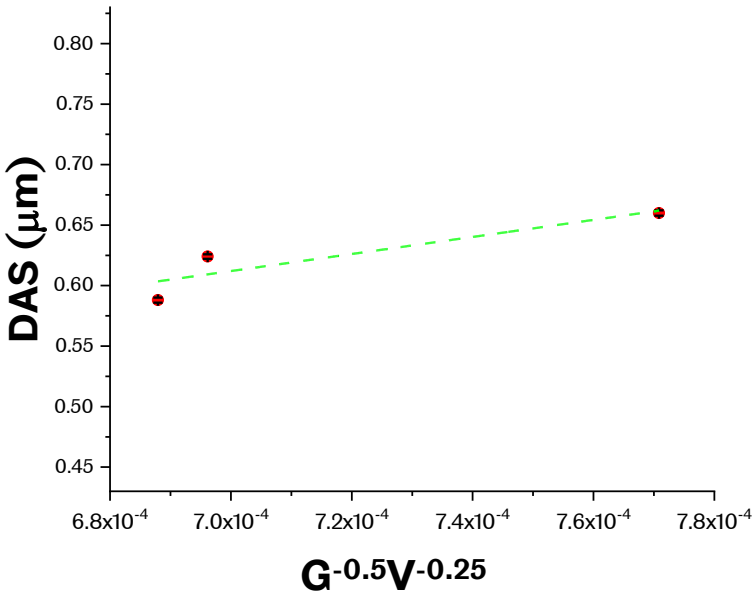

Figure 5-8 - This graph presents the results from the Renishaw builds. The DAS from the micrographs is plotted against $G^{-\frac{1}{2}}V^{-\frac{1}{4}}$.

As the value of $G^{-\frac{1}{2}}V^{-\frac{1}{4}}$ gets larger, so does the DAS. This relationship follows the theory that slower cooling rates and thermal gradients lead to larger DAS. A linear line of best fit can be drawn through the points. The trend is more apparent with these points than in the previous two experiments, as all of these points lie within the keyhole mode of melting.

5.5.4 Comparison with other studies

In order to be able to check if the results agree with the theory, they must be put into context with other results from different studies. These studies incorporate results from LPBF[22]and welding literature[140], and direct energy deposition (DED) [18] on Haynes 282. The inclusion of these studies will give a better view of the overall trend and the characteristic gradient for Haynes 282(Figure 5-9).

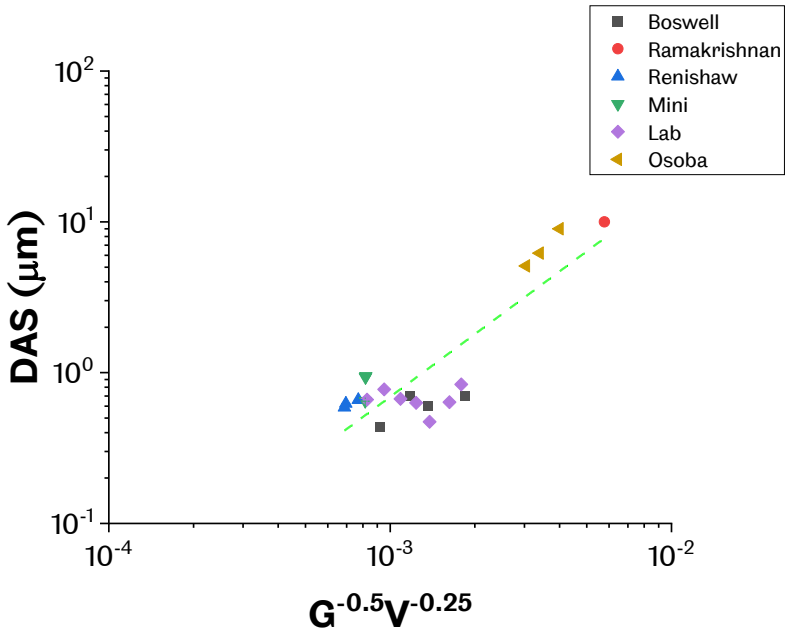

Figure 5-9 - A comparison of the results from this study with those found in the literature. The points plotted from the three machines all occupy the same space on the graph due to the similar thermal gradients and velocities. A gradient can be drawn through all the points. The welding and direct energy deposition literature give data points outside this range and a more accurate characteristic gradient.

The trials on the three machines that were part of this work all sit in a similar region. The results are because both the dendrite arm spacing and $G^{-\frac{1}{2}}V^{-\frac{1}{4}}$ vary by a small amount across the parameters tested. The results from Boswell [22]occupy the same region as they were also measured on samples processed by LPBF. The results from Boswell overlay onto the results from this work, suggesting that the observed results in this work are valid. The data from the welding literature occupies a different space in the graph due to the low cooling rates and slower beam velocities found in welding compared to LPBF. When the gradient for the line of best fit is calculated, it was found to be $6.83\times 10^{-4}\left(\frac{m^3K^2}{s}\right)^{\frac{1}{4}}$. For comparison, the gradient for In718 processed via LPBF and electron powder bed fusion was between $2\times 10^{-3}\left(\frac{m^3K^2}{s}\right)^{\frac{1}{4}}$ and $3\times 10^{-3}\left(\frac{m^3K^2}{s}\right)^{\frac{1}{4}}$ [142], whilst the gradient for PWA 1483 was $6\times 10^{-4}\left(\frac{m^3K^2}{s}\right)^{\frac{1}{4}}$ when measured for casting samples [143]. As the gradient for this work and the Haynes 282 samples from other literature falls between these two values, the results can be shown to be compatible with one another. More experiments are required to bridge the gap between the LPBF and other studies. This would give a fuller and more accurate picture of the characteristic gradient for Haynes 282.

5.6 Segregation analysis

A segregation analysis was carried out at two different length scales to identify where segregation was taking place and to what degree. This can indicate what type of cracking may be occurring. An EDX map of the sample was taken on the Inspect F50 at 12000x magnification. A spot size of 4mm and a dwell time of 20µs per point were used. A grain boundary was imaged as one of the most likely areas where segregation may have occurred. Maps for all the alloy's constituent elements were made to observe specific segregation patterns. A map is shown in Figure 5-10. From the concentration maps, there are no areas of concentration for any of the elements that were mapped.

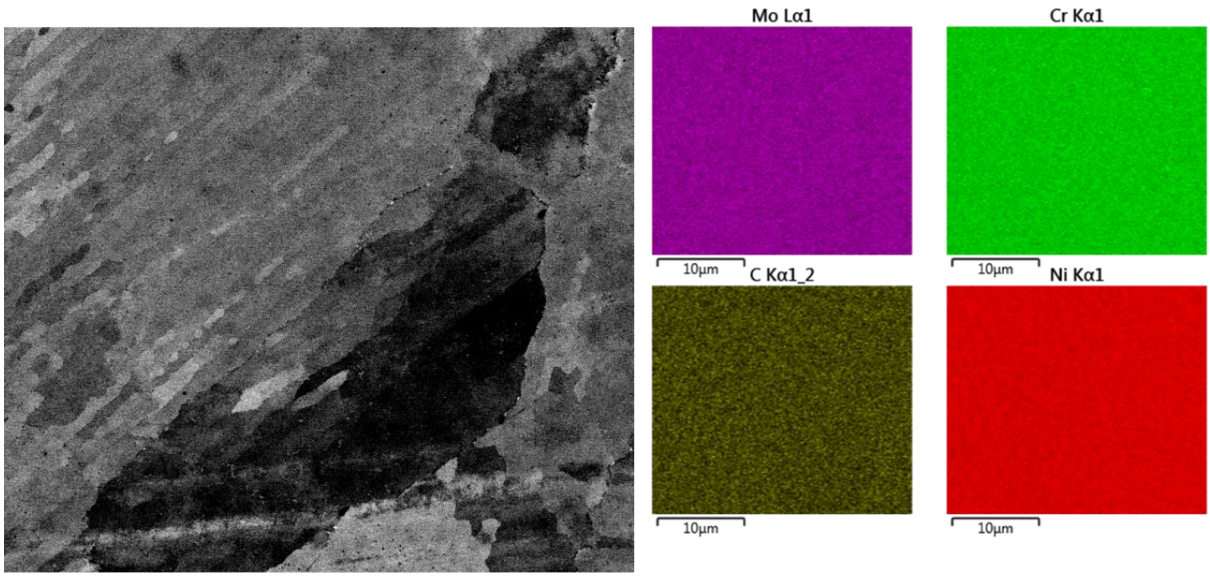

Figure 5-10 - An SEM micrograph of a grain boundary from an as-built section. On this length scale, there does not appear to be any segregation. The cellular structure within the grain can be observed and will be investigated using TEM to see if segregation occurs on the sub-micron scale.

Any segregation on the sub-micron scale would not be identified using SEM. So, a compositional analysis of the cell interior and exterior using the JEOL TEM was conducted to see if there was any difference and, if there was, in what direction certain elements segregated. Figure 5-11 shows a TEM image taken at a magnification of 80000x. The cell interior and boundary are visible, and the dislocations on the boundary.

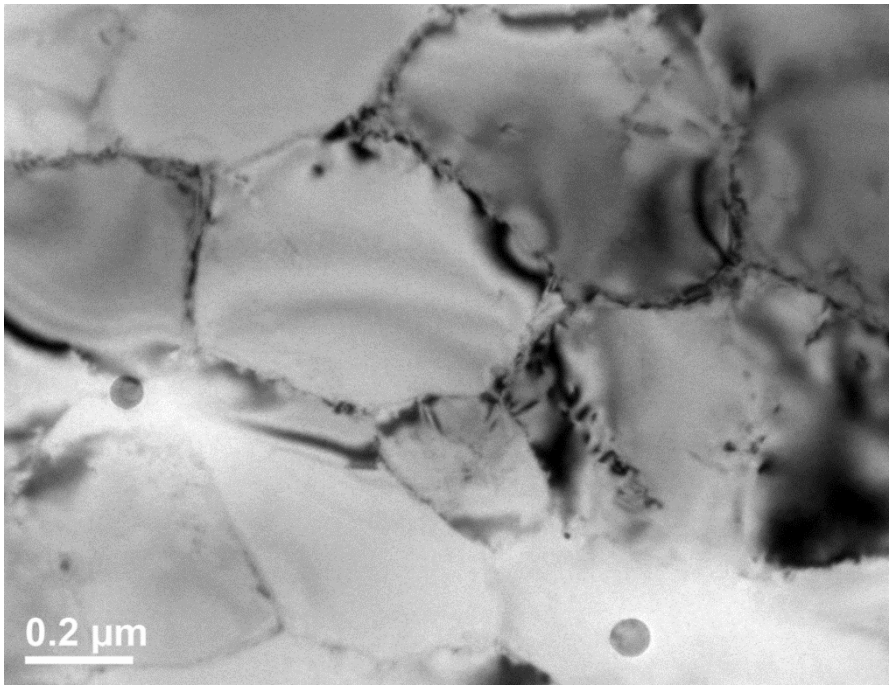

Figure 5-11 - A TEM micrograph showing a cell. Its interior and boundary are visible at this length scale, and a compositional analysis on the nanoscale is possible.

The compositional analysis results of the cell boundary and interior are shown in Table 5-3 below.

Table 5-3 - This table shows the results of the compositional analysis. The alloys are known to form precipitates segregate to the boundary. These results will be used in Section 5.7 to identify what cracking mechanisms may occur.

	Boundary	**Interior**	**Difference**	**Segregation**
Aluminium	1.15	1.16	0.01	Neutral
Cobalt	9.7	10.19	0.49	Interior
Titanium	2.22	1.76	0.46	Boundary
Chromium	18.91	18.37	0.54	Boundary
Molybdenum	11.09	10.3	0.79	Boundary

The results show that precipitates molybdenum, chromium and titanium segregate to the cell boundary whilst matrix elements such as cobalt are more abundant in the centre. Segregation is on the sub-micron level when using LPBF because the cooling rates are high. Kurz-Fisher's analysis of dendrite tip radius [36] states that as the dendrite tip radius is small, there can only be small perturbations in the undercooling and segregation leading to local undercooling being

dominant. This undercooling would allow for segregation to only occur on a local level which is why the precipitates are so small.

The composition of the cell interior and boundary will be used in a Scheil calculation without solute trapping as the composition is already known. The calculations will be compared to the Scheil calculation for the bulk material. The solidus for the cell interior will be investigated concerning the bulk material to see if liquation cracking can occur.

5.7 Cracking Mechanisms Analysis

Having obtained the results from the stress rupture testing. The solidification of Haynes was modelled to find to what cracking mechanisms Haynes 282 was susceptible. Three main mechanisms were investigated. These were hot cracking, liquation cracking and strain age cracking. Different parameter sets used within this chapter and other sources were compared to see which specific cracking mechanisms became prominent. These results were compared to other alloys that exhibit these mechanisms to see if Haynes 282 was less susceptible.

5.7.1 Hot Crack sensitivity

In this investigation, the thermal gradient, beam velocity, measured dendrite arm spacing, and other intrinsic material properties were used to predict how sensitive a sample built using those parameters was to hot cracking. This HCS value was compared to other results from different authors to compare the sensitivities predicted to see if studies with no hot cracking had higher predicted HCS. So, samples with a lower HCS would have no hot cracking.

The values of the thermal gradient were obtained from Freeman's model [80]. The gradient was taken at the back of the meltpool. This gradient was combined with the input beam velocity and the measured dendrite arm spacings from the etched cross-sections or reported from the studies. These values were input into the HCS equation (Equation 5-2)

$$F(\dot{\varepsilon}_{p\,max}) = \frac{{\lambda_2}^2}{180}\frac{G}{(1+\beta)\mu}\Delta p_c - v_T\frac{\beta}{1+\beta}H$$

Equation 5-2

$\dot{\varepsilon}_{p\,max}$ is the maximum deformation rate, λ_2 is the secondary dendrite arm spacing, G is the thermal gradient, β the shrinkage factor, μ is the viscosity, Δp_c is the change in cavitation pressure and v_T. Within the equation H is found through the equation:

$$H = \int_{T_S}^{T_L}\frac{f_s(T)^2}{(1-f_s(T))^2}dT$$

Equation 5-3

Furthermore, $f_s(T)$ the solid fraction at a given temperature and governed by the equation:

$$f_s(T) = \frac{1}{1-2\alpha_s^* k}\left[1 - \left[\frac{T_m - T}{T_m - T_L}\right]^{\frac{1-2\alpha_s^* k}{k-1}}\right]$$

Equation 5-4

Where k is the partition coefficient and α_s^* is related to the Fourier number α_s by the relationship:

$$\alpha_s^* = \alpha_s\left(1 - e^{-\alpha_s^{-1}}\right) - 0.5e^{-0.5\alpha_s^{-1}}$$

Equation 5-5

Where:

$$\alpha_s = D_s t_f / {\lambda_2}^2$$

Equation 5-6

The maximum change in cavitation pressure Δp_{max} can be found using:

$$\Delta p_{max} = \frac{180}{{\lambda_2}^2}\frac{(1+\beta)\mu}{G}\int_{T_S}^{T_L}\frac{E(T){f_s(T)}^2}{(1-f_s(T))^3}dT + \frac{180}{{\lambda_2}^2}\frac{v_T\beta\mu}{G}\int_{T_S}^{T_L}\frac{{f_s(T)}^2}{(1-f_s(T))^2}dT$$

Equation 5-7

$$E(T) = \frac{1}{G}\int f_s(T)\,\dot{\varepsilon}_p(T)dT$$

Equation 5-8

The partition coefficient is velocity-dependent so that it can be found from:

$$k = \frac{k_e + a_0 v_T/D_i}{1 + a_0 v_T/D_i}$$

Equation 5-9

where k_e is the equilibrium partition coefficient,v_T is the solidification velocity, a_0 is the lattice parameter, and D_i is the diffusion coefficient in liquid nickel. The equilibrium partition coefficients were found from Thermocalc simulations of the alloys, a_0 was taken to be 4×10^{-9} [39] Moreover, the diffusion coefficients were found through Thermocalc.

Solidification time can be found with

$$t_f = 2\left(\frac{a^2}{3\alpha}\right)\ln\left(\frac{T_P - T_0}{T_L - T_0}\right)$$

Equation 5-10

where a is the radius of the droplet, α is the thermal diffusivity, T_P is the superheat temperature, T_L is the liquidus temperature, and T_0 is the ambient temperature. The strain rate is related to the beam velocity by the equation:

$$\dot{\varepsilon} = \frac{\beta v_T}{\lambda}$$

Equation 5-11

λ_2, β, T_0 are constant, μ, D_i, D_s, T_m T_L, $\alpha, k_e$are material constants so cannot be changed. G ,a and T_P can be found from Freeman's [80] application of the Eagar equation[98]. G will be taken from the back as this will be the point most prone to hot cracking within the meltpool. v_T is the beam velocity and λ is DAS.

Table 5-4 - These are the input terms into the HCS equation. They are obtained from literature as well as models and other equations.

Term	Value	Unit	Reference
a Radius of the meltpool	Various	m	[80]
α Thermal diffusivity	2.88	mm^2/s	[5]
G Thermal Gradient	Various	K/m	[80]
D_s Diffusion Coefficient	$3x10^{-9}$	m^2/s	[144]
D_i Diffusion in liquid coefficient	Various	m^2/s	Thermocalc
T_P Superheat Temperature	Various	K	[80]
μ Viscosity of liquid	5	mPa.s	[145]
k Velocity dependent partition coefficient of boron	Various		From Equation 5-9
k_e Equilibrium partition coefficient of Boron	0.008		[146]
T_0 Initial Temperature	295	K	Room Temperature
β Shrinkage Factor	0.1		[147]
T_m Melting temperature	1643	K	[5]
T_L Liquidus Temperature	1643	K	[5]
v_T Beam Velocity	Various	m/s	Machine Parameter
λ Primary Dendrite arm spacing	Various	m	Measured from SEM Micrographs

Using these equations, the HCS can be found from the relationship:

$$HCS = \frac{1}{\dot{\varepsilon}_{p\ max}}$$

Equation 5-12

This value was then plotted against the calculated $G^{-0.5}V^{-0.25}$ for each set of parameters. The relative position of each point was then examined compared to samples that had seen no hot cracking to examine if hot cracking was possible in the samples built in this current work using Haynes 282.

5.7.1.1 Results

Below is the graph of $G^{-0.5}V^{-0.25}$vs DAS. Data from this work, LPBF literature [22], and Haynes 282 welding [18], [140] are plotted.

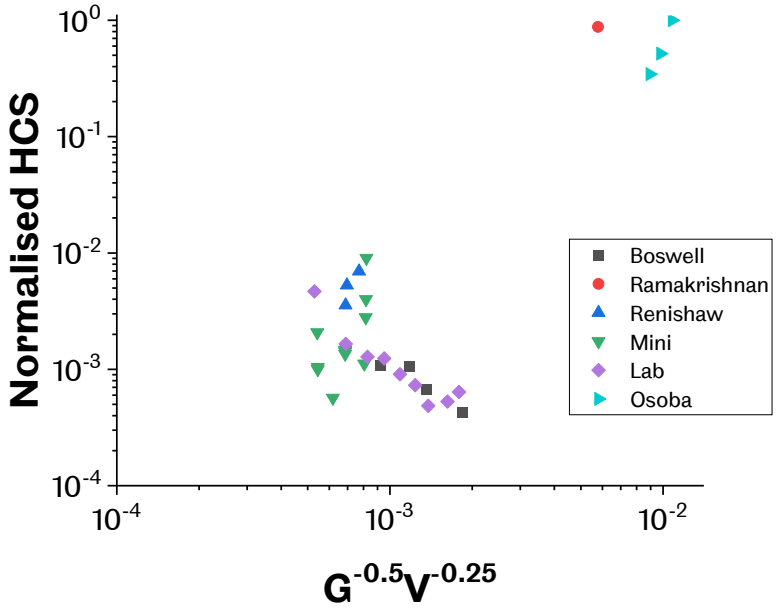

Figure 5-12 - This graph shows the HCS for the different parameter sets. The current work and Boswell's results overlap as they both used LPBF. Osoba and Ramakrishnan's results sit to the right of the graph. This result is due to the slower cooling rates associated with these manufacturing methods.

From the graph, the points that arise from LPBF are grouped in the bottom left as they all have a similarly high thermal gradient and velocity. The data from this current work sits within Boswell[22], and the points from each machine overlap and create a continuum. The welding literature sits to the right of the graph due to the lower thermal gradient and velocities. Ramakrishnan used direct energy deposition, which uses high powers to melt the powder stream. This manufacturing method means that the powers are high (around 750W) and have a slow beam velocity (12mm/s). This combination results in a high $G^{-0.5}V^{-0.25}$value. It is noted

in Osoba's [140] analysis of their welding samples that no hot cracks are observed. The HCS of the points within this work are lower than those from Osoba. As a result, there will not be any hot cracking in these samples across all the machines.

Finally, a plot was made of the cavitation pressure and HCS. This plot is shown in Figure 5-13.

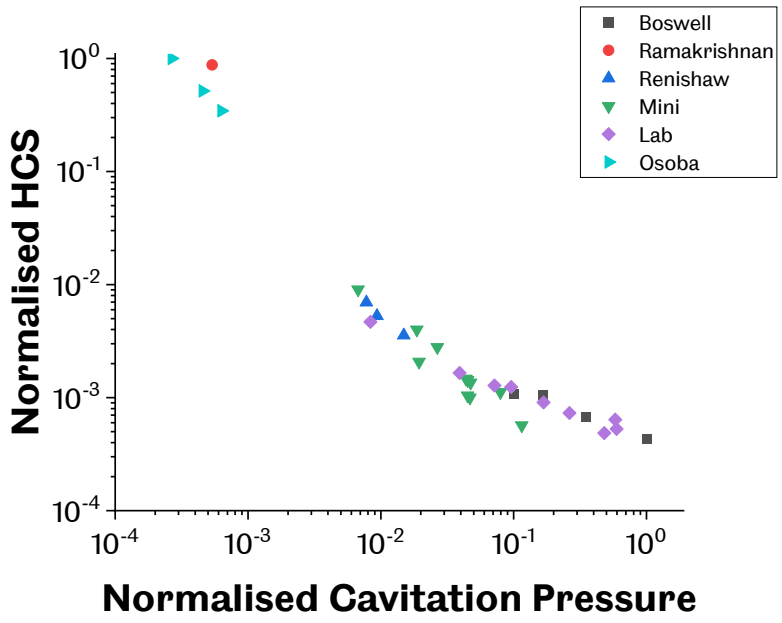

Figure 5-13 - This plot shows the relationship between cavitation pressure and HCS. There is a negative correlation between the two variables due to the cavitation pressure suppressing the creation and movement of hot cracks. The LPBF results form a continuum with low HCSs as the thermal gradients are high and the beam velocities are fast compared to welding or direct energy deposition.

As with the last plot, the results from Boswell overlap with those from this study, validating the findings. The overall trend is that larger cavitation pressures result in a lower HCS. This trend is especially true for LPBF, whose HCS is lower than the other manufacturing methods at a similar cavitation pressure. This result is due to the fast beam velocities and large thermal gradients involved in the process. Cavitation pressure suppresses the propagation of hot cracks as a high cavitation pressure minimises the cavity that may form as an initiator of hot cracking. The pressure reduces the opportunity for any cracks that form to propagate away from the cavity.

The observation that the Haynes 282 samples with the highest HCS still produced no hot cracks means that this rules out hot cracking as a crack mechanism that may cause failure. So, the other two cracking mechanisms must now be investigated to discern if these would cause cracking within the microstructure.

5.7.2 Scheil Cooling

The next step was to investigate how the cooling behaviour is influenced by the compositional change brought about by the changes in velocity.

The composition changes between the lowest and highest velocity state are shown (Figure 5-14 and Figure 5-15). Changes in molybdenum, carbon, boron and silicon are plotted against how the solidus liquidus and freezing range change.

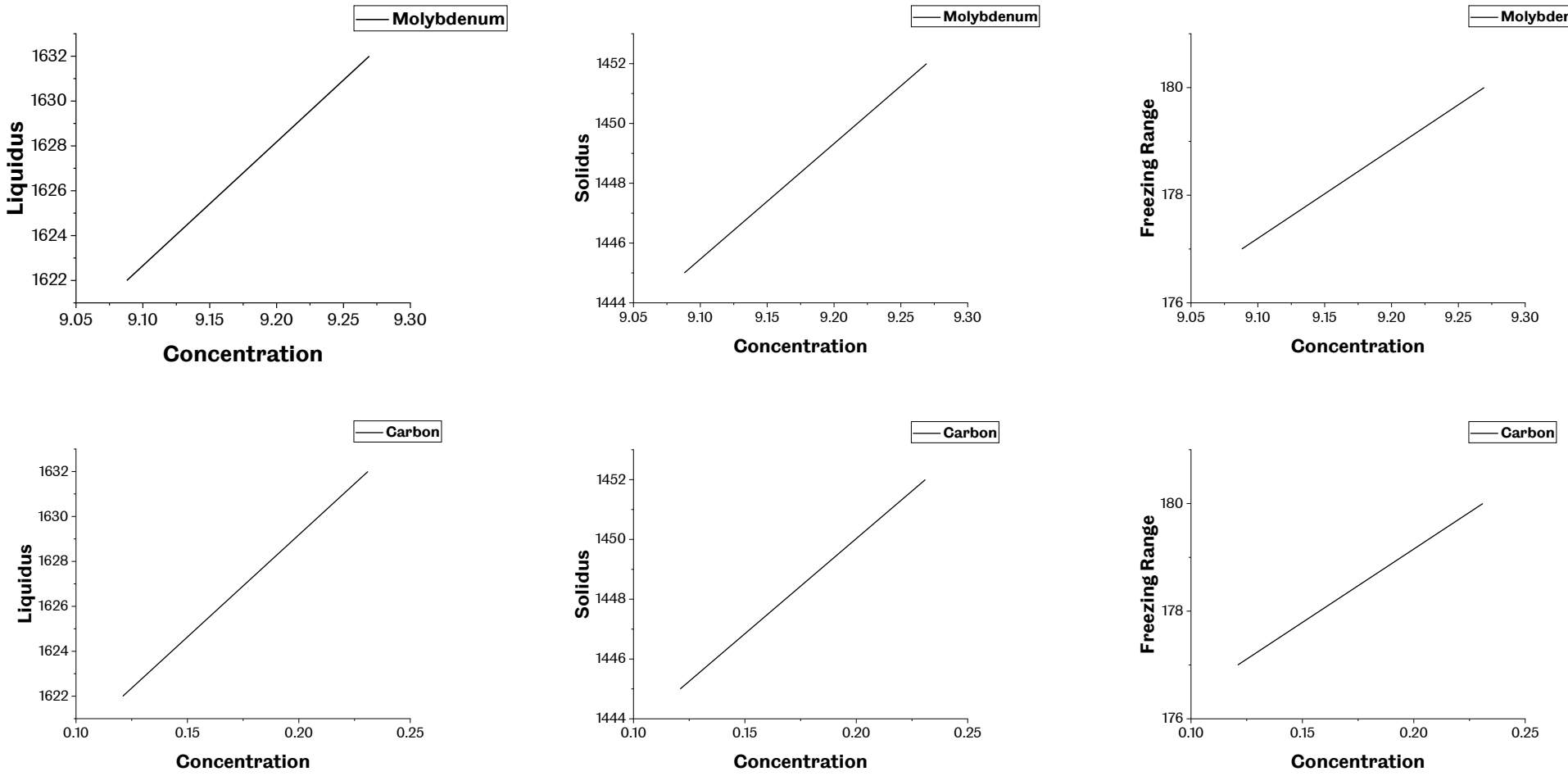

Figure 5-14 - These graphs show how the molybdenum and carbon altering chemistry affects the solidus liquidus and freezing range. All the parameters are raised by an increase in the composition of each element. The liquidus is raised more than the solidus leading to an increase in the freezing range with a higher composition. The molybdenum content varies more, but relatively speaking, the difference in carbon is higher.

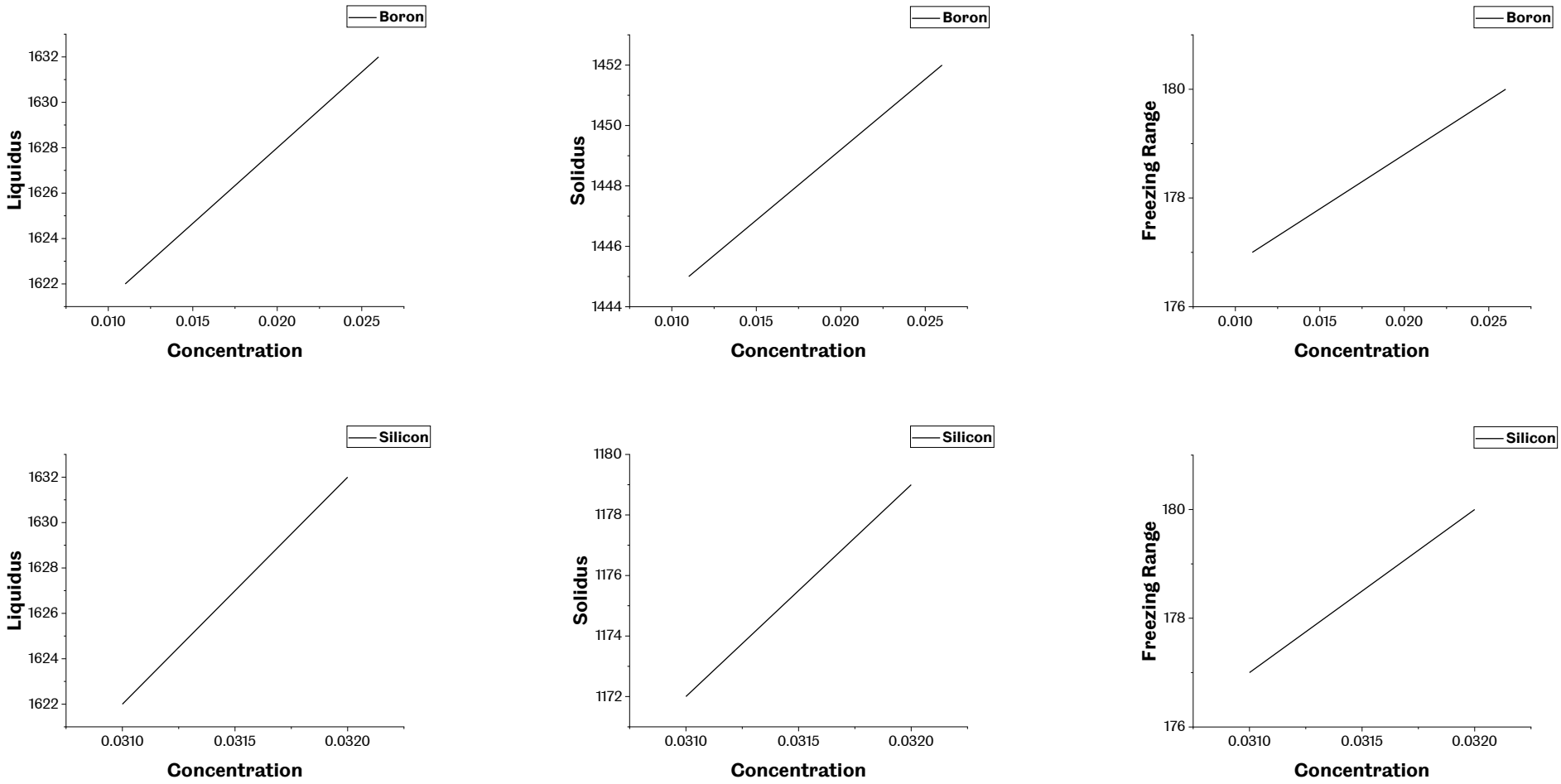

Figure 5-15 - These are the graphs for boron and silicon. Silicon does not vary much compared to its highest and lowest experimental value. Due to its small partition coefficient and fast diffusion coefficient, boron significantly increases relative to its equilibrium abundance between the two velocities.

The trend is that the higher the concentrations raise both the solidus and liquidus. However, they raise the liquidus more, so the freezing range increases with decreased velocity. The concentrations are higher in the lower velocity state as it has more time to partition. The equilibrium partition coefficients k_0 of all the elements which have been plotted are below one and so will be more abundant in the lower velocity condition.

Table 5-5 below gives the temperatures at which the phases are formed and the solidus and liquidus temperature for the velocity (high, medium and low) and compositional (cell boundary and interior) conditions.

Table 5-5 - This table gives phase formation temperatures, solidus and liquidus for the velocities and the composition measured in the cell interior and boundary from the segregation analysis.

	Liquidus	**Solidus**	**Freezing Range**	**γ'**	**μ**	**σ**	**η**
Bulk	1639	1454	185	1547	1493	1470	1470
Boundary Meltpool	1632	1467	165.3	1532	1500	1489	1473
High Velocity Meltpool	1632	1445	187	1556	1495	1496	1450
	Liquidus	**Solidus**	**Freezing Range**	**γ'**	**μ**	**σ**	**M_3B_2**
Low Velocity Meltpool	1622	1452	170	1566	1477	1476	1460
Medium Velocity Meltpool	1628	1435	193	1561	1487	1495	
	Liquidus	**Solidus**	**Freezing Range**	**$M_{23}C_6$**	**μ**	**M_6C**	**η**
Interior Meltpool	1646	1442	204	1473	1467	1467	1455

When compared with the equilibrium phase composition at 750°C, there are differences in the phases formed. Due to the increased rate of cooling associated with the Scheil calculation, some phases have been suppressed whilst others have formed in the absence of the equilibrium phases. The Scheil calculation predicts that no carbides would be formed in any state apart from the cell interior, and it also suggests that μ will form, which is not the case in equilibrium.

In Boig's [39] analysis of IN713c, it was determined that the changes in solidus liquidus and freezing range were solely due to the compositional changes, and there was no influence by the thermal velocity. This influence was tested within Thermocalc using the solute trapping option for the Scheil cooling curve calculation. This calculation was valid due to the relationship between the diffusion in liquid coefficient D_i and interface width (δ). If Equation 5-13 holds, then solute trapping will occur.

$$\frac{D_i}{\delta} < v$$

Equation 5-13

Where v is beam velocity, Table 5-6 gives the diffusion coefficients, and the interface width was found to be between 4-8nm. The smallest interface width was taken for the calculations, leading to the highest barrier for solute trapping to occur.

Table 5-6 - Diffusion coefficients for the alloy's constituent elements are shown in the table. The ratio of these coefficients to the interface is also given. Most of these elements will exhibit solute trapping with the imposed velocities. All the AconityLab tested velocities exceed 0.7m/s, which is the limit of solute trapping.

	Diffusion Coefficient	$\frac{D_i}{\delta}$
Silicon	2.85E-09	0.71
Molybdenum	1.09E-09	0.27
Carbon	9.49E-09	2.37
Boron	9.49E-09	2.37
Nickel	2.88E-09	0.72
Cobalt	2.85E-09	0.71
Chromium	2.85E-09	0.71
Iron	3.02E-09	0.76
Aluminium	2.86E-09	0.72
Titanium	2.85E-09	0.71

Looking at the ratios, most of the elements have ratios ~0.7. This ratio would result in solute trapping occurring with most tested parameters. This solute trapping is because this ratio is lower than the central point of the surface response and is lower than any of the velocities from the AconityLab parameters. It is, however, higher than the velocities tested on the Renishaw and the low-velocity axial points on the surface response. As such, when the medium

or high-velocity conditions are tested, solute trapping will be turned on, but when the low-velocity condition is tested, it will be assumed that there will be no solute trapping.

In their analysis of the effect of chemistry change, Boig [39] found that all changes in solidus liquidus and freezing range could be attributed to changes in chemistry. It was necessary to find if Haynes 282 behaved similarly within this work. Separate Scheil curves with and without velocity effects through solute trapping were considered (Table 5-7).

Table 5-7 - This table shows the results of the velocity affected changes in the melting range. There is a small change in the melting range when only the velocity is considered showing that, unlike IN713c, the change in melting range is not just down to compositional changes.

	Without Changing Chemistry			**With Changing Chemistry**		
	Solidus	**Liquidus**	**Freezing Range**	**Solidus**	**Liquidus**	**Freezing Range**
Low Speed Scheil	1454	1639	185	1452	1622	170
Medium Speed Scheil	1464	1639	175	1435	1628	193
High Speed Scheil	1470	1639	169	1445	1632	187

The effect of just the velocity change can be seen from the table. It does not change the liquidus, which stays constant at 1639K but does increase the solidus with increasing speed. This increase in the solidus temperature has the effect of reducing the freeing range with increasing speed. When chemistry changes are considered, different results show a velocity effect on the alloy and not just its chemistry. The change from no solute trapping to solute trapping from the low speed to the medium speed has the effect of raising the liquidus and lowering the solidus—the high-velocity condition results in a raised liquidus and solidus a reduced freezing range than medium velocity.

Having established the effect that the different velocities have on the chemical composition of the alloy. The effect on the alloy's melting point and freezing range was also observed. These conditions can now be compared in how likely they are to cause cracking in the two cracking mechanisms where chemical composition and thermal velocity directly impact.

These conditions will be assessed for their potential to induce cracking alongside measured chemical composition from within the cell and boundary.

5.7.3 Elemental partitioning and its effect on melting range

The solute trapping option, along with the expected velocity-dependent liquid concentration C_L^* for each element were used within the Scheil calculation performed by Thermocalc. The solidus, liquidus, and freezing ranges for the high and low-velocity conditions were calculated and plotted due to the different elemental compositions found in the different velocity conditions. A calculation was performed to identify if the changes in solidus, liquidus and freezing range were purely down to composition change or if the changes in velocity also played a role. The effect of different velocities on phase formation and the temperature at which this occurred was noted. This phase formation analysis was also performed on the measured local element concentrations at the cell boundary and within the cell.

5.7.3.1 Results

Several different conditions will be tested over the next section (Table 5-8).

Table 5-8 – This shows the different conditions whose equilibrium phase composition at an elevated temperature was modelled in Thermocalc.

Bulk Material
High Velocity (1.755 m/s)
Low Velocity (0.45 m/s)
Medium Velocity (0.9 m/s)
Cell Interior
Cell Boundary

The medium velocity condition is the velocity used as part of the EOS parameter set. The lowest and highest velocity tested as part of the surface response DoE performed in Section 1.2.2 have been used for the low and high velocity conditions respectively. The cell interior and

boundary conditions are those whose compositions have been measured in Section 5.6. These indicate what is occurring on the sub-micron scale within the cells.

Below is the equilibrium phase composition of the different conditions at 750°C. This temperature was chosen as it is representative of the temperatures in which this alloy might be expected to function.

Table 5-9 – This shows the equilibrium phase composition at a representative operating temperature. The table shows the velocity dependence of phase composition with lower velocities leading to higher precipitate content.

@ 750°C	γ	γ'	$M_{23}C_6$	σ	H
Bulk Material	66.0	20.0	1.24	12.6	0.121
High Velocity	63.1	21.2	2.5	13.0	0.272
Low Velocity	59.5	22.5	4.81	12.5	0.621
Medium Velocity	61.7	21.8	3.47	12.7	0.393
Cell Interior	73.6	13.4	1.13	11.6	0.296
Cell Boundary	66.7	16.7	1.2	15.2	0.2

From these compositions, the effect of velocity on precipitation can be seen. The increased cooling rate inhibits the formation of precipitates. The effect that this reduction in precipitation has on strain age cracking will be discussed in Section 5.7.5. When the two cell compositions are considered, there is more precipitation on the boundary. This result is expected as the segregation analysis found more precipitate forming elements on the boundary.

5.7.4 Liquation cracking

To discover if liquation cracking should be expected, Thermocalc was used on the parameters to find out if the velocities used would result in or avoid liquation cracking. Liquation cracking is a cracking mechanism associated with higher velocities. It should be expected that the highest velocity would be most likely to crack, whereas the lowest velocity would be least likely. No parameter set should crack if the high-velocity condition does not result in expected cracking.

To find the compositions at the given velocities, it was necessary first to find out the equilibrium partition coefficient k_e for each element in the alloy. This calculation was done using the Thermocalc equilibrium simulator with elemental compositions found from testing built parts. Once the solid composition and the liquid composition were found from the Thermocalc phase analysis, this ratio gave k_e through the relationship:

$$k_e = \frac{C_s}{C_L}$$

Equation 5-14

Through this, the velocity-dependent partition coefficient k can be found in the relationship in Equation 5-9. This value can then be used to calculate the velocity-dependent liquid composition C_L^* for each element through the equation:

$$C_L^* = \frac{C_L}{1 - (1 - k)Iv(P)}$$

Equation 5-15

Where P is the peclet number with equation $Pe = du/2\alpha$ where d is dendrite radius, u is the beam velocity and α is the liquid diffusion coefficient. If $Pe \gg 1$ then the Ivantsov solution becomes:

$$Iv(Pe) \approx 1 - \frac{1}{Pe} + \frac{2}{Pe^2}$$

Equation 5-16

To model the likelihood of liquation cracking, the method used by Cao and Kou [110] was used. They stated that, during welding, liquation cracking in the partially melted zone (PMZ) would occur if the filler material has a higher solidus than the base metal. This cracking is due to the bulk material not being able to sustain the strain put on it by the cooling meltpool. If the meltpool solidifies before the bulk, this will strain the bulk from the shrinking volume of the solid meltpool. The bulk cannot sustain this strain as it is liquid, so cracks form in the PMZ. This method was applied to LPBF, the bulk material was taken to be the base metal, and the meltpool was taken to be the filler material. For the bulk material, a Scheil calculation was made based on the bulk composition. For the meltpool, the velocity-dependent liquid composition C_L^* was used as well as the option of solute trapping for the medium and high-velocity conditions. This assumption was justified as the conditions satisfied those for solute

trapping. Solute trapping occurs when the ratio of the diffusion coefficient in liquid D_i to the interface width, which was taken to be 4×10^{-9}m [28] is below the interface or beam velocity v_T. As this was the case, the beam velocity could also be inputted into the calculations. Table 5-10 gives the velocities used for the high, medium, and low-velocity conditions.

Table 5-10 - The different velocities used in the cooling curve calculations. These are the lowest and highest velocities used in the three machines' experiments. EOS uses the medium velocity as part of their recommended parameter set for nickel superalloys.

Low Velocity	0.45 m/s
Medium Velocity	0.9 m/s
High Velocity	1.755 m/s

The Scheil calculation for the bulk material was then plotted on the same graph as the Scheil calculation for the meltpool, and the solidification curves were compared. Particular attention was paid to the solidus temperature for both curves.

The calculations were done on the conditions imposed in Osoba's [140] welding experiment with Haynes 282 to check the validity of this method. In their analysis, they note that liquation cracking in the PMZ was observed. If this method predicts liquation cracking, then this would prove the validity. As well as this, the same calculations were made with an alloy that is known to produce liquation cracks. CM247 is very prone to liquation cracking. If this alloy shows a higher propensity to crack, this will further support this method for finding whether liquation cracking may occur.

A thought experiment was performed on how much

segregation would have to occur for the conditions of liquation cracking to be observed. The composition of molybdenum was altered for this experiment. The concentrations tested were 8%, 9%, 12%, and 12.5%. All other concentrations were kept the same as those measured in the bulk material. The Scheil calculations for the four compositions were plotted on the same graph and compared. As with the previous experiments, the final solidus temperature is critical.

The meltpools resulting from different velocity conditions for the parameter sets were compared to the cooling of the bulk material. According to Cao and Kou, if the solidus of the meltpool is above that of the bulk, then liquation cracking will occur. Figure 5-16a and Figure 5-16b show the Scheil curves for different velocity conditions. Figure 5-16b focuses on the

terminus of the cooling curve to ascertain in more detail which velocity conditions resulted in solidus' lower than that of the bulk material.

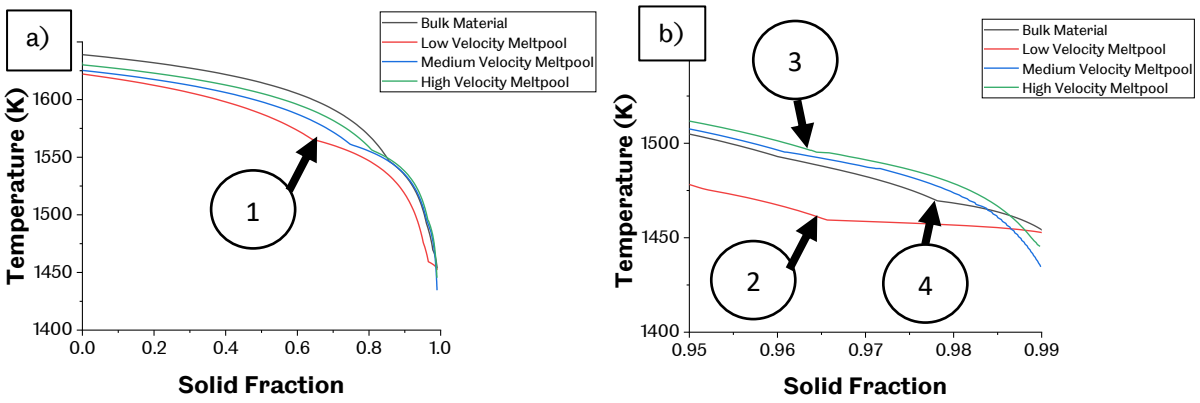

Figure 5-16 - These graphs show the whole (a) and the terminus (b) of the Scheil cooling curve for the different velocity conditions. The meltpool created by these velocities is compared to the bulk material. The velocities result in soliduses below the bulk material so that no liquation cracking will occur.

From the graph, all the conditions should result in no liquation cracking due to the soliduses being lower than the bulk. Though the high velocity is higher than the medium thermal velocity, the low beam velocity resulted in the highest solidus temperature closest to the bulk. This result occurred because solute trapping only occurs at beam velocities above approximately 0.7m/s, as described above. This condition results in the other soliduses being suppressed in comparison, thus allowing for these higher velocities to still result in no liquation cracking. Higher velocities than those used in any of the testing may result in liquation cracking. These results explain the parameter set suggested by EOS as the velocity is high enough to create solute trapping whilst reducing the likelihood of liquation cracking. The low-velocity condition results in a lower solid fraction at which γ' precipitates (0.653 instead of 0.855) (1). Near the terminus point of the solidification, the low velocity precipitates out phases which cause the gradient to get shallower (2). However, the bulk material precipitates out η, which causes a steep drop in liquidity and a higher solidus than the other tested states (3).

The cooling curves for the measured compositions from the cell interior and boundary were compared to the bulk material. The curves and the terminus points are shown in Figure 5-17a and Figure 5-17b, respectively.

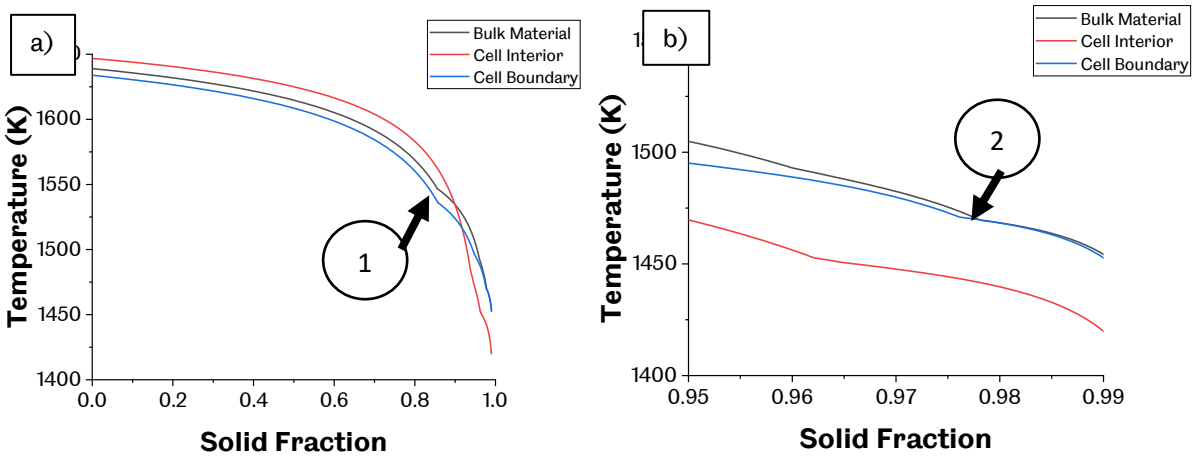

Figure 5-17 - The full (a) and end of (b) the Scheil cooling curve created from the composition observed in the cell interior and boundary. This result shows that liquation cracking will not occur within this cell or at its boundary. The results show that cracks would be more likely to form at the boundary where the precipitates segregate. The cell interior cooling curve gradient is steeper than the boundary gradient. As a result, different phases are formed.

The cooling curve for the interior starts above the bulk, and it has a steeper gradient, especially towards the end. This steep gradient occurs due to the different phases forming (Table 5-5). The carbides result in slower solidification than the γ' or σ phases. Due to this, the interior has a significantly lower solidus than the bulk. However, the boundary has a lower γ' precipitation temperature (1) 1536k compared to 1547K for the bulk. The boundary composition and the bulk material form η phase close to the solidus. This phase forms at a slightly lower solid fraction (2), and so the solidus is lower than that of the bulk material, avoiding liquation cracking. The cell boundary is more likely to exhibit liquation cracking as this is where the precipitates go.

Cao and Kou's [110] method for liquation cracking prediction is untried within LPBF, although it has been tested on AM in general by Wei *et al.* [102]; as such, it must be verified against known results. In their analysis of the welding of Haynes 282, Osoba observed liquation cracks. It is, therefore, possible to input the parameters for welding into Thermocalc and plot the cooling curves. Figure 5-18a shows the entire curve, and Figure 5-18b shows an enlarged view of the end of the curve.

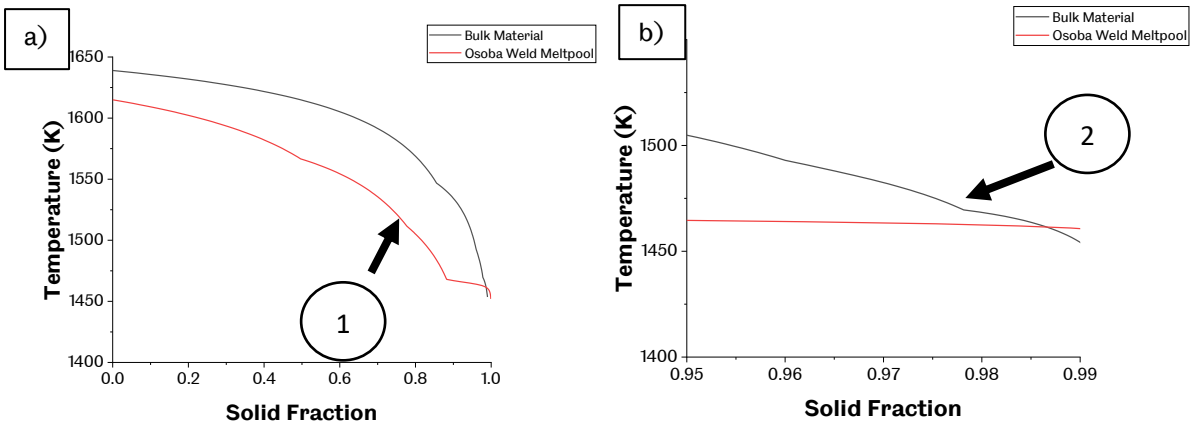

Figure 5-18 - Overall (a) and end of (b) the Scheil cooling curve for the parameters used by Osoba [140] *in their investigation of welding of Haynes 282. In their results, they observed liquation cracking. The results of this model suggest that liquation cracking should occur by the interpretation of Cao and Kou* [110].

The solidus of the weld meltpool is above that of the bulk (Figure 5-18), which would predict the observed liquation cracking. This positive result suggests that this adapted method of prediction might be valid. The curves show γ' precipitation is shifted significantly to a higher temperature (1566K) and a lower solid fraction of 0.50 (1). Due to the steep gradient of the bulk material in the γ' phase formation and in the final phase formation, which included carbides and borides, it had a lower solidus than the weld meltpool, which had a shallow gradient from the γ' phase formation onwards (2). This result led to the prediction of liquation cracking.

Another alloy was investigated using the same parameter sets to help give further evidence that this is a valid prediction method. CM247 is known to crack, and so if this method suggests that it is more prone to cracking than Haynes 282, then this would be positive. Figure 5-19a shows the cooling curve for the different velocities, and Figure 5-19b focuses on the final solid formation.

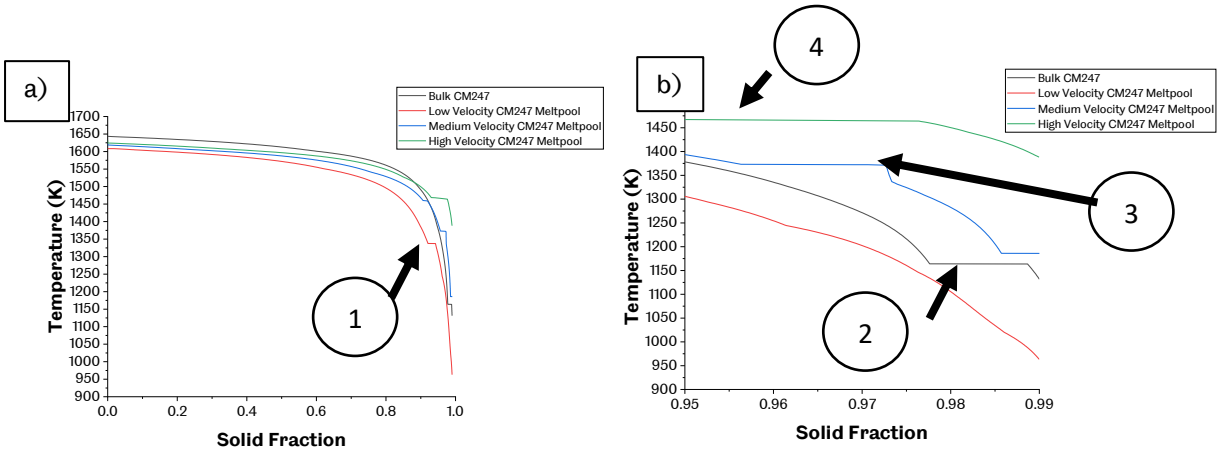

Figure 5-19 - The overall (a) and end (b) of the Scheil cooling curve for CM247 for the different velocities. CM247 can be seen to be more susceptible to liquation cracking as both the medium and high velocities result in the solidus of the meltpool being above that of the bulk material and thus satisfying the condition for liquation cracking to occur.

CM247 follows the trend of higher velocity leading to a higher solidus. From these results, the low velocity should result in no liquation cracking. Whilst this is beneficial, it may cause hot tearing, which becomes more prevalent at lower velocities (See Section 5.6). This method predicts liquation cracking for medium and high-velocity conditions, making it significantly more prone to liquation cracking than Haynes, borne out by existing literature. There is a knee in the bulk cooling curve (1). The precipitates cause the solid fraction to increase quickly over a slight temperature drop. However, the temperature drops significantly over a small increase in solid fraction, leading to a lower solidus than the high and medium velocity meltpools.

There is a horizontal knee near the terminus at 1164K, which causes it to have a higher solidus than the low-velocity condition (2). This velocity behaves differently to the higher velocities as it does not experience solute trapping, which causes the solidus to be higher. All conditions follow the trend of higher velocity higher solidus. The medium velocity experiences its horizontal knee as more phases are precipitated out. This knee has been pushed to a lower solid fraction and higher temperature (0.956 solid fraction and 1373K) (3). These phases precipitate at an even higher temperature with a high velocity at 0.930 and 1469K (4). This phase transformation causes an even higher solidus to occur with a high velocity. It also occurs over a longer increase in solid fraction, so the solidus is higher than the bulk. This analysis suggests a low velocity could eliminate liquation cracking, but this will increase the propensity for hot cracking, so a balance between the two cracking mechanisms is required.

The molybdenum content was varied whilst all other elements stayed at the same abundance except for nickel to find out what compositional conditions would have to be imposed such

that Haynes exhibits hot cracking. Figure 5-20a below shows the results of this experiment, and Figure 5-20b shows the ends of the solidification curves.

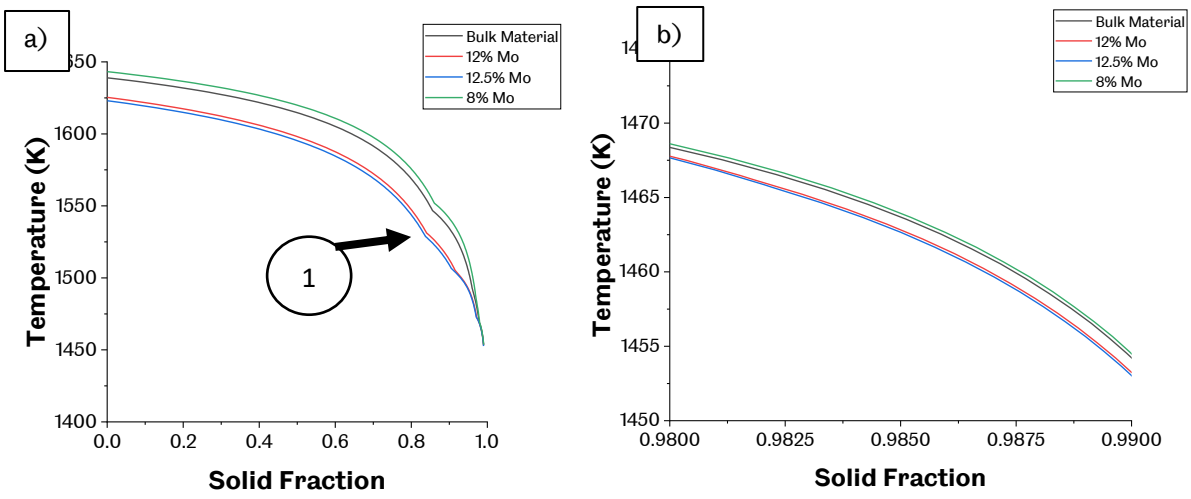

Figure 5-20 - This shows the overall (a) and end (b) of the cooling curves with differing quantities of molybdenum content. The curves show that with an increased molybdenum content to 12% and 12.5%. Both the solidus and liquidus are suppressed, reducing the likelihood of liquation cracking occurring. When the molybdenum content is reduced to 8%, the liquidus and solidus temperatures increase, thus making it more likely that liquation cracking will occur.

Changing the molybdenum content has a small effect on the solidification behaviour. The point labelled (1) is where a new phase is formed. In this case, it is γ'. Increasing molybdenum has the effect of suppressing the temperature at which γ' occurs. In bulk (the black line), γ' starts to form at 1547K and 0.96 solid fraction. However, the 8% molybdenum composition precipitates at 1552K and 0.86 solid fraction, which is a lower solid fraction. For the high molybdenum content at 12%, the γ' precipitates at 0.84 solid fraction and a temperature of 1531K, significantly suppressing the standard composition. 12.5% molybdenum lowers the precipitation temperature further to 1528K. The solid fraction at the formation of γ' is 0.94, similar to the 12% molybdenum. Molybdenum was chosen as it is the only refractory metal of significant abundance (although there was a trace amount of tungsten, this probably came about due to contamination from CM247, which was used in the same machine). Increasing the molybdenum should increase the solidus and liquidus as it has a high melting point. However, this does not seem to be the case, as Figure 5-20a and b show that increasing the molybdenum lowers the solidus and lowering the molybdenum content increases the solidus. As a result, it can be concluded that any molybdenum enrichment will not result in liquation

cracking occurring. Molybdenum depletion must be avoided from Figure 1.6-8a, and b this can lead to a higher solidus than the bulk, so liquation cracking may occur.

This experiment, however, looks at molybdenum's effect in isolation and does not consider other elements that may affect the liquidus or solidus.

This method has been verified on another Haynes 282 study and the liquation cracking prone CM247. These tests show that liquation cracking is unlikely due to the lower soliduses associated with these velocity-dependent compositions. Hot cracking was found to not occur in section 5.6, and now finding that it is likely that liquation cracking does not occur. The last primary cracking mechanism to be studied is strain age cracking, whose prevalence will be assessed in the following sections.

5.7.5 Strain age Cracking

The last primary mechanism that will be examined is strain age cracking. This mechanism is caused by repeated exposures to temperatures near but not over an alloy's melting point[104], as with LPBF. The mechanism is most commonly associated with the γ' or γ" phases. As the material is exposed to elevated temperatures over a long time, residual stresses build up. These are the driving force behind the propagation of cracks. The thermal exposure causes hardening of the alloy matrix. This hardening transfers the residual stress onto the grain boundaries, where carbides can act as crack initiators. Whilst the main hardening phase is regarded as γ', other phases such as μ or σ can cause embrittlement. As an additional cause of stress, the volumetric change between the precipitates and the surrounding bulk can cause strains that propagate cracks. In this section, γ' will first be investigated as a cause for strain age cracking followed by using PHACOMP to determine if μ or σ could occur and EDX maps of the pre-test and post-test microstructure and crack sites to determine what phases surround the cracks.

5.7.5.1 γ' precipitation

Precipitation of the γ' phase can cause premature failure as it has an embrittling effect. Haynes 282, however, has been designed to form γ' more slowly than comparable alloys, thus giving it

higher elongation to failure at a particular temperature (Figure 5-21). This property can be seen in the Haynes brochure [5]

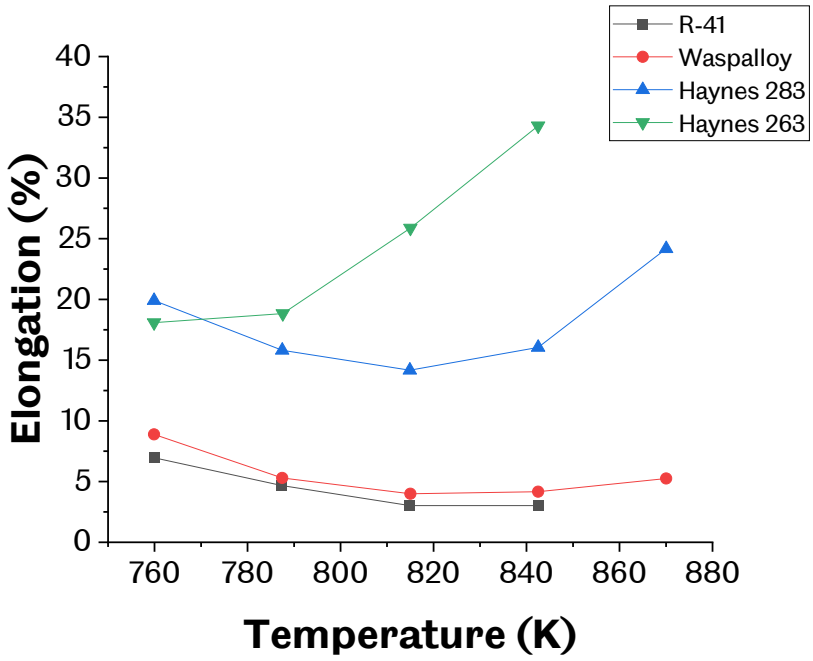

Figure 5-21 - This graph shows how Haynes 282 retains its ductility even at higher test temperatures. This ductility retention is due to the low γ' fraction, leading to slow γ' precipitation kinetics. It has a higher elongation to failure than the two alloys with a higher γ' content. Although it performs worse than 263, its γ' content is designed to withstand loads whilst being ductile enough to sustain them for long periods without fracturing[5].

From the graph, Haynes 282 retains its ability to elongate before fracture better than R-41 or Waspalloy. This retention of ductility is due to the lower γ' fraction, which is kept above 263, allowing Haynes 282 to have greater mechanical strength. Another aspect of Haynes 282's alloy design was that it is slow to precipitate γ'. This slow γ' kinetics increases the time for strain age cracking to occur as the growth of γ' precipitate drives the residual stress towards the grain boundary where the carbides can initiate cracks.

The slow γ' kinetics are demonstrated in (Figure 5-22). As γ' is a hard, brittle phase, its increased presence would coincide with an increase in hardness.

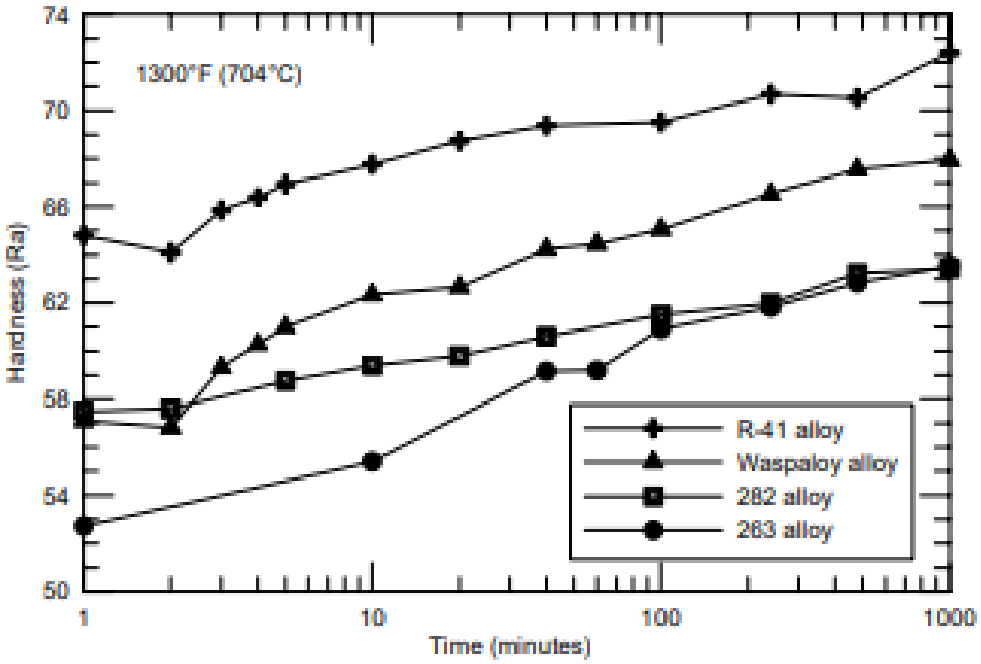

Figure 5-22 - This graph shows the increase in hardness for selected nickel superalloys. In this test, Haynes 282 performs well by having the smallest increase in hardness over the tested time. The slight increase in hardness is due to the slow precipitation kinetics that Haynes 282 exhibits γ' is a harder phase than the γ matrix, so it is the reason why the material becomes harder as it precipitates out at exposure to elevated temperatures[5]*).*

It can be seen from the graph that Haynes 282 has the smallest increase in hardness over the tested time. This slow γ' kinetics comes from the initially low γ' content as an increased γ' content drives faster growth in γ' precipitates[7].

Whilst the γ' kinetics are slow, γ' does still grow, and spherical γ' precipitates are visible within the grains when the tested microstructure is observed. These may have helped cause strain age cracking by driving the residual stresses to the grain boundaries. An effective heat treatment will reduce the residual stresses within the material. Therefore, the precipitates would have less strain to drive towards the boundary-making the part less susceptible to strain age cracking.

5.7.5.2 PHACOMP

The new PHACOMP method [108] was used for the compositions imposed by the different velocities and those measured during the cell boundary and interior compositional analysis.

This method uses the electron valence of different elements and the atomic weight composition of the alloy to identify if the μ or σ phase will occur. The $\bar{M}d$ value was found for the alloy through the rule of mixtures equation.

$$\bar{M}d = \sum_{i=1}^{n} X_i (Md)_i$$

Equation 5-17

The Md values for each element are given in Table 5-11 below.

Table 5-11 - This table gives the Md values for different elements. These values are based on electron valence. The elements with the highest Md values are known to form precipitates readily.

Element	Md Level (eV)
Ti	2.271
Cr	1.142
Fe	0.858
Co	0.777
Ni	0.717
Mo	1.55
W	1.655
Al	1.9
Si	1.9

The $\bar{M}d$ values for the alloy at different velocities and regions within the cell were compared to other alloys, and the critical values of 0.9 and 0.915 for σ and μ phases, respectively. Above these values, σ and μ phases would be expected to form. The propensity for the alloy to form these phases will be compared with Thermocalc, which in its Scheil calculation computes phases that are most likely to occur at specific temperatures.

The results of the PHACOMP analysis are listed below in Table 5-12. Atomic % (A%) and the Md contribution for each constituent element is given. The phase composition was calculated for the as-built material, the high-velocity condition (1.755m/s), the low-velocity condition (0.45m/s), the cell's interior as measured through EDX and the boundary of the cell as measured through EDX.

Table 5-12 - This table gives the atomic weight percentages (A%) and the contribution of these elements to the overall $\bar{M}d$ value. From this table chromium is one of the most significant contributors to the formation of μ phase

as the alloy is almost 20% chromium. Molybdenum is also a contributor as it is the primary strengthening element within the alloy and has a high volume fraction.

Element	As-built		High Velocity		Medium Velocity		Low Velocity		Cell Interior		Cell Boundary	
	A%	Md	A%	Md	A%	Md	A%	Md	A%	Md	A%	Md
Titanium	2.61	5.93	2.68	6.09	2.72	6.18	2.76	6.27	2.16	4.91	2.73	6.20
Chromium	21.7	24.7	22.1	25.2	22.32	25.5	22.54	25.7	20.7	23.7	21.4	24.4
Iron	0.09	0.08	0.09	0.0772	0.09	0.0772	0.09	0.078	0.09	0.08	0.09	0.08
Cobalt	10.1	7.81	9.91	7.70	9.83	7.64	9.73	7.56	10.1	7.88	9.67	7.51
Nickel	56.4	40.4	55.48	39.8	54.95	39.4	54.3	38.9	57.7	41.4	56.4	40.5
Molybdenum	5.41	8.39	5.45	8.45	5.48	8.49	5.52	8.56	6.29	9.75	6.79	10.5
Tungsten	0.01	0.02	0.01	0.0166	0.01	0.0166	0.01	0.0166	0.01	0.017	0.01	0.017
Aluminium	3.42	6.50	3.58	6.80	3.66	6.95	3.76	7.14	2.52	4.79	2.52	4.81
Silicon	0.06	0.114	0.06	0.114	0.06	0.114	0.07	0.133	0.03	0.057	0.06	0.114
$\bar{M}d$	0.940		0.9426		0.9436		0.9442		0.9250		0.9411	

The $\bar{M}d$ values for each condition are given. All of the conditions have $\bar{M}d$ values greater than 0.915, which is the condition for μ phase and σ phase to form. When considering the different velocities, the high-velocity condition is more likely to form these phases than the low velocity. Using the EDX segregation analysis from the TEM sample, the composition for this was inputted and the $\bar{M}d$ values found. When comparing the results to the equilibrium phase analysis done on Thermocalc and shown in Table 5-9, all the conditions cause σ to form,

Although both phases are deleterious to mechanical properties, according to [106], the σ phase is brittle at room temperatures. The dislocations can slide at higher temperatures where this alloy is expected to function, so it becomes less brittle. μ phase absorbs chromium from surrounding regions, thus making them more brittle and more likely to cause cracking[107]. The significant contributors to μ and σ phase formation are chromium, molybdenum as they have relatively high Md values, but there are significant quantities of these elements within the alloy. Titanium and aluminium have high Md values but are less abundant within the alloy. Although all the conditions and regions have $\bar{M}d$ values above 0.915 when solute trapping and the velocity are considered for the different velocity cases with the Scheil and the standard Scheil solidification curves are done on the cell interior, and boundary segregation results in the σ phase being suppressed but the μ phase is present. The effect of the different velocities and phase compositions are discussed in sections 5.7.2 and 5.7.3.

Haynes 282 has a relatively high $\bar{M}d$ when compared to other nickel superalloys as it has a high Chromium and Molybdenum content. Figure 5-23 shows a plot of the different conditions observed for Haynes 282.

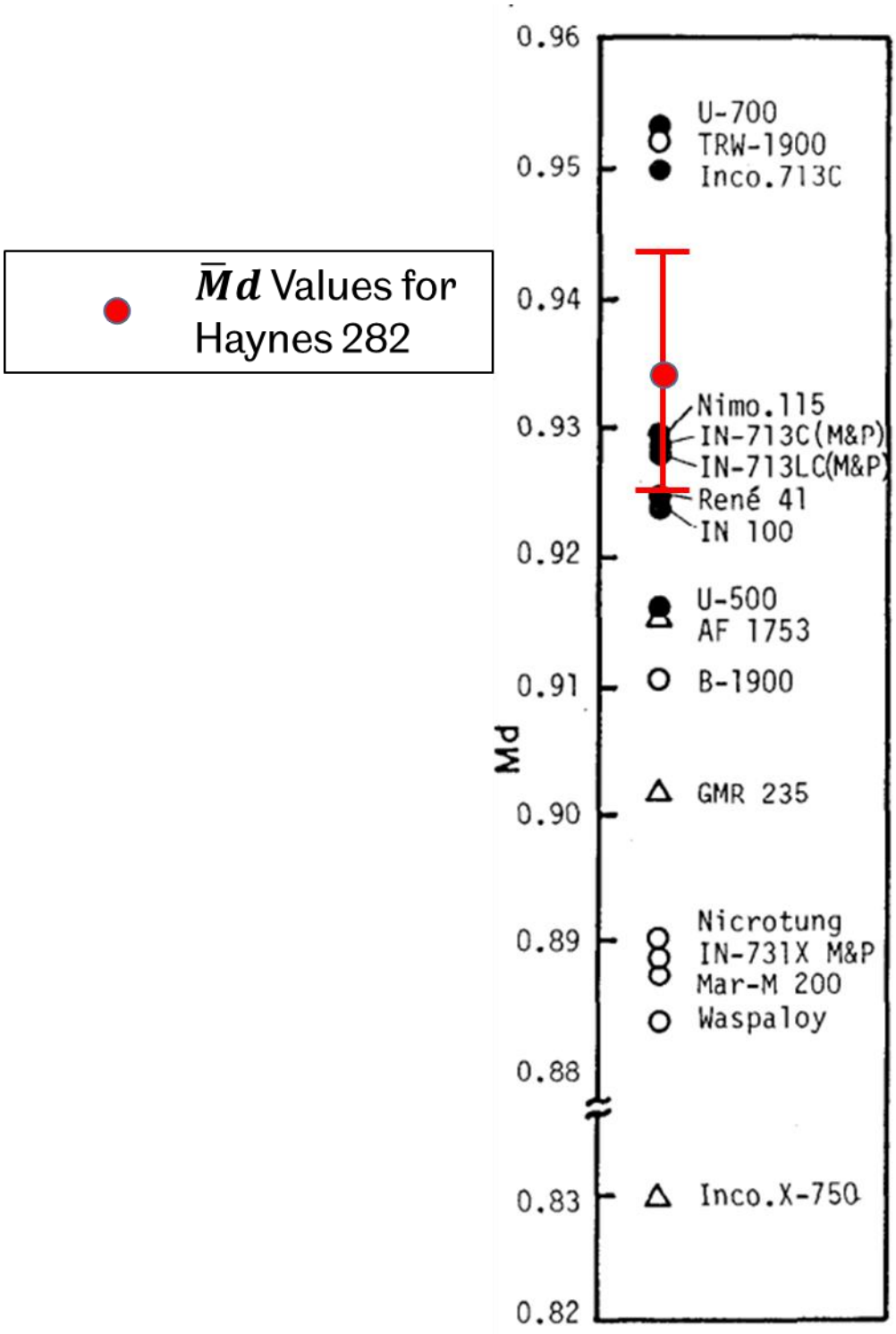

Figure 5-23 - This chart shows the range of $\bar{M}d$ values from the tested conditions. All the conditions result in $\bar{M}d$ values high enough to cause μ phase to form. It is lower in the cell interior as μ forming elements such as molybdenum and chromium have segregated to the boundary.

A minimal effect from velocity and the EDX of cells suggests that these phases are formed within the cells.

Whilst initial segregation measurement using SEM EDX showed no precipitation. This observation was only on the micron scale and above. When TEM was used to observe the cell boundaries, precipitates were formed on the nanoscale (Figure 5-24). The precipitate is approximately 10nm in size and spherical.

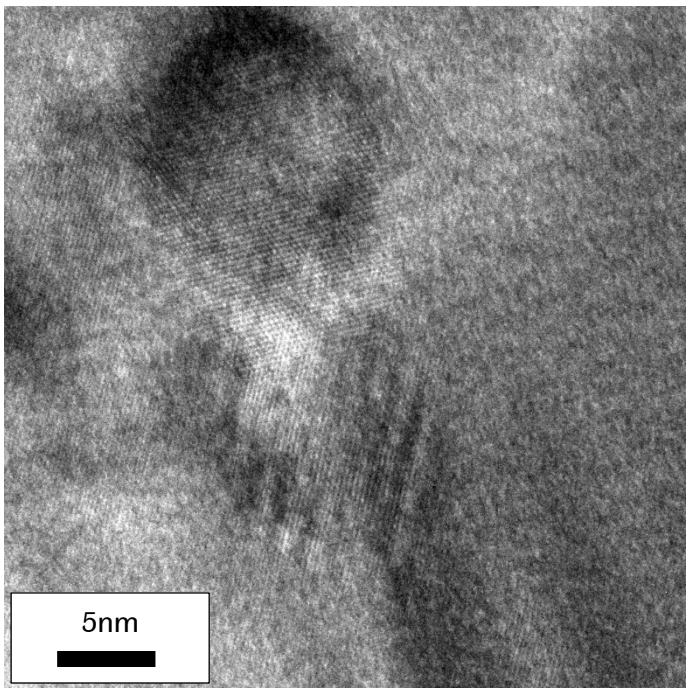

Figure 5-24 - This TEM micrograph shows a precipitate on the cell boundary. This precipitate is approximately 10nm in size and spherical. As the cooling rate is fast, precipitates are on the nanoscale in LPBF built parts. As the material is exposed to elevated temperatures, this precipitate will grow.

This nanoscale precipitate is a known phenomenon when building using LPBF as the cooling rates are so high. Kurz-Fisher's analysis of dendrite tip radius [36]states that as the dendrite tip radius is small, there can only be small perturbations in the undercooling and segregation leading to local undercooling being dominant. This condition would allow for segregation to only occur on a local level which is why the precipitates are so small.

5.7.5.3 Segregation Analysis of the fracture sample

As discussed in Section 5.6, the heat-treated but untested SEM EDX map shows no segregation on the micron scale as the sample is exposed to elevated temperatures for a long duration over the test cycle. The precipitates start to grow and move to the boundary, as shown in Figure 5-25 and Figure 5-26.

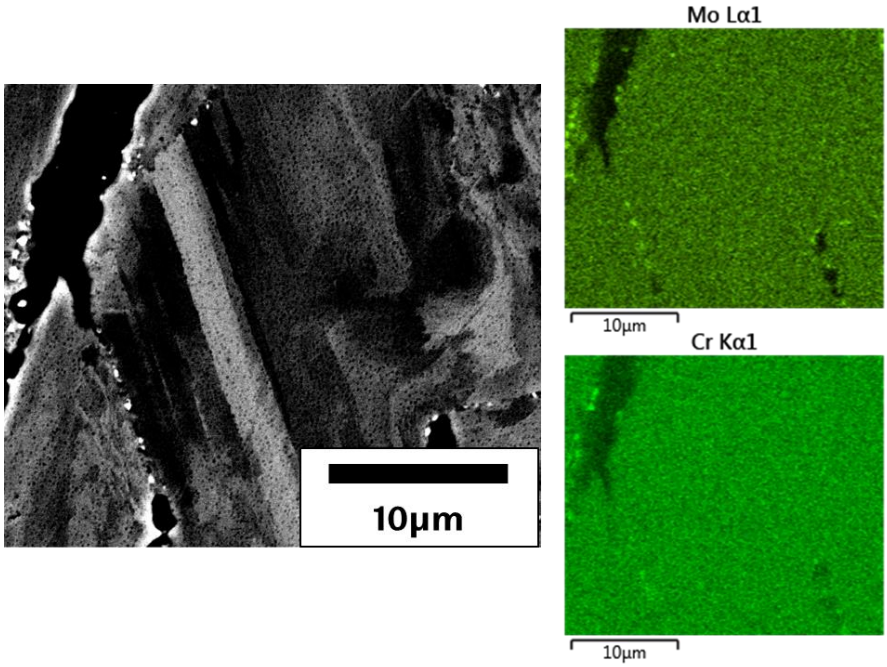

Figure 5-25 - This micrograph and EDX map shows a crack surrounded by chromium and molybdenum. The elements surrounding the crack suggests that the µ phase, or a carbide both rich in these elements, have formed and caused a crack at this grain boundary. Other regions of precipitate formation can be spotted at other grain boundaries in the EDX map, although cracks have not yet been formed due to precipitate presence.

In both cases, the µ phase or a carbide phase surrounds the crack at the boundary. No crystallographic data is available, which would establish a difference. Reducing chromium and molybdenum content can reduce the propensity for µ phase to cause failure. However, there is a trade-off as chromium is necessary for corrosion resistance, and molybdenum is a strengthening element.

Figure 5-26 –A micrograph of a crack seen in the test sample after fracture. It is surrounded by molybdenum, chromium and carbon. The presence of these elements would suggest that carbides have contributed to the crack forming. Molybdenum and chromium can be seen at other grain boundaries. These elements presence would indicate that the µ phase has formed after these elements have segregated to the grain boundaries due to prolonged exposure to

elevated temperatures. shows a crack within the microstructure surrounded by carbon, molybdenum, and chromium. As well as carbides around the crack, μ phase has formed on grain boundaries because of prolonged exposure to high temperatures.

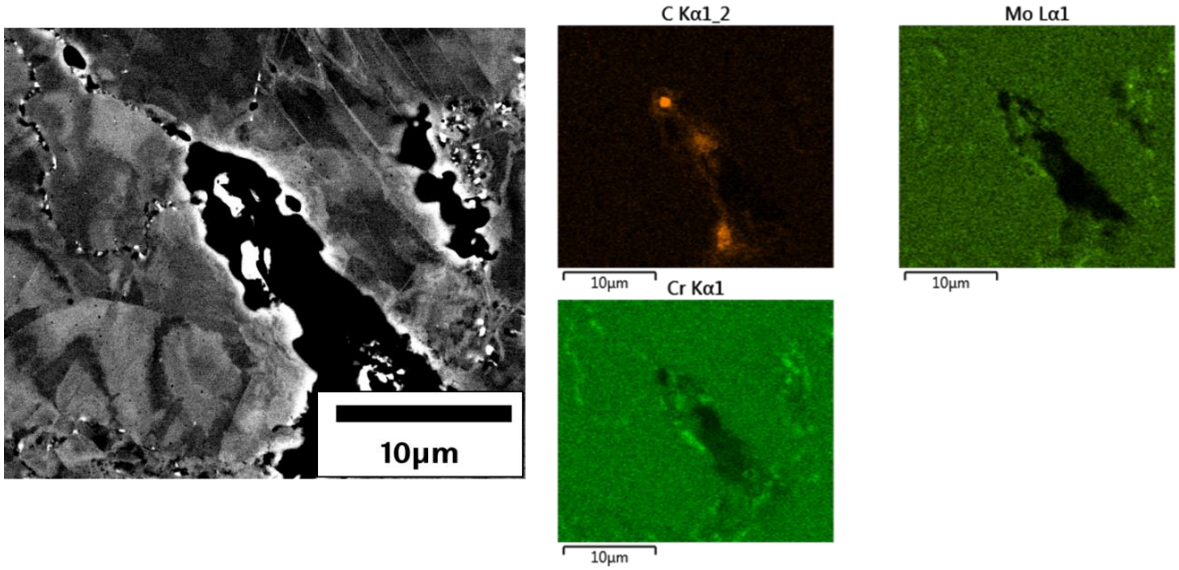

Figure 5-26 –A micrograph of a crack seen in the test sample after fracture. It is surrounded by molybdenum, chromium and carbon. The presence of these elements would suggest that carbides have contributed to the crack forming. Molybdenum and chromium can be seen at other grain boundaries. These elements presence would indicate that the μ phase has formed after these elements have segregated to the grain boundaries due to prolonged exposure to elevated temperatures.

These could be either $M_{23}C_6$ or M_6C as they both contain molybdenum. $M_{23}C_6$ is the most common type after heat treatment and carbide stabilisation, but M_6C is common in alloys with transition metals (the tested Haynes 282 has 10.25% Cobalt) and Molybdenum content above 6% (Haynes 282 has 9%). Unfortunately, time constraints meant that the etching that can be used to distinguish between the two carbides was not done. Further investigations may want to perform this etching to distinguish between the two carbides. Carbides must be distributed evenly throughout the grain to have a beneficial strengthening effect. If they collect on the grain boundary, they can form platelets and sheets. These can have an embrittling effect on the alloy and cause cracks. These two types of carbide distribution are shown in Figure 5-27a and Figure 5-27b.

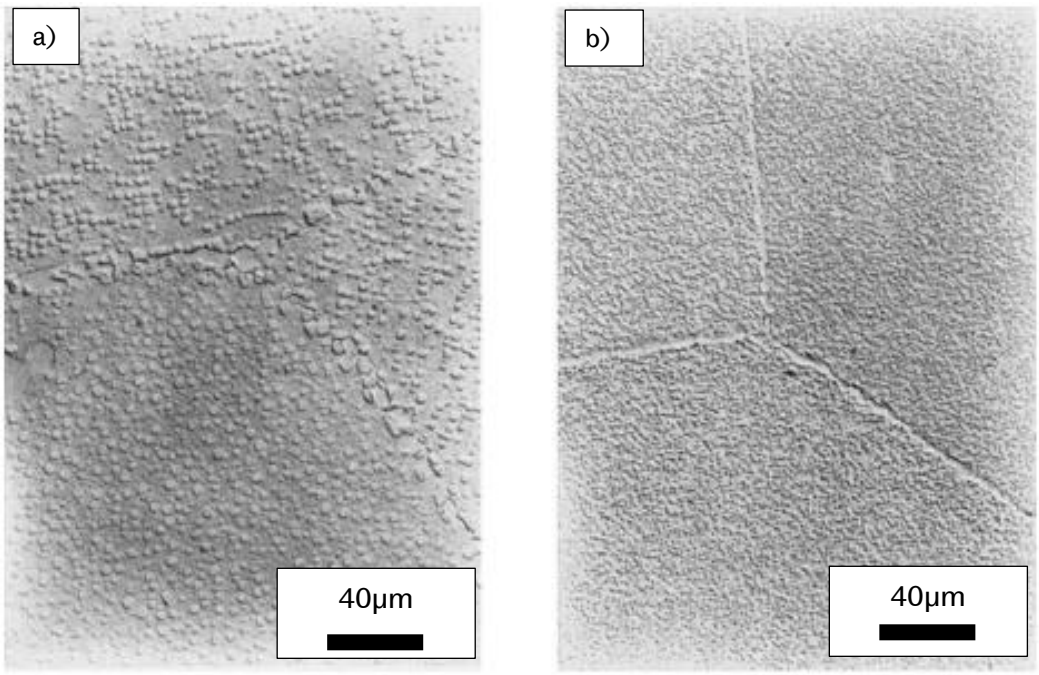

Figure 5-27 - Carbide distributions are shown around the grain boundaries. A (left) shows an even distribution of carbides throughout the matrix, and they are cuboidal in shape. b (right) shows the carbides collecting on the grain boundaries these forms into platelets or sheets, which can act as crack initiators if a load is applied [30].

When the microstructures and the grain boundaries were investigated, the two heat treatments had different effects on the distribution of carbides due to the Haynes heat treatment not having the necessary additional energy to cause carbide redistribution [21]. When this additional energy was overcome by heating to at least 1240°C with the Christofidou heat treatment, the carbides and precipitates were evenly distributed within the grain, as shown in Figure 5-28a. This heat treatment caused carbides to be distributed on the boundary, as seen in Figure 5-28b.

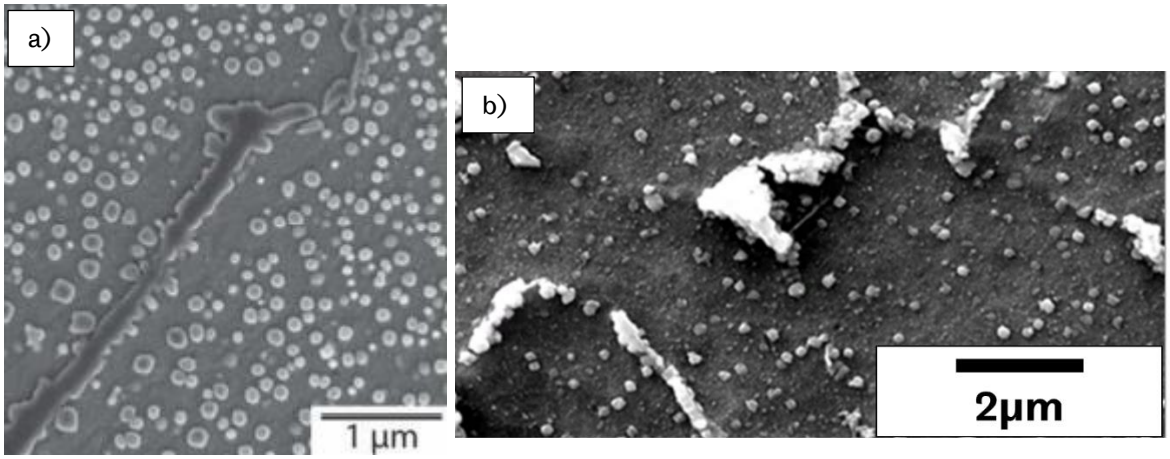

Figure 5-28 - These two micrographs show the different precipitate distributions due to different heat treatments. The left, a) shows the carbides have been distributed evenly as the higher solutionising temperature has allowed the carbides to move. The right, b) shows carbides coalescing on the grain boundary where they are likely to have an embrittling effect and possibly act as crack initiators. This distribution has occurred as the heat treatment solutionising temperature was too low to allow the carbides to be redistributed effectively [21], [148].

The more favourable distribution of carbides corresponds with a similar mechanical performance of samples using the Christofidou heat treatment and the Haynes heat treatment. This mechanical performance is despite more grain boundaries in the test direction due to no recrystallisation of the microstructure using the Haynes heat treatment. More testing is needed to determine if the Christofidou results in similar or improved stress rupture time performance than the Haynes heat treatment.

It can be concluded that both carbides and µ phase can cause cracks within the microstructure and must be considered when improving mechanical properties, particularly stress rupture performance. The deleterious effect of carbide formation can be mitigated by using the correct heat treatment. µ phase is the result of the alloy chemistry and thermal velocity. By reducing the quantity of the elements with the highest Md values (aluminium, titanium, molybdenum and chromium), the quantity of µ phase can be reduced. This change can have detrimental effects on the mechanical properties as molybdenum is a strengthening element, and Chromium is needed to prevent corrosion. As outlined in Table 5-9, a higher velocity will suppress µ phase formation where the high-velocity condition resulted in the lowest percentage of either γ' or σ phase. When looking at the phase formation for different conditions, it can be seen that although the µ phase starts forming at a higher temperature Table 5-5 when the thermal velocity is high, the solidus is also higher than when the thermal

velocity is lower. This change in the liquidus and solidus results in a smaller temperature range over which it can form and a shorter time due to the faster cooling rate.

5.8 Conclusion

In conclusion, this chapter supports the overall aim of this project to reduce the uncertainty associated with processing Haynes 282 and other nickel superalloys using LPBF. The microstructure was characterised and compared to the microstructures observed in other studies. A characteristic gradient of $6.83\times 10^{-4}\left(\frac{m^3K^2}{s}\right)^{\frac{1}{4}}$ This gradient was compared to the gradient from other nickel superalloys and found to agree with them. The stress rupture times of the tested samples were compared to those from other studies and found to form a continuum with those results. Unfortunately, no conclusive proof of the effect on mechanical properties of either tested heat treatment was found despite micrographs and EBSD maps of the microstructures resulting from these heat treatments. This result shows that Christofidou's heat treatment has fully recrystallised the microstructure and distributed the carbides evenly amongst the grain. In contrast, the Haynes suggested heat treatment retained the columnar grain structure and caused carbides to migrate to the grain boundary.

Different causes of cracking were examined for if they could be the primary source of cracking within the alloy. Hot cracking was tested by using a hot-cracking criterion equation. This assertion was verified by using data from other studies. Some of these studies had reported no hot cracks, but their HCS was higher than those found for parameters in this work. This observation suggests that no hot cracking occurred in the LPBF samples.

Segregation analysis was performed first using EDX on an SEM and then compositional analysis on a TEM. This analysis found segregation on the nanoscale due to segregation being dominated by local undercooling as the dendrite tip radius is small. It was found that precipitate forming elements such as titanium, molybdenum, and chromium segregated o the cell boundary whilst nickel and cobalt became more abundant in the cell interior. This analysis helped give a clearer understanding of the microstructure in the as-built condition with Haynes 282. One of this project's objectives is to understand the microstructure. Fully understanding the alloy's microstructure makes it more likely to be used in service. The velocity-dependent partition coefficient was found, and this was used to determine if specific velocities could cause cracking to occur in the form of liquation cracking. This condition required the solidus of the meltpool to be below that of the bulk material. This method was adapted from predicting liquation cracks in the partially melted zones of welds. This method suggested that no liquation cracks would form at the velocities tested within the part manufacture process. This method was validated by it correctly predicting liquation cracks

would form in a Haynes 282 welding experiment from another study where liquation cracking was reported. It was also used on an alloy more susceptible to liquation cracking. It predicted that both the high and medium velocity conditions (1.755m/s and 0.9m/s respectively) would lead to liquation cracks being formed. Only the low velocity (0.45m/s) would avoid these types of cracks.

Lastly, strain age cracking was examined. γ' precipitation was investigated. Haynes 282 has been designed to have enough γ' to make it a strong alloy but not so much as to cause it to be brittle. As such, this was discounted as a phase that could cause cracking. PHACOMP was used to analyse what phases might occur. μ and σ were found to occur due to elemental composition. When the equilibrium phase content was investigated, carbides in the form of $M_{23}C_6$ were present and the σ phase. However, when the Scheil cooling curve was performed, μ phase precipitated out instead, and the carbides were suppressed. An analysis of cracks within the test samples after fracture revealed that carbides and μ phase surrounded the cracks suggesting that this was the cause of failure. It was found that higher velocities led to a lower precipitate content within the solidifying material. This velocity would reduce sensitivity to strain age cracking as the precipitates would be initially suppressed. Effective heat treatments such as that done by Christofidou led to the carbides being redistributed evenly within the matrix. If these carbides could be stabilised, this would eliminate one of the phases causing failure.

The crack mechanism investigation has revealed the crucial role that beam velocity plays in crack formation. For hot cracking, a slower speed leads to a greater HCS. In contrast, higher velocities make the alloy more susceptible to liquation cracking. Finally, higher beam velocities suppress precipitates, making the material less susceptible to strain age cracking. As a result, a balance must be struck that reduces the propensity for all cracks to form. This velocity will be different for different alloys as they may be susceptible to different cracking mechanisms. However, this analysis does not consider the beam's return, which would affect the meltpool dynamics and crack formation. Further work would take this into account.

Overall, this chapter has shown how an alloy may be characterised and its crack mechanisms identified. Although this has focussed on Haynes 282, it could be applied to any alloy to find optimal parameters based on fundamental solidification mechanics.

6. Machine Characterisation and Parameter Conversion

6.1 Introduction

This chapter seeks to characterise two Laser Powder Bed Fusion (LPBF) machines, the AconityMini and the Renishaw SLM125, using melt track analysis. They will be characterised separately, and the results compared to identify a method of translating parameters between the two machines. The AconityMini has a continuous beam laser, whereas the Renishaw 125 has a quasi-continuous laser[79]. The differences between these two laser types are discussed in Section 1.6.1.2.

The machine needs to be characterised in order to be able to control the process. By understanding how the machine operates and interprets the input commands, parameters can be chosen that work optimally on the machine to reduce error. This reduction in error is crucial to increasing the adoption of LPBF. Errors in parameters such as point distances and hatch distances can cause differences in thermal history and pore formation; by minimising and understanding the error margins, local differences in microstructural and mechanical properties can be eliminated.

Previous studies [76], [84], [86] have focussed on parameter optimisation when evaluating how to process a material. Whilst this is important, other factors contribute to defects in the built parts. By characterising the machine and understanding the uncertainties in input parameters, these can be accounted for and altered to reduce these errors. Studies have been done into machine characterisation by creating test artefacts ([75]). These artefacts require powder and can be expensive and time-consuming to produce. In addition, there are potential defects in the powder [100] it is hard to distinguish between powder induced porosity and machine induced porosity. As a result, this chapter will analyse and characterise the laser without powder to eliminate this kind of porosity. a lack of powder has the added benefit of reducing cost and time.

LPBF and AM, in general, are competing with established forging and cutting techniques that operate with a high degree of precision. As a result, LPBF must be shown to be precise and repeatable. These errors can be reduced by characterising the machine, and the build process can be made more precise and reproducible. Currently, there are other defect sources within the process, such as the powder and how it has been processed [100]. As these are reduced,

this characterisation will become even more helpful as the machine and its operation become a relatively more significant source of defects.

A whole machine characterisation is necessary to avoid erroneous assumptions about the machine that lead to defects in built parts. This characterisation will distinguish between what is expected to happen through the input. These lead to different parameter sets being used either because they are the machine manufacturer's default set or used in other studies on a similar material. This study will focus on exploring power and hatch spacing on the AconityMini and exposure time and point distance in addition to power and hatch spacing on the Renishaw as these are the controllable variables that are easiest to measure the error in. The effect of changing focus offset on the weld track width will also be measured. These variables contribute to normalised energy density [86] but crucially can be changed, whereas other components are material constants that cannot be changed without altering the alloy chemistry.

The effect of the exposure time will be investigated as the Renishaw uses a quasi-continuous laser. The reduction in energy input resulting from the laser having to ramp up to full power will be quantified by looking at the meltpool resulting from the pulses.

The shape of these meltpools will be investigated to assess the melting mode. The onset of keyhole melting [89]will be investigated to determine whether keyhole defects will be formed.

This study will include a wide range of parameters as these have been used in previous experiments([149]). Both machines do not limit the parameters, and as such, it is possible to choose parameters that will result in defects or parameters that will not follow the inputted values. A wide parameter study will find these parameters so that further studies will know the limits.

Freeman's model [80]will be used to measure the sensitivity of the meltpool to uncertainties in the input parameters. This model can be used to find parameter sets that minimise errors in the resultant meltpool and reduce thermal history differences.

Reproducibility is a critical characteristic that will be needed if LPBF as a technology is to see wider adoption. This characterisation will help improve this by identifying parameter sets that reduce uncertainties.

Finally, the characterisation of both the machines will be used to attempt to find a conversion between the two machines. Studies have shown normalised conversion between machines and machine types [86]. This chapter will use weld tracks and characterisation to create a

conversion. If possible, this conversion will be useful in quickly transferring successful build parameters from one machine to another. The method used will be applicable between any LPBF machine with either a continuous or quasi-continuous laser.

6.2 Laser and Scanner Accuracy

6.2.1 Renishaw Laser and Scanner Accuracy

The AutoFabMTT software was used to create single layer melt tracks. These tracks were performed with a power of 40W and an exposure time of 20µs that created a definite mark in the plate whilst being small enough to assess the parameter precision. A range of both hatch spacings and point distances were chosen to observe the accuracy and precision of the laser. The point distance and the hatch space were measured at 5µm intervals between the ranges outlined in Table 6-1.

Table 6-1 - Parameters used in the scanner accuracy experiments to determine the error in point distance and hatch spacing.

	Range
Point Distance (µm)	5 -90
Hatch Spacing (µm)	10-160

A fresh (unmarked) steel baseplate was spray painted black with chalkboard paint. This paint helped highlight any marking that the laser made on the baseplate. Melt tracks were then lased onto the plate under an inert (<1000ppm O2) atmosphere. The pressure inside the chamber was kept constant at 50mbar above atmospheric pressure. The tracks were grouped by parameters in 10mm squares. Once tracks had been lased, the baseplate was removed from the machine and placed under a CLEMEX Optical Microscope. The distance between the marks made by the laser was measured and compared with the inputted parameters. This measurement was done for both hatch and point distances, and the percentage deviation from the expected values was plotted.

Focus offset is the distance that the focal point of the laser is from the powder bed. To measure the effect of altering the offset, weld tracks 2mm apart were made with the parameters outlined in Table 6-2. The power, point distance, and exposure time were kept constant, but the focus offset was systematically increased from 0-5mm in 1mm increments.

Table 6-2 - Parameters used to determine the effect of focus offset on the melt width and at what offset the beam is most in focus.

Power (W)	190
Point Distance (µm)	10
Exposure Time (µs)	80
Focus Offset (mm)	0-5mm

The welds were examined using the CLEMEX microscope, and the width of the region that had the paint removed by the laser was measured.

The start and ends of weld tracks were also investigated to see how the laser approaches the initial hatch as well as how it turns between hatches.

Using the Clemex Microscope the lased weld tracks were examined. As well as indenting into the substrate, the laser also burnt off the blackboard paint near the laser, which helps make the tracks more identifiable. Figure 6-1 shows the indents that have been made from the laser pulses. These have been circled, the distance between the top edges was measured as the meltpool middle is obscured by the next meltpool.

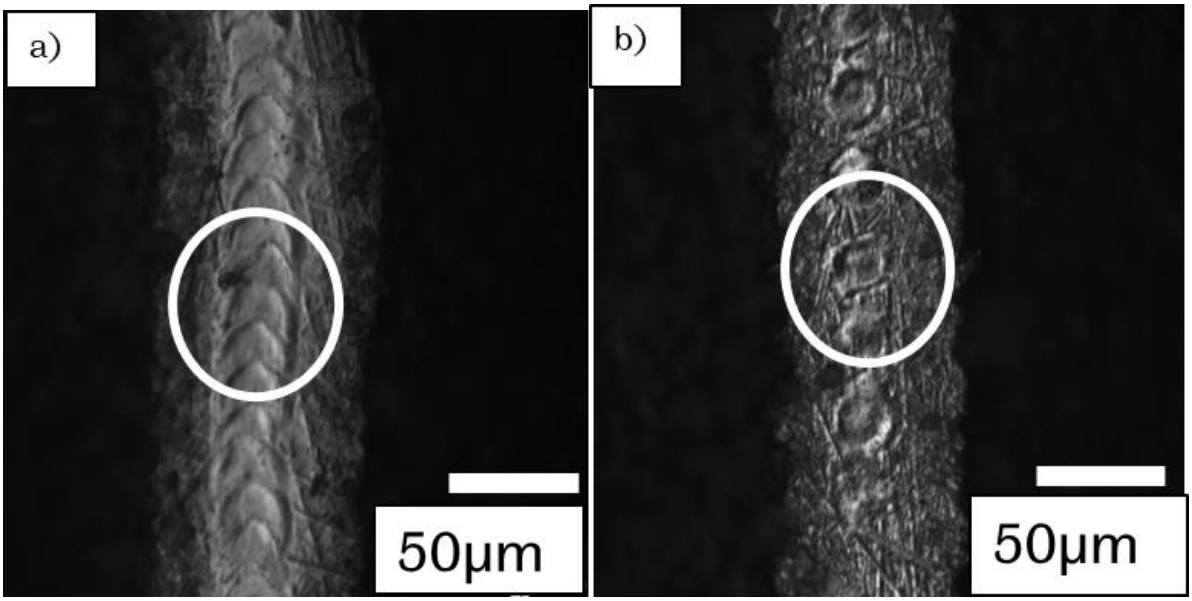

Figure 6-1 - These show the melt tracks used to measure the point distance accuracy on the Renishaw SLM125. a) shows a point distance of 10µm. The indents are made from each pulse and can be seen to interact with one another as the indent edges are drawn upwards (circled). b) shows a point distance of 30µm. The indents do not interact and are circular (circled).

Figure 6-1a was made using 10µm point spacing, whereas Figure 6-1b used a 30µm point spacing. There is more interaction between meltpools in Figure 6-1a as the meltpools are drawn upwards in the direction that the laser travelled. This teardrop shape contrasts Figure 6-1b, where the meltpools are circular. This morphology suggests that there is little to no interaction between the meltpools. The indents from the laser make measuring easier and more accurate as the middle of the pulse can be identified much more clearly than when a lower power had been used. A larger power would have caused the indents to be larger, and measurements between two adjacent pulses would have been less precise.

Point spacings of between 5µm and 90µm were measured. The error compared to the expected distance was plotted and shown in Figure 6-2.

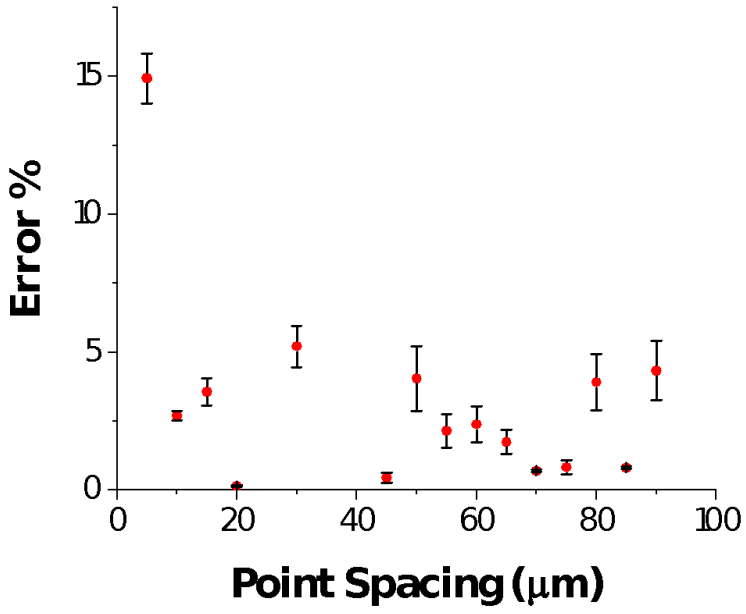

Figure 6-2 - This graph shows the error in the point distance output compared to the expected value. The error is constant at values of 10µm and higher. At these values, the error is <5%. Below this, the error jumps to 15%. This error is due to limitations in the scanner hardware, which makes this distance inaccurate.

From the graph, the error in point spacings is consistent in spacings over 10µm. The error is less than 5%. At 5µm, the error jumps to 15%. This error suggests that a limit has been reached. The error comes from the scanner accelerating and then decelerating to a stop by the next point. This graph shows that for spacings above 10µm, it is possible to achieve the separation, but a 5µm spacing cannot be achieved accurately.

An ideal point spacing cannot be defined from the results. However, spacings larger than 10µm are required. The constant relative error suggests that the cause of the error is consistent throughout the spacings and that the scanner can reach jump speed (target speed between points) before stopping at the next stop at spacings above 10µm.

The point distance parameter and the exposure time are unique to pulsed lasers, so this type of error is not found in continuous beam lasers. This error adds extra uncertainty and reduces the efficiency of these types of lasers. This drop in efficiency is due to the time taken to move between spots and for the laser to ramp up to full power. Laser ramp-up time and the amount of energy lost as a result are discussed in Section 6.4.

The errors in point distance were input in Freeman's Model [80]. The expected change in meltpool volume was plotted against the errors observed between the expected and measured point distances. These are plotted in Figure 6-3

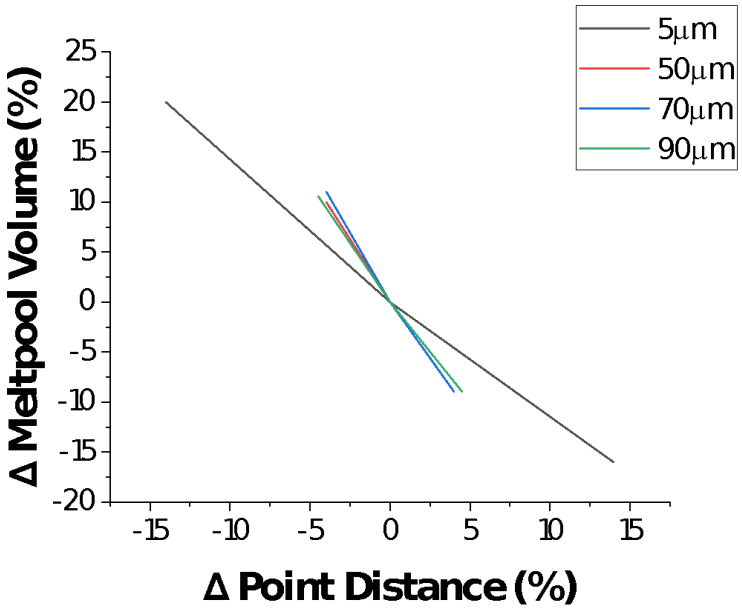

Figure 6-3 - A graph showing the effect that an error in the output point distance has on the resultant meltpool as simulated by Freeman's model. The errors in the output from the 10µm, 50µm, and 90µm point spacings result in similar changes in meltpool volume. The 5µm point distance has a higher output uncertainty (14%), resulting in the highest meltpool volume change of 20%.

The disproportionate effect that errors in point distance have on the meltpool can be seen from the figure. This effect can be seen in the 10µm, 50µm, and 90µm distances errors of approximately 5% result in volume changes of 10%. There is a consistent gradient across these inputs. The 5µm point distance creates the most significant % uncertainty in meltpool volume. This result is due to the uncertainty in the observed point distance being more

significant than for the other point distances. However, the meltpool volume is proportionately less affected by this error. The reduced effect could be due to the short distance and time between pulses as the laser has less distance to travel between points.

As part of the accuracy testing, the accuracy of hatch spacings was also investigated. This investigation was achieved by measuring the perpendicular distance between two adjacent hatches. Hatch spacings between 10µm and 160µm were measured. Figure 6-4a and b show hatch spacings of 20µm and 50µm, respectively. As with the point distances, the laser pulses have created small indentations. The horizontal distance between two spots was measured from the left hand most point of the indentations.

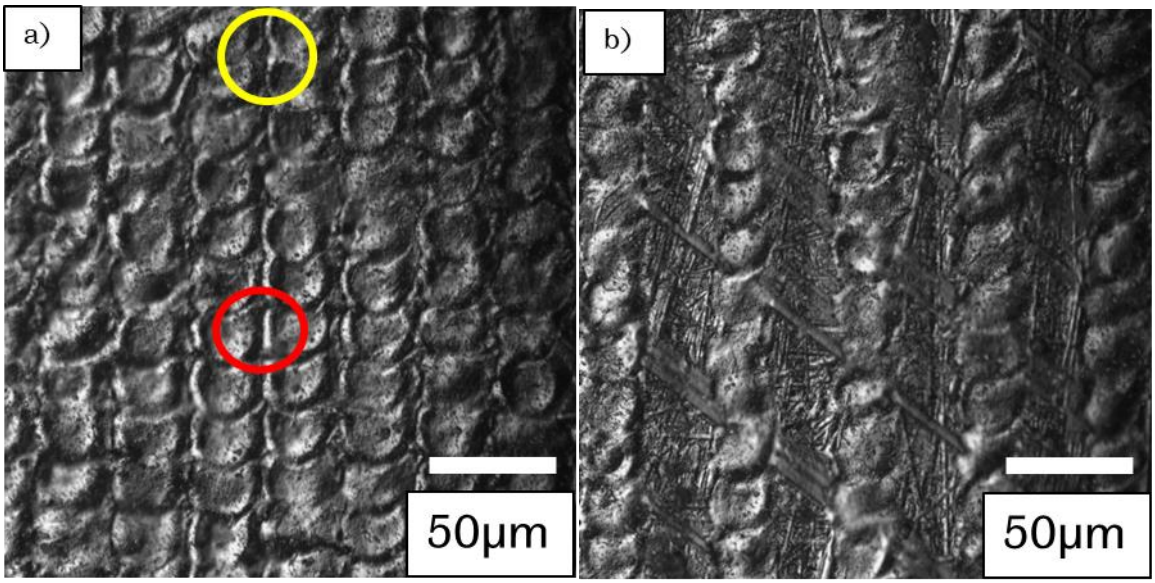

Figure 6-4 - Indents from the hatch spacing accuracy experiments. a) shows hatching of 20µm. The pulse indents can be seen to be parallel to each other in each column. This scanner behaviour leads to gaps in the indents (circled in red) and overlap (circled in yellow). These, in turn, may lead to defects forming due to underheating or overheating. b) shows a 50µm hatch spacing. The indents are still parallel, showing that this behaviour is intentional.

From the figures, the indentations are parallel to one another, and this is important as it could mean excess defects are formed. Lack of Fusion (LoF) defects are expected to form in the gaps between spots (circled in red) and keyhole defects in the overlap between spots (circled in yellow). The gaps occur as pulses are circular. In tessellating circles across a flat plane, there are areas of greater (circled in red on Figure 6-4) and lesser overlap (circled in yellow on Figure 6-4), leading to the potential for keyhole and LoF defects to form, respectively. In addition, the spots are in line with each other leading to overlaps and gaps between the pulses. An offset between adjacent hatches would reduce the regions of gaps and overlap.

The measured hatch distances were compared with the desired values, and the errors between these two values were plotted for each hatch distance in Figure 6-5.

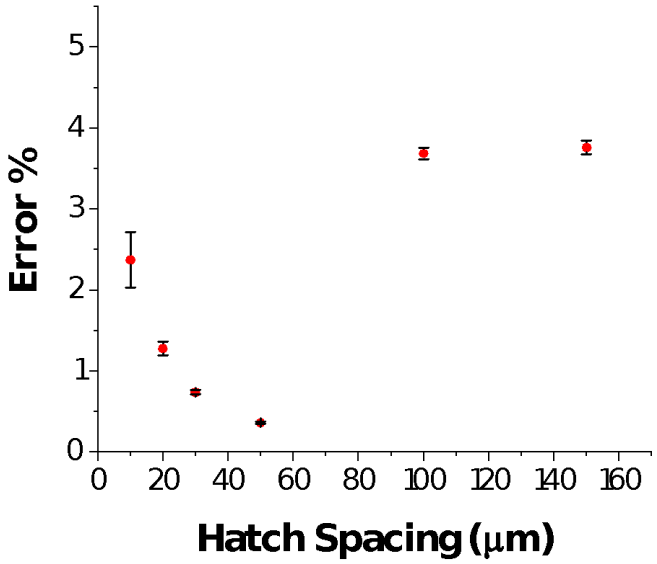

Figure 6-5 - Plot of error in the hatch distance when measured compared to expected. The error is lowest at 50μm but increases at low spacings due to the tight arc that the laser must trace to reach the next hatch (*Figure 6-8*) and high spacings as the distance travelled to reach the adjacent hatch is large.

There seems to be an ideal hatch distance from the figure, unlike point distance. This hatch distance is 50μm, which has an error of less than 0.5%. Overall the errors are less than those for the point distance, with all errors less than 4%. The uncertainty in these values is also smaller than for the point distance, which is understandable given that for a hatch to be accurate, it must maintain a straight line. In contrast, for a point, it must stop after a particular distance which is more difficult. This error is inherent within pulsed lasers and cannot be removed.

When the errors in hatch spacing are input into Freeman's model, they come up with only minor changes in meltpool of 0.003% for 10μm, 0.01% for 50μm and 0.44% for 100μm. This is shown in Figure 6-6 below.

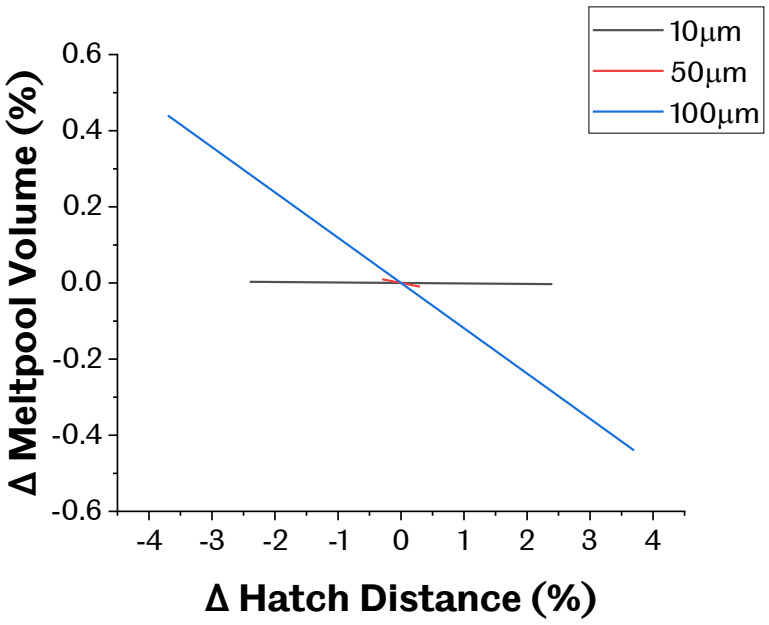

Figure 6-6 - A graph showing the potential variation in meltpool due to the error in hatch spacings on the Renishaw. The errors are low as there is a large return time before the laser interacts with the meltpool again. Due to this, the difference in thermal history within the upper and lower limits of hatch distance error is small. Even at large hatch distances of 100µm, the error is only 0.44%. The change in meltpool volume is even more minor for the smaller hatch distances.

This reduced effect can be attributed to the time taken for the laser to return for the subsequent hatch. This mechanism would cause the meltpool to change by a smaller percentage than the point distance for an equal output error.

The ideal hatch spacing can be explained by observing the ends of the hatches and how the laser turns around and lines up for the next hatch. Figure 6-8 shows this. The laser can be seen to take a wider arc as it lines up to the next hatch, similar to the line in a hairpin bend. This arc is much larger than the spacing for low hatches, but the arc is similar to the spacing for larger hatch spacings, so this is less of an issue. For larger hatch spacings, the error comes in the larger distance required to get to the next hatch, which increases the likelihood of an error in the distance between the two hatches. These two causes of error are at a minimum at 50µm hatch spacing.

As well as how the laser turns between hatches, how the laser approaches the first hatch was also investigated. Figure 6-7 shows this approach and the beginning of the hatch. The direction the laser approached is visible by the laser indents coming in from the right at an angle. These

four indents are premature firings of the laser and can be seen to get larger the closer to the start of the hatch that the laser gets.

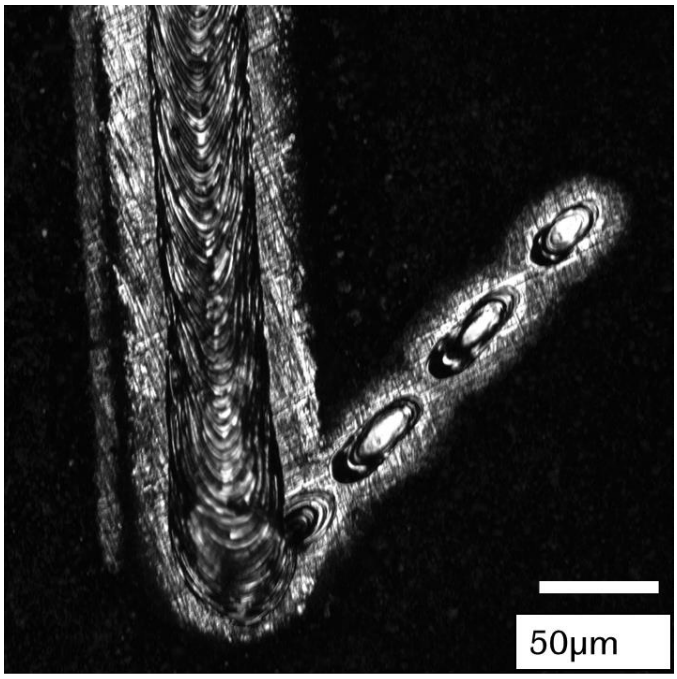

Figure 6-7 - At the start of a hatch, the laser turns on prematurely, creating progressively larger meltpools as it moves towards the first hatch. This behaviour is indicative of the laser scanner software not being adjusted for a pulsed laser as this ramping up is necessary on a continuous beam laser (Aconity) to make sure it is at full power for the start of the hatch and, as such, avoid LoF defects.

This ramp-up to full power is usually necessary in continuous beam machines in order to ensure that the laser is at full power when it starts the actual hatch and avoid lack of fusion defects. This ramp-up, however, is unnecessary for a pulsed laser as it turns on and off with each pulse. This indent suggests an issue in the laser and scanner software which makes it act as if it was a continuous laser machine. The Renishaw 125 was the first SLM machine from Renishaw, so this peculiarity could not have been discovered before it was manufactured. This problem is also found in the ends of hatches as the laser turns around (Figure 6-8). The laser turns off as it ends a hatch before turning around and returning for the next one. This behaviour is necessary for continuous beam lasers and this machine to reduce excess heat input and the chance of keyhole defects forming due to the short time between one hatch ending and another beginning. However, the laser continues to fire as it turns around the corner, which is unnecessary. The laser should turn on for the first pulse at the start of the hatch.

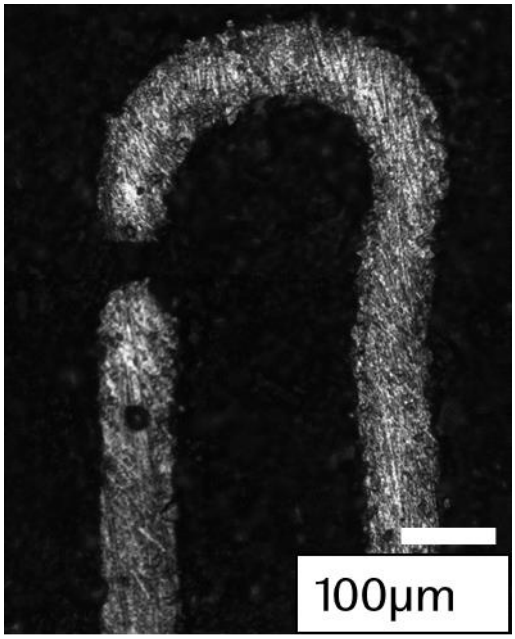

Figure 6-8 - This shows how the laser behaves between hatches. It turns off in order to reduce overheating due to the short time between the end of one hatch and the beginning of another. It turns back on as it travels a wider arc than the hatch spacing round to start the next hatch. The turning on as it turns around suggests that the software has not been altered for use on a pulsed laser compared to a continuous one.

The effect of focus offset on the width of the weld track was measured. Using the parameters in Table 6-2. The weld tracks were imaged using the Clemex Microscope, and Figure 6-9 shows the 2mm focus offset weld track.

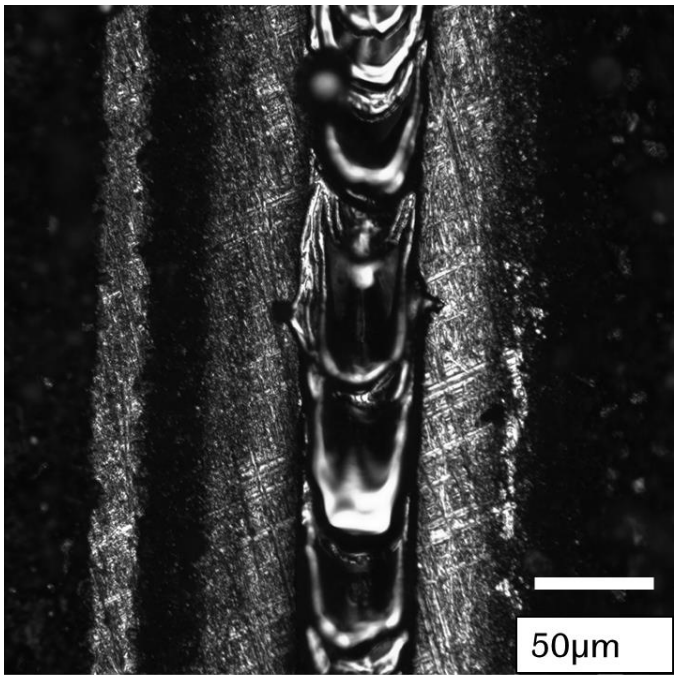

Figure 6-9 - Weld track used to measure the effect of focus offset. The measure for melt width was taken from where the laser had burnt the paint on each side. This distance was chosen as it was clearly defined, and there was less error in readings than the interior melt width.

The indent in the middle is surrounded by exposed substrate where the laser burnt the blackboard paint. This exposed distance was measured to measure melt width, as it represented the region affected by the laser. This distance was chosen as there was less variability in readings, and it was identifiable. Tracks with focus offsets between 0 and 5mm were measured, and the results are plotted in Figure 6-10 below

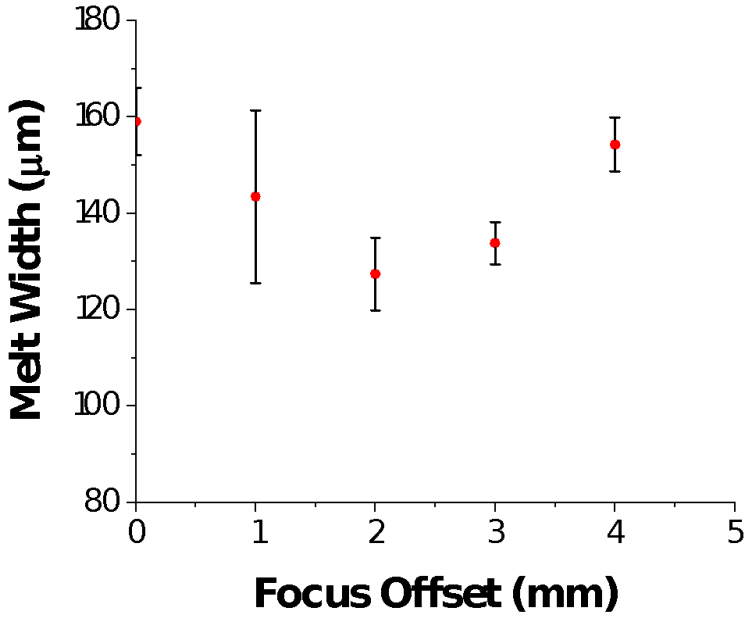

Figure 6-10 - This graph shows the change in melt width with focus offset. The lowest melt width comes at a focus offset of 2mm, suggesting this is the most in-focus beam. The focus point on the machine has changed since its last calibration.

The graph shows the melt width decreasing between 0mm and 2mm before increasing up to 5mm. This graph suggests that the focal point is directly on the substrate at a focus offset of 2mm. The reason for this deviation could be due to the machine being moved since it was last calibrated or that it had not been appropriately calibrated since the laser and scanner system had to be replaced, which happened shortly before these tests were performed.

The uncertainty in the readings comes from determining which width to measure. Though different measurements could have been taken, the objective of this experiment was to find the focal point and to see the effect that changing the focus offset has on beam width relative to the focal point.

As a result of the accuracy tests, a range of possible point spacings as well as an ideal hatch spacing were determined. The uncertainties associated with particular spacings were also quantified. The laser path between hatches was identified. Finally, the true focal point for the laser was determined to be 2mm. As a result, for later experiments in this chapter, the focus offset was adjusted such that the focal point was at 0mm. This new 0mm focus point was used in later experiments such that this 0mm focus would make the focal point on the top of the powder layer to be melted.

6.2.2 Aconity Laser and Scanner Accuracy

On the AconityMini machines, the hatch distance accuracy was measured similarly to that of the Renishaw. A single layer build file with 10mm squares of varying hatch lengths was created. The parameters for these build files are given in Table 6-3.

Table 6-3 - Input parameters for the AconityMini scanner hatch spacing accuracy experiment.

Power (W)	40
Velocity (m/s)	1.125
Hatch Spacing (µm)	10-200

These parameters were lased onto a fresh baseplate sprayed with black chalkboard paint to highlight the markings made by the laser. The observed difference between the inputted and observed hatch distance was measured using images from the CLEMEX microscope. The error between these two values was plotted against hatch distance. This was compared to the error found on the Renshaw to highlight discrepancies between the machines.

As with the Renishaw, the ends of hatches were investigated to see how the laser responds with changing direction.

In this set of experiments, the accuracy of the laser scanner system within the AconityMini machine was tested. The ends of hatches were imaged to identify how the system turns around for the next hatch.

Figure 6-11 shows hatches melted into a substrate. These hatches were imaged and analysed using the Clemex microscope.

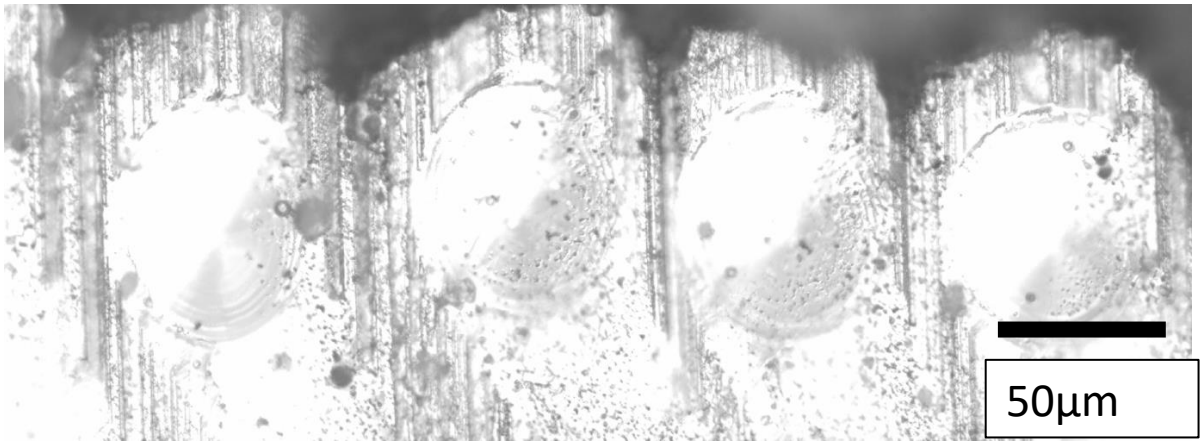

Figure 6-11 - Micrograph of the accuracy test hatches made on the Aconity. The perpendicular distance between the centres of the hatches was measured. The circular meltpool at the end of hatches occurs when the laser turns around, and so the distance between adjacent circular pools is twice the hatch spacing.

The hatch distance was measured by calculating the perpendicular distance between two hatches. The indents at the hatch ends occur when the laser turns around. The hatch distance can be found by measuring the distance between the midpoint of these indents and dividing by two.

These distances were compared to the expected values as with the Renishaw. The errors were plotted as shown in Figure 6-12.

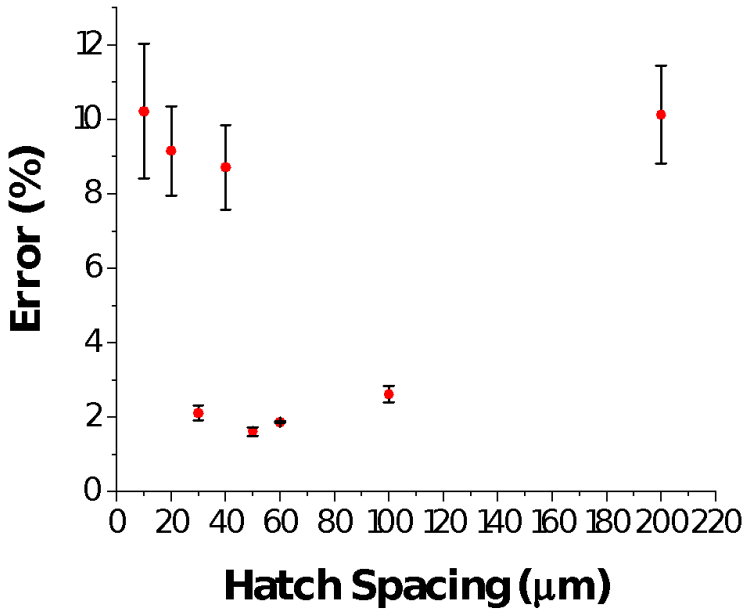

Figure 6-12 - This graph shows the results of the hatch accuracy tests. The error in measured compared to expected values is plotted. Like the Renishaw, there is a hatch spacing that results in the lowest error, and this is at 50µm. Overall the error in hatch spacings is higher than for the Renishaw as the laser is constantly moving.

Overall the errors are larger than with the Renishaw. The error can reach upwards of 10%, whilst the lowest is 1.8%. This increased error can be explained by the continuous beam constantly moving, whereas the pulsed laser stops at each point. This slower movement and the stopping allows the scanner to be more accurate. As with the Renishaw, there is an ideal hatch distance of around 50µm. This error will cause an increase in the variability of the thermal history within the part. Further experiments are required to determine whether this error is consistent across different beam velocities.

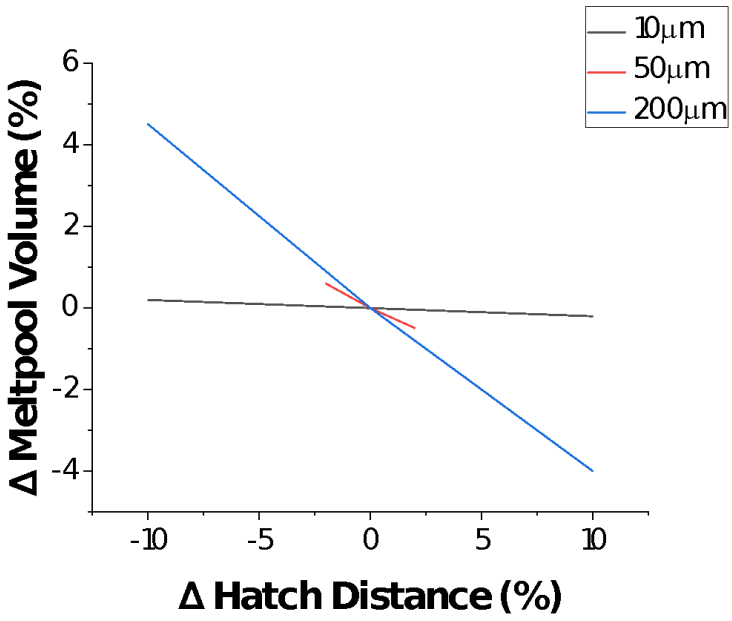

Figure 6-13 - A graph showing the potential variation in meltpool due to the error in hatch spacings on the AconityMini. The errors are higher than for the Renishaw. Due to this, the difference in thermal history within the upper and lower limits of hatch distance error is small. Even at large hatch distances of 100µm, the error is only 0.44%. The change in meltpool volume is even smaller for the smaller hatch distances.

The ends of hatches were then investigated to identify the scanner behaviour at the turning point. Figure 6-14 shows the indent created as the laser turns around.

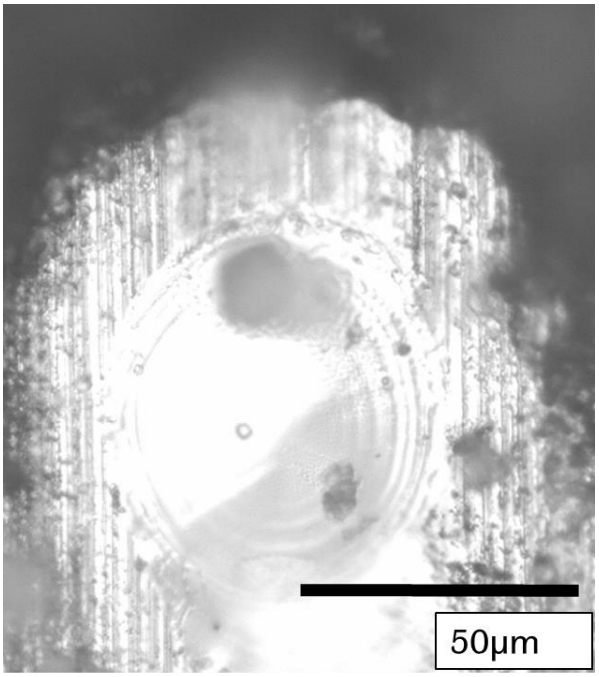

Figure 6-14 - An enlarged view of the end of a hatch. This deeper meltpool is caused by the short return time as the laser turns around. This deep meltpool is usually remedied by the machine lowering the laser power at the ends of hatches. These "skywriting" parameters need to be optimised in further experiments. Without adjusting these parameters overheating will occur at these edges, and keyhole defects are more likely to occur.

This keyholing occurs as the return time is so short that the meltpool does not have enough time to cool, so the meltpool is deeper. The scan strategy does not account for this in the way that the Renishaw does. It needs to reduce the power as it reaches the end of the hatch and increase the power as it comes back to start the next hatch. This reduction in power would avoid the chance of keyholing. This control of the scanner at the ends of hatches and between hatches is called skywriting. This skywriting has not been altered as it requires further experimentation to ascertain the best skywriting parameters. Depending on the beam's velocity, power, and hatch spacing, these parameters will change. Without this correction, there is increased thermal history variability depending on where in the part the region under investigation is.

6.3 Laser Parameters Study

6.3.1 Methods

The effect of focus offset was investigated by keeping the exposure time and point distance constant and varying the power and focus offset. The parameters are outlined in Table 6-4 below.

Table 6-4 - These parameter ranges are for the melt tracks to establish the effect of power and focus offset on the ability of the Renishaw pulsed laser to melt bulk Haynes 282.

Power (W)	110-190
Focus Offset (mm)	0-8
Point Distance (µm)	45
Exposure Time (µs)	40
Hatch Distance (mm)	2

These weld tracks were performed on a bulk Haynes 282 sample to observe the specific effect on this alloy. The weld tracks were first measured using the CLEMEX Optical Microscope from above. A cross-section perpendicular to the build direction was taken, and the depth and shape of the weld tracks were investigated. The widths and depths at specific focus offsets and powers were plotted.

In combination with this, a similar study on the AconityMini was conducted, weld tracks were lased onto a bulk Haynes 282 sample at 2mm intervals. The parameter ranges investigated are shown in Table 6-5 below.

Table 6-5 - These parameter ranges are for the melt tracks to establish the effect of power and focus offset on the ability of the AconityMini continuous laser to melt bulk Haynes 282.

Power (W)	110-190
Velocity (m/s)	1.125
Focus Offset (mm)	0-8

The tops of these weld tracks were again imaged, and the width measured. A cross-section of the weld tracks was taken, and their depths were also measured. These widths and depths were plotted for each parameter set, and the results were compared with the Renishaw tracks. This comparison formed the basis of an attempt to convert between the two machines interchangeably.

6.3.2 Results

The perpendicular cross-sections created as a result of the weld tracks are shown in Figure 6-15

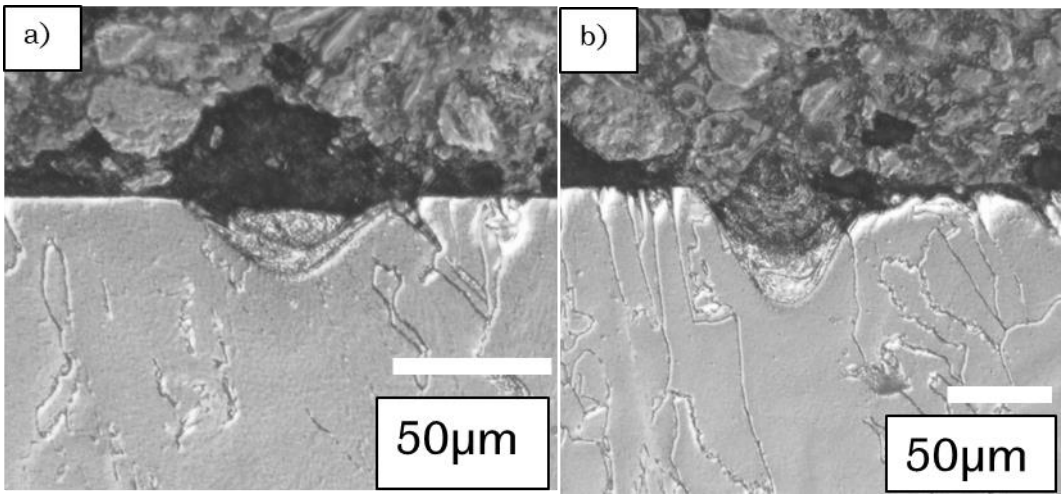

Figure 6-15 - These are cross-sections of the melt tracks. a) shows the 130W, 0mm offset track. The melt pool is u-shaped and, as such, in conduction mode. b) was made using 190W at 0mm offset. This higher energy has resulted in a much deeper meltpool but only a slightly wider meltpool. This micrograph suggests that this is on the limit of transitioning to keyhole mode melting.

Figure 6-15a on the left is 130W with 0mm offset and Figure 6-15b on the right is 190W with 0mm offset. Figure 6-15a shows a conduction mode melting and a u-shaped meltpool, and Figure 6-15b shows a deeper meltpool that is potentially on the verge of keyholing. The depths of these meltpools are shown in Figure 6-16 below.

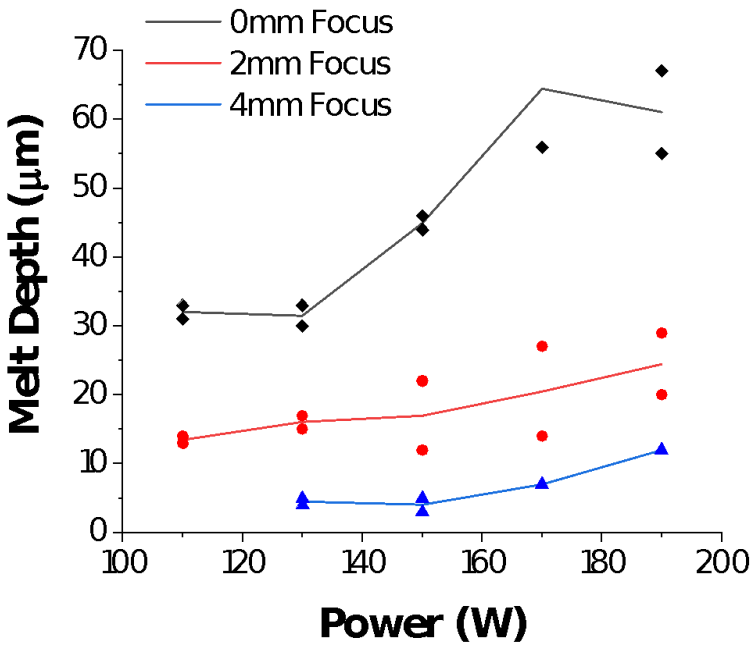

Figure 6-16 - This graph plots the recorded melt depths for the weld tracks. 0mm focus offset results in the largest depth. Although 8mm offset weld tracks were performed, no depths were recordable. For the others, the depths increase gradually. 0mm does decrease slightly at the end, indicating transition mode melting. Higher powers (above what the laser is capable of) would be needed to ascertain if this is the case.

From the figure, a larger power results in a deeper meltpool with the 0mm focus, seeing a large increase in depth as the power increases. There is a slight decrease in depth at 190W, which could signify that the laser has started melting in the transition mode between conduction and keyholing. Unfortunately, the laser used was 200W, so further experiments at higher powers are not possible on this machine. For the other focus offsets, the increase in depth is not as large as they have a larger melt width (see Figure 6-17) and are melting a larger volume. Within the 4mm offsets, a measurable depth was not found for the 110W track. This lack of measurement was the case with all the powers at 8mm focus offset. This lack of indent shows a critical level of energy density that is not reached as the beam is too diffuse and it has not reached the threshold to melt the Haynes 282 alloy.

Figure 6-17 shows how the melt width changes with power and focus offset. The graph shows that the width of the 2mm focus offset is generally higher than that of the 0mm. This width is due to the more diffuse beam. With the 4mm beam, the width starts low and quickly rises to

be equal to that of the 2mm beam at 190 due to the beam being too diffuse to melt the width of the beam at low powers. If the power were to increase, the width would be higher than that of the 2mm offset. The 8mm offset does not register any melt width, as was the case with the depths.

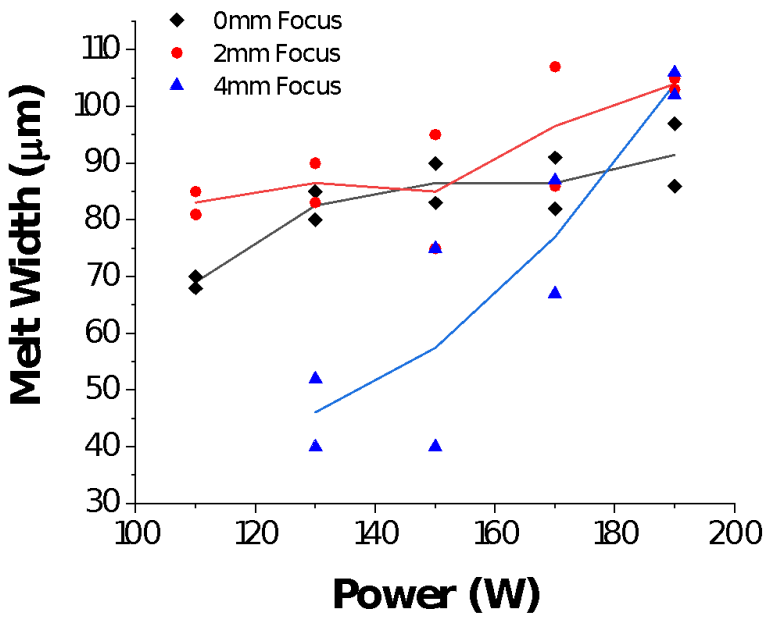

Figure 6-17 - This plot shows the widths of the melt pools. 2mm offset is generally larger than 0mm which is consistent with a more diffuse beam. 4mm offset starts off small but then get larger very quickly. The beam is too diffuse to melt the whole beam widths at the lower powers.

These experiments give an understanding of how the laser interacts with the bulk Haynes 282 alloy at a representative speed. The depths and widths at the powers will be used in a further experiment to convert between two machines; one pulsed one continuous. The results of this experiment are outlined in Section 6.5.

The same experiment was conducted on the AconityMini as on the Renishaw to examine the effect of changing power and focus offset on the width and depth of weld tracks lased onto bulk Haynes 282. A constant velocity of 1.125m/s was used, the same as the equivalent speed used in the Renishaw experiments. In Figure 6-18, the meltpools for the weld tracks are shown

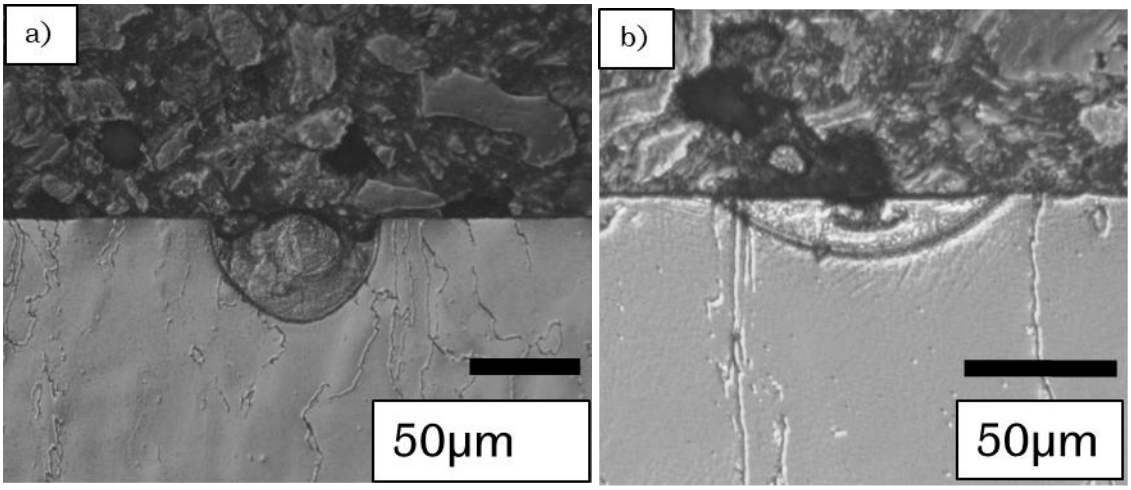

Figure 6-18 - These are melt track cross-sections. a) shows the 170W 0mm offset. The beam power is more evenly distributed than for the Renishaw as the edges of the meltpool are convex instead of concave. b) shows the 150W 4mm offset meltpool. The melt width is larger because the beam is more diffuse, and the edge is convex, showing an evenly distributed power within the beam.

Figure 6-18a shows the 170W at 0mm focus offset, and Figure 6-18b shows the 150W at 4mm. Figure 6-18a shows a u-shape. Compared to the Renishaw meltpool of Figure 6-15a, the meltpool is less concentrated in the middle, but the drop off on the edges is larger. Looking at the figures, the Renishaw and the AconityMini have concave edges. For Figure 6-18b, the diffuse beam is obvious due to the larger width, but the meltpool has an even convex curved edge which means the beam is still evenly spreading the power whilst being diffuse. Figure 6-18a displays no keyholing despite more input power. The beam is always on, so there is a gradual temperature change as the laser moves towards and away from the spot. The beam creates a more consistent thermal history than the pulsed laser, where the power is ramped up or down for each exposure.

The widths and depths of these meltpools were measured and then plotted in Figure 6-19 and Figure 6-20.

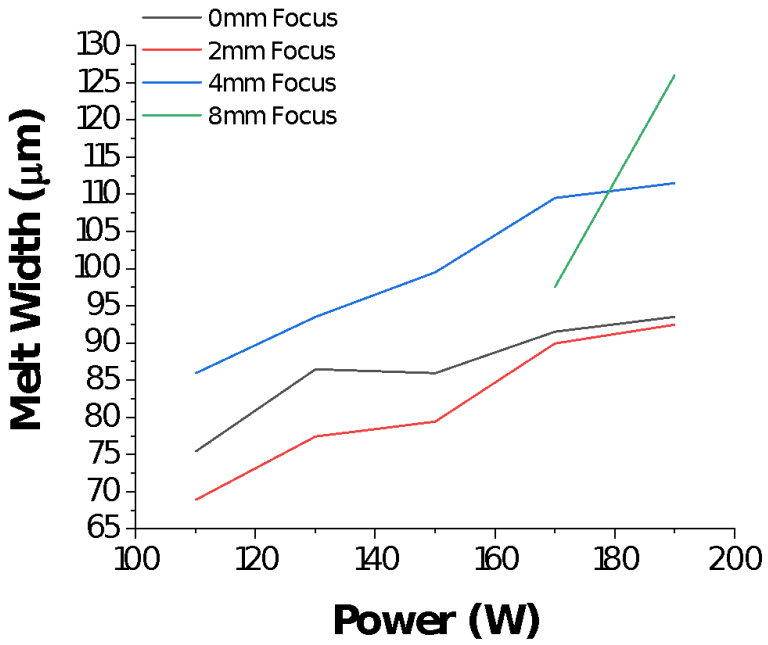

Figure 6-19 shows how the melt width changes with power and focus offset on the Aconity. 2mm has the lowest width, indicating that it is the most focused. The focus point has changed due to the machine being moved since the last major calibration. 4mm produces meltpools at all powers, and 8mm produces pools at the two highest, showing that more energy is transferred to the bulk than with the pulsed laser. By 190W, the full width of the 8mm beam is being utilised as this results in the widest meltpool.

Figure 6-19 shows that the widths are consistently getting larger with higher powers, suggesting that keyhole mode melting has not yet occurred. 2mm focus offset has consistently the smallest width suggesting that just like the Renishaw, the focal point is on the surface of the substrate closer to 2mm than to 0mm. This different value may have occurred as the machine has been moved several times since it was first installed, and the focus tests that were performed to recommission the machine were not as accurate as required. The machine has subsequently been moved to a permanent location, so melt depths will be used to ensure that the machine is calibrated accurately.

The 8mm test resulted in meltpools being measurable at only 170W and 190W. As with the Renishaw, the beam starts narrow and gets wide quickly at 190W as it utilises the full width of the beam. The beam widths for the AconityMini are in general higher than for the Renishaw. For the low offsets, this is due to the Renishaw being more in focus, but for the larger focus offsets, the beam power is more evenly spread enables it to melt a larger volume.

Figure 6-20 shows the melt depths for the parameter sets.

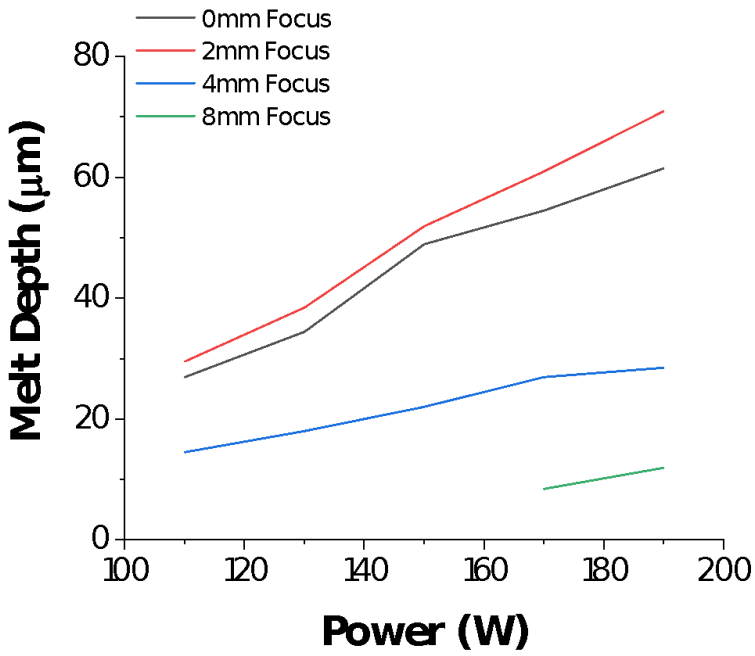

Figure 6-20 - The melt depths at the powers and focus offsets are plotted on this graph. 2mm has the deepest meltpools, which confirms that it is the most in focus. All the depths increase at a constant rate with no sudden increase suggesting that keyhole mode melting has not been reached.

The depths increase gradually as with the widths, confirming that only conduction mode melting has occurred. A focus offset of 2mm achieves the deepest meltpools, which suggests that this beam is more focused than the 0mm offset. The depths of the AconityMini parameters are deeper than for the Renishaw. There is a recorded depth for parameters at 8mm offset where there was not one on the Renishaw. This lack of indent is due to the duty cycle, the proportion of time that the laser takes to get to full power using a pulsed laser. The difference in depths is small for the lower powers, but the difference in melt depths between the two machines gets greater as the powers get larger. This result is because a greater proportion of the energy input is lost ramping up to the higher powers.

These weld tracks have helped map out the laser's effect on the bulk by using these depths and widths to compare the two systems. There are parameter sets where the widths and depths are the same, and in Section 6.5 these will be used to try and convert parameter sets between the two machines.

6.4 Laser Ramp-Up and Keyholing

An experiment into keyholing and the time taken for the laser to ramp up to full power was performed. As the laser turns on and then off for each point, the laser is not at full power for the whole of the exposure time. To find the melting mode weld tracks with parameters listed in Table 6-6 were performed and investigated in cross-section.

Table 6-6 - Parameters used to investigate the transition from conduction mode to keyhole mode melting.

Power (W)	190
Point Distance (µm)	10
Exposure Time (µs)	20-180

The exposure time was varied between 20µs and 180µs to observe the transition from conduction mode melting to keyholing. The polished surface of the bulk Haynes 282 sample was etched using glyceregia, and the width and depth of each meltpool for a specific exposure time was measured. The gradients were measured to see the effect of keyholing on the depth of the meltpool as well as the X-axis intercept, to see the relative energy loss in equivalent exposure time as the laser ramps up to full power.

A critical aspect of laser interaction with any alloy or machine's powder and bulk material is the transition from conduction to keyhole melting. This is critical due to the potential appearance of keyhole defects if keyhole mode melting occurs.

The weld tracks were made using the parameters in Table 6-6, and perpendicular cross-sections were taken. Figure 6-21 shows the cross-sections for 40µs (left) and 180µs (right).

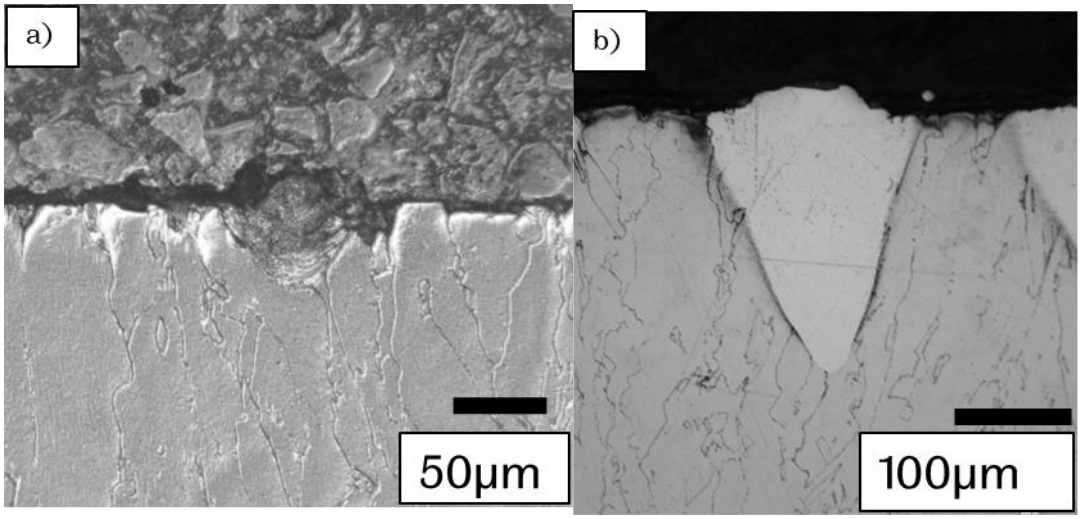

Figure 6-21 - These micrographs show the meltpools from the weld tracks. a) shows a meltpool in conduction mode melting with a u-shape. b) shows a keyhole mode meltpool. The depth is much larger than the width, forming a V-shaped pool.

The difference between these two images shows the transition from conduction mode melting to keyhole melting. The images show the shape of the meltpool changing from a u-shape in Figure 6-21a to a V-shape in Figure 6-21b. This meltpool shape is due to the keyhole melting phenomena outlined in Section 1.8. The laser reflects within a cavity formed in the meltpool, which causes the meltpool depth to increase faster than the width. Despite keyholing, there is no characteristic keyhole defect at the bottom of the meltpool. The widths and overall melt areas are plotted in Figure 6-22 and Figure 6-23 below.

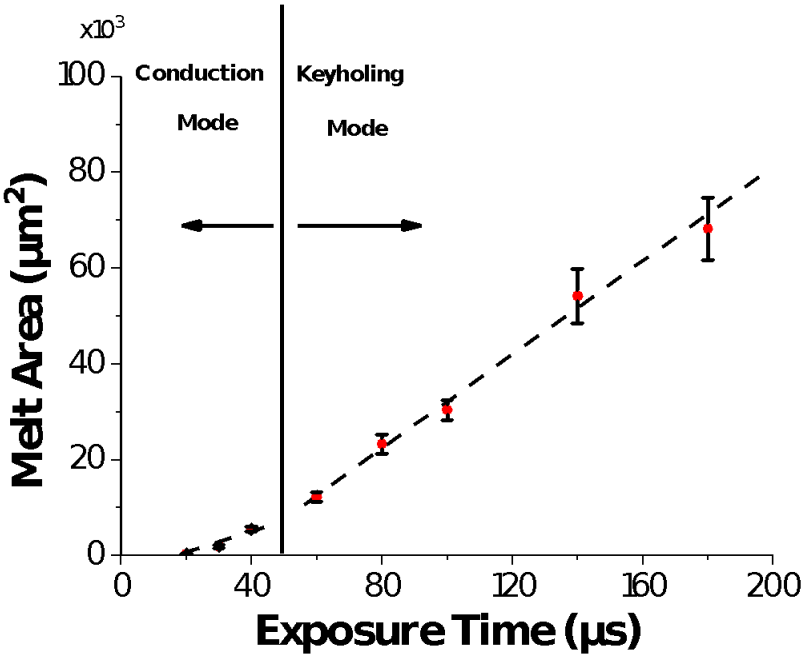

Figure 6-22 - This is the plotted melt area against exposure time, showing two clear regions with different gradients. To the left with a shallower gradient is the conduction mode, and to the right with a steeper gradient is keyhole mode. The steeper gradient occurs as the keyhole cavity traps the laser and causes it to absorb more of the laser's power, driving the meltpool deeper and increasing the melt area.

There is a distinction between the gradients of the two regions with the melt area. To the left, the gradient is shallower, representing conduction mode as the laser reflects only off the surface of the meltpool. So, absorption of the laser power is only achieved through the top surface. At 60µs exposure and above keyhole melting occurs. At this point, a cavity is formed in which the laser reflects off the walls causing more power to be absorbed and the meltpool to grow in the vertical direction. As the melt area grows, the error grows as the absorption process is not exact, and the size of the cavity formed will affect the depth of the meltpool.

Figure 6-23 shows the melt width at different exposure times. This figure shows the opposite relationship where conduction mode causes the width to increase faster as it transitions into keyhole melting. The width increases slower as more of the laser's energy is spent increasing the meltpool in the vertical direction instead of the horizontal one.

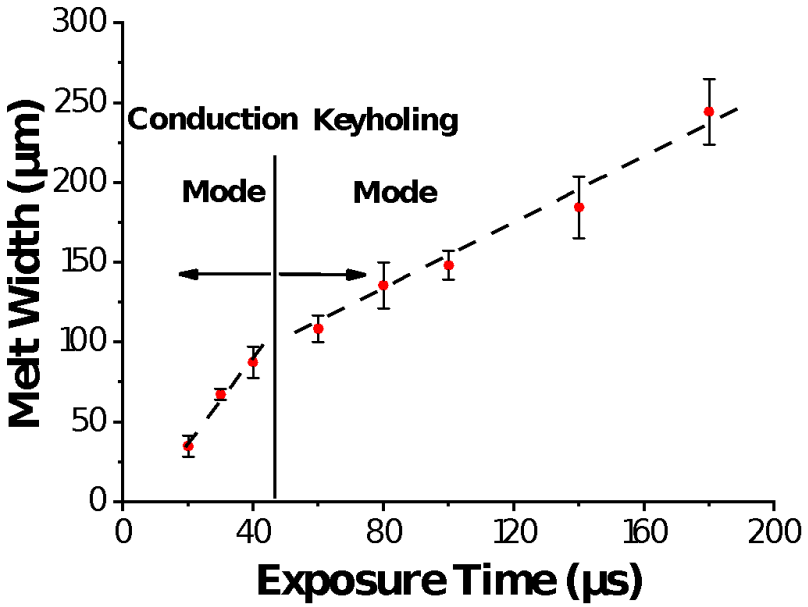

Figure 6-23 - The reverse relationship can be seen in this graph. As the melting mode transitions to keyholing, the width increase reduces as keyholing causes the depth of the meltpool to increase much more rapidly. The trend line for the conduction mode melt width and melt area (*Figure 6-22*) shows that the average x-axis intercept is the effective energy loss, approximately 10-15µs.

The error increases with the exposure time as the melting process becomes more complex and uncertain with the melt area. One common feature across the area and width is an x-intercept greater than 0. This is energy lost. Due to the nature of the pulsed laser, it must ramp up to full power for each pulse. This means there is lost energy as it ramps up to full power. From the graphs, this energy loss is equivalent to around 10-15µs at 190W. This loss will be less for lower powers as it will take less time to reach these levels. For low exposures, this loss can be significant. The lowest exposure which can be set within the software is 20µs. An experiment was conducted in which the ramp-up time's effect on the meltpool volume was tested. Freeman's [80] meltpool model was run before and after the ramp-up time had been considered. The change in meltpool volume is noted in Table 6-7

Table 6-7 - This table depicts the calculated loss in meltpool volume due to the ramp-up to full power. These values were calculated using Freeman's [80] meltpool model.

Exposure Time (µs)	Δ Meltpool Volume (%)
20	76
50	49
80	22
100	21

With the lost energy, only between 24% and 79% of the expected power is used to melt the material. As the exposure time increases, this equivalent lost energy gets proportionally less. This result shows there is some benefit to increasing the exposure time to avoid the excess LoF defects that may appear due to the lower exposure times being more affected by the ramp up time. The duty cycle is the difference between the expected energy input and the actual energy input. It must be considered when comparing parameter sets between pulsed and continuous machines. The pulsing also causes a different thermal history between pulsed and continuous lasers. The sudden drop in power resulting from the laser being turned off and the sudden increase when it is turned on caused a difference in thermal history when considering the two lasers types. This difference in thermal history was accounted for when the experiment to convert equivalent parameters and build qualities across the two machines was conducted. For the conversion builds, a 40µs exposure was used as this was the highest exposure time that did not result in keyholing.

6.5 Inter-Machine Conversion

The results of both machine characterisations were compared, and there were parameter sets that gave similarly shaped meltpools. Four different parameters sets for each machine were chosen, and these varied in meltpool size. One set gave a small meltpool region, two a medium-sized one and an additional set that resulted in a large melt region.

Table 6-8 - These parameters are those chosen from the parameter studies that had meltpool dimensions most similar to each other. 11mm cuboids were built using these parameters, and the resulting build quality from each set was compared to the equivalent set on the other machine.

Machine	Power (W)	Velocity (m/s)	Focus Offset (mm)	Hatch Distance (µm)	Point Distance (D) (µm)	Exposure Time (t) (µs)	Specimen ID
Renishaw	130	-	0	35	45	40	R130
AconityMini	130	1.125	0	35	-	-	AM130
Renishaw	150	-	0	35	45	40	R150
AconityMini	150	1.125	0	35	-	-	AM150-0
Renishaw	110	-	0	35	45	40	R110
AconityMini	110	1.125	2	35	-	-	AM110
Renishaw	170	-	2	35	45	40	R170
AconityMini	150	1.125	4	35	-	-	AM150-4

11mm cuboids of height 8mm were built on both machines. Three repeats of each parameter set were built on each machine for a total of 12 parts per build. To maintain the same building conditions across each machine, the time taken for the Renishaw to build a layer was measured, and the AconityMini was forced to take the same amount of time. The oxygen content was kept below 1000ppm between the two builds and maintained the same build layout and positioning as much as possible between the two machines. This constant build

layout was done using the same software (Netfabb) to define the laser paths and divide the part into slices for both builds. Once the builds had been performed, the parts were extracted and then removed from the baseplate using EDM. A cross-section in the XY plane was taken, and the surface polished. The porosity for each parameter set was then measured using ImageJ software from images taken using the CLEMEX Optical Microscope. These porosities were then plotted to find equivalence between the two machines.

This experiment was to see if the parameter sets that resulted in the most similar meltpools resulted in similar quality builds when applied to parts. Of the four sets, one had a smaller depth, two had a medium depth, and one had a larger depth. The parameters were used to build 10mm cubes, and the XY cross-sections are shown in Figure 6-24, Figure 6-26, Figure 6-28, and Figure 6-29.

Figure 6-24 and Figure 6-26 shows the cross-section from the Renishaw builds, and Figure 6-24 is the densest of the samples. This is R170.

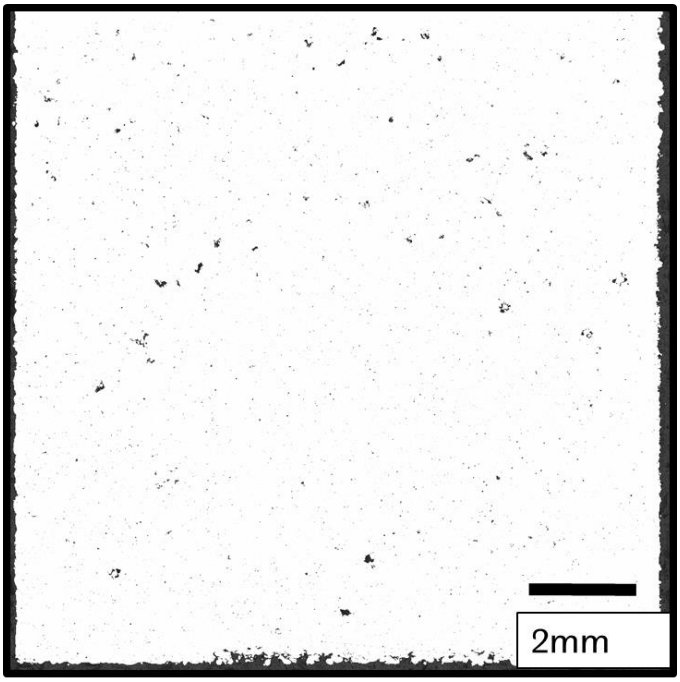

Figure 6-24 - The XY cross-section of R170. Whilst this build resulted in the best relative density; there are a few LoF defects and many gas pores. This porosity is due to the volatile nature of the pulsed laser meltpool, which ejects powder from the meltpool and causes voids to form. The melt depth from the bulk track experiments suggested that these parameters would be enough to create a fully consolidated part. However, the interaction between laser and powder results in smaller meltpools due to the air gaps between powder particles reducing heat transfer.

This sample has a few LoF defects characterised by a low circularity (high perimeter to area ratio) and large size. There are also gas porosity defects identifiable by their circularity and small area. These defects have caused the density to drop below the level of fully dense. The

gas porosity is caused by the laser pulses ejecting powder from the meltpool, causing pores to form. Powder particles being ejected from the meltpool was found to be an issue when a high framerate video (Figure 6-25) of the meltpool was taken.

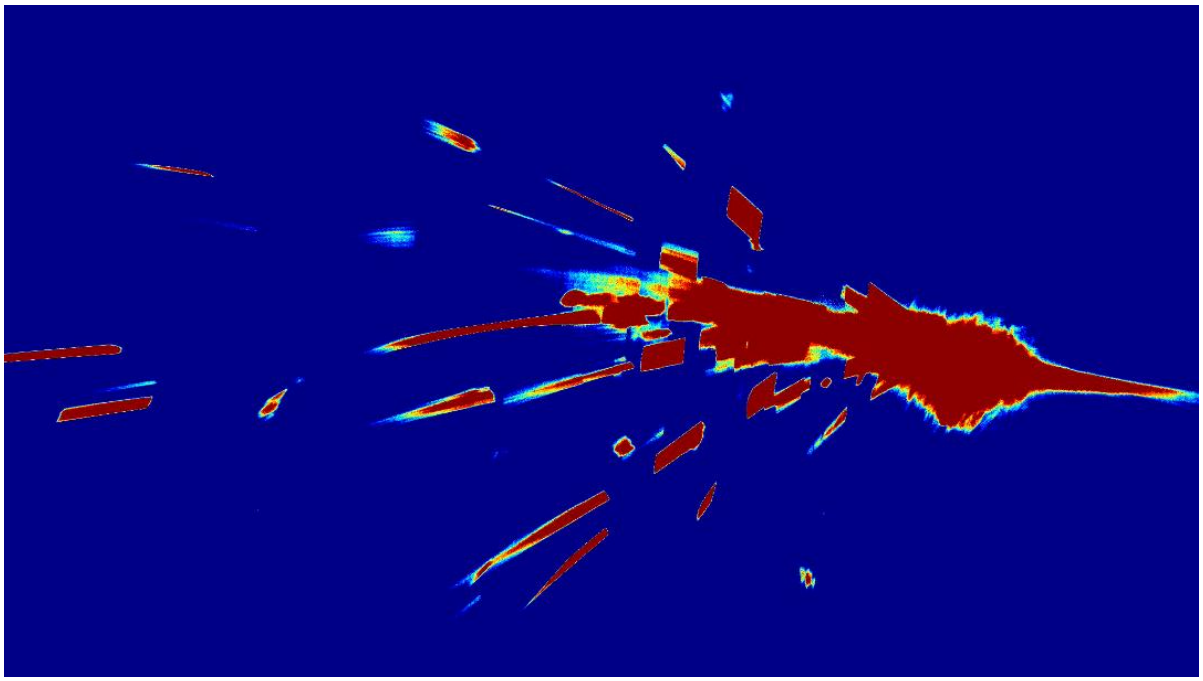

Figure 6-25 - High framerate video of the meltpool the spatter has been distinguished from the background due to its higher temperature. Large powder particles can be seen being ejected from the meltpool.

In this video, large powder particles can be seen to be ejected from the meltpool in all directions. Figure 6-28 shows that using the same powder results in fewer gas pores confirming that the pulsed nature of the laser is causing these excess gas pores.

Figure 6-26 shows the least dense part. This is R110.

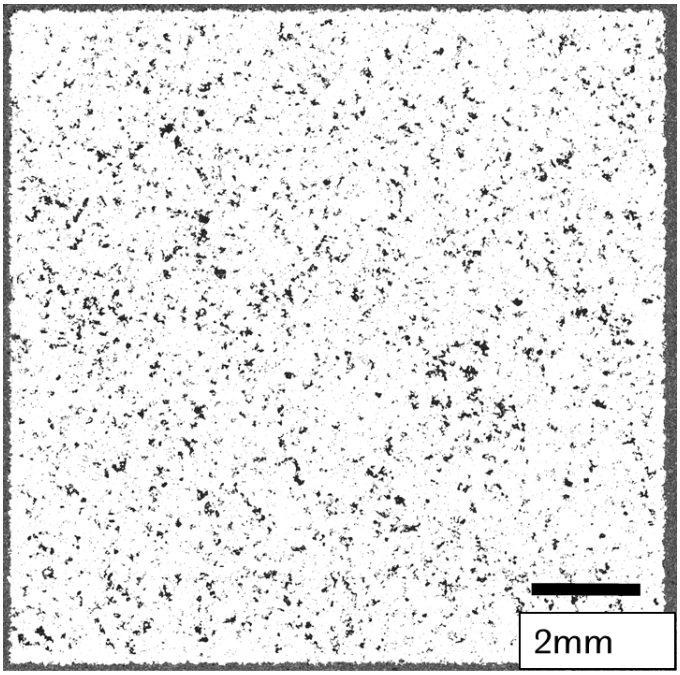

Figure 6-26 - This cross-section is R110. There is massive LoF characterised by large irregularly shaped voids, and there are also gas pores between the LoF voids suggesting that the same volatile meltpool dynamics are present in this build as with the 170W build.

From the figure, massive amounts of LoF defects can be observed. These defects have caused a sharp drop in the relative density. Gas porosity is still an issue as small circular pores can be seen between the LoF defects. The defects come from the laser powder interaction, and the gas pores are formed for the same reason as outlined in the previous figure. The LoF defects are due to the meltpool not being deep enough.

Both parameter sets have not performed as expected. For the R170, the melt depth should have been enough to create a fully dense part especially given that only one weld track was melted. With multiple weld tracks next to each other, they would have interacted thermally to create a deeper meltpool. Whilst more defects were expected in the r110 as the meltpool was shallower, the number of defects was unexpected.

The discrepancy is due to different interactions between laser and powder than between laser and bulk material. The powder does not conduct the heat between the particles as there is gas between the powder particles, whereas the bulk is solid. The laser and powder interaction results in a lower meltpool depth and a higher chance of LoF defects.

The densities for all the parameter sets are plotted in Figure 6-27.

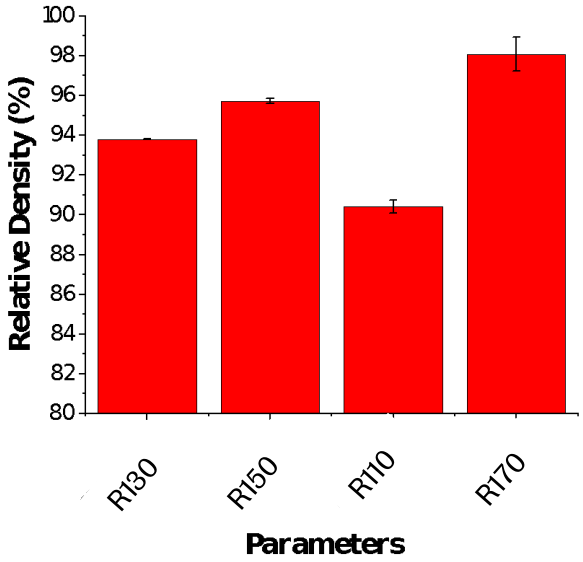

Figure 6-27 - The relative densities from the Renishaw builds are plotted in this graph. There is a trend that the higher the meltpool area, the higher density, which suggests that higher energy densities are required for denser parts. None of the parameters have resulted in a fully dense part, despite the melt track depth suggesting that this should have been the case.

This figure shows that all the sets resulted in depths larger than 90%, but none had an average density higher than 98%. The plot shows that with increased energy density, the relative density increases. This relative density increase means that the optimal parameters have not been reached, and a higher energy density is required. Despite evidence from the weld tracks showing that this should have occurred due to the large melt depths seen in those experiments.

The AconityMini build was analysed similarly and Figure 6-28 and Figure 6-29 show the polished XY cross-sections of two of the builds.

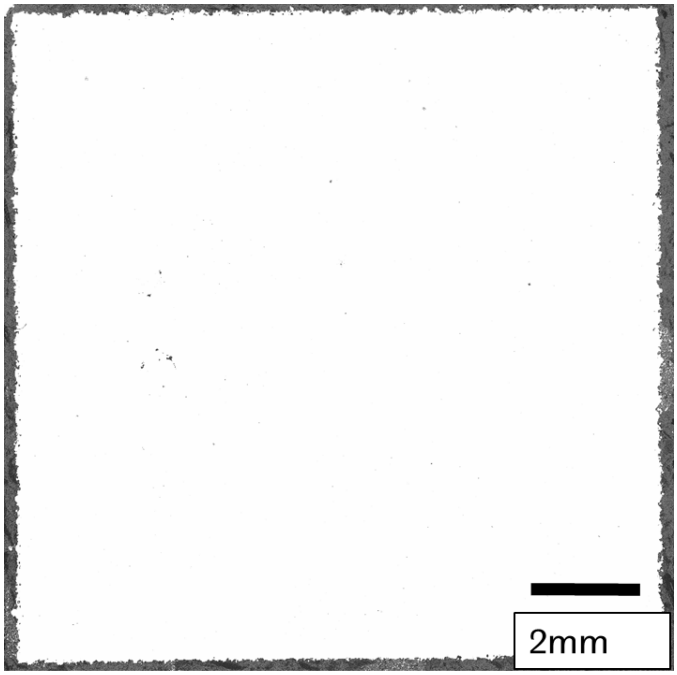

Figure 6-28 - Micrograph of the XY cross-section for AM130. There is very little porosity, including gas pores, and this shows that the gas pores in the Renishaw builds occurred due to the laser behaviour as the same powder was used across both machines.

Figure 6-28 shows AM130. It is a fully dense part with few pores and minimal gas porosity. This difference in density is despite using the same powder feedstock. This result is because the continuous beam creates a more even thermal field that allows gas pores to escape, and this also does not create voids or eject powder from the meltpool.

Below is Figure 6-29; this is the cube resulting from the AM150-4. This parameter set has achieved a very porous structure with massive LoF defects.

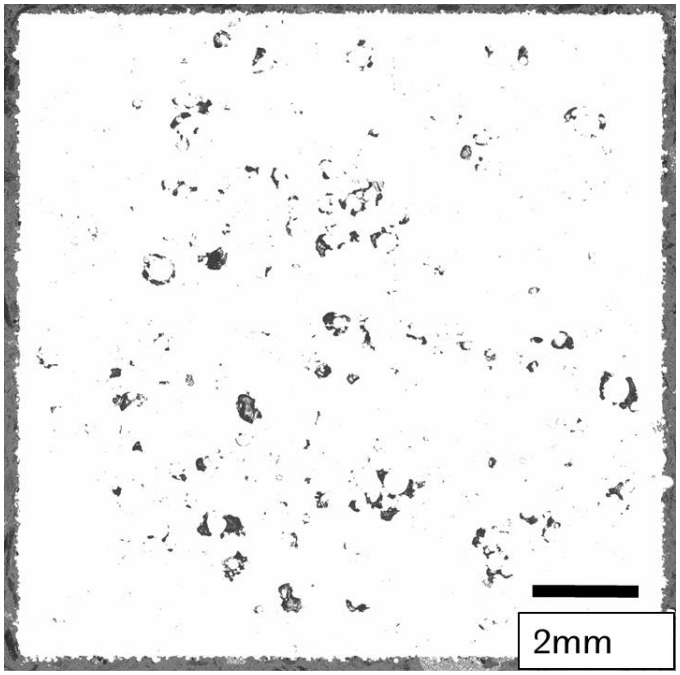

Figure 6-29 - The XY cross-section of AM150-4. There are many LoF defects despite the depth of the weld track created by these melt tracks being the same as that of the optimal parameters from the surface DoE (Section 7.2). This result suggests that diffuse beams behave different from focussed beams with powder, and due to the air gaps between the powder particles, the laser penetrates even less.

The melt depth of the weld track was the same as that of the optimal parameters from the surface design of experiments (DoE) (Section 7.2) but resulted in a much lower relative density. This lower relative density was due to a difference in how a focussed and diffuse beam interacts with solid material as opposed to powder. The lower densities than expected from the weld tracks result from the difference between the laser/bulk and the laser/powder interaction also seen in the Renishaw. Additionally, the lower densities than the surface DoE in Section 7.2 are due to the increased time between layers. In order to keep conditions similar between the two machines, the time between layers on the AconityMini was artificially lengthened to match up with the Renishaw. This extra time was over 80 seconds which would have caused the build to cool down much more than during the surface response DoE. This cooling will result in a lower initial surface temperature smaller meltpools, and so it will be more likely to have LoF defects.

Below in Figure 6-30 are the plotted densities from the AconityMini builds. The range of densities achieved is from above 99.9% to around 97.5%

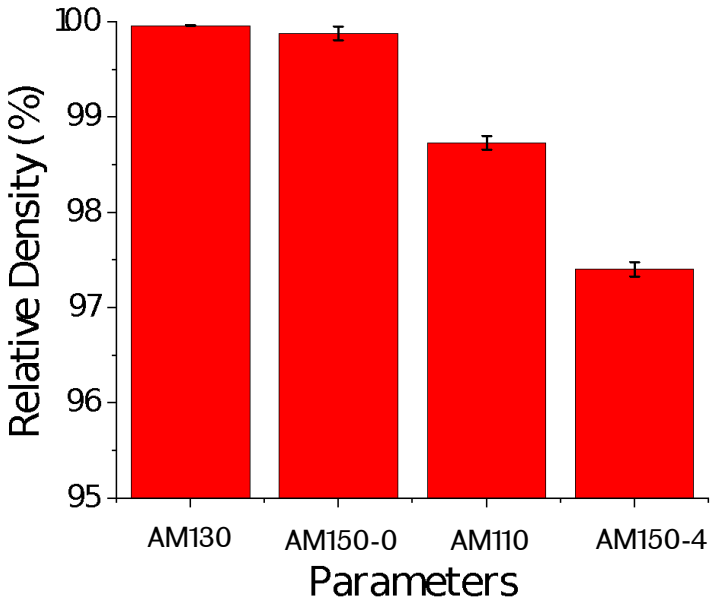

Figure 6-30 - Relative densities for the AconityMini builds. These densities are higher than for the Renishaw. Both AM130 and AM150-0 achieve a fully dense part within the optimal range of parameters. AM110 should have resulted in a fully dense part based on the surface DoE done in Section 7.2. The fully dene part has not happened as a longer time was left between the layers to make it equivalent to the Renishaw.

Overall, the densities are much higher than the Renishaw for the same meltpools. There is, however, not a trend where twin sets of parameters will result in the best or worst performance on both machines. This result means that it is impossible to translate parameters interchangeably between the AconityMini and the Renishaw. Anecdotal evidence from other researchers is that it is possible to translate parameters from the Renishaw to the AconityMini using the duty cycle consideration and equivalent speed. However, when going from the AconityMini to the Renishaw, adding the point distance and exposure time parameters means conversions in this direction are impossible. The Renishaw to AconityMini conversions tended to be less efficient as they have much slower velocities to reduce the effect of the duty cycle on the Renishaw. Exposure time is a critical parameter from the experiment on laser Ramp-up and keyholing (Sections 1.6.1.2 and 1.8). So, an equivalent velocity does not result in the optimal value being used in all circumstances.

Future experiments performing the tests with a powder layer and not just bulk may result in a more accurate meltpool and more optimised parameters. However, this would be more expensive, time-consuming, and require powder, which would defeat part of the purpose of these experiments, which aimed to simplify the parameter selection process.

As a result of these experiments, parameter selection studies need to be conducted on both machines due to the different input parameters available and different laser characteristics that create different meltpool dynamics.

6.6 Conclusion

In conclusion, the accuracy of the laser scanner and systems, the focal point as well as ideal hatch spacings for two different types of LPBF machines was assessed. For the Renishaw, the lower limit on the usable point distance was found at 10µm. How the laser moves before as well as between hatches was analysed and observed. The fact that the laser system needs to compensate for ends of hatches was established.

The effect of uncertainties in output point distance and hatch spacing on the Renishaw was modelled, resulting in point distance uncertainty being more significant in affecting meltpool volume. Point distance errors could cause variations in meltpool volume of 10%, whereas the errors in hatch spacing had a negligible effect.

Further experiments need to be conducted on the AconityMini to find these "skywriting" parameters to compensate for this as currently, the scanner makes no such compensation. This lack of compensation contrasts the Renishaw, which considers this even though it does not need to, resulting in extra hatches being lased in certain circumstances. How the laser traces a large arc between hatches was found in the Renishaw, and this arc was wider than the hatch spacings and led to additional error in the hatch spacings at low values. Although the arc was not observed in the AconityMini, the smaller hatch spacings had a higher error than the medium spacings, which would suggest that the laser moves similarly. It was found that the lowest error in hatch spacing occurred at around 50µm for both machines. This spacing was large enough that the wider arc did not cause an error as it moved back into position for the next hatch but not so large as to cause an error as the laser moves a larger distance to get to the next hatch.

These accuracy tests did not require powder and, as such, were less expensive and easier to do than existing methods. Combining many different tests into one build also made the process quicker.

Weld tracks lased on the Renishaw were used to investigate the transition between conduction and keyhole melting. The same experiment found that ramping up the laser to full power resulted in a loss of between 10 -15µs of exposure time at 190W.

The experiment into finding a way to convert between the two different machines found that whilst there are parameters that result in the same width and depth meltpool when lased onto bulk material; this does not translate into similar build densities due to the different ways in which the lasers interact with the powder. For the Renishaw, the volatile nature of the meltpool

created by the pulsed laser caused powder to be ejected from the meltpool and gas pores to form. It was found that trying to convert between the two machines was hampered by the extra parameters of point distance and hatch spacing. These parameters can be converted to an equivalent velocity on the AconityMini. However, the reverse cannot be done due to the results of the keyholing experiment, which showed that different exposures melt the powder by different modes.

For these reasons, separate parameter studies need to be done for pulsed and continuous laser systems to find optimal parameters. Using the weld track on to bulk material technique, the continuous laser system's parameters can be narrowed down. It could be useful in finding a region in which to do full parameter optimisation studies. These studies must include powder as melting onto bulk, and melting powder produces two different meltpools, which caused parameters that from the bulk meltpools should have resulted in fully dense parts cause LoF defects to occur when melting powder. The powderless weld track technique cannot be used for the pulsed laser system as the interaction between the laser and powder is so crucial that the parameters cannot be narrowed down without using powder.

From these experiments, it can be concluded that pulsed lasers are less efficient, create a more complex thermal history and cause more gas pores to form due to the laser ejecting powder from the meltpool. However, it is more accurate and more suitable for fine features. Therefore, it is necessary, so a machine that could do both stationary pulsing and continuous beam melting would be useful. If this is not possible, the requirements and geometry of the part must be taken into consideration such that a suitable machine is chosen.

This experiment did achieve the overall aim of improving the parameter selection process. The machines have been characterised such that they are better understood. By understanding how the laser systems function, parameters can be selected to work with the scanner and laser system. These experiments have outlined which parameters work within the machines and why and which parameters do not work due to the limitations of both the laser and scanner system. This result was achieved by using an accuracy test build that combined different parameter accuracy tests into one build and doing it without powder. These have helped with the objective of finding a more generalised and efficient way to characterise a machine.

These methods have been used to reduce the time to find optimal processing parameters on the continuous beam by narrowing down the region. Powder would have to be used for the weld tracks or to build parts to optimise further. The time taken to optimise parameters has

not been reduced for pulsed laser as no narrowing of the range of parameters can be done without powder.

Unfortunately, a way to convert from pulsed to continuous laser systems was not found. Due to the extra parameters of point distance and exposure time, a generalised conversion method would not be possible.

The cause of some differences in thermal history due to the laser behaviour at the hatch ends was found, and parameters that need to be adjusted in order to reduce these differences were identified. Further work is required, though, to optimise these parameters for different beam powers, velocities and hatch spacings.

7. Using Measurements and Machine Learning to Control Parameters In-situ

7.1 Introduction

In this chapter, two methods of determining and controlling build parameters (power and velocity) are compared against parameter control through a machine learning algorithm (MLA). Overall, part density and pyrometry response in the form of emissivity measurements from each build layer were recorded. These two measurements were correlated to understand the origins of defect generation. Further experiments were conducted to control defects and porosity and analyse how pyrometry data is recorded in sections of different sizes.

Parameter selection is necessary for AM as different materials and alloys require different parameters. A map of normalised energy parameters can be used to show a commonality across materials and AM methods[86]. This map can select a central point, and a surface response can be made around it to find the optimal parameters.

This parameter selection method and others, such as weld tracks [85], are material and geometry specific. Phenomena such as return time [90] mean that geometry affects the thermal properties. As a result, parameters need to be able to change to account for this. Parameters must be altered to avoid differences in thermal history between the centre and edge of the part. [150]

Machine learning is seen as integral to materials development. One area that machine learning has been used is in materials optimisation and experiment development [5]. For these experiments, the objective was to use machine learning (ML) as the build was occurring and implement in-situ process monitoring and control. ML has been identified as one of the most-needed technologies [151] for the broader adoption of AM.

In-situ measurement and control have not been achieved due to the quantity of data to analyse and the short period of analysis and implementation. In order to achieve this, a probabilistic neural network was used with cross-sample entropy [152]. This probabilistic entropy targeting system (PETS) algorithm combines the advantages of neural networks with cross-sample entropy. Neural networks are well suited to materials science but require large datasets to

reach the optimal solution[153]. Cross-sample entropy reduces the data required to populate the model and the likelihood that the algorithm will converge on the wrong solution [152].

The reduced need for data using PETS is coupled with high-speed pyrometry, which produces a small data file compared to other techniques such as thermal imaging by providing the meltpool emissivity in the temperature range during the build [9]. These two factors will reduce the processing time and implementation time to use the code "on the fly".

The target pyrometry value will be found from an initial surface response DoE. The MLA will then be trained, and an experiment will be conducted that will show how well the MLA can target this value when it has been trained compared to when it has not been trained. A measure of success will be how well the MLA targets this value and whether the variation has been reduced.

Whilst ML is a powerful tool, it is unaware of any real-world implications of the suggested parameters. The objective is to achieve a fully dense part. Due to this, constraints will be introduced which have been found from experimentation and theory [8]. The results of straying outside these constraints will be found, including the type of defects observed and whether these match up with defects found in other experiments [99].

Finally, an analysis of pyrometry data will be conducted. This data distribution analysis will help inform how parts are divided up to reduce differences in return time and whether a part size cannot be used as the pyrometry readings for the meltpool cannot be distinguished from the background noise. The relationship between part size and distribution of pyrometry data will be investigated. Finally, an experiment will be conducted to see how parameter alterations can affect this distribution and whether they can reduce this.

7.2 Target Finding

Conventional design of experiments (DoE) is the most popular method through which a robust set of build parameters is determined for LPBF. Hence, this forms the first method investigated herein. The same surface response DoE was used as was carried out in Section 5.5.1. The relative density was measured through the Archimedes principle (Methods 3.8.1). The responses to parameter changes were analysed, allowing an emissivity value to be determined that reflected the highest density components (Figure 7-1).

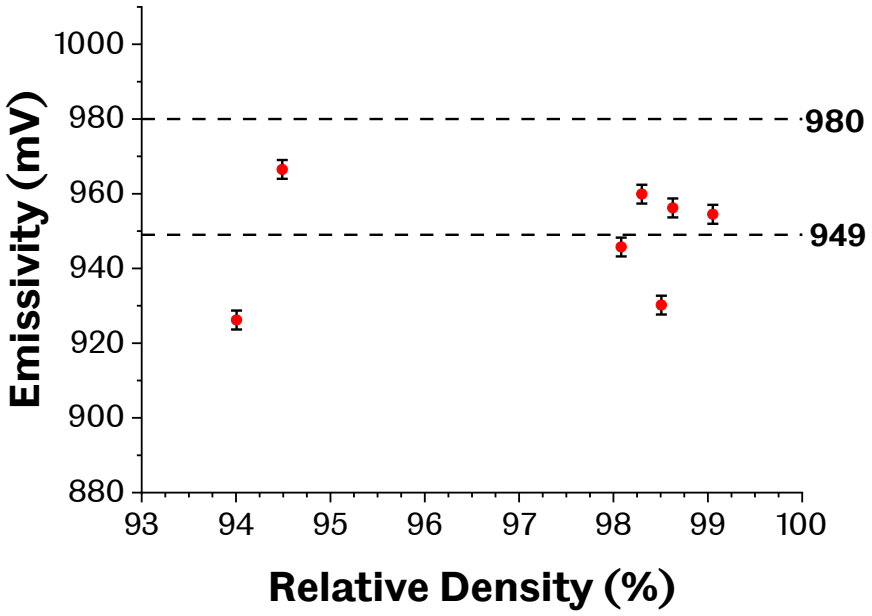

Figure 7-1 - Pyrometer recorded a similar emissivity for all cubes. Average emissivity of the five highest density parts was 949 mV. Emissivities above 980mV corresponded to failure (Table 7-1). Failure was due to swelling, and therefore the target was kept below that level. The target was raised above 949mV to avoid lack of fusion (LoF) defects prevalent in the completed cubes' cross-sections. The added time between layers, due to computational time, meant that a higher target than the 949mV average was necessary.

Cubes with a relative density above 98% had an average emissivity of 949 mV. Normalised energies, hatches, and recorded pyrometry readings for the samples that had to be suppressed due to part swelling were identified (Table 7-1).

Table 7-1 - Parameters that resulted in failed builds. All parameters result in emissivities higher than those for successful builds. As a result, the target was set below these values in order to avoid a failed build

Specimen ID	Normalised Hatching	Normalised Energy	Emissivity (mV)
SR4	0.66	5.01	1026
SR13	0.86	3.07	988
SR20	0.86	6.15	1073
SR6	1.14	11.40	1054
SR11	1.14	5.01	992
SR8	0.86	8.88	1044
SR19	0.86	4.44	983
SR18	1.43	8.88	1012
SR9	1.14	6.54	1023

Emissivity readings for swelled parts are higher than those built successfully, suggesting higher emissivities result in swelling and failure. From this conclusion, an upper limit of ~980mV for the average recorded emissivity was introduced to increase probability of a successful build.

There is uncertainty in pyrometry readings; because the emissivity changes due to the surface reflectivity. For example, the solid part, powder, and meltpool exhibit different emissivities. Hence, the readings are heavily influenced by the surrounding temperature of both the part and powder. The pyrometer also has an aperture of 1mm diameter, which is much larger than the 100 µm width of the meltpool.

When the cross-section of the cube associated with lowest density and emissivity was analysed, it exhibited substantial lack of fusion (LoF) defects (Figure 7-2).

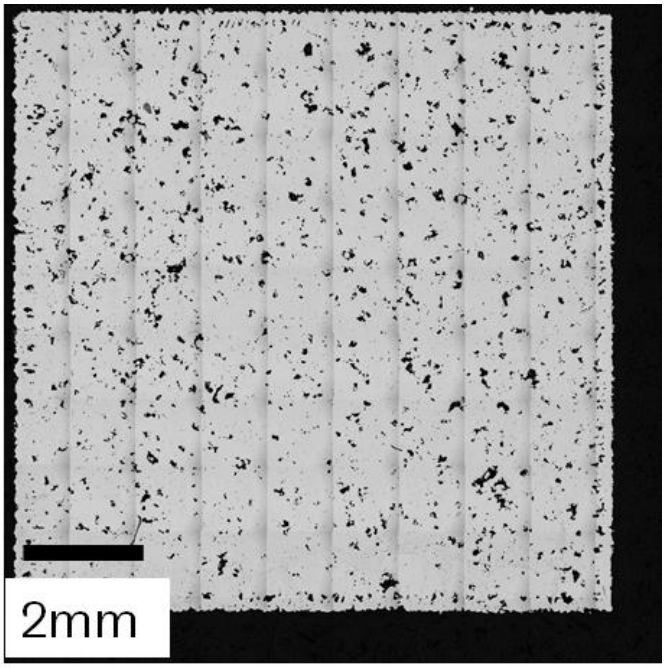

Figure 7-2 - This shows the highest porosity part for which an emissivity value of 924mV was recorded. The defects are non-circular, indicating LoF porosity. The target emissivity value was chosen to be 980mV to avoid these defects.

Defects are non-circular, which is indicative of LoF. LoF was found to be the primary defect by area when the cross-sections were examined (Methods 3.8.2), suggesting that LoF is the most common defect to be avoided by the ML algorithm. The ML target was 980mV, avoiding swelling associated with higher emissivities whilst minimising LoF defects associated with lower readings. The emissivity target was set at the upper bound to account for ML's temporal delays. As the MLA takes time to calculate and recommend new parameters between layers, this would allow the samples more time to cool between layers, increasing the likelihood that LoF defects would form. Thus, a higher surface temperature and emissivity are needed to counteract this cooling.

7.3 Creating a Training Dataset and Comparing Optimised Solutions

A training dataset for a Machine Learning Algorithm (MLA) examining how the pyrometer reading was affected by changes to the parameters was designed and carried out. The target emissivity was set at 980mV to train the MLA. The algorithm used was Probabilistic Entropy Targeting System (PETS)[152]. This Model-based reinforcement learning (MBRL) algorithm combines efficient sampling using cross-sample entropy sampling with uncertainty aware learning of probabilistic neural networks. This algorithm removes the massive datasets typically necessary for reinforcement learning whilst not converging on a non-optimal solution, as is the case with other MBRLs that do not take uncertainty into account.

The dataset used to train the MLA comprised 78 groups of four cubes. Four 5mm by 5mm cubes were separated by 2mm but treated as one part by the laser path. Although the laser-treated the four cubes as one part, an average pyrometer reading was taken from each of the four cubes. This method increased the number of data points available to train the model. Figure 7-3 is a schematic drawing of the geometry, and the red represents the laser path dashed lines. Within this chapter, the scan strategy used is meander with a 90° rotation and a 45° initial offset, as shown in Figure 7-3.

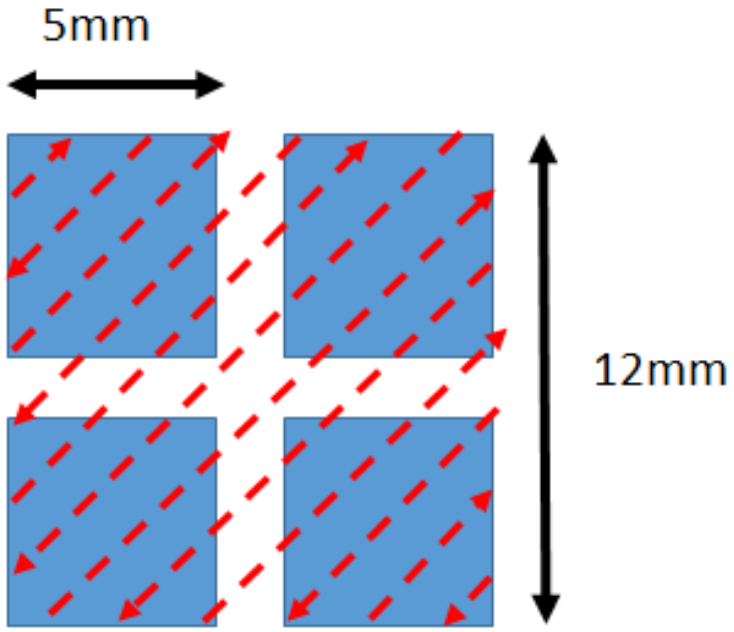

Figure 7-3 - Schematic diagram of the group of cubes. Cubes were in groups of four with a 2mm gap to keep them thermally separate. Although the laser treated the four cubes as one part, an average pyrometer reading could be taken from each cube. This method increased the number of data points available in order to train the model

Each set of four was given a set of parameters within bounds set out (Table 7-2) and designed such that no combination of parameters would create a part that would fail to build either due to swelling (overheating) or LoF (underheating) as explained above. The builds were completed on an AconityMini machine under an inert Argon atmosphere (<1000ppm O_2) (Methods 3.1.2).

Table 7-2 - Range of parameters for the MLA training dataset. The range was designed such that no combination of parameters could create a part that would fail to build either due to swelling (overheating) or LoF (underheating).

	Range
Power (W)	75-140
Velocity (m/s)	0.57-1.8
Hatch Spacing (μm)	35
Layer Height (μm)	30

Optimal parameters from the training dataset were compared to optimal parameters from the surface response DoE to look at foundations of the model.

The contour plot (Figure 7-4) depicts how close parameter sets used in the training dataset were to the target of 980mV.

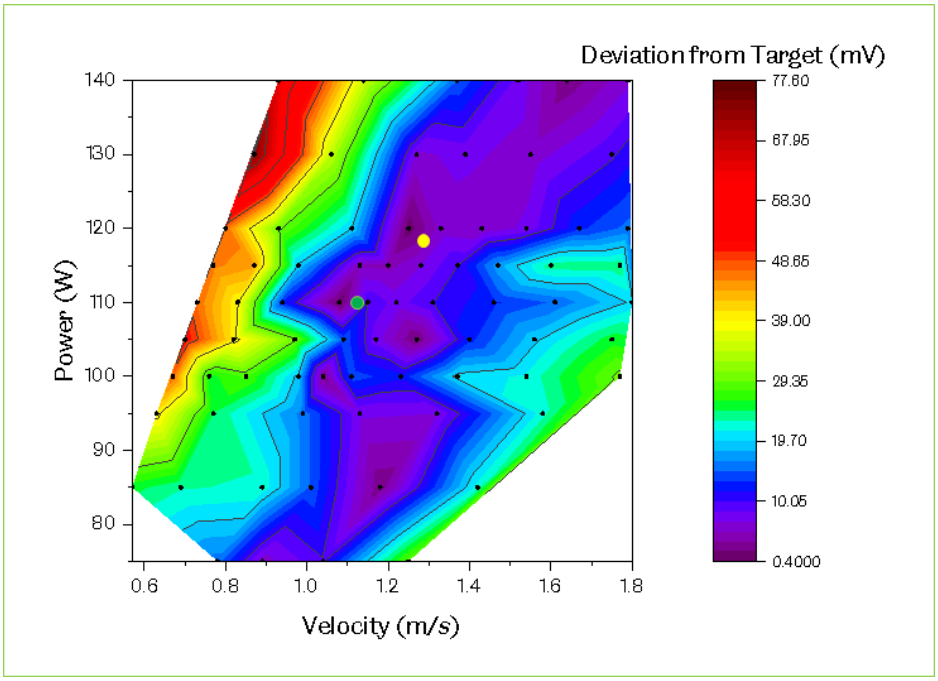

Figure 7-4 - This graph shows the emissivities of parameter combinations with respect to the target. The two closest points to the target correspond to the parameter sets chosen by the algorithm and the surface response DoE. A band of parameters in the middle produces emissivities close to the target, and the emissivities deviate further from the target outside of these bands.

The yellow circle shows the set that the model chose as the optimal parameters. These were chosen using a neural network with three hidden layers and 750 neurons per layer. The parameter set that achieved the lowest deviation from the 980mV target is at 120W and 1.25m/s (Figure 7-4), the nearest point to the optimal parameters recommended by the MLA.

There is a central region running from the bottom left of middle to the top right where the deviation from the target is the least. This band corresponds to equal volumetric energy input. The green circle is the parameter set found through the surface response DoE. This point is close to the measured value at 110W and 1.08m/s from the training data and the 980mV target, showing different methods of reaching the optimised solution.

Individual 5mm cubes were built to directly compare the two optimised solutions (training data and surface response). Ten cubes were built using the training data optimised solution (TDOS) and the surface response optimised solution (SROS). Parameters used are given in Table 7-3 below.

Table 7-3 - Parameters used in comparing optimised solutions build. These builds were done in an inert argon atmosphere, and the scan rotation was 90° with an initial 45° offset.

	Power (W)	Velocity (m/s)	Hatch Spacing (µm)	Layer Height (µm)
TDOS	118	1.29	35	30
SROS	110	1.125	35	30

The cubes were cross-sectioned, polished and imaged under an optical microscope to investigate the internal porosity (Methods 3.8.2). The porosity is minimised in both samples(Figure 7-5a and Figure 7-5b), even though the geometry used to optimise the parameters was different.

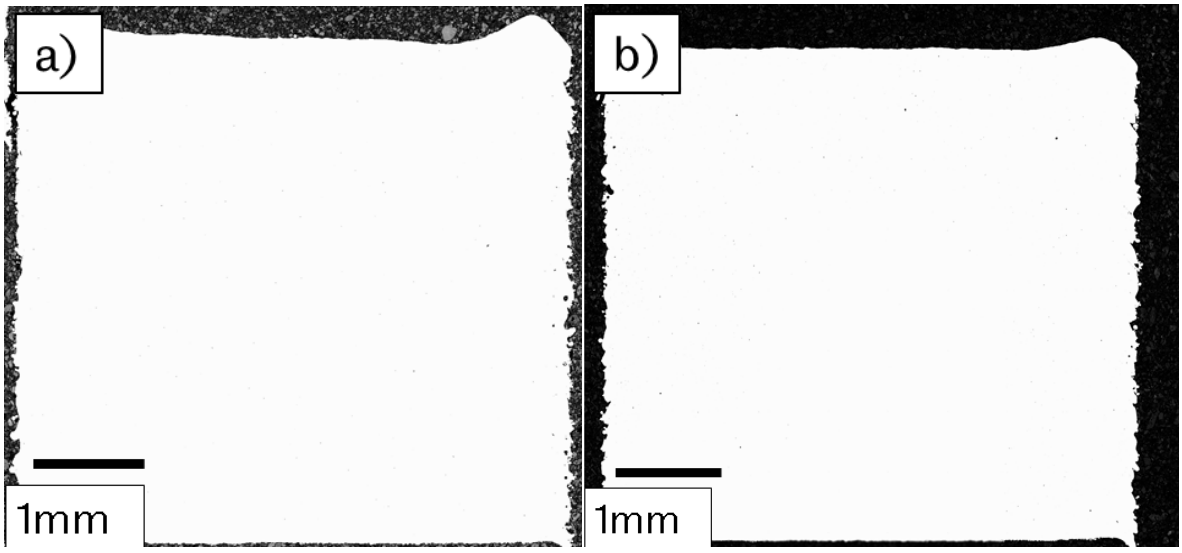

Figure 7-5 - These cross-sections show the fully dense cubes created by the fixed parameters TDOS a) and SROS b). Even though the parameters were found on different geometries, full density has been achieved.

In the case of the SROS (Figure 7-5b), parameters were found by building 10mm cubes, and for the TDOS (Figure 7-5a), the parameters were found from the groups of four 5mm cubes (Figure 7-3). Whilst a small amount of gas porosity is present, this is negligible, and both samples can be described as fully dense. The resolution of pores which can be identified is 0.5468µm. The SROS cube is 99.96% dense, and the TDOS cube is 99.98% dense. The cubes were placed in a pycnometer to capture the whole cube density rather than the surface

porosity. The method to measure the density is given in Methods 3.8.3. The results are shown in Figure 7-6 below.

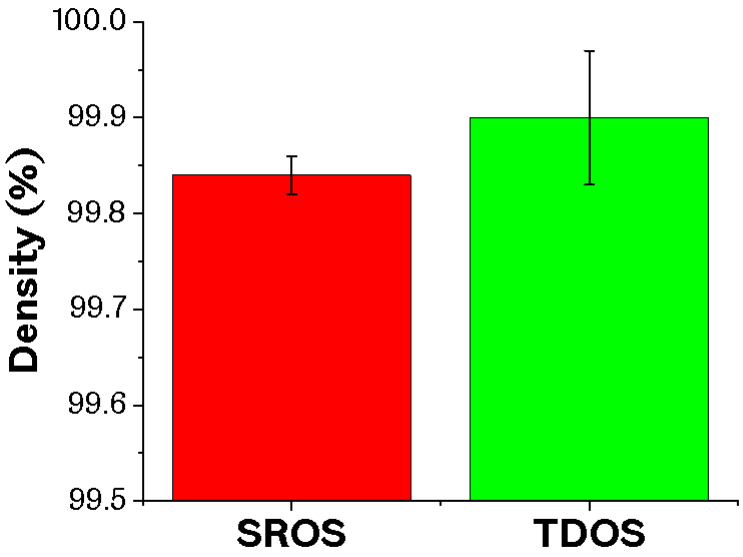

Figure 7-6 - These show the density for the cubes found using a pycnometer. Both cubes achieve full density despite being trained on different geometries, and this result also validates both methods for finding optimal fixed parameters.

This result shows that the cubes are fully dense throughout, and both sets of parameters achieve the same result when used on this different geometry. During this experiment, pyrometry readings were measured to investigate whether there was a difference due to the different geometry of the parts built in this experiment compared to the experimental training dataset. The results are shown in Figure 7-7 (SROS) and Figure 7-8 (TDOS).

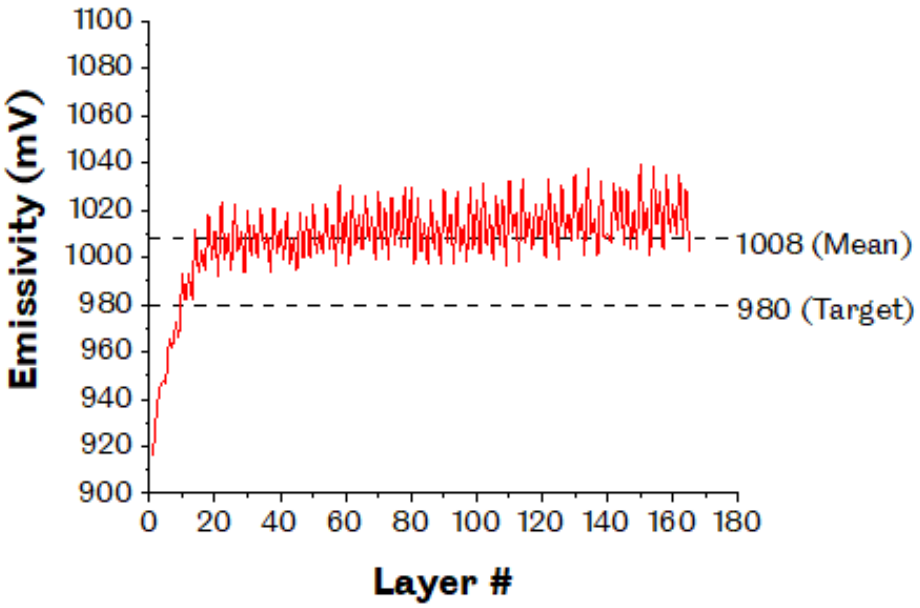

Figure 7-7 - Emissivity for the SROS method. After rising slowly through the first layers, the emissivity oscillates around values above the target. This oscillation is due to the parameters being optimised on a different sized cube. Whilst initially stable, the emissivities seem to be rising towards the end of the build. The rise may be due to thermal build-up as it moves away from the substrate.

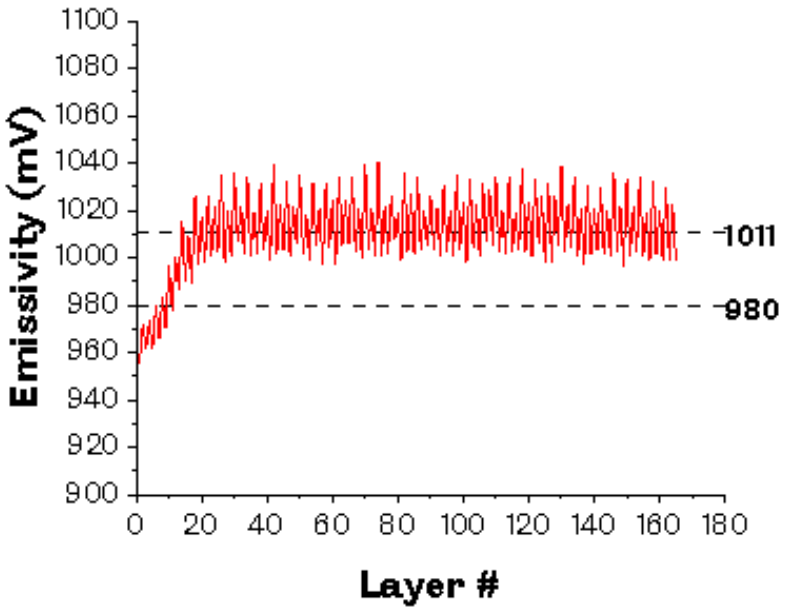

Figure 7-8 - This graph shows the emissivity for the TDOS cube. As with SROS, the emissivity rises slowly towards the target but overshoots and fluctuates around 1011mV. Neither method can account for the changes in thermal behaviour as the build progresses and the layers get further from the substrate.

After the pyrometer reading increases through the initial layers, both readings eventually settle and deviate to a similar degree away from the target. The mean emissivity obtained was higher than the target.

This trend is seen in both fixed parameters methods as they cannot adjust for the high reading with a corresponding drop in energy input. The initially slow increase to reach the mean value is due to the substrate acting as a sink which dissipates any heat built up in the part. The substrate cannot dissipate the heat as the parts get taller, and the emissivity readings increase. After 20 layers, the emissivity stabilises and oscillates around a mean value of 1008mV for the SROS, and 1011mV for the TDOS methods, respectively, which were higher than the target. The target was obtained from larger geometries. As a result, the return time is shorter than expected, leading to a greater thermal build up that increases the emissivity of the part.

Despite the parameters resulting in higher emissivity readings, the parts were fully dense. This finding suggests that keyholing has not occurred from the hotter temperatures during the building. The higher emissivities show how dependent on geometry the emissivity is and that the same parameters can result in different emissivities depending on geometry.

This experiment demonstrates a need to react to changes in emissivity readings with parameter changes to maintain the target value. Consequently, the following experiment was designed to investigate this using closed-loop control. The machine changes the parameters as necessary based on the measured outputs with no user input. This experiment will use the same model used to optimise the parameters from the training data. However, after each layer, the model is updated with the measured outputs to suggest and implement new parameters for the next layer.

7.4 Closed-Loop Control with Machine Learning

This experiment looked at how effectively the PETS MBRL algorithm when incorporated into a closed-loop control (CLC), targeted the desired emissivity. The model trained in the previous experiment was used as the base. After receiving the emissivity values from the current layer, the algorithm updated the model. The algorithm then recommended and implemented new parameters that would result in the target emissivity. For this experiment, two CLC methods were investigated. These were a PETS MBRL algorithm that used the previous training data to inform its recommendation (pretrained) and the same algorithm, but this one had not been trained and thus was learning from each layer as the machine built them.

These MLAs were implemented on an AconityMini using their inbuilt API Client, allowing an external program to control the inline altering of the parameters. The program that was built read the pyrometry data for each part and layer as it was made. This data was then inputted into the MLA that outputted a recommendation of power and velocity. The client implemented these onto the machine for the next layer. This process was repeated for every layer until the parts were built.

A test build of 30 parts was performed. These consisted of three groups of 10 samples each, using a different level of CLC. The groups are summarised in Table 7-4 below. This build aimed to understand the ability of different control methods to reduce the variability in average emissivity readings between layers. 5mm cubes were built to reduce the computational time needed to produce and implement recommendations.

Three groups of test builds were created to allow the systematic investigation of the MLA in parameter control compared to a random set of fixed parameters. These consisted of two MLA sets; one pretrained on the data collected to create the model and another untrained. The untrained model incorporated active learning and learned as it was introduced to the pyrometry data while the cubes were built. Finally, a random set of parameters was used as a control state. These random parameters were chosen for each layer between the parameter bounds shown in Table 7-4 to find a benchmark for pyrometer readings.

Table 7-4 - Parameters used in each control method. For the closed-loop control methods, the ranges of possible parameters are given.

	Power (W)	Velocity (m/s)	Hatch Spacing (μm)	Layer Height (μm)
Pretrained	75-140	0.57-1.8	35	30
Untrained	75-140	0.57-1.8	35	30
Random	75-140	0.57-1.8	35	30

The average pyrometer reading for each layer was extracted and compared to the target value once the cubes were built. The root mean squared error (RMSE) was determined between the average pyrometer reading for that cube and the target. The RMSE for each group of cubes was then compared and plotted on the same graph. This graph is shown in Figure 7-13. The interlayer and intralayer standard deviations in pyrometer readings were also obtained from the data.

As determined by part density, the part quality was measured using a pycnometer. The cubes were inspected by taking a cross-section in the XZ plane and analysing it using the Clemex optical microscope at 100x magnification (resolution 0.5486μm). The results from the machine learning sets of cubes were compared to the fixed parameter sets.

An average pyrometer reading was plotted for each layer for a specific cube from the experiment that used an MLA to implement closed-loop control. Figure 7-9 shows this plot for a representative cube from the group of pre-trained cubes. A mean emissivity value was obtained at 1017 mV. The emissivity of the first layers deviated from the mean value significantly and then plateaued within 20 layers (~ 0.6mm). After this, emissivity only varied approximately 15mV from the mean. However, this mean was higher than the target emissivity of 980mV. This behaviour was consistent for all ten cubes in the pretrained CLC group.

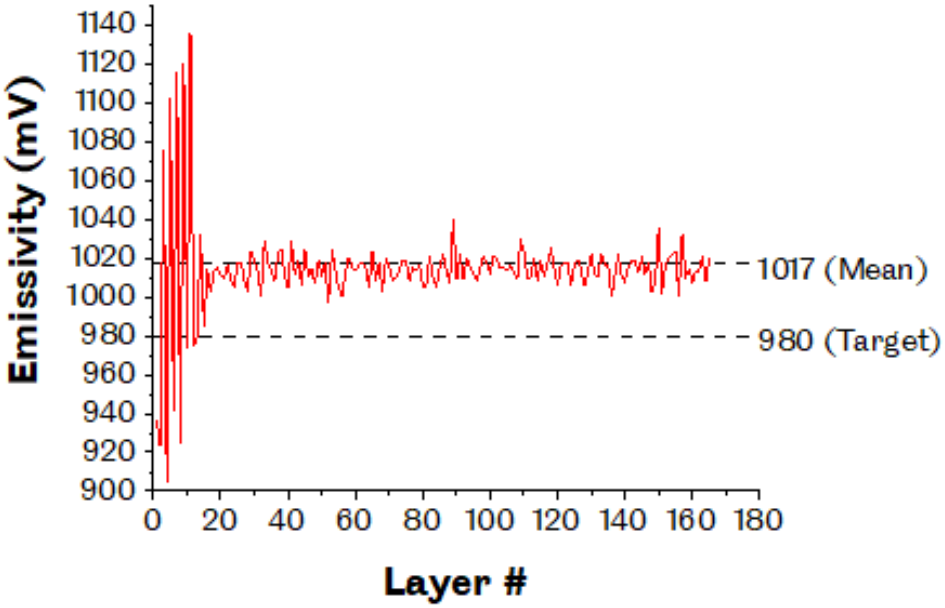

Figure 7-9 - Graph showing how emissivity changes throughout the build for a representative cube from the group of pre-trained cubes. After fluctuating significantly during the initial layers, the emissivity stabilises after ~ 20 layers. However, the mean is higher than the target as it has been trained on a different geometry and cannot accurately adapt to the desired emissivity value of 980mV.

The initial variations in readings can be attributed to the aggressive search algorithm in the MLA. This search algorithm causes the MLA to vary the parameters by large amounts to find the set that results in the reading closest to the target. From Figure 7-10, the line energy is initially pushed up to 140 Ws/m, and it quickly settles down to between 60-110 Ws/m. From Figure 7-9, the emissivity reading lags the line energy in settling. This lag can be accounted for because the current layer's pyrometer value is affected by the preceding layers. Comparing the two figures, no direct correlation between parameters in a layer and the emissivity reading for that layer can be obtained.

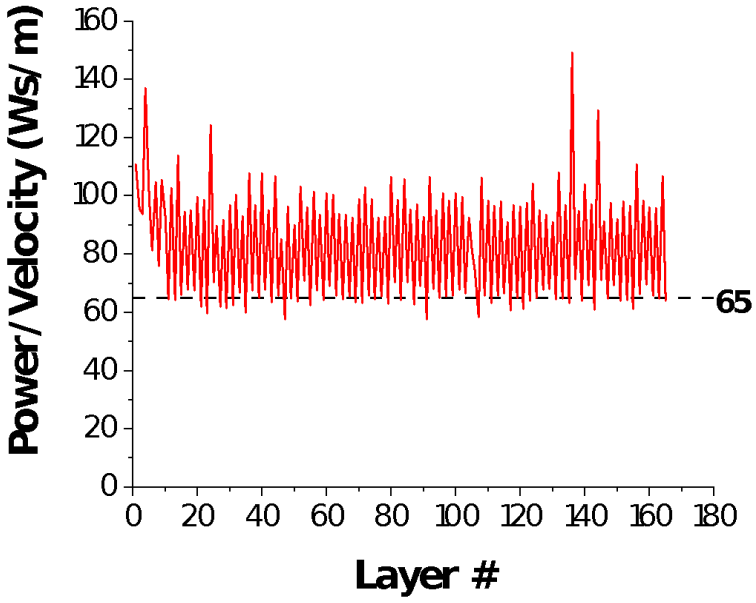

Figure 7-10 - Line energy for each layer in the pre-trained build. The energy input stabilises between 60-110Ws/m after layer 10, which occurs earlier than the stabilisation in emissivity. This lag is due to the emissivity value being affected by the previous and current layers. There is no correlation between high energy input and high emissivity for a specific layer.

As outlined in Figure 7-9, the mean emissivity value recorded for the builds was found to be above the target value by ~37mV. This error is believed to be due to data used in MLA training being on a different sample geometry. This geometry was chosen as a generic geometry that could train the MLA to deal with different sized parts. The training dataset was obtained from sets of four 5mm cubes grouped and treated as one part by the machine (See Figure 7-3) to maximise the available data points for training. The cubes were 2mm apart to be thermally separate, but the return times were longer than those for individual cubes. However, from the results, this appears not to have worked and resulted in the higher emissivities recorded. The MLA expects the return time to be longer and the preceding hatch to have cooled more by the time it returns. Hence, it does not reduce the parameters accordingly.

These results demonstrate that it is necessary to include different geometries in the training data set to reach the target emissivity value using a trained model accurately. However, this would increase the cost and complexity of the model as it would require multiple builds to acquire enough data points to train the algorithm. A set of builds was performed using the MLA but without training to explore the extent to which the algorithm was successful. Figure 7-11 shows the emissivity for each layer for a representative cube from the untrained set of cubes.

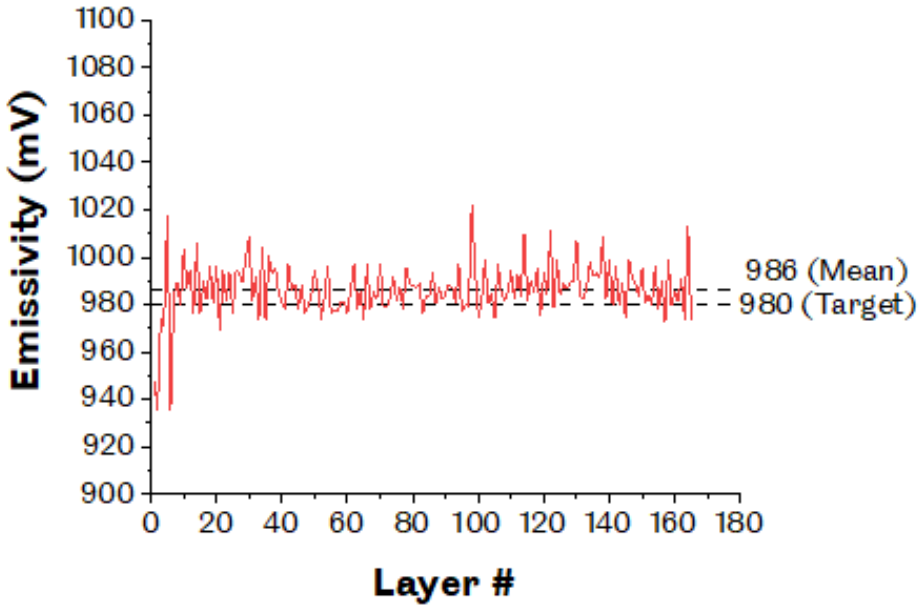

Figure 7-11 - Average emissivity for each layer for an untrained CLC cube. This method produces the closest mean reading to the target value of 980mV. This error is due to the model being untrained on a different geometry and altering parameters between the layers.

After an initial search, the MLA settles around a mean pyrometer reading of 986mV within ten layers (around 0.3mm) within 1% of the 980mV target. This change is quicker than the trained model as it is not expecting a different geometry but learning from the presented one. Fluctuations about the mean are similar to those seen in the trained model at around 15-20mV.

Consequently, no advantages could be discerned by using the trained MLA, whereas the untrained model offers the distinct advantage of being geometry agnostic. When considering the line energy inputted into each layer (Figure 7-10), as with the trained model, there is no clear correlation between the line energy and emissivity. After an initial aggressive search, the line energy settles to between a minimum of 45Ws/m and a maximum of 110Ws/m. In contrast, the trained model has a similar maximum but a minimum of 60Ws/m.

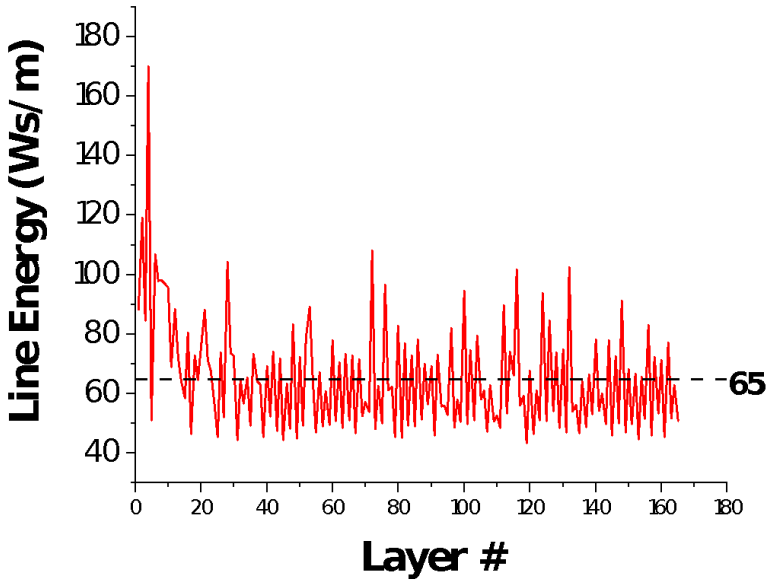

Figure 7-12 - Line energy input for each layer for the untrained CLC cube. After layer ten, the parameters stabilise, allowing the algorithm to choose any parameter sets within the ranges given the energy input falls below 65Ws/m, which may cause porosity, as was the case in the surface response DoE.

The two methods of closed-loop control (CLC), where the parameters can be adjusted, were compared to the static optimised parameters TDOS and SROS from the previous experiment. Figure 7-7 shows the average emissivity per layer for the dataset where the optimised parameters from the DoE were used on the 5mm cubes. The control methods were compared to each other in targeting the set value of 980mV. This comparison was made by calculating the root mean square error (RMSE) of each layer's emissivity away from the target. The average of the RMSEs for each group was then found and is shown in Figure 7-13.

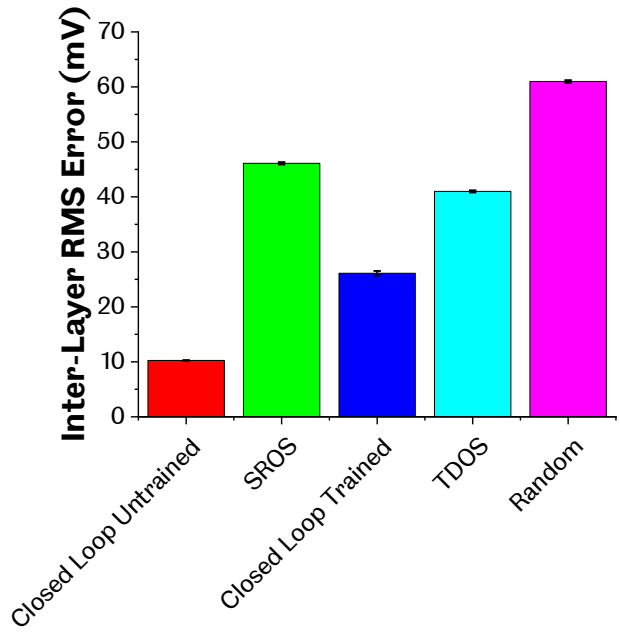

Figure 7-13 - Inter-layer deviation across the control methods show the effectiveness of CLC and, in particular, the untrained model in reducing RMSE away from the target. The untrained model worked best as it was not trained or optimised on a different geometry.

From Figure 7-13, the untrained group performed the best as it kept the pyrometer reading closest to the target. It also shows that CLC kept to the targets better than the fixed parameters, which shows the benefit of controlling them. The TDOS found through the training data performed better than the SROS. This result is due to the increased data on which the optimisation was based. The TDOS was based on the response from 78 different parameter sets instead of 16 sets for the SROS. All control methods compare favourably to the random control method, which shows that they all have a positive effect.

The CLC methods used could only determine one set of parameters per layer. These parameter sets can be optimised to reduce intralayer variability. The mean pyrometer value for a layer is plotted against standard deviation in emissivity readings (Figure 7-14).

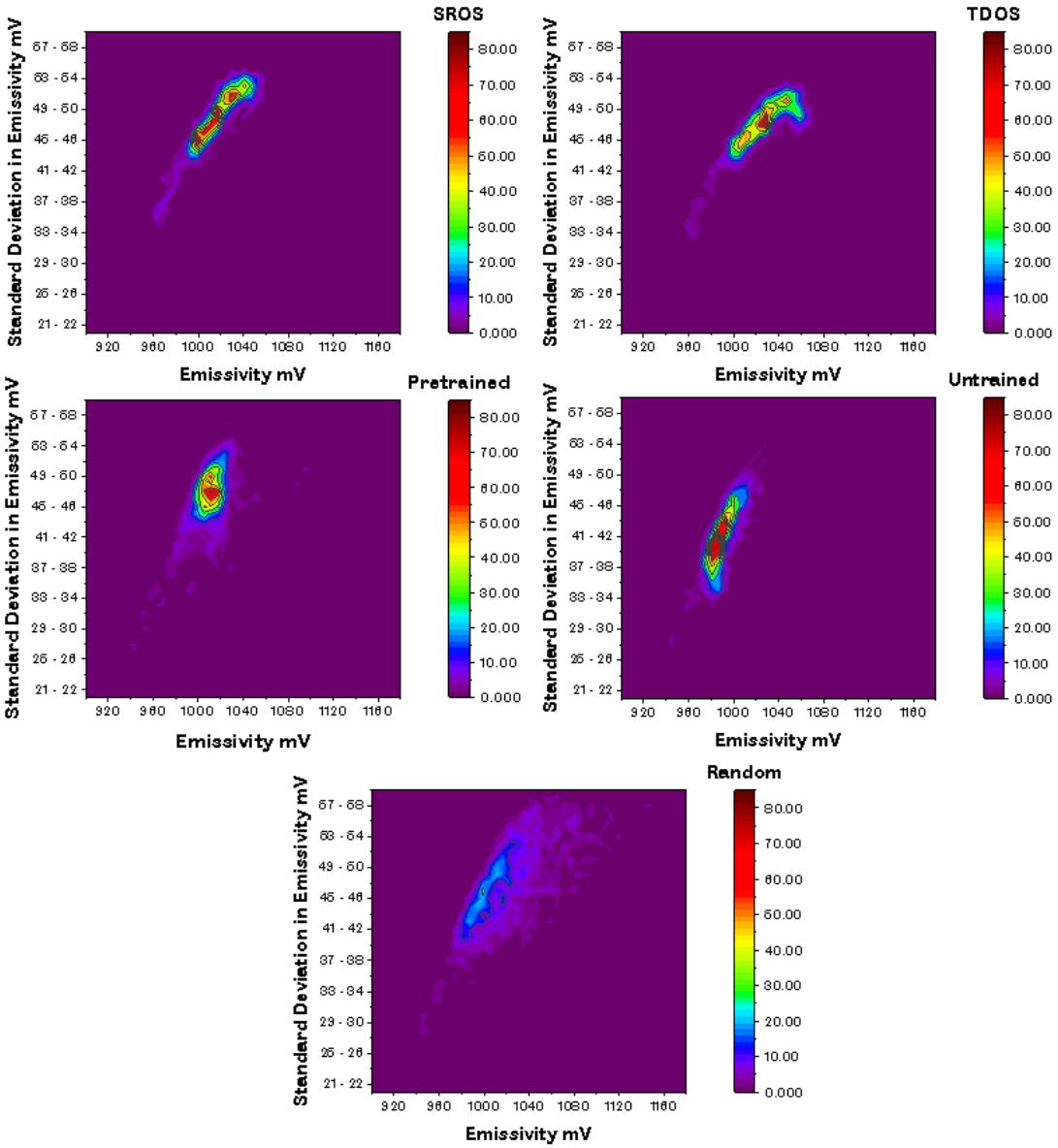

Figure 7-14 - Intra-layer deviation in pyrometry results between control methods shows the effect of control between layers. The MLA has performed better than the other control methods. These results suggest that further improvements may be derived by adjusting parameters within a layer, not just between layers, as demonstrated herein.

Different patterns emerge for the different control methods. The fixed parameters produce a similar shape, although the tail for the SROS parameters is longer (circled) than for TDOS, and the mean value is lower. As with the interlayer variance, choosing parameters has a strong effect. The random parameter control method produced the largest spread of results overall with no apparent concentration in data points compared to the other control methods. The pretrained control method showed a lower standard deviation in emissivity than the fixed

parameter methods and the tightest spread of standard deviations and mean emissivities. The untrained model had the closest emissivity to the target of 980mV; it also had the lowest absolute standard deviation. This decrease in deviation with the CLC methods is due to a secondary goal within the algorithm that aims to minimise variability. This decrease is not seen in the pre-trained cubes. The model was trained on a different geometry that causes the model to choose parameters that result in higher intralayer deviation. Overall the intralayer variance is increased due to fixed parameters within a layer. These parameters are used for hatches that vary significantly in length. At the corner, the minimum hatch length is 10 µm, whereas the length can be as much as 7mm in the middle. This difference is only exacerbated in larger parts with more significant variations in hatch lengths. This intra-layer variability needs to be reduced as much as possible to keep the thermal history consistent. In order to understand the effect that section size has on the pyrometry readings and variation, a separate experiment was conducted, and the results are reported in Section 7.5. This experiment investigated how the pyrometer records data within sections of different sizes, and the effect on the distribution of data points was observed.

A quantitative analysis of the difference between the control methods was carried out using a Kruskal Wallace ANOVA[154] in addition to the graphical representation of the data (Figure 7-14). This non-parametric test was necessary as the Levenes measure showed a non-homogeneity in the variance of results between the groups. Figure 7-15 shows the results of the comparison of mean rank between the control methods when observing mean emissivity.

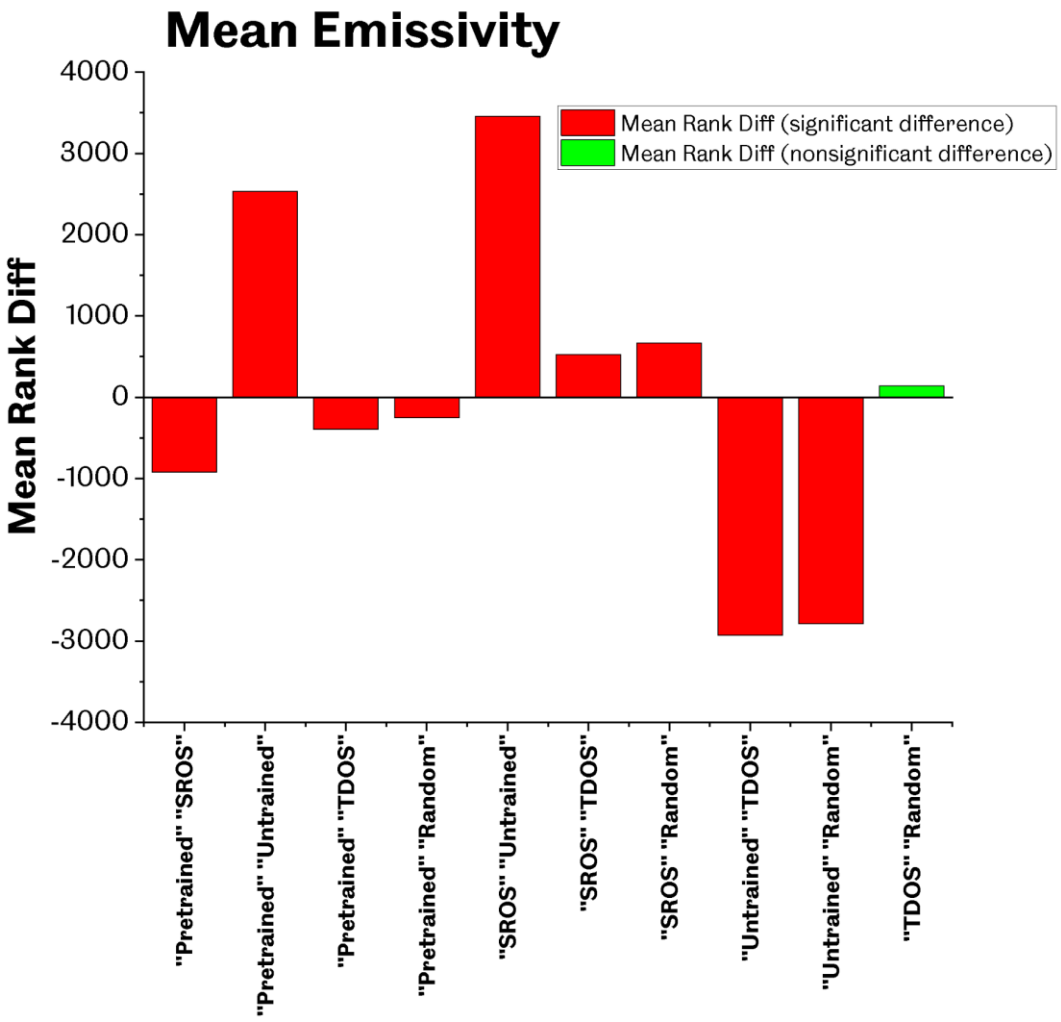

Figure 7-15 - These are the results of the Kruskal-Wallace ANOVA test for the mean emissivity. These results prove the effect that being able to change the parameters has. It also shows the benefit of having an untrained model as this achieved the most significant difference from choosing random parameters. The TDOS parameters show no difference from choosing random parameters.

The results show the difference that altering parameters can have. The first observation is that the SROS and TDOS control methods result in statistically different results. This result can be explained by how the solutions were chosen (from a surface response DoE and the training data, respectively.) They were also optimised on different geometries. The training has been shown to have a significant effect. The most considerable difference is between untrained and the other control methods. These results show the benefit of parameter control as one of the fixed-parameter methods - TDOS is statistically indistinguishable (at the 99% confidence level) from the random parameter selection method. This observation shows the need for

parameter control. Figure 7-16 shows the Kruskal-Wallace ANOVA analysis from the intralayer emissivity standard deviation.

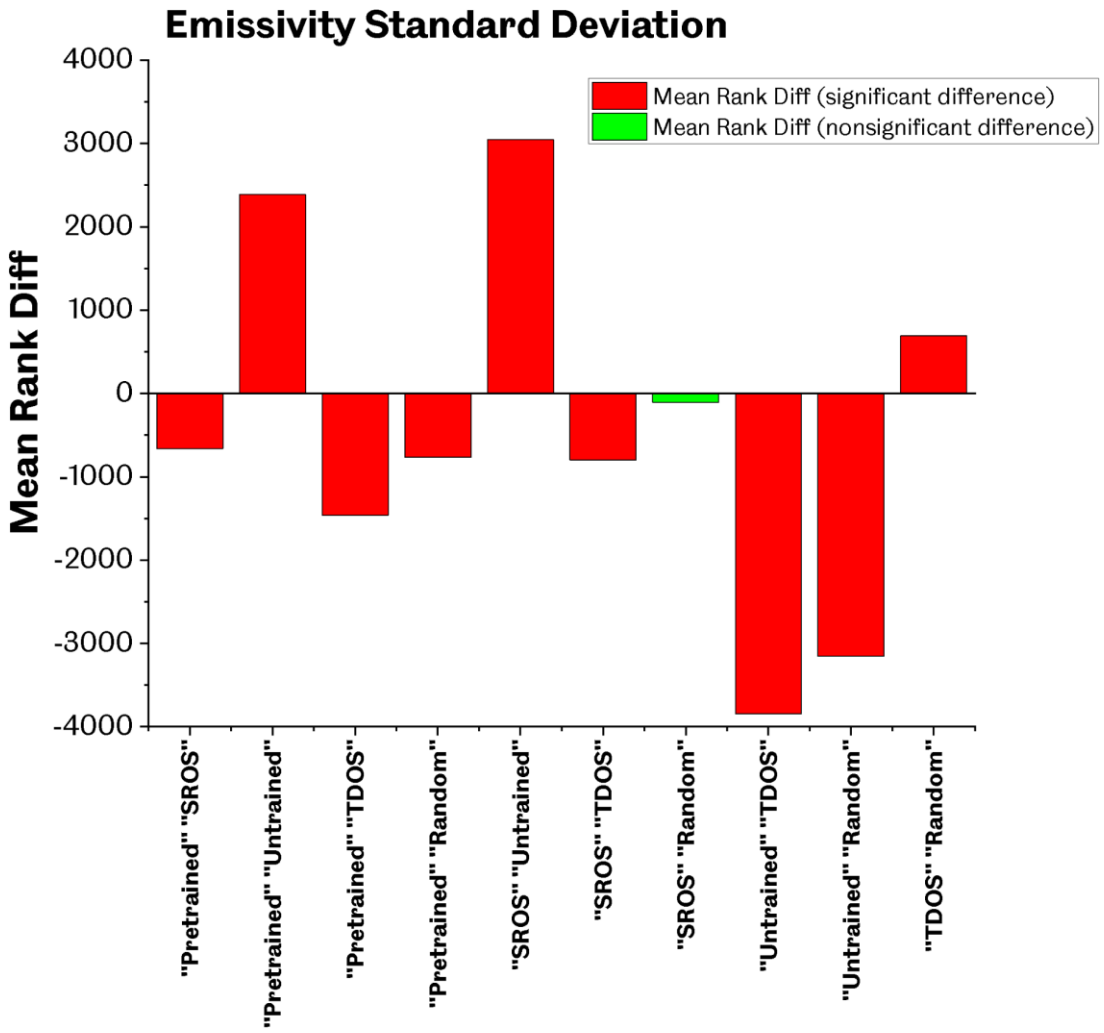

Figure 7-16 shows the Kruskal-Wallace ANOVA test for the emissivity standard deviation. The untrained model resulted in the most significant difference from the random parameters as with the previous test. The other ANOVA shows the benefit of parameter control as the SROS parameters show no difference from the random parameters.

As with Figure 7-15, the advantages of adjustable parameters is statistically evident. The untrained CLC shows significant control when compared to the random parameters. Similarly, to the mean emissivity, one fixed parameter group was statistically the same (at the 99% confidence level) as the random parameters. This time it was the SROS parameters.

ANOVA tests show the need for parameter control; without it, mean emissivity and deviation in emissivity are no different from random parameters.

A physical investigation of the samples was needed having investigated the pyrometry data. The densities of the groups of cubes were investigated and plotted in Figure 7-17 below.

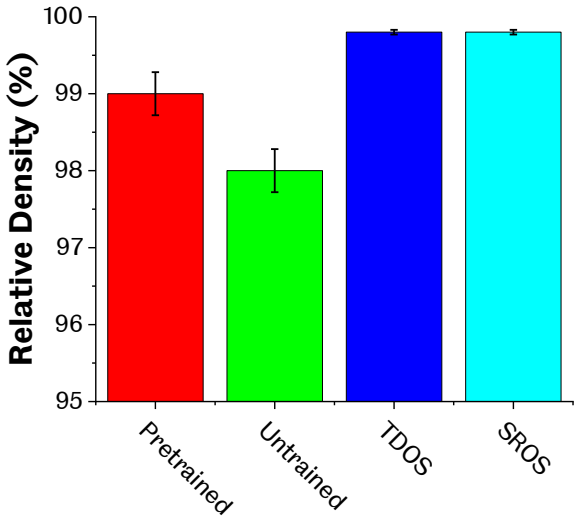

Figure 7-17 - Relative density for different control methods. From this, the fixed optimised parameter control methods have achieved the highest relative densities as they have avoided inputting parameters that cause defects. Trained performed better than untrained as the line energy inputted did not drop below 65 Ws/m as often as in the untrained.

From the graph, the fixed optimised parameters result in better part densities compared to CLC. The SROS and TDOS parameters achieve a consistent relative density of nearly 100% with a tight spread of +/- 0.1%. On the other hand, CLC achieves a lower relative density with more significant variation. The trained model achieves an average relative density of 99%, though it achieved as high as 99.9% and as low as 98%. The untrained model performed worse with an average density of 98%. The cause of this is due to how the MLA maintained the target emissivity of 980mV. When the parameters for each layer are plotted as shown in Figure 7-12, the line energy regularly drops below 65Ws/m. This limit was breached in the surface response DoE, which led to excess porosity.

Similarly, although when the trained CLC parameters are plotted, the line energies are consistently higher, which would lead to a higher density, some layers were found to fall below 65Ws/m. This line energy would lead to the formation of porosity that explains the drop in density seen when using the trained CLC method. The variability in both CLC methods can be explained through the aggressive search function that allowed large deviations of inline energy between layers. The fully dense parts from the fixed-parameter methods did not encounter

porosity despite having an average emissivity above the target, as Haynes 282 is resistant to cracking and keyhole formation. In addition, a significant time gap between the lasing of each layer (around 60s) was obtained in the CLC as the subsequent layer parameters had to be defined by the MLA only once the current data could be analysed, leading to further cooling between layers. Consequently, the propensity towards LoF defects increased, whereas keyholing decreased.

The explanation of the reduced line energy in specific layers causing porosity was further supported through optical characterisation, as shown in Figure 7-18. The XZ cross-section taken from one untrained CLC cube shows that the porosity was confined to specific layers.

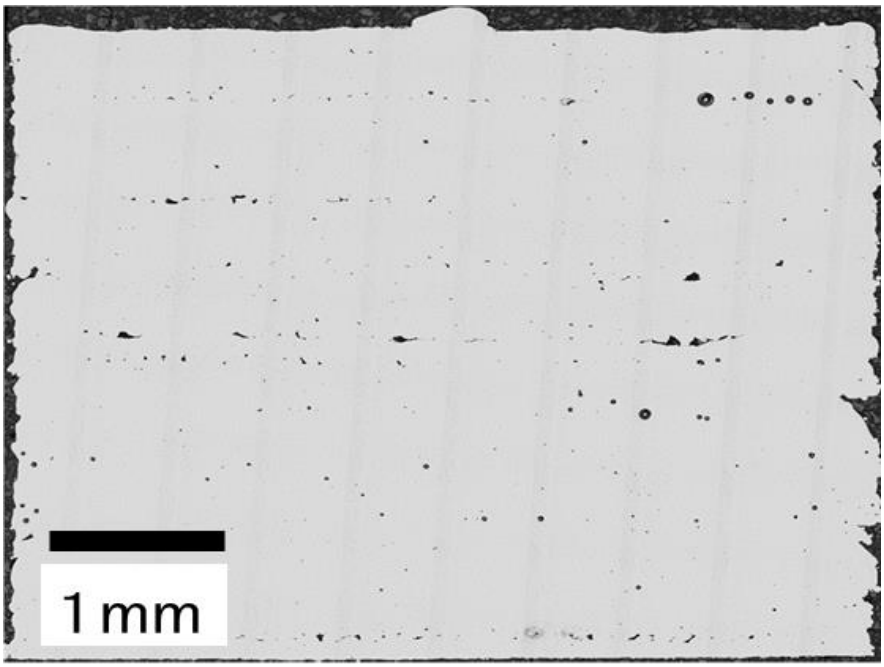

Figure 7-18 - Micrograph showing porosity in specific layers of an untrained CLC cube. Distinct layers of defects can be identified, and they are suspected to be LoF due to their morphology. The energy input plot (Figure 7-12) displays multiple layers where the line energy input is below that shown in the DoE to cause porosity.

The porosity can be identified as LoF due to the morphology. Although the reduced line energy of specific layers causes the porosity, there is no direct correlation between the line energy of a specific layer and defects. Line energy must be below this level for consecutive layers before the laser cannot melt all the powder, leading to LoF defects. An experiment conducted (Section 1.5) where the parameters were forced to specific line energies for one, two or three layers was used to observe the effect on porosity and microstructure of both a drop in line energy and when maintaining this energy over consecutive layers.

Figure 7-19 shows the XZ cross-section for a fixed parameter cube with minimal porosity. It can be shown that the porosity is not confined to specific layers and has a spherical morphology suggesting that it is gas porosity.

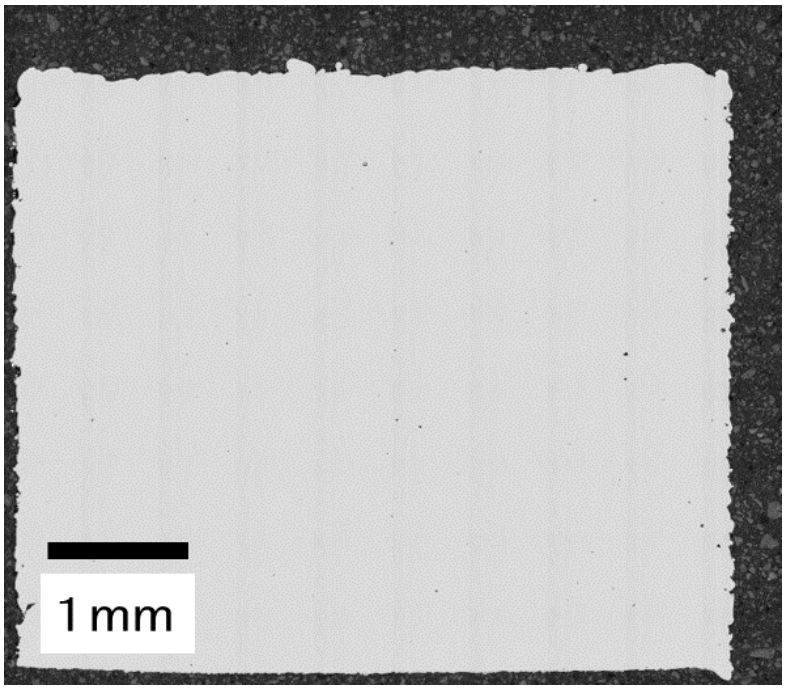

Figure 7-19 - Micrograph of an XZ cross-section of an SROS cube. There is minimal porosity, and the size and morphology of the pores identified suggest that they are gas pores. Compared to Figure 7-18, the advantage of fixed parameters is shown by the absence of porosity on specific layers.

Analysis of pyrometry data and physical specimens shows that whilst the MLA accurately targeted the value set, it did not achieve a fully dense part. Other methods resulted in a higher mean emissivity; this could be because the target value was wrong and a higher value was needed to achieve a fully dense part, or that parameter sets need to be constrained to avoid low energy layers. Therefore, a further experiment, shown in Section 7.5, was needed to see if it could achieve a fully dense part by constraining the parameters between an upper and lower limit.

7.5 Constraining Parameters to Increase Part Density and Induce Porosity

Due to results from initial machine learning (ML) builds, a further experiment was conducted where parameter ratios were constrained between two bounds. These bounds were obtained from equations in literature (Section 1.8) and experimentation (Section 7.2). During this experiment, the model was modified. After every 20 layers, parameters were forced out of bounds, either above or below, for 1, 2 or 3 layers depending on the cube. The frequency of deviation from "ideal" parameters is 20 layers because this equates to ~0.6mm; this is outside the heat-affected zone of the meltpools and indicates the number of layers after which pyrometer readings have stabilised. Deviation from the set bounds increased with cube height. The parameter sets are outlined in Table 7-5 below. Three repeats of each cube were made to obtain statistically significant data.

Table 7-5 - Parameters used in the deviated layers and the ranges of possible parameters between the deviated layers. Three cubes were used for each deviation condition for a total of 18 cubes.

	Forced Up		Forced Down	
	Power (W)	**Velocity (m/s)**	**Power (W)**	**Velocity (m/s)**
Intermediate Layers	75-140	0.57-1.8	75-140	0.57-1.8
Layer 21, Layer 21 & 22 or Layer 21-23	111.4	1.125	67.5	1.125
Layer 41, Layer 41 & 42 or Layer 41-43	116.7	1.125	61.9	1.125
Layer 61, Layer 61 & 62 or Layer 61-63	122.0	1.125	56.3	1.125
Layer 81, Layer 81 & 82 or Layer 81-83	127.3	1.125	50.6	1.125
Layer 101, Layer 101 & 102 or Layer 101-103	132.6	1.125	45.0	1.125
Layer 121, Layer 121 & 122 or Layer 121-123	137.9	1.125	39.4	1.125
Layer 141, Layer 141 & 142 or Layer 141-143	143.2	1.125	33.8	1.125

Cross-sections of each cube were taken in the XZ plane to see how the constrained parameters affected porosity and at what point the forcing of the parameters beyond the bounds started to induce porosity. Etching with glyceregia was also carried out to see the

shape of the meltpools and cell morphology. Both analyses were conducted on the Clemex Microscope. Average pyrometer readings for a particular layer were plotted and compared to the parts' porosity.

The initial control experiment identified that the parameters selected by the untrained ML algorithm resulted in line energies below the values deemed critical for LoF formation in the initial surface response DoE. Consequently, a second experiment was designed to explore the line energy as a lower limit for parameter sets. The upper limit for the parameters was determined from King's equation [89] for the onset of keyholing. This has been simplified into a ratio of power and velocity below.

$$\frac{\Delta H}{h_s} = \frac{AP}{\rho c T_m \sqrt{\pi D u \sigma^3}} \approx 6$$

Equation 7-1

Where ΔH is specific enthalpy, $h_s$is the enthalpy at melting, A is the absorptivity coefficient of LPBF, P is the power, ρ is the density, c is specific heat capacity, T_m is the melting point, D is thermal diffusivity, u is velocity, and σ is the spot size. For the Haynes 282 alloy discussed herein, Equation 1.2-1 becomes:

$$\frac{P}{\sqrt{u}} \approx 104$$

Equation 7-2

The algorithm was adjusted to limit power and velocity selection to satisfy the following relationships.

$$\frac{P}{u} > 65$$

Equation 7-3

$$\frac{P}{\sqrt{u}} < 104$$

Equation 7-4

After adjusting the parameters to meet these criteria, the resulting parameter ratios were plotted for each layer. An example of the input parameters for the cubes forced upwards for two layers is shown in Figure 7-20 and Figure 7-21 below.

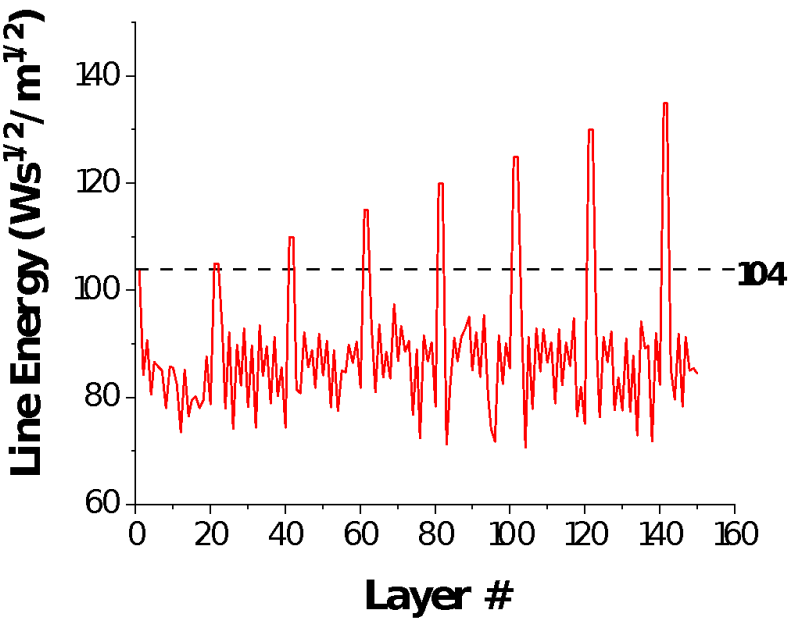

Figure 7-20 - Graph showing the line energy from Equation 1.2-4 input into a two-layer deviation cube. The code deviates the parameters by the required amount at 20-layer intervals. In between, the line energy remains below the upper bound.

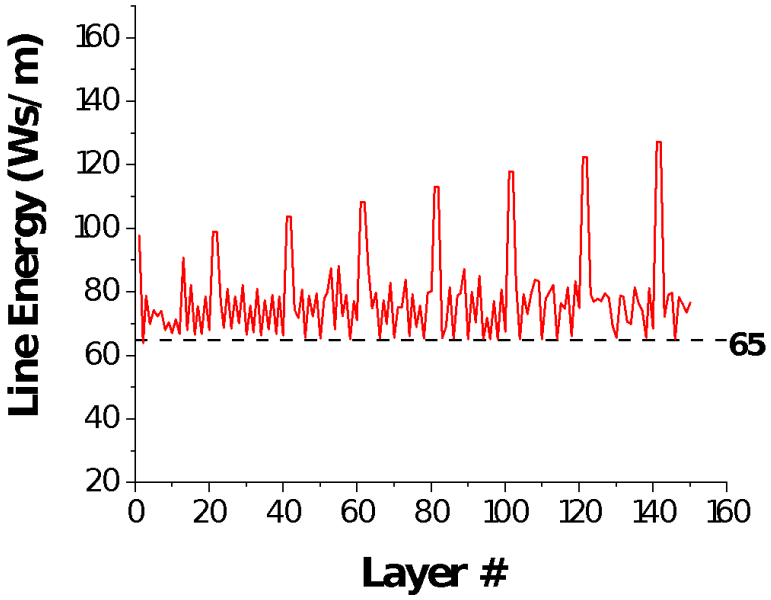

Figure 7-21 - Graph showing the line energy according to Equation 1.2-3. This result shows the lower bound restricting the line energy from falling below the 65 Ws/m boundary. The line energy regularly being restricted by the lower limit shows the importance of the lower bound and that the code is functioning as expected.

The figures show how the parameters are successfully adjusted to lie between the limits. Every 20 layers' parameters are intentionally forced upwards by 5 Ws/m increments, to a maximum of 30 Ws/m away from baseline. After deviation, parameters are adjusted to the bottom limit to compensate for the increase in the pyrometer reading. The pyrometer readings for each layer are shown in Figure 7-22

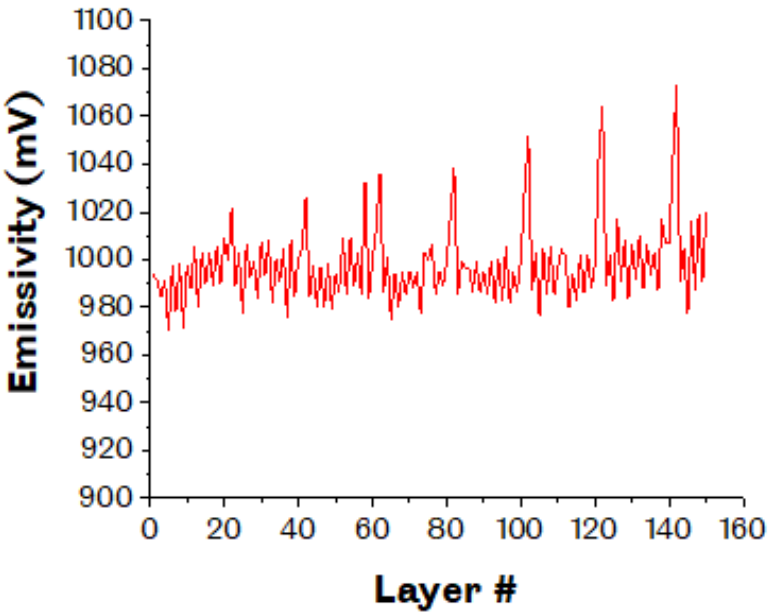

Figure 7-22 - Pyrometry data for each layer. The programmed deviations every 20 layers manifest as spikes in the emissivity, and these spikes get more pronounced as the deviations get larger. Between the spikes, the emissivity drops close to the target of 980mV, showing that the CLC is working. However, a slight increase in the baseline emissivity can be seen between the 120-140 layer deviations.

Peaks can be seen where the parameters are forced upwards every 20 layers. Between these peaks, the reading drops to fluctuating at or above the target of ~ 980 mV. Compared to the unconstrained experiment, the readings fluctuate between the same ranges, approximately 975-1020mV. These fluctuations suggest that a 20 layer break between deviations gives time for readings to stabilise and that CLC is working. There is evidence from the 120-140-layer section that overall emissivity increases as readings are higher than in previous sections. A further experiment where the deviations are increased further is necessary to confirm whether this is the case.

Figure 7-23 shows a similar analysis of line energy for cubes that were forced to values below the 65 Ws/m minimum and how line energy evolved throughout the build. The parameters quickly shift upwards after the deviation; however, they do not reach the upper bound (Figure 7-24). This result shows that the upper bound is never reached with the current geometry and

time between layers to calculate the following set parameters. Further experiments should involve different geometries and reduce the time taken to instigate new parameters such that the upper bound can be tested more thoroughly.

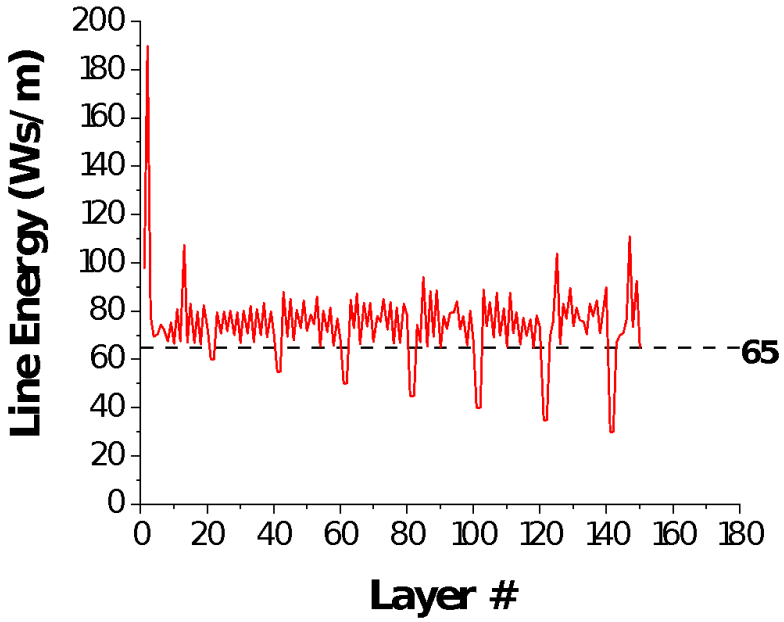

Figure 7-23 - Graph showing the line energy according to Equation 1.2-3. This plot shows the increasing two-layer deviations every 20 layers, and the line energy is restricted by the lower bound between these deviations.

From Figure 7-23, the parameters regularly are constrained by the lower bound. This result proves that the code is working as designed.

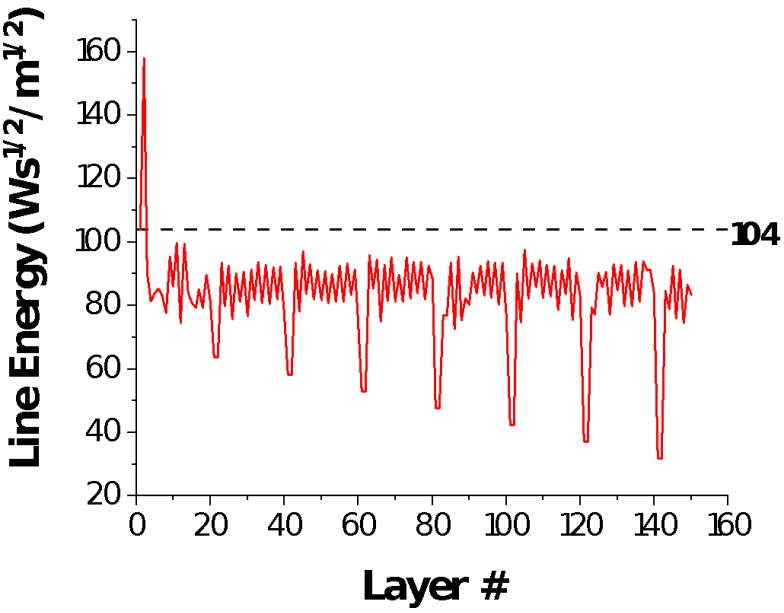

Figure 7-24 - Graph showing line energy input into each layer according to Equation 1.2-4. The upper bound is never reached during the build process, even after the deviations.

The data shown in Figure 7-25 is for a two-layer deviation. The spike downward can be seen from layers 60 onwards, though the response is delayed and preceded by an upwards spike as the parameters are lowered. This spike is due to incomplete melting of the layer, which leaves powder particles behind. These powder particles increase emissivity and cause an uptick in the emissivity reading. When the algorithm returns to within the bounds, the emissivity is lowered as the layer is completely melted but on cooler previous layers leading to a lower surface temperature and a lower reading. The cause of the reduced response compared to the upwards forced parameters is unclear but could be due to the lower reading being masked by the background noise as the lowest reading from the pyrometer is around 850mV.

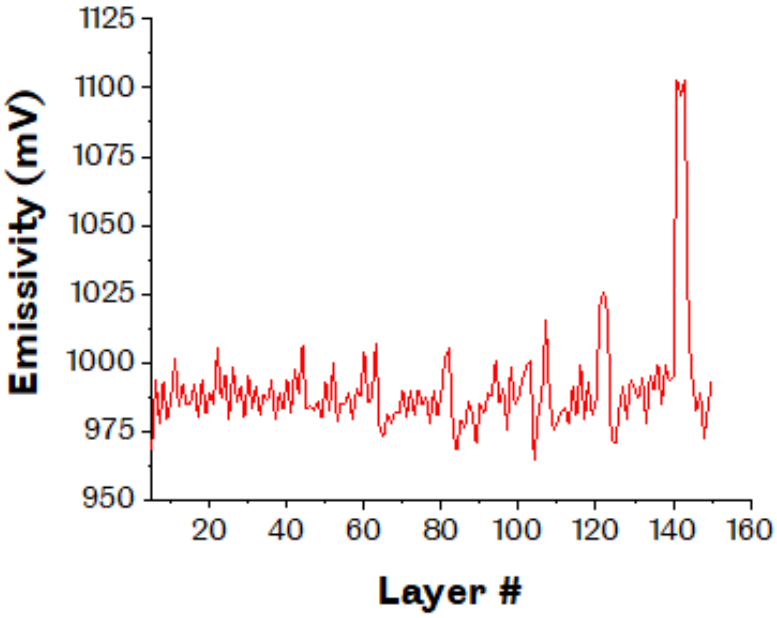

Figure 7-25 - Pyrometry data for the downward deviated cube. The downward spikes are much less distinguishable than the spikes on the upward deviated cube. There is a defined spike from layer 60 onwards though it is delayed. From layer 120 onwards, there is not a downwards spike but upwards. This spike is due to the laser melting pure powder, which retains its heat longer and leads to a higher emissivity than bulk material.

This result demonstrates that it is much easier to accurately and precisely increase a pyrometer reading, whereas for decreasing the reading, a decrease in input energy does not have an exact and immediate effect. This delay must be considered in any future control algorithm.

From layer 120 onwards, there is a large positive spike. This phenomenon is seen in the 1- and 3-layer deviations, respectively, to a lesser and greater extent. This result is because the laser predominantly melts pure powder from these points onwards, leading to greater emissivities. This increase in emissivity is because the powder insulates the meltpool better than bulk material or substrate. So, the meltpool retains its heat better and causes an increase in emissivity.

In order to simplify the process of analysing the parts, the cubes were built on wireframe supports. When the cubes were built directly onto the supports, this caused the algorithm to crash as the emissivity reading was too high, and the ML could not effectively compensate for this variation. For this reason, 20 layers were built before the algorithm was implemented to allow the stabilisation of pyrometer readings.

Figure 7-26 shows the effect of constraining the parameters on the part porosity and demonstrates that the porosity associated with layers has been eliminated. This cross-section confirms that LoF defects have been removed by implementing the lower bound. However, no keyhole defects were detected, which means that the boundary for creating them has not been reached, and further experiments may be needed to reach this.

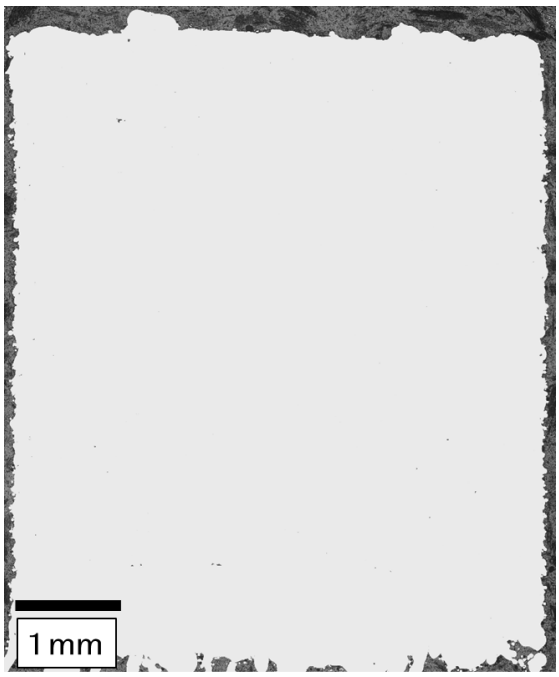

Figure 7-26 - This is the XZ cross-section of an upwards deviated cube. There is little to no porosity either during the deviations or between them. This cross-section shows the effectiveness of the lower bound whilst suggesting that the boundary for keyhole defects to form has not yet been reached in any deviations.

Figure 7-27 shows the cross-section of a cube with the parameters forced down for two layers. As can be seen, the effect is much more noticeable than that of the cube shown in Figure 7-26, where the parameters were forced upwards. Further up the cube, the porosity gets more significant as the parameters are further away from the ideal values. The porosity becomes noticeable at layer 60, which corresponds with line energy of 50 W/m. This result further corroborates the presence of porosity in the unconstrained parameters where the line energy regularly dropped to around 45 W/m. The regions are fully dense in between the forced deviations, showing that the material heals quickly once the parameters return to being constrained. By layer 140, there is almost a complete layer of porosity, and the subsequent layers are held together at only a few small points.

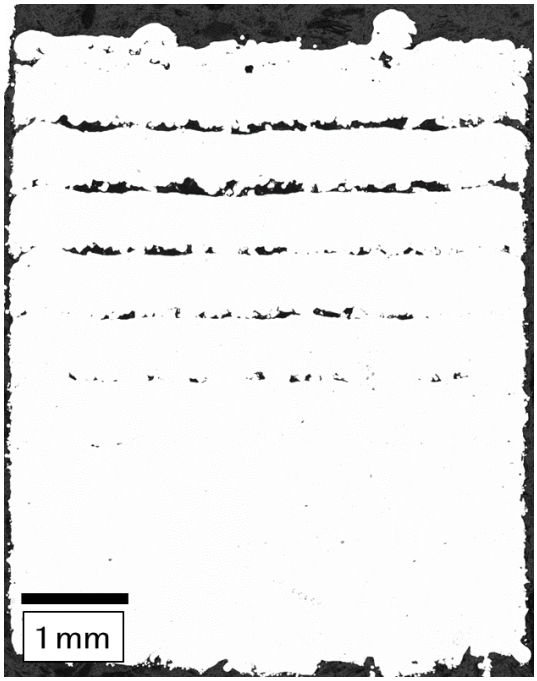

Figure 7-27 shows the XZ cross-section of a downwards deviated cube. The induced porosity is noticeable at layer 60 and becomes more pronounced with each deviation. The section after layer 140 is almost detached from the rest of the cube. This detachment causes a different microstructure to be formed, identified in Figure 7-30 and Figure 7-31.

The XZ cross-sections were then etched to observe the effect of the deviations on the meltpool geometry and microstructure. Figure 7-28 and Figure 7-29 show the upwards forced cubes at layers 120 (middle) and layer 100 (bottom) and a magnified view of the 120-layer deviations. As can be seen, the meltpools are larger for these layers. Circled in red is a meltpool in the conductive mode of melting. This meltpool is larger than those above or below. Circled in yellow is a meltpool that has started to keyhole but has not produced the associated defect. The lack of defects seen in these figures suggests that stable keyholing has occurred. These layers are distinguishable from the interim layers by their darker etching. This darker colour appears due to the increased length and quantity of columnar cells. The cellular size and morphology of both the in-between and the forced layers appear to be the same with large columnar grains that have grown perpendicular to the meltpool present in both. Due to the lack of keyholing in these layers or the forcing at layer 140, further experiments will be needed at high line energies to examine the onset of keyhole porosity. The size and morphology of meltpool before and after deviation are similar, suggesting that the constrained parameters return the microstructure to a baseline quickly after any deviation above the constraints.

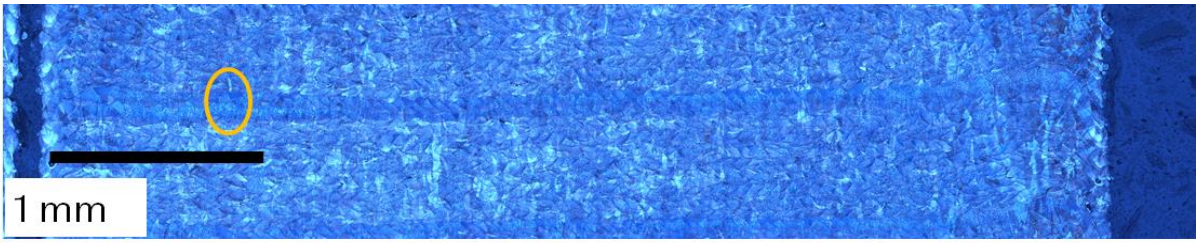

Figure 7-28 - Micrograph showing the etched microstructure around the deviation at layer 120. There is no porosity, and the deviation can be identified by the darker appearance after etching (due to the increased quantity and length of columnar cells). Figure 7-29 shows an enlarged view of the deviation and the microstructure produced as a result. Circled in orange is the region magnified in Figure 7-29

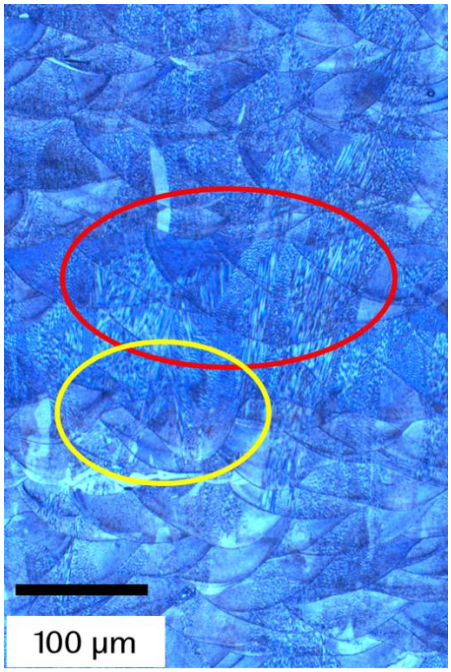

Figure 7-29 - Micrograph of the deviations at layer 120 for this cube where the energy input has been forced up. Though there is no defect formation circled in yellow is a meltpool that has started to keyhole and in red a large conduction mode meltpool indicating the increase in energy input. Outside of the deviation, the meltpools have a similar size and morphology, which suggests that the constrained parameters return the microstructure to the baseline very quickly after a deviation

Figure 7-30 shows the etched downward deviated cube. Figure 7-31 shows the microstructure of the layers after layer 120. In contrast to the microstructure of the constrained layers, fine equiaxed cells are being formed in the layers following the constrained parameters. This microstructure is due to layers being lased onto unmelted powder unconnected from bulk material. This isolation causes the pyrometer reading to spike and explains the need to build foundation layers before implementing MLA. The spike in pyrometer readings from building

on to fresh powder after the supports had been built caused the MLA to crash. Subsequent iterations of the MLA must account for this and ensure that the algorithm is robust and can effectively manage these spikes when encountered.

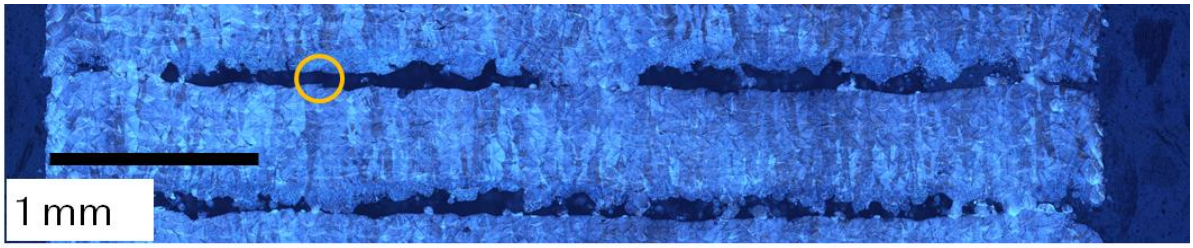

Figure 7-30 - Micrograph shows the voids layers caused by the deviations at layers 100 and 120. Both deviations have caused the subsequent layers to be almost separate from the previous sections. In between these deviations, the microstructure is similar to that seen in in-between sections of the upwards deviated cubes. Circled in orange is the area magnified in Figure 7-31.

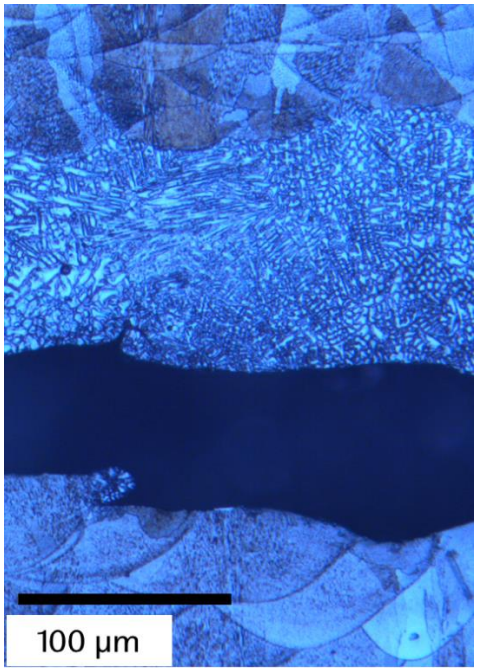

Figure 7-31 - Micrograph of layer 120. The fine cellular microstructure can be seen directly above the void caused by the low energy input. After a few layers, the standard cell and meltpool structure return. The equiaxed microstructure is caused by the laser melting powder that is unconnected from the bulk material.

After fine cellular layers and constrained parameters, the meltpool and cellular morphology return to that seen before deviation. This microstructure can be seen in Figure 7-31.

When looking at the layers between the deviations, both Figure 7-28 and Figure 7-30 look similar. This return to building fully dense layers demonstrates the effectiveness of the constrained parameters to heal the microstructure after the deviations quickly.

The results shown in this chapter highlight the benefits of constraining the parameters to reduce defect formation and the necessity of the lower bound in preventing LoF porosity from forming.

7.6 Analysing the effect of part size and parameter selection on pyrometry readings

From the initial machine learning build, the parameter alterations affected the intralayer variance in emissivity readings. How parameter selections within a layer can affect pyrometry readings was investigated, an experiment was conducted into how the pyrometer records different sections of a part based on hatch length. A 10mm cube was separated into hatches of a similar length irrespective of where they are in the part. The grouping of hatches is shown in a schematic drawing (Figure 7-32), and hatch lengths are given (Table 7-6).

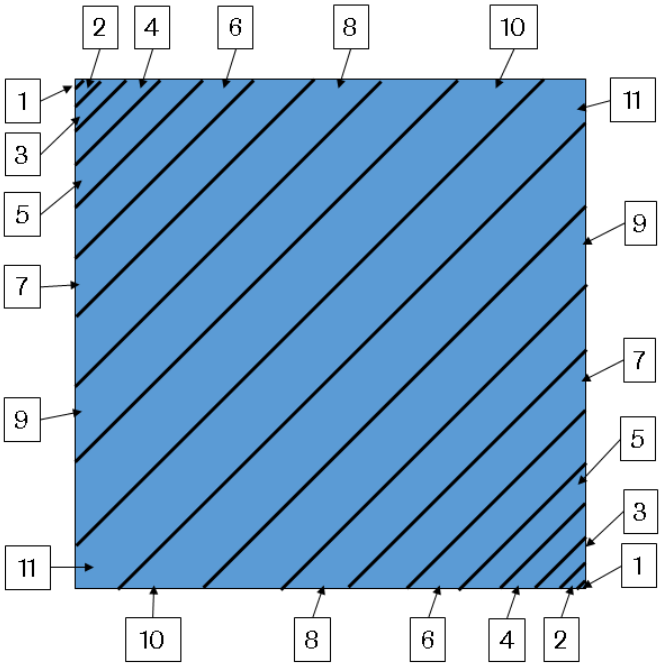

Figure 7-32 - This schematic diagram shows how the part is divided into sections with similar hatch lengths. The sections ear the corner have only a few hatches, whereas the bulk of the hatches lie within the sections in the middle.

Table 7-6 - This table defines the parts through their hatch lengths. All hatches between each bound are grouped irrespective of where they are in the part. Different parameters can be used on different parts to keep the emissivity and, by extension, the thermal history similar.

Part #	Hatch Length Range (µm)
1	<100
2	167-100

3	279-167
4	466-279
5	778-466
6	1299-778
7	2170-1299
8	3623-2170
9	6052-3623
10	10106-6052
11	>10106

For the first build, each part was given the same parameters and the distribution of results recorded. Parameters were adjusted using data depending on whether they were above or below the mean pyrometer reading of 965mV. The build was then repeated with the adjusted parameters to determine whether the intralayer emissivity deviation had been reduced, reducing the deviation in thermal history.

To ascertain whether part quality, as determined by the part density, had been maintained by altering parameters, both cubes were cut in the XY plane, and their porosity was inspected. The cubes were then etched to investigate the joins between the hatch groupings to see if there was a noticeable seam.

Below in Table 7-7 are the results of the original parameters and once they had been adjusted.

Table 7-7 - Results of the adjustment of the different hatch length parts. Initial pyrometer reading, adjusted pyrometer reading and whether the reading was adjusted towards the original mean emissivity value is noted. Overall the adjustments have had the desired effect, though some of the readings have been adjusted such that they are barely distinguishable from background emissivity readings.

Hatch Lengths (µm)	Initial Pyrometer Reading (mV)	Adjusted Pyrometer Reading (mV)	Adjusted Closer to Original Mean Value?
<100	868	863	No
100-167	1044	844	No
167-279	845	863	Yes
279-466	873	864	No
466-778	898	866	No
778-1299	900	975	Yes
1299-2170	1120	864	Yes
2170-3623	992	948	Yes
3623-6052	1016	985	Yes
6052-10106	1031	991	Yes
>10106	1026	990	Yes

From the pyrometer readings, the original and adjusted results are dominated by the first peak ≈ 850mV. The recording of the actual hatches is impossible, so these results should not be considered representative of actual emissivities from the meltpools.

The noise quantity is because there were only a few hatches in each segment, and the hatch lengths were small. It can also be attributed to how the data is recorded. The pyrometer starts recording when the laser moves from the origin to start the first hatch. This recording causes much noise to be picked up as the pyrometer records over virgin powder. Measures were taken to mitigate this by placing the centre of the part over the origin to minimise the time that the laser was taking to travel to the first hatch of the part. Sometimes, there was a delay in starting the laser movement due to the software lag in executing the required command.

Consequently, this will have affected the average pyrometer reading. The code used to analyse the data and determine the average reading accounts for the first peak of noise data. However, in instances where the noise was hard to separate from the meltpool data, the reading was low and could not be distinguished mathematically. The size of the parts made this separation harder as some of the sections consisted of only one or two hatches. Figure 7-33 shows the histogram for the pyrometer readings associated with the hatches less than 100µm.

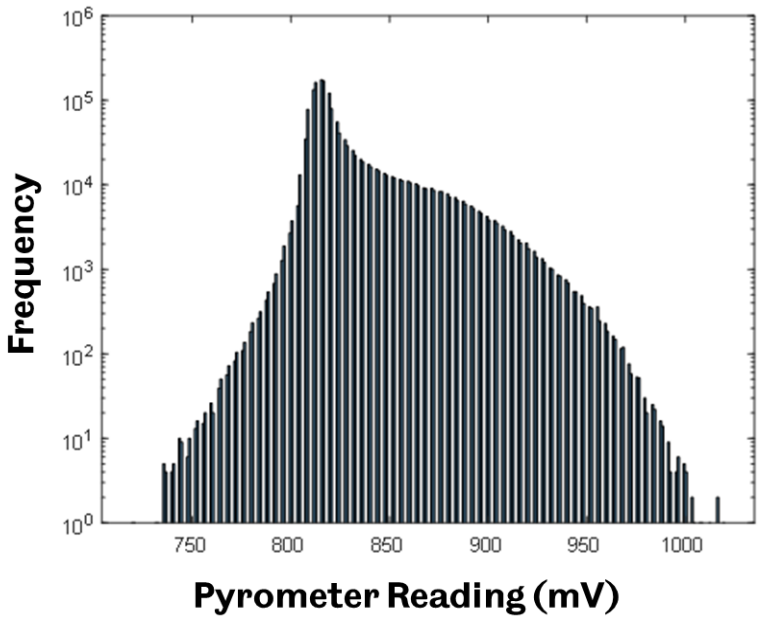

Figure 7-33 shows the emissivity distribution histogram for the section with hatches less than 100 µm. Due to the small size of the hatches and the short time the laser was on, there is no peak to signify the meltpool emissivity. The peak shown is background noise recorded as the laser moves to either start the hatch or return to the middle of the substrate.

Figure 7-33 shows no second peak above the background noise around 815mV. As the readings for the lased hatches cannot be distinguished from the background, the average pyrometer readings for these groups cannot be used.

These results show that these segments were too small, and so in future, the segments should be made larger to capture more meltpool emissivities and make the second peak distinguishable. For the 778-1299µm segment, the benefit of adjusting the parameters is evident in Figure 7-34 and Figure 7-35. There is no clear second peak for the unadjusted parameters, and the results are spread over a larger range. The adjusted parameters show a clear second peak that can be separated from the background noise.

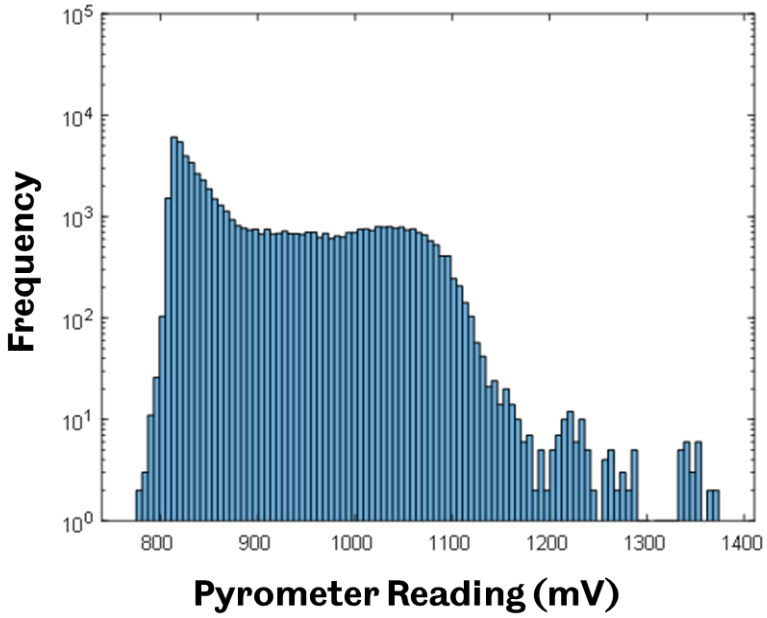

Figure 7-34 - The unadjusted parameters for the 778-1299µm segment. There is no clear second peak, only a plateau, and the results are also spread over a larger range than the adjusted parameters.

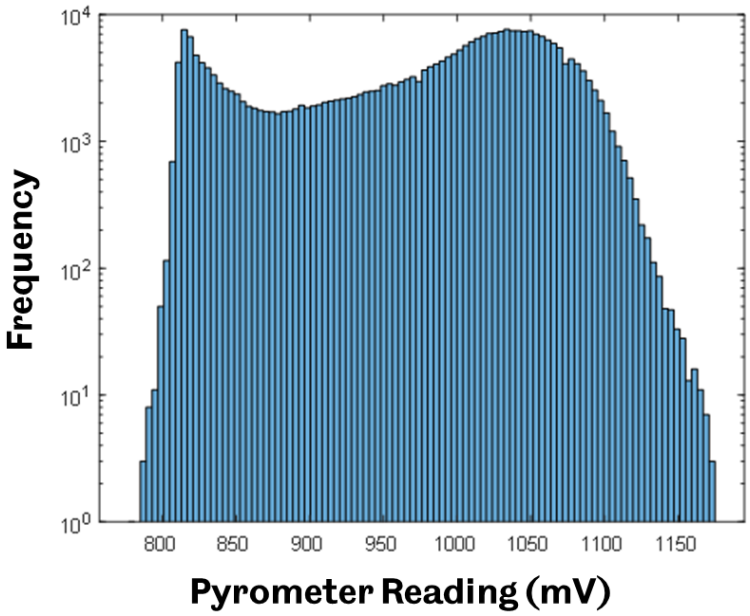

Figure 7-35 - This histogram shows the adjusted 778-1299µm segment. There is a clear second peak where the emissivity from the meltpool can be observed. The emissivities are spread over a tighter range, the drop off is also smoother, and there are no further smaller peaks.

The data is cleaner, and there are no data clusters at higher emissivities that do not follow the overall distribution. The second peak gets larger for both the adjusted and unadjusted parameters as the segments get larger. This second peak is prominent in the histogram for the hatches above 10106µm, and Figure 7-36 shows this.

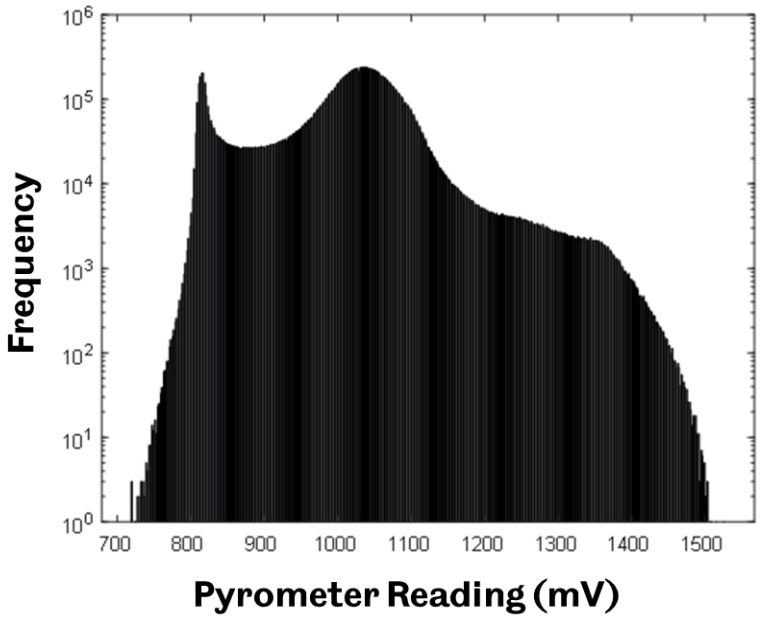

Figure 7-36 - This histogram shows the results for the section above 10106µm. There is a prominent second peak signifying the meltpool emissivities. This second peak can be isolated, and the average emissivity for the meltpools can be found.

The recorded readings from the hatches can be distinguished from the noise by the second peak with these readings. A more accurate and representative average emissivity can be found and compared.

Return time was expected to affect the readings. For smaller hatch lengths, the emissivity readings should be higher (Section 1.7.2). This does not seem to be the case from analysing the initial parameters. The average emissivity does not reduce with increased hatch length. This lack of reduction in emissivity will be due to several issues. There were only a few hatches in each section for the smaller hatch lengths, which would not have been enough to build up heat and cause readings to spike. The laser returned to the centre of the build plate after each part, allowing sections to cool after being lased, reducing thermal build up. The cube was placed in the buildplate centre to reduce this effect, but it still has been an issue. In future, it would be preferable if the laser could lase all sections of the part without returning to the centre of the baseplate.

There were issues in the recording of pyrometry data. There is no second peak in the histogram for the adjusted 1293-2170µm group of hatches, suggesting an error in this section's measuring.

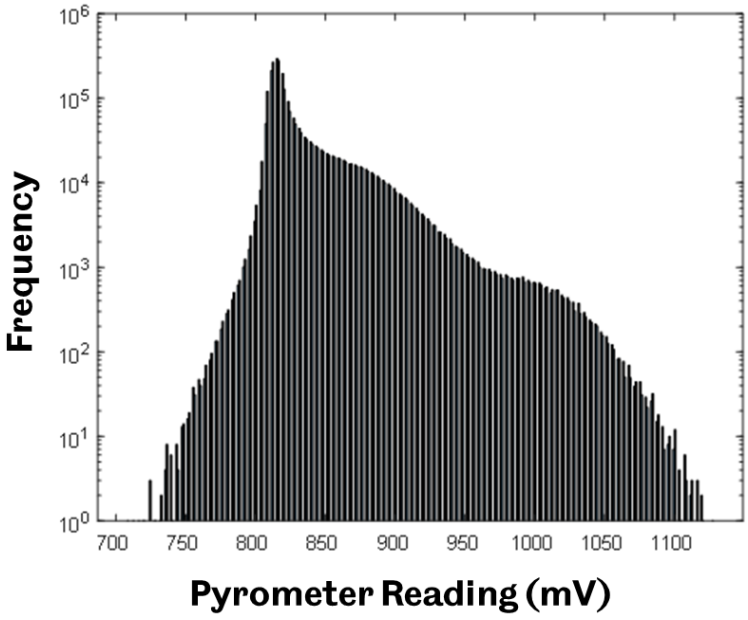

Figure 7-37 - The adjusted 1293-2170μm group of hatches. There has been an error in recording results, and no second peak can be observed. As a result, it cannot be compared to its unadjusted counterpart.

Due to this, this section cannot be compared to its unadjusted counterpart. The adjustments have had the desired effect of altering emissivity to be closer to the initial mean emissivity. Comparing the emissivity histograms for the 6052-10106μm sections. The effect of the adjustment can be seen (Figure 7-38 and Figure 7-39)

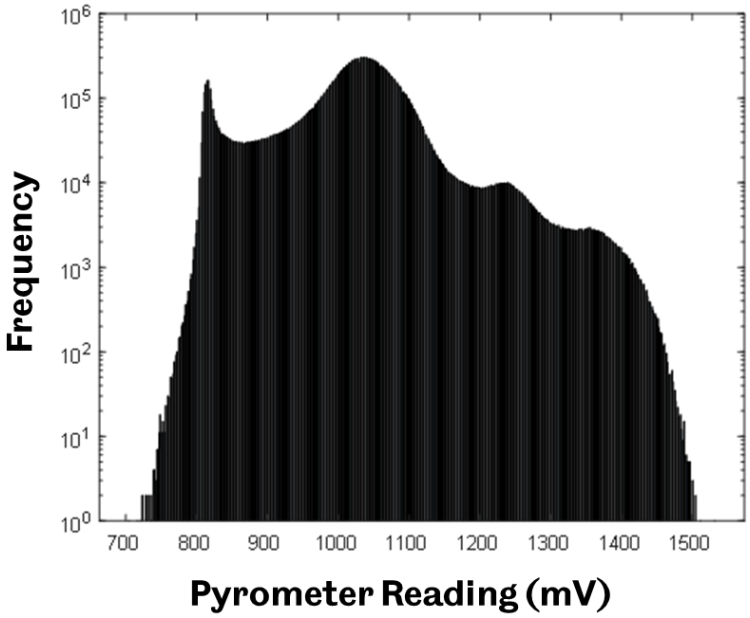

Figure 7-38 - This histogram shows the largest section, the unadjusted 6052-10106µm section. There are third and fourth peaks though these are less prominent than the first two. The results are spread over a large range from 720mV to 1510 mV

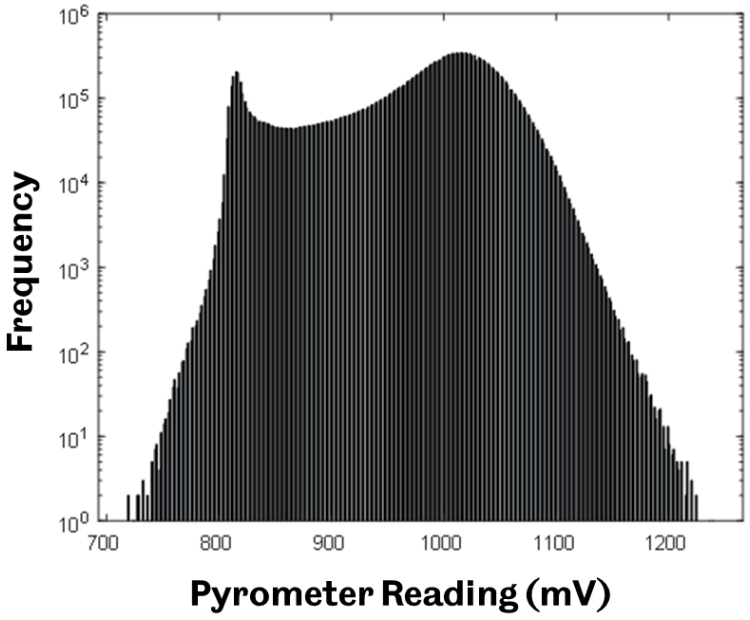

Figure 7-39 - This histogram shows the adjusted 6052-10106µm section results. A clear second peak is more prominent than the peak for the background noise, and there are only two peaks and the results are spread over a tighter range from 720mV to 1220mV.

The adjustment has reduced the number of peaks within the data from four to two. In addition, the spread of data has been reduced, with the highest readings being around 1200mV compared to 1500mV. This adjustment has the effect of reducing variation within the layer.

The effect of the adjustment on variation in the comparable sections was analysed by comparing the intralayer standard deviation.

The deviations for all sections above the 2170µm threshold were averaged according to how many hatches were in them so that the standard deviation across all these sections could be obtained. The intralayer variation for both the original and adjusted hatches is plotted in Figure 7-40 below.

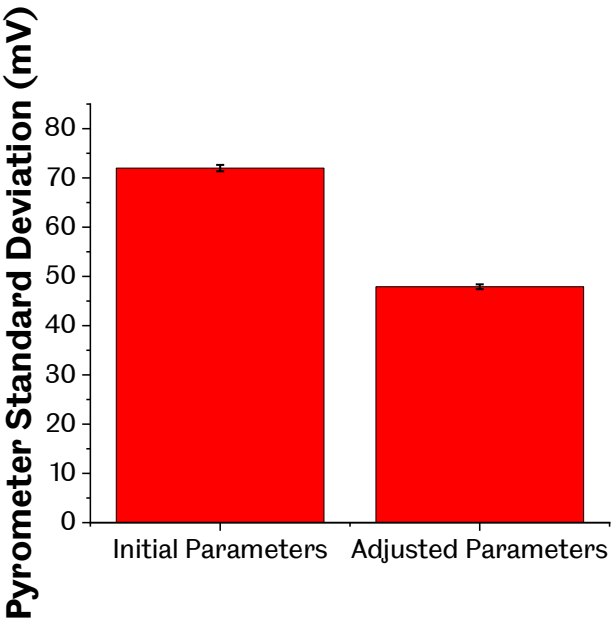

Figure 7-40 - Difference in Pyrometer standard deviation between the two builds. The adjustments have had the desired effect of reducing the deviation in pyrometer readings within a layer.

There is a clear improvement in the intralayer deviation between the two cubes. The adjusted hatches produce a much lower standard deviation (47.9) from the mean pyrometry value than the unadjusted (72). The uncertainty in this deviation is also lower for the adjusted than for the initial parameters.

The intralayer standard deviation of the closed-loop control experiment (47.9) is comparable to the standard for the untrained closed-loop control (44), which had been specifically optimised to reduce intralayer variations.

The parts' porosity as shown in Figure 7-41, Figure 7-42 and Table 7-8 indicate that the adjusted parameters still result in a part that has a relative density of 99.83%.

Table 7-8 - The image analysis results show the porosity in the initial and adjusted parameter builds. There is a slight increase in porosity. However, the part still has a relative density of 99.83%, which is acceptable. This result shows that the variation in thermal history can be reduced whilst maintaining part density.

Initial Parameters Porosity	Adjusted Parameters Porosity
0.06%	0.17%

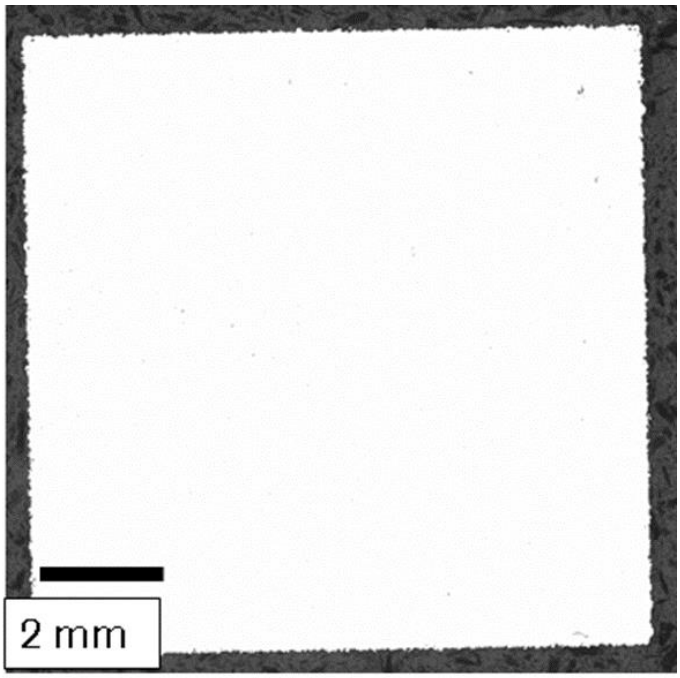

Figure 7-41 - This shows the XY cross-section of the non-adjusted parameters. There is minimal porosity and what porosity there is, is spherical in morphology and less than 45μm in size, suggesting its gas porosity.

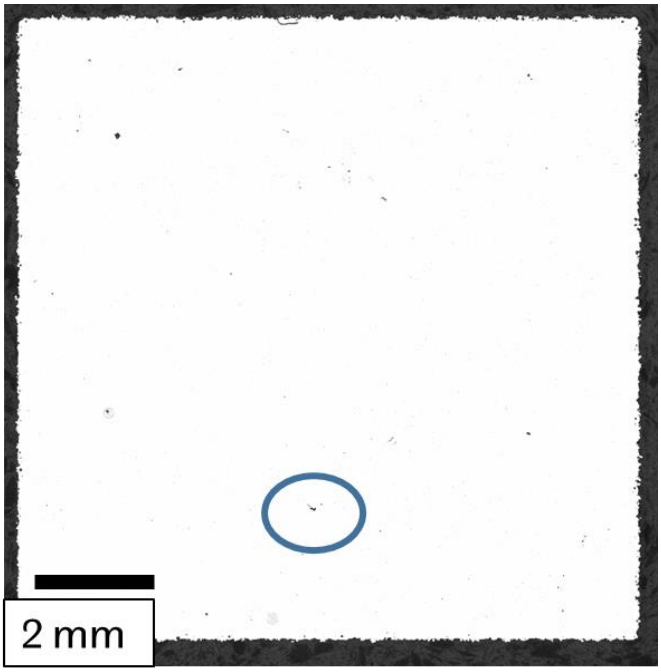

Figure 7-42 - This micrograph shows the XY cross-section of the adjusted parameters part. The part only has a small amount of porosity. Circled is an LoF defect that has been identified due to its morphology. If the energy input were to be lowered, this would cause these defects to become more common.

As the cross-sections shown in Figure 7-41 and Figure 7-42 were taken in the XY plane, it is hard to distinguish if the circular-shaped porosity highlighted in the figures is keyholing or gas porosity. The size of the pores (less than 45µm) and lack of keyholing in the constrained parameter experiment (e.g. Figure 7-26) within this chapter suggests that this is likely gas porosity that has come from the powder. Figure 7-42 shows a small amount of LoF porosity (circled), indicating that the energy input cannot be lowered much more before LoF defects become more prevalent. This LoF onset must be accounted for as with overall layer parameters in the constrained parameters experiment in Section 7.5.

One region of concern was the areas between the parts. From the cross-sections, Figure 7-43, it appeared that there was no additional porosity in these areas. As the machine lased all similar hatch groupings as one part, this meant that there might be seams of porosity where one grouping stopped, and another began. The surface was etched with glyceregia (Figure 1.6-12) to confirm this.

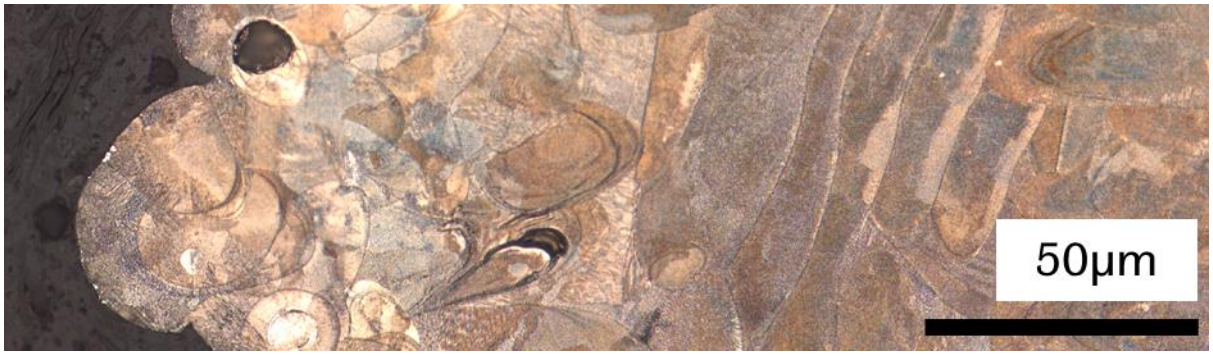

Figure 7-43 - Micrograph of the adjusted parameters XY cross-section corner. There are no seams between the adjoining parts. As the machine did not lase the parts that were next to each other, there was a danger that there would be a gap between the hatch groupings.

The corner of the sample was imaged as this was where there would be the shortest hatches, and so the number of similar hatched parts would be greatest as these parts consist of only one or two hatches. Close to the corner, the hatching is more varied, showing the different parts in this region. Towards the right, the hatching becomes more regular in direction. Despite these irregular hatches, there does not appear to be significant gaps between hatches suggesting that the gaps between the parts of the cube have been fully consolidated. In the future, it would be helpful to allow the algorithm to control the parameter adjustments to minimise the intralayer variation. This MLA control could achieve the goal of lowering the intralayer emissivity variation. This would likely improve on the manual adjustment performed in this experiment. This on-the-fly adjustment could not be made with the existing algorithm as it can only work with rectangular geometries.

7.7 Conclusion

In conclusion, a set of experiments was conducted to examine if it was possible to use machine learning to control the building process of a part. These parameter adjustments were proved possible using a control algorithm developed in house and applying it using the software supplied with the LPBF machine. An initial set of target parameters was determined using the average pyrometer reading associated with the highest density parts in a surface response DoE. A set of builds was completed to provide a training database for the algorithm. This dataset population was done on a generic geometry that consisted of clusters of four 5mm cubes treated as one part by the machine but were thermally separate. An average pyrometer value could be determined for each cube. In turn, this increased the size of the training dataset for the ML. When applied to individual 5mm cubes, the algorithm performed best when it was untrained but able to change parameters for each layer instead of having fixed parameters throughout the build. This result is encouraging for future experiments as an untrained model is quicker and cheaper to implement whilst also geometry agnostic. The interlayer error from the target value was least in the untrained model, but this did not translate into a reduction in intralayer deviation. Although the parameters were fixed within a layer, they were optimised to reduce intralayer variance. In addition, when the density and porosity were examined, it was found that the untrained model resulted in the least dense and the most porous parts, although the cubes were still >96% dense. The cause of this was thought to be due to parameters for many layers dropping below the line energy that had caused lack of fusion defects. An experiment where the parameters were constrained between this experimentally found value and theorised by King *et al.* [1] to cause keyholing was performed. This experiment showed that constraining the parameters worked and that the lower limit was needed to prevent defects from forming. The upper limit was less necessary as parameters that caused keyhole defects were not reached for this alloy, which is weldable and therefore less susceptible to keyholing defects.

Finally, an experiment was carried out to analyse how pyrometry data is recorded for different sized segments. This experiment divided the part into sections of a similar hatch length. The original parameters were adjusted after the first cube had been built to bring the average section reading closer to the overall average. This had the effect of making meltpool emissivities distinguishable from background data. As such, mean emissivity of these segments could be measured accurately.

This chapter has achieved several of the aims and objectives for this project. It has improved the parameter selection process by simplifying it. Using an untrained but constrained control algorithm, it is possible to build fully dense parts if target emissivity values can be determined. It is hoped that this emissivity target could eventually be experimentally derived to reduce the need for an initial surface response DoE. By having a target to aim for, different geometries can be built as the target emissivity will be the same no matter the geometry, and the control algorithm can be used to alter the parameters to achieve the target.

Furthermore, this chapter has achieved the objective of using "on-the-fly" control to adjust parameters. This control leads to achieving the objective of reducing the time taken to achieve optimal parameters.

The experiments within this chapter have achieved the objective of reducing the variation in thermal history within a part as measured using a pyrometer. This reduction in variation was made mainly by the algorithm between layers, and manual adjustment based on an initial reading resulted in no reduction in intralayer variation. However, the experiment did show that individual segments must be large enough to distinguish the meltpool emissivities from the background noise.

8. Future Work

8.1 Stress Rupture Sample Analysis

Future work could focus on increasing the resolution of the stress-rupture results. This increased resolution can be achieved by performing more stress rupture tests in both the as-built and heat-treated states at different stresses and temperatures to verify if the as-built condition gives the best stress rupture properties. Investigating the stress rupture properties in the horizontal build direction would demonstrate the benefits of a successful heat treatment on anisotropic properties. As a starting point the heat treatments developed by Haynes and Christofidou should be compared. Fracture surface and volume analysis will be useful in determining the type of fracture taking place especially in the horizontal direction as in the as-built condition this is more susceptible to brittle fracture, particularly if defects in the microstructure occur.

EBSD maps and further characterisation of the fracture volume should be carried out to see the effect of the heat treatment and testing on the microstructure. This will tell us if recrystallisation has occurred and to what degree grain growth has occurred due to extended exposure to elevated temperature.

After showing that the results from the stress rupture tests were in a continuum with those achieved using other manufacturing methods, the next stage would be to examine whether other material properties are also in a continuum with existing methods. This should include fatigue testing as this is traditionally a property that LBPF manufactured parts have achieved lower cycles to failure. This is due to defects in the microstructure acting as fatigue crack initiators. Achieving comparable results to those from existing methods would therefore show that a defect free microstructure has been achieved.

8.2 Understanding Cracking Mechanisms to Improve Mechanical Properties

The beam velocity was crucial to cracking mechanisms within the part. However, these calculations did not consider return time in all mechanism equations. An experiment that accounts for return time into the propensity to crack needs to be undertaken.

This current work used EBSD maps and micrographs from other studies to visualise the effect of different heat treatments. Future researchers could produce these maps to ensure that the alloy performs as expected, particularly recrystallisation. This recrystallisation would confirm that the heat treatment has the desired effect.

The three main cracking mechanisms were studied in this work, and the propensity to cause cracking in Haynes 282 was found. In the future, other mechanisms could be studied particularly, ductility dip cracking, to find if this contributes to crack creation and propagation. The conditions that cause this type of cracking could be identified so that they can be avoided or mitigated with the right process conditions or parameters.

Twinning within the microstructure has not been studied within this work. Further work should incorporate a characterisation of twinning within Haynes 282. It is one of the strengthening mechanisms within Haynes 282, which can form annealing twins. Processing conditions should be altered to form twins within the microstructure to optimise mechanical properties, which hinder dislocation motion.

Deleterious phases have been identified surrounding a crack in a post stress rupture sample. However, the exact phase has yet to be determined. An etch is required to distinguish between carbides which could be performed. In addition, X-ray crystallography could determine whether a TCP or carbide phase surrounds the crack.

Having identified how the cracking mechanism can be avoided with an optimised parameter set, further research could implement the findings from this chapter into a built part to observe through material and mechanical characterisation if the properties have been improved or the microstructure altered. This work could progress into representative geometries to see if the conclusions made in this chapter hold when a part for use in-service is manufactured.

8.3 Machine Characterisation and Parameter Conversion

Further work could include using the methods of laser scanner accuracy and beam behaviour on a new uncharacterised machine to characterise the machine quickly. More detail could be given in the keyholing forming experiment, and it could also be performed on the Aconity with powder to see the difference in behaviour. A high-speed camera could be used on the Renishaw to image the other build parameters to find which combinations reduce spatter and denudation of the powder and therefore reduce defects within the part.

An experiment into skywriting (how the laser moves between hatches) would reduce potential lack of fusion or keyhole defects at the edge of parts. The laser can be controlled to slew up and down to keep meltpool geometry constant across the part. The skywriting parameters may need to be adjusted depending on the power or velocity of the beam.

When a part is qualified for use in-service, it is tied to a particular machine. Whilst the inter-machine conversion experiment in the current work did not achieve the aim of allowing conversion between machines of different laser types. This conversion may be possible when the machines have the same laser type, and fully characterised machines would enable the conversion between machines with the same laser type. This conversion would then separate the part from the machine and allow the part to be built on different machines whilst still being qualified for use in-service. This ability would be particularly beneficial if the part must be manufactured for a long time. This characterisation would allow the part to be manufactured on new machines as they become available and replace legacy machines.

When comparing machines future work should include mechanical characterisation of parts built using the different machines. This is important as the part performance is more important result of the manufacturing process. Characterising performance in different build orientations would be advantageous as this could measure the anisotropy that a particular machine and parameter set imparts on a part and how it compares to another machine. The tests to be carried out should include testing the creep and fatigue performance as these properties are sensitive to defects in the microstructure and so having comparable results across different machines would show that the machines are equivalent.

8.4 Using Measurements and Machine Learning to Control Parameters In-situ

There are several avenues of exploration for future work to achieve this that could build upon the current work towards this goal. An experiment must be devised to see how closed-loop control operates on geometries other than cubes. This experiment would require a new closed-loop control algorithm, as the current program requires the cross-section to be a square. This new algorithm would test the benefits of the control method in being geometry agnostic. A successful geometry agnostic control method would allow the manufacture of a complex component whilst targeting an emissivity that is known to produce fully dense parts.

As well as the long-range temperature measurements from the pyrometer, future work could focus on integrating measurement devices that record other meltpool features, including temperature at the centre, its size, and shape. If these were kept constant through parameter variation, the thermal history of the built part would be more consistent. This consistency would reduce uncertainty in the properties of the parts and allow the better modelling of how the part will perform in service.

One of the difficulties with the control method used in the experiments was the time it took to calculate and implement changes to the parameters. Work could be undertaken to reduce this time. A field gate programmable array (FPGA) would make calculating the adjusted parameters more efficient and faster as it is purpose-built for this role. Sampling methods were not explored in detail within this project but could improve the performance of the control method. These would reduce computation time, but care must be taken to keep the overall trends and features of the data.

An experiment into CLC of divided hatches within a single layer would expand the capability of the CLC and demonstrate more control. The MLA would need to be adjusted to allow for his control, leading to lower intralayer variation and a more consistent thermal history. It would allow the building of complex geometries as the hatches with similar hatch return times would be grouped.

In order to be able to use a new alloy without first performing a test build, it will be necessary to be able to convert the target values based on material properties. One property that may allow for this tar*get al*teration is the melt viscosity. However, further work is needed to verify if this is a viable method.

One significant advantage of recording these measurements for different aspects of the meltpool is that this data could be used to reconstruct the part digitally. This digital twin would

be tested, and service stresses could be modelled. This testing would inform how often maintenance is required and when the component needs to be replaced.

In order to ascertain the validity of any control method or model, mechanical testing and characterisation is needed. This testing should focus on dynamic properties such as fatigue or creep resistance as these are properties which are more susceptible to being affected by defects formed in the microstructure. As such the benefit of the control method will be evident by improved performance in these tests.

9. Conclusions

The different sections in this work all serve the title objective of this work, namely optimising the LPBF process.

By characterising and understanding the LPBF machine, a better part can be created. The chapter on the machine characterisation showed parameter ranges in which the specific machines prefer to operate. These in conjunction with more general tools for parameter selection can ensure that optimal parameter sets are found more quickly and that these give the desired resulting part.

The stress rupture analysis has put the process, the achieved microstructure and the mechanical performance into context both with other LPBF work and traditional processing techniques. More work is needed to characterise the material in different orientations but the use of different heat treatments has shown the need to tailor heat treatments to LPBF, as previously derived heat treatments do not achieve the desired microstructural change.

Delving further into the microstructure and the cracking mechanism in particular has helped outline rules into which cracking mechanisms are prevalent under what conditions and by knowing these rules it is now possible to optimise parameters for whatever future requirements a user might have. This work has been careful not give specific optimal parameters but act as a guide for a future user. This is because parameters need to be optimised for a specific application and mechanical characteristic and so different parameters may be required.

Finally, closed-loop control has been studied in hope of optimising control over part properties. Successful parameter alterations have been made “on the fly” in response to measured changes in the meltpool. Being able to adjust parameters will mean that complex geometries can be built whilst build quality is kept consistently high throughout the part.

This work has focussed on characterising Haynes 282. However, the methods used in this project apply to other alloys, and future work could apply the analysis methods used in this project to other alloys.

The key result of this work is to show that the alloy used in this project behaves no differently in LPBF compared to other manufacturing methods. This behaviour will give confidence, and future work should optimise these properties for specific applications.

10. References

[1] C. T. Sims, “A history of superalloy metallurgy for superalloy metallurgists,” *Superalloys*, vol. 1984, pp. 399–419, 1984.

[2] Y. J. Liu *et al.*, “Microstructure, defects and mechanical behavior of beta-type titanium porous structures manufactured by electron beam melting and selective laser melting,” *Acta Mater.*, vol. 113, pp. 56–67, 2016.

[3] X. Wang, L. N. Carter, B. Pang, M. M. Attallah, and M. H. Loretto, “Microstructure and yield strength of SLM-fabricated {CM247LC} Ni-Superalloy,” *Acta Mater.*, vol. 128, pp. 87–95, 2017.

[4] R. Engeli, T. Etter, S. Hoevel, and K. Wegener, “Processability of different IN738LC powder batches by selective laser melting,” *J. Mater. Process. Technol.*, vol. 229, pp. 484–491, 2016.

[5] Haynes, “HAYNES ® 282 ® alloy,” 2017.

[6] L. M. Pike, “Long term thermal exposure of Haynes 282 alloy,” *Superalloy*, vol. 718, pp. 644–660, 2010.

[7] L. M. Pike, “HAYNES® 282™ Alloy: A New Wrought Superalloy Designed for Improved Creep Strength and Fabricability,” *Processing*, no. 42398, pp. 1031–1039, 2006.

[8] S. K. Srivastava, J. L. Caron, and L. M. Pike, “Recent developments in the characteristics of Haynes 282 alloy for use in A-USC applications,” in *Proceedings of the 7th International Conference, on Advances in Materials Technology for Fossil Power Plants*, 2014, pp. 120–130.

[9] J. N. DuPont, J. C. Lippold, and S. D. Kiser, *Welding Metallurgy and Weldability of Nickel Base Alloys*. 2009.

[10] J. W. Brooks and P. J. Bridges, “Metallurgical stability of Inconel alloy 718,” *Superalloys*, vol. 88, pp. 33–42, 1988.

[11] H.-E. Huang and C.-H. Koo, “Characteristics and mechanical properties of polycrystalline CM 247 LC superalloy casting,” *Mater. Trans.*, vol. 45, no. 2, pp. 562–568, 2004.

[12] K. L. Kruger, “HAYNES 282 alloy,” in *Materials for ultra-supercritical and advanced*

ultra-supercritical power plants, Elsevier, 2017, pp. 511–545.

[13] L. Wang *et al.*, "Effect of heterogeneous microstructure on the tensile and creep performances of cast Haynes 282 alloy," *Mater. Sci. Eng. A*, vol. 828, p. 142099, 2021.

[14] L. O. Osoba and O. A. Ojo, "Influence of laser welding heat input on HAZ cracking in newly developed Haynes 282 superalloy Influence of laser welding heat input on HAZ cracking in newly developed Haynes 282 superalloy," vol. 0836, no. May, 2012.

[15] L. O. Osoba, R. G. Ding, and O. A. Ojo, "Improved resistance to laser weld heat-affected zone microfissuring in a newly developed superalloy HAYNES 282," *Metall. Mater. Trans. A*, vol. 43, no. 11, pp. 4281–4295, 2012.

[16] M. M. Kirka, K. A. Unocic, K. Kruger, and A. Forsythe, "Process Development for Haynes® 282® Using Additive Manufacturing," Oak Ridge National Lab.(ORNL), Oak Ridge, TN (United States), 2018.

[17] K. A. Unocic, M. M. Kirka, E. Cakmak, D. Greeley, A. O. Okello, and S. Dryepondt, "Evaluation of additive electron beam melting of haynes 282 alloy," *Mater. Sci. Eng. A*, vol. 772, p. 138607, 2020.

[18] A. Ramakrishnan and G. P. Dinda, "Microstructure and mechanical properties of direct laser metal deposited Haynes 282 superalloy," *Mater. Sci. Eng. A*, vol. 748, pp. 347–356, 2019.

[19] R. Otto, V. Brøtan, A. S. Azar, and O. Åsebø, "Processing of Haynes® 282® Alloy by Laser Powder Bed Fusion Technology," in *TMS 2019 148th Annual Meeting & Exhibition Supplemental Proceedings*, 2019, pp. 503–510.

[20] A. S. Shaikh, F. Schulz, K. Minet-Lallemand, and E. Hryha, "Microstructure and mechanical properties of Haynes 282 superalloy produced by laser powder bed fusion," *Mater. Today Commun.*, vol. 26, p. 102038, 2021.

[21] K. A. Christofidou *et al.*, "Microstructural control and optimization of Haynes 282 manufactured through laser powder bed fusion," in *Superalloys 2020*, Springer, 2020, pp. 1014–1023.

[22] J. Boswell, J. Jones, N. Barnard, D. Clark, M. Whittaker, and R. Lancaster, "The effects of energy density and heat treatment on the microstructure and mechanical properties of laser additive manufactured Haynes 282," *Mater. Des.*, vol. 205, p. 109725, 2021.

[23] Steel University, “Solid Solution Strengthening.” [Online]. Available: https://steeluniversity.org/product/solid-solution-strengthening/. [Accessed: 25-Mar-2020].

[24] Y. Mishima, S. Ochiai, N. Hamao, M. Yodogawa, and T. Suzuki, “Solid solution hardening of nickel—role of transition metal and B-subgroup solutes—,” *Trans. Japan Inst. Met.*, vol. 27, no. 9, pp. 656–664, 1986.

[25] E. Nembach and G. Neite, “Precipitation hardening of superalloys by ordered γ′-particles,” *Prog. Mater. Sci.*, vol. 29, no. 3, pp. 177–319, 1985.

[26] B. Dubiel and J. Sieniawski, “Precipitates in Additively Manufactured Inconel 625 Superalloy,” *Materials (Basel).*, vol. 12, no. 7, p. 1144, 2019.

[27] G. Marchese *et al.*, “Influence of heat treatments on microstructure evolution and mechanical properties of Inconel 625 processed by laser powder bed fusion,” *Mater. Sci. Eng. A*, vol. 729, pp. 64–75, 2018.

[28] A. J. Goodfellow *et al.*, “Gamma prime precipitate evolution during aging of a model nickel-based superalloy,” *Metall. Mater. Trans. A*, vol. 49, no. 3, pp. 718–728, 2018.

[29] X. Fan, Z. Guo, X. Wang, J. Yang, and J. Zou, “Morphology evolution of γ′ precipitates in a powder metallurgy Ni-base superalloy,” *Mater. Charact.*, vol. 139, pp. 382–389, 2018.

[30] G. P. Sabol and R. Stickler, “Microstructure of Nickel-Based Superalloys,” *Phys. status solidi*, vol. 35, no. 1, pp. 11–52, 1969.

[31] R. E. Smallman and A. H. W. Ngan, “Plastic deformation and dislocation behaviour,” *Mod. Phys. Metall.*, pp. 357–414, 2014.

[32] J. Humphreys, G. S. Rohrer, and A. Rollett, “Chapter 2 - The Deformed State,” J. Humphreys, G. S. Rohrer, and A. B. T.-R. and R. A. P. (Third E. Rollett, Eds. Oxford: Elsevier, 2017, pp. 13–79.

[33] K. A. Rozman, “Characterization of high temperature fatigue mechanisms in Haynes 282 nickel based superalloy,” 2014.

[34] T. Sourmail, P. Openacker, G. Hopkin, and H. Bhadeshia, “Annealing twins,” *PPT] Phase Transform. complex Prop. Res. Gr. Univ. Cambridge. Retrieved from http//www. msm. cam. ac. uk/phasetrans/abstracts/annealing. twin. html*.

[35] W. C. Winegard, “Fundamentals of the solidification of metals,” *Metall. Rev.*, vol. 6, no. 1,

pp. 57–100, 1961.

[36] W. Kurz and D. J. Fisher, *Fundamentals of solidification*. Trans Tech Publications, 1998.

[37] D. R. Askeland, P. P. Fulay, and W. J. Wright, *The Science and Engineering of Materials, SI Edition*. Cengage Learning, 2011.

[38] W. Kurz and R. Trivedi, "Rapid solidification processing and microstructure formation," *Mater. Sci. Eng. A*, vol. 179, pp. 46–51, 1994.

[39] C. Boig, "The application of additive manufacturing to nickel-base superalloys for turbocharger applications." University of Sheffield, 2019.

[40] N. J. Harrison, I. Todd, and K. Mumtaz, "Reduction of micro-cracking in nickel superalloys processed by Selective Laser Melting: A fundamental alloy design approach," *Acta Mater.*, vol. 94, pp. 59–68, 2015.

[41] P. Tao, H. Li, B. Huang, Q. Hu, S. Gong, and Q. Xu, "The crystal growth, intercellular spacing and microsegregation of selective laser melted Inconel 718 superalloy," *Vacuum*, vol. 159, pp. 382–390, 2019.

[42] C. Hayzelden, J. J. Rayment, and B. Cantor, "Rapid solidification microstructures in austenitic Fe Ni alloys," *Acta Metall.*, vol. 31, no. 3, pp. 379–386, 1983.

[43] N. A. Ahmad, A. A. Wheeler, W. J. Boettinger, and G. B. McFadden, "Solute trapping and solute drag in a phase-field model of rapid solidification," *Phys. Rev. E*, vol. 58, no. 3, p. 3436, 1998.

[44] M. Fousova, D. Dvorsky, M. Vronka, D. Vojtech, and P. Lejcek, "The use of selective laser melting to increase the performance of AlSi9Cu3Fe alloy," *Materials (Basel).*, vol. 11, no. 10, p. 1918, 2018.

[45] H. Davies, N. Shohoji, and D. Warrington, "The structures of rapidly quenched nickel-based superalloy ribbons produced by melt spinning," in *Rapidly Solidification and Technologies*, 1980, pp. 153–164.

[46] A. Popovich and V. Sufiiarov, "Metal powder additive manufacturing," in *New trends in 3D printing*, IntechOpen, 2016.

[47] C. Huang, T. Liu, X. Wang, C. Lu, D. Li, and Z. Lu, "Magnetic properties of nanocrystalline powder cores fabricated by mechanically crushed powders," *J. Iron Steel Res. Int.*, vol. 22, no. 1, pp. 67–71, 2015.

[48] K. Riener *et al.*, “Influence of particle size distribution and morphology on the properties of the powder feedstock as well as of AlSi10Mg parts produced by laser powder bed fusion (LPBF),” *Addit. Manuf.*, vol. 34, p. 101286, 2020.

[49] L. C. Ardila *et al.*, “Effect of IN718 recycled powder reuse on properties of parts manufactured by means of selective laser melting,” *Phys. Procedia*, vol. 56, pp. 99–107, 2014.

[50] N. L. Loh and K. Y. Sia, “An overview of hot isostatic pressing,” *J. Mater. Process. Technol.*, vol. 30, no. 1, pp. 45–65, 1992.

[51] W. T. Carter and M. G. Jones, “Direct Laser Sintering of Metals,” *Proceeding SFF Symp.*, pp. 51–9, 1993.

[52] C. W. Hull, “Apparatus for production of three-dimensional objects by stereolithography,” *United States Patent, Appl., No. 638905, Filed*, 1984.

[53] K. Cooper, *Rapid Prototyping Technology: Selection and Application*. Taylor & Francis, 2001.

[54] S. Mellor, L. Hao, and D. Zhang, “Additive manufacturing: A framework for implementation,” *Int. J. Prod. Econ.*, vol. 149, pp. 194–201, 2014.

[55] M. E. Lynch *et al.*, “Design and topology/shape structural optimisation for additively manufactured cold sprayed components: This paper presents an additive manufactured cold spray component which is shape optimised to achieve 60% reduction in stress and 20% reduction in weigh,” *Virtual Phys. Prototyp.*, vol. 8, no. 3, pp. 213–231, 2013.

[56] N. Serres, D. Tidu, S. Sankare, and F. Hlawka, “Environmental comparison of MESO-CLAD® process and conventional machining implementing life cycle assessment,” *J. Clean. Prod.*, vol. 19, no. 9–10, pp. 1117–1124, 2011.

[57] D. S. Thomas and S. W. Gilbert, “Costs and cost effectiveness of additive manufacturing,” *NIST Spec. Publ.*, vol. 1176, p. 12, 2014.

[58] E. Atzeni and A. Salmi, “Economics of additive manufacturing for end-usable metal parts,” *Int. J. Adv. Manuf. Technol.*, vol. 62, no. 9–12, pp. 1147–1155, 2012.

[59] E. O. Olakanmi, R. F. Cochrane, and K. W. Dalgarno, “A review on selective laser sintering/melting (SLS/SLM) of aluminium alloy powders: Processing, microstructure,

and properties," *Prog. Mater. Sci.*, vol. 74, pp. 401–477, 2015.

[60] R. Otto *et al.*, "Roadmap for additive manufacturing of HAYNES® 282® superalloy by laser beam powder bed fusion (PBF-LB) technology," *Mater. Des.*, vol. 204, p. 109656, 2021.

[61] M. Vaezi, H. Seitz, and S. Yang, "A review on 3D micro-additive manufacturing technologies," *Int. J. Adv. Manuf. Technol.*, vol. 67, no. 5–8, pp. 1721–1754, 2013.

[62] J. J. Lewandowski and M. Seifi, "Metal additive manufacturing: a review of mechanical properties," *Annu. Rev. Mater. Res.*, vol. 46, pp. 151–186, 2016.

[63] W. E. King, A. T. Anderson, R. M. Ferencz, N. E. Hodge, and C. Kamath, "Laser powder bed fusion additive manufacturing of metals ; physics , computational , and materials challenges," vol. 041304, no. 2015, 2017.

[64] C. Y. Yap *et al.*, "Review of selective laser melting: Materials and applications," *Appl. Phys. Rev.*, vol. 2, no. 4, p. 41101, 2015.

[65] N. T. Aboulkhair, I. Maskery, C. Tuck, I. Ashcroft, and N. M. Everitt, "On the formation of AlSi10Mg single tracks and layers in selective laser melting: Microstructure and nano-mechanical properties," *J. Mater. Process. Technol.*, vol. 230, pp. 88–98, 2016.

[66] T. Qi, H. Zhu, H. Zhang, J. Yin, L. Ke, and X. Zeng, "Selective laser melting of Al7050 powder: Melting mode transition and comparison of the characteristics between the keyhole and conduction mode," *Mater. Des.*, vol. 135, pp. 257–266, 2017.

[67] S. M. Thompson, L. Bian, N. Shamsaei, and A. Yadollahi, "An overview of Direct Laser Deposition for additive manufacturing; Part I: Transport phenomena, modeling and diagnostics," *Addit. Manuf.*, vol. 8, pp. 36–62, 2015.

[68] S. L. Sing, C. F. Tey, J. H. K. Tan, S. Huang, and W. Y. Yeong, "3D printing of metals in rapid prototyping of biomaterials: Techniques in additive manufacturing," in *Rapid prototyping of biomaterials*, Elsevier, 2020, pp. 17–40.

[69] A. J. Pinkerton, W. Wang, and L. Li, "Component repair using laser direct metal deposition," *Proc. Inst. Mech. Eng. Part B J. Eng. Manuf.*, vol. 222, no. 7, pp. 827–836, 2008.

[70] K. Shah, I. ul Haq, A. Khan, S. A. Shah, M. Khan, and A. J. Pinkerton, "Parametric study of development of Inconel-steel functionally graded materials by laser direct metal

deposition," *Mater. Des.*, vol. 54, pp. 531–538, 2014.

[71] N. Shamsaei, A. Yadollahi, L. Bian, and S. M. Thompson, "An overview of Direct Laser Deposition for additive manufacturing; Part II: Mechanical behavior, process parameter optimization and control," *Addit. Manuf.*, vol. 8, pp. 12–35, 2015.

[72] F. I. Azam, A. M. A. Rani, K. Altaf, T. Rao, and H. A. Zaharin, "An in-depth review on direct additive manufacturing of metals," in *IOP Conference Series: Materials Science and Engineering*, 2018, vol. 328, no. 1, p. 12005.

[73] F. Calignano *et al.*, "Overview on additive manufacturing technologies," *Proc. IEEE*, vol. 105, no. 4, pp. 593–612, 2017.

[74] D. Deng, J. Moverare, R. L. Peng, and H. Söderberg, "Microstructure and anisotropic mechanical properties of EBM manufactured Inconel 718 and effects of post heat treatments," *Mater. Sci. Eng. A*, vol. 693, pp. 151–163, 2017.

[75] S. Moylan, J. Slotwinski, A. Cooke, K. Jurrens, and M. A. Donmez, "An additive manufacturing test artifact," *J. Res. Natl. Inst. Stand. Technol.*, vol. 119, p. 429, 2014.

[76] K. J.P., W. X., L. T., and F. L., "Lasers and materials in selective laser sintering," *Assem. Autom.*, vol. 23, no. 4, pp. 357–371, Jan. 2003.

[77] O. S. Fatoba, P. A. I. Popoola, S. L. Pityana, and O. S. Adesina, "Computational Dynamics of Anti-Corrosion Performance of Laser Alloyed Metallic Materials," *Fiber Laser*, p. 345, 2016.

[78] B. Wang and L. Gallais, "A theoretical investigation of the laser damage threshold of metal multi-dielectric mirrors for high power ultrashort applications," *Opt. Express*, vol. 21, no. 12, pp. 14698–14711, 2013.

[79] L. Caprio, A. G. Demir, and B. Previtali, "Influence of pulsed and continuous wave emission on melting efficiency in selective laser melting," *J. Mater. Process. Technol.*, vol. 266, pp. 429–441, 2019.

[80] F. Freeman, "Structuring difference: the additive manufacture of spatially & functionally differentiated microstructures." University of Sheffield, 2018.

[81] A. G. Demir, P. Colombo, and B. Previtali, "From pulsed to continuous wave emission in SLM with contemporary fiber laser sources: effect of temporal and spatial pulse overlap in part quality," *Int. J. Adv. Manuf. Technol.*, vol. 91, no. 5–8, pp. 2701–2714, 2017.

[82] A. Stwora and G. Skrabalak, “Influence of selected parameters of Selective Laser Sintering process on properties of sintered materials,” *J. Achiev. Mater. Manuf. Eng.*, vol. 61, no. 2, pp. 375–380, 2013.

[83] I. Koutiri, E. Pessard, P. Peyre, O. Amlou, and T. De Terris, “Influence of SLM process parameters on the surface finish, porosity rate and fatigue behavior of as-built Inconel 625 parts,” *J. Mater. Process. Technol.*, vol. 255, pp. 536–546, 2018.

[84] Y. M. Arısoy, L. E. Criales, T. Özel, B. Lane, S. Moylan, and A. Donmez, “Influence of scan strategy and process parameters on microstructure and its optimization in additively manufactured nickel alloy 625 via laser powder bed fusion,” *Int. J. Adv. Manuf. Technol.*, vol. 90, no. 5–8, pp. 1393–1417, 2017.

[85] J.-P. Kruth, L. Froyen, J. Van Vaerenbergh, P. Mercelis, M. Rombouts, and B. Lauwers, “Selective laser melting of iron-based powder,” *J. Mater. Process. Technol.*, vol. 149, no. 1–3, pp. 616–622, 2004.

[86] M. Thomas, G. J. Baxter, and I. Todd, “Normalised model-based processing diagrams for additive layer manufacture of engineering alloys,” *Acta Mater.*, vol. 108, pp. 26–35, 2016.

[87] A. Hilaire, E. Andrieu, and X. Wu, “High-temperature mechanical properties of alloy 718 produced by laser powder bed fusion with different processing parameters,” *Addit. Manuf.*, vol. 26, pp. 147–160, 2019.

[88] H. Hilal, R. Lancaster, S. Jeffs, J. Boswell, D. Stapleton, and G. Baxter, “The influence of process parameters and build orientation on the creep behaviour of a laser powder bed fused Ni-based superalloy for aerospace applications,” *Materials (Basel).*, vol. 12, no. 9, p. 1390, 2019.

[89] W. E. King *et al.*, “Observation of keyhole-mode laser melting in laser powder-bed fusion additive manufacturing,” *J. Mater. Process. Technol.*, vol. 214, no. 12, pp. 2915–2925, 2014.

[90] H. E. Helmer, C. Körner, and R. F. Singer, “Additive manufacturing of nickel-based superalloy Inconel 718 by selective electron beam melting: Processing window and microstructure,” *J. Mater. Res.*, vol. 29, no. 17, pp. 1987–1996, 2014.

[91] M. Dimter, R. Mayer, L. Hümmeler, R. Salzberger, J. Kotila, and T. Syvänen, “Method and device for manufacturing a three-dimensional object.” Google Patents, 11-Oct-2011.

[92] K. Guan, Z. Wang, M. Gao, X. Li, and X. Zeng, “Effects of processing parameters on tensile properties of selective laser melted 304 stainless steel,” *Mater. Des.*, vol. 50, pp. 581–586, 2013.

[93] L. Thijs, F. Verhaeghe, T. Craeghs, J. Van Humbeeck, and J.-P. Kruth, “A study of the microstructural evolution during selective laser melting of Ti–6Al–4V,” *Acta Mater.*, vol. 58, no. 9, pp. 3303–3312, 2010.

[94] L. Thijs, M. L. M. Sistiaga, R. Wauthle, Q. Xie, J.-P. Kruth, and J. Van Humbeeck, “Strong morphological and crystallographic texture and resulting yield strength anisotropy in selective laser melted tantalum,” *Acta Mater.*, vol. 61, no. 12, pp. 4657–4668, 2013.

[95] P. Laakso *et al.*, “Optimization and simulation of SLM process for high density H13 tool steel parts,” *Phys. Procedia*, vol. 83, pp. 26–35, 2016.

[96] C. Panwisawas *et al.*, “Keyhole formation and thermal fluid flow-induced porosity during laser fusion welding in titanium alloys: Experimental and modelling,” *Acta Mater.*, vol. 126, pp. 251–263, 2017.

[97] C. Qiu, C. Panwisawas, M. Ward, H. C. Basoalto, J. W. Brooks, and M. M. Attallah, “On the role of melt flow into the surface structure and porosity development during selective laser melting,” *Acta Mater.*, vol. 96, pp. 72–79, 2015.

[98] T. W. Eagar and N. S. Tsai, “Temperature fields produced by traveling distributed heat sources,” *Weld. J.*, vol. 62, no. 12, pp. 346–355, 1983.

[99] R. Snell *et al.*, “Methods for Rapid Pore Classification in Metal Additive Manufacturing,” *JOM*, vol. 72, no. 1, pp. 101–109, 2020.

[100] G. K. L. Ng, A. E. W. Jarfors, G. Bi, and H. Y. Zheng, “Porosity formation and gas bubble retention in laser metal deposition,” *Appl. Phys. A*, vol. 97, no. 3, p. 641, 2009.

[101] H. L. Wei, J. W. Elmer, and T. DebRoy, “Crystal growth during keyhole mode laser welding,” *Acta Mater.*, vol. 133, pp. 10–20, 2017.

[102] H. L. Wei *et al.*, “Mechanistic models for additive manufacturing of metallic components,” *Prog. Mater. Sci.*, vol. 116, p. 100703, 2021.

[103] M. B. Henderson, D. Arrell, R. Larsson, M. Heobel, and G. Marchant, “Nickel based superalloy welding practices for industrial gas turbine applications,” *Sci. Technol. Weld. Join.*, vol. 9, no. 1, pp. 13–21, 2004.

[104] L. N. Carter, M. M. Attallah, and R. C. Reed, “Laser powder bed fabrication of nickel-base superalloys: influence of parameters; characterisation, quantification and mitigation of cracking,” *Superalloys*, vol. 2012, pp. 577–586, 2012.

[105] L. M. Pike, “Development of a fabricable gamma-prime (γ′) strengthened superalloy,” *Superalloys 2008*, pp. 191–200, 2008.

[106] E. O. Hall and S. H. Algie, “The sigma phase,” *Metall. Rev.*, vol. 11, no. 1, pp. 61–88, 1966.

[107] X. Z. Qin, J. T. Guo, C. Yuan, G. X. Yang, L. Z. Zhou, and H. Q. Ye, “μ-Phase behavior in a cast Ni-base superalloy,” *J. Mater. Sci.*, vol. 44, no. 18, pp. 4840–4847, 2009.

[108] M. Morinaga, N. Yukawa, H. Adachi, and H. Ezaki, “New PHACOMP and its applications to alloy design,” *Superalloys 1984*, pp. 523–532, 1984.

[109] K. Zhao, Y. H. Ma, and L. H. Lou, “Improvement of creep rupture strength of a liquid metal cooling directionally solidified nickel-base superalloy by carbides,” *J. Alloys Compd.*, vol. 475, no. 1–2, pp. 648–651, 2009.

[110] G. Cao and S. Kou, “Predicting and reducing liquation-cracking susceptibility based on temperature vs. fraction solid,” *Weld. JOURNAL-NEW YORK-*, vol. 85, no. 1, p. 9, 2006.

[111] J. Zhang and R. F. Singer, “Hot tearing of nickel-based superalloys during directional solidification,” *Acta Mater.*, vol. 50, no. 7, pp. 1869–1879, 2002.

[112] M. Rappaz, J. Drezet, and M. Gremaud, “A New Hot-Tearing Criterion,” vol. 30, no. February, pp. 449–455, 1999.

[113] K. L. S. Sharma, “6 - Automation Strategies,” K. L. S. B. T.-O. of I. P. A. (Second E. Sharma, Ed. Elsevier, 2017, pp. 53–74.

[114] S.-H. Kim, *Electric motor control: DC, AC, and BLDC motors*. Elsevier, 2017.

[115] J. G. Carbonell, R. S. Michalski, and T. M. Mitchell, “An overview of machine learning,” in *Machine learning*, Elsevier, 1983, pp. 3–23.

[116] Y. Li, “Deep reinforcement learning: An overview,” *arXiv Prepr. arXiv1701.07274*, 2017.

[117] I. Goodfellow *et al.*, “cleverhans v0. 1: an adversarial machine learning library,” *arXiv Prepr. arXiv1610.00768*, vol. 1, 2016.

[118] D. F. Specht, “Probabilistic neural networks,” *Neural networks*, vol. 3, no. 1, pp. 109–118, 1990.

[119] J. S. Richman and J. R. Moorman, “Physiological time-series analysis using approximate entropy and sample entropy,” *Am. J. Physiol. Circ. Physiol.*, vol. 278, no. 6, pp. H2039–H2049, 2000.

[120] K. Lovegrove and W. Stein, *Concentrating solar power technology: principles, developments and applications*. Elsevier, 2012.

[121] S. L. Wright, R. F. Marks, and W. I. Wang, “Reproducible temperature measurement of GaAs substrates during molecular beam epitaxial growth,” *J. Vac. Sci. Technol. B Microelectron. Process. Phenom.*, vol. 4, no. 2, pp. 505–506, 1986.

[122] Kleiber, “High speed pyrometer with fibre optics for very fast temperature measurements •.”

[123] H. Watanabe, M. Susa, H. Fukuyama, and K. Nagata, “Phase dependence (liquid/solid) of normal spectral emissivities of noble metals at melting points,” *Int. J. Thermophys.*, vol. 24, no. 1, pp. 223–237, 2003.

[124] H. Watanabe, M. Susa, H. Fukuyama, and K. Nagata, “Phase (liquid/solid) dependence of the normal spectral emissivity for iron, cobalt, and nickel at melting points,” *Int. J. Thermophys.*, vol. 24, no. 2, pp. 473–488, 2003.

[125] Z. L. Kowalewski and A. Ustrzycka, “Creep deformation,” *Encycl. Contin. Mech.*, pp. 499–508, 2020.

[126] X. Song, L. Tang, Z. Chen, and R. Zhou, “Micro-mechanism during long-term creep of a precipitation-strengthened Ni-based superalloy,” *J. Mater. Sci.*, vol. 52, no. 8, pp. 4587–4598, 2017.

[127] Z. Chen *et al.*, “Anisotropy of nickel-based superalloy K418 fabricated by selective laser melting,” *Prog. Nat. Sci. Mater. Int.*, vol. 28, no. 4, pp. 496–504, 2018.

[128] K. Kunze, T. Etter, J. Grässlin, and V. Shklover, “Texture, anisotropy in microstructure and mechanical properties of IN738LC alloy processed by selective laser melting (SLM),” *Mater. Sci. Eng. A*, vol. 620, pp. 213–222, 2015.

[129] V. A. Popovich, E. V Borisov, V. Heurtebise, T. Riemslag, A. A. Popovich, and V. S. Sufiiarov, “Creep and Thermomechanical Fatigue of Functionally Graded Inconel 718 Produced by Additive Manufacturing BT - TMS 2018 147th Annual Meeting & Exhibition Supplemental Proceedings,” 2018, pp. 85–97.

[130] F. T. Furillo, S. Purushothaman, and J. K. Tien, “Understanding the Larson-Miller parameter.[for extrapolating stress rupture and creep properties of steels and superalloys],” 1977.

[131] B. Vrancken, L. Thijs, J.-P. Kruth, and J. Van Humbeeck, “Heat treatment of Ti6Al4V produced by Selective Laser Melting: Microstructure and mechanical properties,” *J. Alloys Compd.*, vol. 541, pp. 177–185, 2012.

[132] D. Deng, R. L. Peng, H. Brodin, and J. Moverare, “Microstructure and mechanical properties of Inconel 718 produced by selective laser melting: Sample orientation dependence and effects of post heat treatments,” *Mater. Sci. Eng. A*, vol. 713, pp. 294–306, 2018.

[133] J. Schneider, B. Lund, and M. Fullen, “Effect of heat treatment variations on the mechanical properties of Inconel 718 selective laser melted specimens,” *Addit. Manuf.*, vol. 21, pp. 248–254, 2018.

[134] S. Raghavan *et al.*, “Effect of different heat treatments on the microstructure and mechanical properties in selective laser melted INCONEL 718 alloy,” *Mater. Manuf. Process.*, vol. 32, no. 14, pp. 1588–1595, 2017.

[135] C. Joseph, C. Persson, and M. H. Colliander, “Influence of heat treatment on the microstructure and tensile properties of Ni-base superalloy Haynes 282,” *Mater. Sci. Eng. A*, vol. 679, pp. 520–530, 2017.

[136] R. Ghiaasiaan, N. Ahmad, P. R. Gradl, S. Shao, and N. Shamsaei, “Additively manufactured Haynes 282: effect of unimodal vs. bimodal γ′-microstructure on mechanical properties,” *Mater. Sci. Eng. A*, vol. 831, p. 142234, 2022.

[137] S. Tammas-Williams, “Private Communications.” 2017.

[138] A. Antonysamy, “Haynes 282 Heat Treatment.” 2018.

[139] A. Antonysamy, “Private Communications.” 2020.

[140] L. Osoba, “Microstructural analysis of laser weld fusion zone in Haynes 282 superalloy,” *Mater. Charact.*, vol. 65, no. March, pp. 93–99, 2012.

[141] D. A. Metzler, “Strain-age cracking susceptibility of Ni-based superalloys as a function of strain rate, temperature, and alloy composition,” *Weld. J.*, vol. 91, no. 6, p. 64, 2012.

[142] S. J. Foster *et al.*, “Process-defect-structure-property correlations during laser

powder bed fusion of alloy 718: role of in situ and ex situ characterizations," *Metall. Mater. Trans. A*, vol. 49, no. 11, pp. 5775–5798, 2018.

[143] M. Lamm and R. F. Singer, "The effect of casting conditions on the high-cycle fatigue properties of the single-crystal nickel-base superalloy PWA 1483," *Metall. Mater. Trans. A*, vol. 38, no. 6, pp. 1177–1183, 2007.

[144] N. Raghavan *et al.*, "Localized melt-scan strategy for site specific control of grain size and primary dendrite arm spacing in electron beam additive manufacturing," *Acta Mater.*, vol. 140, pp. 375–387, 2017.

[145] R. F. Brooks, A. P. Day, R. J. L. Andon, L. A. Chapman, K. C. Mills, and P. N. Quested, "Measurement of viscosities of metals and alloys with an oscillating viscometer," *High Temp. High Press.*, vol. 33, no. 1, pp. 73–82, 2001.

[146] K. Eckler, D. M. Herlach, and M. J. Aziz, "Search for a solute-drag effect in dendritic solidification," *Acta Metall. Mater.*, vol. 42, no. 3, pp. 975–979, 1994.

[147] R. N. Abdullaev, R. A. Khairulin, S. V Stankus, and Y. M. Kozlovskii, "Density and volumetric expansion of the Inconel 718 alloy in solid and liquid states," *Thermophys. Aeromechanics*, vol. 26, no. 5, pp. 785–788, 2019.

[148] A. Antonysamy, "Private Commuications." .

[149] B. Vandenbroucke and J.-P. Kruth, "Selective Laser Melting of Biocompatible Metals for Rapid," *Rapid Prototyp. J.*, vol. 13, no. 4, pp. 148–159, 2007.

[150] Z. Wang, E. Denlinger, P. Michaleris, A. D. Stoica, D. Ma, and A. M. Beese, "Residual stress mapping in Inconel 625 fabricated through additive manufacturing: Method for neutron diffraction measurements to validate thermomechanical model predictions," *Mater. Des.*, vol. 113, pp. 169–177, 2017.

[151] M. Mani, S. Feng, L. Brandon, A. Donmez, S. Moylan, and R. Fesperman, *Measurement science needs for real-time control of additive manufacturing powder-bed fusion processes*. CRC Press, 2017.

[152] K. Chua, R. Calandra, R. McAllister, and S. Levine, "Deep reinforcement learning in a handful of trials using probabilistic dynamics models," *arXiv Prepr. arXiv1805.12114*, 2018.

[153] H. Bhadeshia, R. C. Dimitriu, S. Forsik, J. H. Pak, and J. H. Ryu, "Performance of neural

networks in materials science," *Mater. Sci. Technol.*, vol. 25, no. 4, pp. 504–510, 2009.

[154] W. H. Kruskal and W. A. Wallis, "Use of ranks in one-criterion variance analysis," *J. Am. Stat. Assoc.*, vol. 47, no. 260, pp. 583–621, 1952.

11. Appendices

11.1 Appendix – MATLAB Code

11.1.1 Code for Freeman's Pulsed Laser Meltpool Model

```
%% Eager Moving Gaussian Beam
%Assumes no heat loss from top surface
%Scaling in Y and Z only
warning('off','MATLAB:integral2:maxFunEvalsPass')

%Main laser parameters
clear all
tic

Qlist=[200    200       200       200       200       ];
Elist=[0.00004    0.000100    0.000100    0.000100    0.000100   ];
Hlist=[0.00004 0.000034    0.000040    0.000052    0.000090   ];
Plist=[0.00005 0.000034    0.000040    0.000052    0.000090   ];
Nlist=[0.45       0.45       0.45       0.45       0.45      ];
Llist=[0.00003   0.000040    0.000040    0.000040    0.000040   ];

for aa=1:1
Qmax=Qlist(aa);
point=Plist(aa);
tau=Elist(aa);
hatch=Hlist(aa);              %Hatch spacing (m)
n_abs=Nlist(aa);              %Absorbtivity factor
layer=Llist(aa);              %Layer thickness (m)

%Simulation size
step=0.0001;                        %Step size for simulation (m)
x=round(((-0.0035):step:(0.00012)),6);      %Horizontal extent for simulation - travel direction
y=round(((-0.00018):step:(0.00018)),6);     %Horizontal extent for simulation - across width
z=round(((-0.00022):step:0),6);             %Vertical extent for simulation - depth

[X,Y,Z]=meshgrid(x,y,z);
dtmax=1;                            %Limiting temperature change for points in simulation
```

```
Samplesize=0.01;            %Sample size in beam travel direction (m)

%Other laser parameters
c=4.1;                      %Laser travel speed between points (m/s)
sigma=0.000035;             %Spot radius at half maximum (m)
v=(point)./(tau+(point./c));    %Apparent speed
nabla=(200./0.000013);      %Gradient of ramp up to maximum laser power, determined
experimentally by Alistair Lyle
tau_ramp=(Qmax./nabla);     %Time to reach maximum power
Q=@(t) ((nabla.*t).*(t<=tau_ramp))+(Qmax.*(t>tau_ramp));    %Time dependent power
VBoil_Limit_Low=5E-14;      %Threshold for keyhole melting (m3)
VBoil_Limit_High=45E-14;    %Threshold for keyhole melting (m3)

%Material properties (17-4PH Stainless Steel)
T0=(25+273);                %Initial temperature (K)
Tliq=(1375+273);            %Liquidus Temperature (K)
Tsol=(1300+273);            %Solidus Temperature (K)
Tboil=3100;                 %Boiling Temperature (K)
rho=8240;                   %Density (kg/m3)
cp_sol=436;                 %Specific Heat by mass for solid 17-4PH (J/kgK)
cp_liq=(cp_sol).*(0.2/0.17);    %Specific Heat for liquid 17-4PH (J/kgK)
k=10.3;                     %Thermal Conductivity (W/mK)
LHm=280600;                 %Latent Heat of melting (J/kg)
a_sol=(k)./(rho.*cp_sol);   %Thermal Diffusivity of Solid (m2/s)
a_liq=(k)./(rho.*cp_liq);   %Thermal Diffusivity of Liquid (m2/s)
cp_v_sol=(cp_sol*rho);      %Specific Heat by volume for solid 17-4PH (J/m3K)
THAZ=(0.5).*Tsol;           %Heat affected zone temperature (K)
R=8.314;                    %Gas constant (J/mol K)
Qrec=476000;                %Activation energy for dislocation recovery (J/mol)
TeqHT=(800+273);            %Heat treatment equivalent temperature (K)



if abs(max(x)-min(x))>Samplesize
   disp('***ERROR: Please adjust x extent of sample size***')
   return
else
   if abs(max(y)-min(y))>Samplesize
      disp('***ERROR: Please adjust y extent of sample size***')
```

```
        return
    end
end

%Scaling parameters - uses normalised energy density
scaling=1;

%Steady state temperature calculation
for count=1:2
    T=(X.*0)+T0;

    %Hatch 1 - beam centreline
    for i1=0:round((-1)*((Samplesize./(-2))./point),0)
        if i1==0
            tmax=(tau);
            F=@(t) ((Q(t).*n_abs)./(pi.*rho.*cp_sol.*((4.*pi.*a_sol).^(1/2)))).*((t.^(-
1/2))./((2.*a_sol.*t)+(sigma.*sigma)))...
                .*(exp(((-1).*(((X.^2)+(Y.^2))./((4.*a_sol.*t)+(2.*(sigma.*sigma)))))...
                -(((Z./scaling).^2)/(4.*a_sol.*t))));
            dT=integral(F,0,tau,'ArrayValued',true);
        else
            tmax=(tau)+(i1.*(tau+(point./c)));
            i2=(i1*(-1));
            F=@(t) ((Q(t).*n_abs)./(pi.*rho.*cp_sol.*((4.*pi.*a_sol).^(1/2)))).*(((tmax+(t-tau)).^(-
1/2))./((2.*a_sol.*(tmax+(t-tau)))+(sigma.*sigma)))...
                .*(exp(((-1).*((((X-(i2.*point)).^2)+(Y.^2))./((4.*a_sol.*(tmax+(t-
tau)))+(2.*(sigma.*sigma)))))...
                -(((Z./scaling).^2)/(4.*a_sol.*(tmax+(t-tau))))));
            dT=integral(F,0,tau,'ArrayValued',true);
        end
        T=T+dT;
    end

    %Previous Hatches
    for j1=1:round((-1)*((Samplesize./(-2))./hatch),0)
        for i2=((-1)*i1):i1
            if mod(j1,2)==0
                i3=i2*(-1);
```

```
        else
            i3=i2;
        end
        tmax=(tau)+((Samplesize./v).*j1)+((i3+j1)*(tau+(point./c)));
        F=@(t) ((Q(t).*n_abs)./(pi.*rho.*cp_sol.*((4.*pi.*a_sol).^(1/2)))).*(((tmax+(t-tau)).^(-
1/2))./((2.*a_sol.*(tmax+(t-tau)))+(sigma.*sigma)))...
            .*(exp(((-1).*((((X-(i2.*point)).^2)+((Y+(j1.*hatch)).^2))./((4.*a_sol.*(tmax+(t-
tau)))+(2.*(sigma.*sigma)))))...
            -(((Z./scaling).^2)/(4.*a_sol.*(tmax+(t-tau))))));
        dT=integral(F,0,tau,'ArrayValued',true);
        T=T+dT;
        if i2==0
            maxdT=max(max(max(dT)))
        end
    end
    if maxdT<dtmax
        break
    end
end

%Size above boiling point
Qsol=(rho.*cp_sol.*(Tsol-T0).*(step.^3));          %Heat input for a cell to reach solidus
Qmelt=(rho.*(step.^3)).*LHm;                       %Heat input for a cell to melt
Qboil=(rho.*cp_liq.*(Tboil-Tsol).*(step.^3));      %Heat input for a cell to reach boiling point
Qsum=Qsol+Qmelt+Qboil;                             %Total heat for a cell to get from T0 to boiling point

DeltaT=T-T0;
DeltaQ=(rho.*cp_sol.*DeltaT.*(step.^3));           %Heat input to each cell, model assumes no
phase change so use cp_sol
maxDQ=max(max(max(DeltaQ)));

if max(max(max(DeltaQ)))>Qsum
    DeltaQ_side=transpose(squeeze(DeltaQ(find(~y),:,:)));
    [C1,~]=contour(x,z,DeltaQ_side,[Qsum,Qsum]);   %Contour where heat in cell sufficient to
reach boiling point
    [~, Aboil]=convhull(transpose(C1(1,2:end)),transpose(C1(2,2:end)));
    A6_VBoil(aa)=(2/3)*pi()*(((2.*Aboil./pi())^(0.5))^3);   %Volume of melt pool at or above
boiling point
```

```
    else
        A6_VBoil(aa)=0;
    end

    if count==1
        if A6_VBoil(aa)<VBoil_Limit_Low
            break
        else
            if A6_VBoil(aa)<VBoil_Limit_High
                scaling=(2E12 * A6_VBoil(aa))+1;
            else
                scaling=2;
            end
        end
    else
        break
    end
end

%melt length, depth & side view
figure(1)
T_side=transpose(squeeze(T(find(~y),:,:)));
T_side2=T_side;                    %Added in to aid thermal gradient calcs
[C4,~]=contour(x,z,T_side,[Tsol,Tsol]);
A1_MeltLength(aa)=((C4(1,end))-(C4(1,2)));
A2_MeltDepth(aa)=((-1)*min(C4(2,2:end)));
clf
hold on
contourf(x,z,T_side,[T0,THAZ,(0.6).*Tsol,(0.7).*Tsol,(0.8).*Tsol,(0.9).*Tsol,Tsol]);
axis image
colormap jet;
h = colorbar;
ylabel(h, 'Temperature (K)')
axis([min(x) max(x) min(z) max(z)])
line('XData', [min(x) max(x)], 'YData', [(-1*layer) (-1*layer)], 'LineStyle', '- -','Color','w','LineWidth', 2);
line('XData', [min(x) max(x)], 'YData', [(-2*layer) (-2*layer)], 'LineStyle', '- -','Color','w','LineWidth', 2);
line('XData', [min(x) max(x)], 'YData', [(-3*layer) (-3*layer)], 'LineStyle', '- -','Color','w','LineWidth', 2);
line('XData', [0 0], 'YData', [(min(z)) (max(z))], 'LineStyle', '-','Color','y','LineWidth', 2);
```

```
set(gca, 'XAxisLocation', 'bottom');
set(gca, 'YAxisLocation', 'left');
set(gca,'fontsize',30)
title('Melt Pool Profile - Side');
xlabel('Length (m)');
ylabel('Depth (m)');

[~, vol]=convhull(transpose(C4(1,2:end)),transpose(C4(2,2:end)));
radius=(2.*vol./pi())^(0.5);
A5_MeltPoolVolume(aa)=(2/3)*pi()*(radius^3)*1000000*1000000*1000000;

%melt width & top view
figure(2)
T_top=(T(:,:,end));
[C5,~]=contour(x,y,T_top,[Tsol,Tsol]);
A3_MeltWidth(aa)=(max(C5(2,2:end)))-(min(C5(2,2:end)));
clf
hold on
contourf(x,y,T_top,[T0,THAZ,(0.6).*Tsol,(0.7).*Tsol,(0.8).*Tsol,(0.9).*Tsol,Tsol]);
axis image
colormap jet;
h = colorbar;
ylabel(h, 'Temperature (K)')
axis([min(x) max(x) min(y) max(y)])
line('XData', [min(x) max(x)], 'YData', [(0) (0)], 'LineStyle', '- -','Color','w', 'LineWidth', 2);
line('XData', [min(x) max(x)], 'YData', [(-1*hatch) (-1*hatch)], 'LineStyle', '- -','Color','w','LineWidth', 2);
line('XData', [min(x) max(x)], 'YData', [(-2*hatch) (-2*hatch)], 'LineStyle', '- -','Color','w','LineWidth', 2);
line('XData', [0 0], 'YData', [(min(y)) (max(y))], 'LineStyle', '-','Color','y','LineWidth', 2);
set(gca, 'XAxisLocation', 'bottom');
set(gca, 'YAxisLocation', 'left');
set(gca,'fontsize',30)
title('Melt Pool Profile - Top');
xlabel('Length (m)');
ylabel('Width (m)');

%front view
profile1=0;
f=find(~x);
```

```
for g=0:f
   T1=squeeze(T(:,(f-g),:));
   T1(T1<Tsol)=0;
   T1(T1>=Tsol)=1;
   profile2=sum(sum(T1));
   if profile2>profile1
      profile1=profile2;
   else
      g=(g-1);
      break
   end
end
T_front=transpose(squeeze(T(:,(f-g-1),:)));
figure(3)
clf
hold on
contourf(y,z,T_front,[T0,THAZ,(0.6).*Tsol,(0.7).*Tsol,(0.8).*Tsol,(0.9).*Tsol,Tsol]);
axis image
colormap jet;
h = colorbar;
ylabel(h, 'Temperature (K)')
axis([min(y) max(y) min(z) max(z)])
set(gca, 'XAxisLocation', 'bottom');
set(gca, 'YAxisLocation', 'left');
title('Melt Pool Profile - Front');
xlabel('Width (m)');
ylabel('Depth (m)');

%Calculate heat treatment profile
maxlayer=floor((abs(min(z))-A2_MeltDepth(aa))./layer);  %maxmimum number of layers within
calculation space and below melt pool
maxhatch=floor(max(y)./hatch);                  %maxmimum number of hatches within calculation
space
HT1=[];
for layerid=0:(maxlayer-1)
   layerdata=interpn(y,x,z,T,y,x,(((-1)*A2_MeltDepth(aa))-(layer./2)-(layerid.*layer)),'linear');
   for hatchid=((-1)*maxhatch):maxhatch
      hatchdata=interpn(y,x,layerdata,(hatchid*hatch),x,'linear');
```

```
      hatchdata=transpose(hatchdata);
      HT1=cat(1,HT1,hatchdata);
      if hatchid==0
         max_HT=max(hatchdata);
      end
   end
   if max_HT<TeqHT
      break;                    %stop when temperature immediately below laser drops below THAZ (50%
Tsol)
   end

end

for gc=size(HT1,1):-1:1
   if HT1(gc,1)>Tsol
      HT1=HT1((gc+1):end,:);
      break
   end
end

HT3=(transpose(0:1:(size(HT1,1)-1))).*(step./v);          %calculate time steps for plot of temperature v.
time
HT4=((step./v).*(exp((Qrec./R).*((1./TeqHT)-(1./HT1)))));  %calculate equivalent time at specified
equivalent temperature
A7_HeatTreat(aa)=sum(HT4);

figure(4)
clf
hold on

yyaxis left
plot(HT3,HT1);
ylabel('Temperature (K)');
xlabel('Time (s)');
title('Time at Temperature - In-Situ Heat Treatment');
line('XData', [min(HT3) max(HT3)], 'YData', [TeqHT TeqHT], 'LineStyle', '- -', 'LineWidth', 1);
```

```
yyaxis right
plot(HT3,HT4);
ylabel('Equivalent Time (s)');

%Create solidus contour for cooling rate calculation
figure(6)
clf
T_side=transpose(squeeze(T(find(~y),:,:)));
[C6,~]=contour(x,z,T_side,[Tsol,Tsol]);

%adjust temperatures within melt pool for latent heat of melting
Qmelt=(rho.*(step.^3)).*LHm;              %Latent heat of melting for a cell
T1=T;
T1(T1<Tsol)=0;                    %Identify cells above the solidus
T1(T1>=Tsol)=(T1(T1>=Tsol)-T0);          %Delta T for cells above solidus
Q2=(rho.*cp_sol.*T1).*(step.^3);         %Heat input from laser to each cell
QSol=(rho.*cp_sol.*(Tsol-T0).*(step.^3));  %Heat required for a cell to reach solidus
Q2(Q2>0)=(Q2(Q2>0))-(QSol);              %Excess heat after reaching solidus
Q2(Q2<Qmelt)=0;                   %If excess heat less than latent heat of melting set to zero
Q2(Q2>=Qmelt)=(Q2(Q2>=Qmelt))-Qmelt;      %Excess heat after reaching solidus
T1=(Q2)./(rho.*cp_liq.*(step.^3));       %Recalculate delta T from adjusted heat using liquid specific
heat capacity
T(T>=Tsol)=(Tsol);                %Clear additional temperature from cells above solidus in main
temperature matrix
T=(T+T1);                         %Add back in to main temperature matrix



T_check=T(:,:,end);

%cooling rate plot
T1=(squeeze(T(find(~y),:,end)));
plot(x,T1);
title('Surface Temperature Profile with Solidus and Liquidus');
axis([min(x) 0 T0 2000])
set(gca, 'XAxisLocation', 'bottom');
set(gca, 'YAxisLocation', 'left');
xlabel('Length (m)');
ylabel('Temperature (K)');
```

```
line('XData', [min(x) max(x)], 'YData', [Tliq Tliq], 'LineStyle', '- -', 'LineWidth', 1);
line('XData', [min(x) max(x)], 'YData', [Tsol Tsol], 'LineStyle', '- -', 'LineWidth', 1);

%Cooling rate calculations
[C6,~]=contour(x,z,T_side,[(Tliq-5),(Tliq-5)]);    %generate a contour at 5C below liquidus
[C7,~]=contour(x,z,T_side,[(Tliq+5),(Tliq+5)]);    %generate a contour at 5C above liquidus

%At the back (tail) of the melt pool
C6Back=C6(1,(find(~(C6(2,:)),1,'first')));        %identify the x position where the 'below' contour
reaches the surface
C7Back=C7(1,(find(~(C7(2,:)),1,'first')));        %identify the x position where the 'above' contour
reaches the surface

A4_G_back(aa)=(10)./(C7Back-C6Back);              %calculate thermal gradient from the difference in x
positions
A4_V_back(aa)=v;                                  %solidification front velocity is equal to beam velocity
A4_Tdot_back(aa)=A4_G_back(aa)*A4_V_back(aa);     %Tdot = G * V

%At the base of the melt pool
[C6Base,C6ID]=min(C6(2,:));                       %identify the z position of maximum depth for the 'below'
contour
C7Base=min(C7(2,2:end));                          %identify the z position of maximum depth for the 'above'
contour

Vvert_dt=(abs((C6(1,C6ID))-(C6(1,(C6ID-5))))./v;  %calculate the delta time for five meshgrid steps
Vvert_dz=(abs((C6(2,C6ID))-(C6(2,(C6ID-5)))));    %calculate the delta depth for five meshgrid steps

A4_G_base(aa)=(10)./(C7Base-C6Base);              %calculate thermal gradient from the difference in z
positions
A4_V_base(aa)=Vvert_dz./Vvert_dt;                 %calculate the vertical isotherm velocity at the base of
the melt pool
A4_Tdot_base(aa)=A4_G_base(aa)*A4_V_base(aa);     %Tdot = G * V

%output individual results
Results=[A1_MeltLength(aa),A2_MeltDepth(aa),A3_MeltWidth(aa),A4_Tdot_back(aa),A5_MeltPoolVolu
me(aa),A6_VBoil(aa),A7_HeatTreat(aa)];
```

```
%close all

end

save('Results.txt','A1_MeltLength','A2_MeltDepth','A3_MeltWidth','A4_Tdot_back','A5_MeltPoolVolume','
A6_VBoil','A7_HeatTreat','-ascii')

toc
```

11.1.2 Code for Freeman's Continuous Laser Meltpool Model

```
%% 3D steady state Rosenthal for Semi Infinite Solid (eq 43)
%Assumes no heat loss from top surface
warning('off','MATLAB:integral2:maxFunEvalsPass')

Qlist=[285  90       90  110  130];  %Laser power (W)
vlist=[0.9 1.5      0.75      .494      0.75      ];  %Apparent speed (m/s)
Hlist=[0.00011  0.00003   0.00003   0.000040   0.000040  ];  %Hatch spacing (m)
Llist=[0.00003    0.000030    0.00003   0.000030   0.000030  ];  %Layer thickness (m)
Slist=[0.01    0.010000   0.010000   0.010000   0.010000  ];  %Hatch return length (m)

for aa=1      %If only running one condition put a breakpoint at line 191

%Laser parameters
Qmax=Qlist(aa);
v=vlist(aa);
hatch=Hlist(aa);
layer=Llist(aa);
Samplesize=Slist(aa);
n_abs=3;                %Absorbtivity factor
sigma=0.0005;           %Spot radius at half maximum (m)

%Material properties (Haynes 282)
T0=(300);               %Initial temperature (K)
Tliq=(1573);            %Liquidus Temperature (K)
Tsol=(1648);            %Solidus Temperature (K)
Tboil=3287;             %Boiling Temperature (K)
```

```
rho=8240;                   %Density (kg/m3)
cp_sol=436;                 %Specific Heat by mass for solid 17-4PH (J/kgK)
cp_liq=(cp_sol).*(0.2/0.17);   %Specific Heat for liquid 17-4PH (J/kgK)
k=10.3;                     %Thermal Conductivity (W/mK)
LHm=272500;                 %Latent Heat of Fusion (J/kg)
a_sol=(k)./(rho.*cp_sol);      %Thermal Diffusivity of Solid (m2/s)
a_liq=(k)./(rho.*cp_liq);      %Thermal Diffusivity of Liquid (m2/s)
cp_v_sol=(cp_sol*rho);         %Specific Heat by volume for solid 17-4PH (J/m3K)
THAZ=(0.5).*Tsol;           %Heat affected zone temperature (K)
VBoil_Limit_Low=5E-14;         %Threshold for keyhole melting (m3)
VBoil_Limit_High=45E-14;       %Threshold for keyhole melting (m3)
R=8.314;                    %Gas constant (J/mol K)
Qrec=476000;                %Activation energy for dislocation recovery (J/mol)
TeqHT=(800+273);            %Heat treatment equivalent temperature (K)


%Simulation size
step=0.0001;                        %Step size for simulation (m)
x=round(((Samplesize*(-0.5)):step:(Samplesize*0.5)),6);     %Horizontal extent for simulation - travel direction - assumed in centre of hatch return distance Samplesize*(-1)):step:(Samplesize*1)
y=round(((Samplesize*(-0.05)):step:(Samplesize*0.05)),6);     %Horizontal extent for simulation - across width - assumed in centre of hatch return distance
z=(-0.01):step:0;                   %Vertical extent for simulation - depth
[X,Y,Z]=meshgrid(x,y,z);

%3D steady state Rosenthal, multiplied by 2 for semi-infinite solid
T=T0;
%Scaling parameters - uses normalised energy density
scaling=1;

%Steady state temperature calculation
for count=1:1
for hatchid=0:round(Samplesize./hatch)

dT=(((n_abs.*Qmax)./(2.*pi.*k.*(sqrt(((X-
(hatchid*Samplesize)).^2)+((Y+(hatchid*hatch)).^2)+(Z.^2))))).*(exp((-v.*((X-
(hatchid*Samplesize))+(sqrt(((X-
(hatchid*Samplesize)).^2)+((Y+(hatchid*hatch)).^2)+(Z.^2)))))/(2.*a_sol))));
```

```
dT_top=(dT(:,:,end));
  if mod(hatchid,2)==1
    dT=fliplr(dT);
  end
T=T+dT;
dTmax=max(max(max(dT)));
  if dTmax<5
    break
  end
end
%Size above boiling point
  Qsol=(rho.*cp_sol.*(Tsol-T0).*(step.^3));          %Heat input for a cell to reach solidus
  Qmelt=(rho.*(step.^3)).*LHm;                       %Heat input for a cell to melt
  Qboil=(rho.*cp_liq.*(Tboil-Tsol).*(step.^3));      %Heat input for a cell to reach boiling point
  Qsum=Qsol+Qmelt+Qboil;                             %Total heat for a cell to get from T0 to boiling point

  DeltaT=T-T0;
  DeltaQ=(rho.*cp_sol.*DeltaT.*(step.^3));           %Heat input to each cell, model assumes no
phase change so use cp_sol
  maxDQ=max(max(max(DeltaQ)));

  if max(max(max(DeltaQ)))>Qsum
    DeltaQ_side=transpose(squeeze(DeltaQ(find(~y),:,:)));
    [C1,~]=contour(x,z,DeltaQ_side,[Qsum,Qsum]);     %Contour where heat in cell sufficient to
reach boiling point
    [~, Aboil]=convhull(transpose(C1(1,2:end)),transpose(C1(2,2:end)));
    A6_VBoil(aa)=(2/3)*pi()*(((2.*Aboil./pi())^(0.5))^3);   %Volume of melt pool at or above
boiling point
  else
    A6_VBoil(aa)=0;
  end

  if count==1
    if A6_VBoil(aa)<VBoil_Limit_Low
      break
    else
      if A6_VBoil(aa)<VBoil_Limit_High
        scaling=(2E12 * A6_VBoil(aa))+1;
```

```
        else
            scaling=2;
        end
    end
  else
    break
  end
end
%melt length, depth & side view
figure(1)
T_side=transpose(squeeze(T(find(~y),:,:)));
[C4,~]=contour(x,z,T_side,[Tsol,Tsol]);
A1_MeltLength(aa)=((C4(1,end))-(C4(1,2)));
A2_MeltDepth(aa)=((-1)*min(C4(2,2:end)));
clf
hold on
contourf(x,z,T_side,[T0,THAZ,(0.6).*Tsol,(0.7).*Tsol,(0.8).*Tsol,(0.9).*Tsol,Tsol]);
axis image
colormap jet;
h = colorbar;
ylabel(h, 'Temperature (K)')
axis([min(x) max(x) min(z) max(z)])
line('XData', [min(x) max(x)], 'YData', [(-1*layer) (-1*layer)], 'LineStyle', '- -','Color','w','LineWidth', 2);
line('XData', [min(x) max(x)], 'YData', [(-2*layer) (-2*layer)], 'LineStyle', '- -','Color','w','LineWidth', 2);
line('XData', [min(x) max(x)], 'YData', [(-3*layer) (-3*layer)], 'LineStyle', '- -','Color','w','LineWidth', 2);
line('XData', [0 0], 'YData', [(min(z)) (max(z))], 'LineStyle', '-','Color','y','LineWidth', 2);
set(gca, 'XAxisLocation', 'bottom');
set(gca, 'YAxisLocation', 'left');
set(gca,'fontsize',30)
title('Melt Pool Profile - Side');
xlabel('Length (m)');
ylabel('Depth (m)');
[~, vol]=convhull(transpose(C4(1,2:end)),transpose(C4(2,2:end)));
radius=(2.*vol./pi())^(0.5);
A5_MeltPoolVolume=(2/3)*pi()*(radius^3)*1000000*1000000*1000000;

%melt width & top view
figure(2)
```

```
T_top=(T(:,:,end));
[C5,~]=contour(x,y,T_top,[Tsol,Tsol]);
A3_MeltWidth(aa)=(max(C5(2,2:end)))-(min(C5(2,2:end)));
clf
hold on
contourf(x,y,T_top,[T0,THAZ,(0.6).*Tsol,(0.7).*Tsol,(0.8).*Tsol,(0.9).*Tsol,Tsol]);
axis image
colormap jet;
h = colorbar;
ylabel(h, 'Temperature (K)')
axis([min(x) max(x) min(y) max(y)])
line('XData', [min(x) max(x)], 'YData', [(0) (0)], 'LineStyle', '- -','Color','w', 'LineWidth', 2);
line('XData', [min(x) max(x)], 'YData', [(-1*hatch) (-1*hatch)], 'LineStyle', '- -','Color','w','LineWidth', 2);
line('XData', [min(x) max(x)], 'YData', [(-2*hatch) (-2*hatch)], 'LineStyle', '- -','Color','w','LineWidth', 2);
line('XData', [0 0], 'YData', [(min(y)) (max(y))], 'LineStyle', '-','Color','y','LineWidth', 2);
set(gca, 'XAxisLocation', 'bottom');
set(gca, 'YAxisLocation', 'left');
set(gca,'fontsize',30)
title('Melt Pool Profile - Top');
xlabel('Length (m)');
ylabel('Width (m)');

%front view
profile1=0;
f=find(~x);
for g=0:f
   T1=squeeze(T(:,(f-g),:));
   T1(T1<Tsol)=0;
   T1(T1>=Tsol)=1;
   profile2=sum(sum(T1));
   if profile2>profile1
      profile1=profile2;
   else
      g=(g-1);
      break
   end
end
T_front=transpose(squeeze(T(:,(f-g-1),:)));
```

```
figure(3)
clf
hold on
contourf(y,z,T_front,[T0,THAZ,(0.6).*Tsol,(0.7).*Tsol,(0.8).*Tsol,(0.9).*Tsol,Tsol]);
axis image
colormap jet;
h = colorbar;
ylabel(h, 'Temperature (K)')
axis([min(y) max(y) min(z) max(z)])
set(gca, 'XAxisLocation', 'bottom');
set(gca, 'YAxisLocation', 'left');
title('Melt Pool Profile - Front');
xlabel('Width (m)');
ylabel('Depth (m)');

%Calculate heat treatment profile
maxlayer=floor((abs(min(z))-A2_MeltDepth(aa))./layer);  %maxmimum number of layers within
calculation space and below melt pool
maxhatch=floor(max(y)./hatch);                  %maxmimum number of hatches within calculation
space
HT1=[];
for layerid=0:(maxlayer-1)
   layerdata=interpn(y,x,z,T,y,x,(((-1)*A2_MeltDepth(aa))-(layer./2)-(layerid.*layer)),'linear');
   for hatchid=((-1)*maxhatch):maxhatch
      hatchdata=interpn(y,x,layerdata,(hatchid*hatch),x,'linear');
      hatchdata=transpose(hatchdata);
      HT1=cat(1,HT1,hatchdata);
      if hatchid==0
         max_HT=max(hatchdata);
      end
   end
   if max_HT<TeqHT
      break;                  %stop when temperature immediately below laser drops below THAZ (50%
Tsol)
   end

end
```

```
for gc=size(HT1,1):-1:1
   if HT1(gc,1)>Tsol
      HT1=HT1((gc+1):end,:);
      break
   end
end

HT3=(transpose(0:1:(size(HT1,1)-1))).*(step./v);          %calculate time steps for plot of temperature v.
time
HT4=((step./v).*(exp((Qrec./R).*((1./TeqHT)-(1./HT1)))));  %calculate equivalent time at specified
equivalent temperature
A7_HeatTreat(aa)=sum(HT4);
figure(4)
clf
hold on

yyaxis left
plot(HT3,HT1);
ylabel('Temperature (K)');
xlabel('Time (s)');
title('Time at Temperature - In-Situ Heat Treatment');
line('XData', [min(HT3) max(HT3)], 'YData', [TeqHT TeqHT], 'LineStyle', '- -', 'LineWidth', 1);

yyaxis right
plot(HT3,HT4);
ylabel('Equivalent Time (s)');
%Create solidus contour for cooling rate calculation
figure(6)
clf
T_side=transpose(squeeze(T(find(~y),:,:)));
[C6,~]=contour(x,z,T_side,[Tsol,Tsol]);

%adjust temperatures within melt pool for latent heat of melting
Qmelt=(rho.*(step.^3)).*LHm;              %Latent heat of melting for a cell
T1=T;
T1(T1<Tsol)=0;                        %Identify cells above the solidus
T1(T1>=Tsol)=(T1(T1>=Tsol)-T0);          %Delta T for cells above solidus
Q2=(rho.*cp_sol.*T1).*(step.^3);         %Heat input from laser to each cell
```

```
QSol=(rho.*cp_sol.*(Tsol-T0).*(step.^3));  %Heat required for a cell to reach solidus
Q2(Q2>0)=(Q2(Q2>0))-(QSol);              %Excess heat after reaching solidus
Q2(Q2<Qmelt)=0;                          %If excess heat less than latent heat of melting set to zero
Q2(Q2>=Qmelt)=(Q2(Q2>=Qmelt))-Qmelt;      %Excess heat after reaching solidus
T1=(Q2)./(rho.*cp_liq.*(step.^3));        %Recalculate delta T from adjusted heat using liquid specific heat capacity
T(T>=Tsol)=(Tsol);                       %Clear additional temperature from cells above solidus in main temperature matrix
T=(T+T1);                                %Add back in to main temperature matrix



T_check=T(:,:,end);

%cooling rate plot
T1=(squeeze(T(find(~y),:,end)));
plot(x,T1);
title('Surface Temperature Profile with Solidus and Liquidus');
axis([min(x) 0 T0 2000])
set(gca, 'XAxisLocation', 'bottom');
set(gca, 'YAxisLocation', 'left');
xlabel('Length (m)');
ylabel('Temperature (K)');
line('XData', [min(x) max(x)], 'YData', [Tliq Tliq], 'LineStyle', '- -', 'LineWidth', 1);
line('XData', [min(x) max(x)], 'YData', [Tsol Tsol], 'LineStyle', '- -', 'LineWidth', 1);

%Cooling rate calculations
[C6,~]=contour(x,z,T_side,[(Tliq-5),(Tliq-5)]);    %generate a contour at 5C below liquidus
[C7,~]=contour(x,z,T_side,[(Tliq+5),(Tliq+5)]);    %generate a contour at 5C above liquidus

%At the back (tail) of the melt pool
C6Back=C6(1,(find(~(C6(2,:)),1,'first')));       %identify the x position where the 'below' contour reaches the surface
C7Back=C7(1,(find(~(C7(2,:)),1,'first')));       %identify the x position where the 'above' contour reaches the surface

A4_G_back(aa)=(10)./(C7Back-C6Back);             %calculate thermal gradient from the difference in x positions
```

```
A4_V_back(aa)=v;                        %solidification front velocity is equal to beam velocity
A4_Tdot_back(aa)=A4_G_back(aa)*A4_V_back(aa);      %Tdot = G * V

%At the base of the melt pool
[C6Base,C6ID]=min(C6(2,:));                 %identify the z position of maximum depth for the 'below'
contour
C7Base=min(C7(2,2:end));                    %identify the z position of maximum depth for the 'above'
contour

Vvert_dt=(abs((C6(1,C6ID))-(C6(1,(C6ID-5))))./v;  %calculate the delta time for five meshgrid steps
Vvert_dz=(abs((C6(2,C6ID))-(C6(2,(C6ID-5)))));    %calculate the delta depth for five meshgrid steps

A4_G_base(aa)=(10)./(C7Base-C6Base);          %calculate thermal gradient from the difference in z
positions
A4_V_base(aa)=Vvert_dz./Vvert_dt;             %calculate the vertical isotherm velocity at the base of
the melt pool
A4_Tdot_base(aa)=A4_G_base(aa)*A4_V_base(aa);      %Tdot = G * V

%output individual results
Results=[A1_MeltLength(aa),A2_MeltDepth(aa),A3_MeltWidth(aa),A4_Tdot_back(aa),A5_MeltPoolVolu
me(aa),A4_G_base(aa),A4_G_back(aa),A4_Tdot_base(aa)];

%close all

end

save('Results.txt','A1_MeltLength','A2_MeltDepth','A3_MeltWidth','A4_Tdot_back','A5_MeltPoolVolume','
A4_G_base','A4_G_back','A4_Tdot_base','-ascii')
```

11.1.3 Code for HCS Calculation

```
% This tool uses the RDG model to calculate Pressure drop the equation is found in
%https://doiorg/101007/s11661-999-0334-z (Equation 12)



% The constants are defined Tm = melting temperature of nickel
```

```
% L is dendrite Length, u is viscosity, sf is shrinkage factor, Tl is the liquidus temperature of
%the alloy,Tcg is the grain coalescing temperature, G is the thermal
%gradient, strain is the strain, vt is the velocity of the isotherms
Tm=1728;
L=0.5E-06;
Ltwo=0.9E-06;
u=4.5E-03;
sf=0.1;
Tl=1648;
Tcg=1367.59;
tdiff=0.00000288;
k=0.18;
DVel=9;
HCS=zeros(length(EVGValues),2);
% SuperT=EVGValues(:,4);
% MeltD=EVGValues(:,5);
% T0=295;
%[VT,G]=(vt,G);
%G=8E5
%vt=001
%strainrate=(sf*VT)/L;
%
% tf=2*((MeltD^2)/(3*tdiff))*ln((SuperT-T0)/(Tl-T0));
i=1
for i=1:length(EVGValues);
G=EVGValues(i,2);
VT=EVGValues(i,3);
L=EVGValues(i,4);
kvel=((VT/DVel)+k)/(1+(VT/DVel));
strainrate=(sf*VT)/L;
% It is useful to group all the contributinng factors outside of the
% integral together for ease of calculation these are called PreA and PreB
PreA=(180/(Ltwo^2))*(((1+sf)*u)/G);
PreB=(180/(Ltwo)^2)*((VT*sf*u)/G);
% T is defined as a symbol for ease of integration
syms T
fs=(1-(((Tm-T)/(Tm-Tl))^(1/(kvel-1))));
display('Starting FS Integration')
FS=int(1-(((Tm-T)/(Tm-Tl))^(1/(kvel-1))));
```

```
display('FS Integration Done !')
%the different parts of the equation involing fration of solid are defined
display('Starting FS2 Calculation')
FS2=fs^2;
display('FS2 Integration Done !')
%Aspects of the equation are calculated seperately in order to check that
%it  is functioning properly
display('Starting ET Integration')
ET= (strainrate/G)*int(fs);
display('ET Integration Done !')
display('Starting FS3')
FS3=((1-fs)^3);
display('FS3 Done !')
display('Starting FS4')
FS4=((1-fs)^2);
display('FS4 Done !')
%The Integrals are defined and then integrated
display('Starting fstrain')
fstrain= ((ET*(fs^2))/(((1-fs)^3)));
display('fstrain Done !')
display('Starting h calculation')
h=(((fs^2)/(((1-fs)^2))));
display('h calculation Done !')
display('Starting FStrain Integration')
%Fstrain= int(fstrain);
display('FStrain Integration Done !')
display('Starting H Integration')
%H=int(h);
display('H Integration Done !')
%They are then converted into functions and the limits are introduced
display('Starting fstrain Matlab Function')
Fstrain=matlabFunction(int(fstrain));
display('fstrain Matlab Function Done !')
display('Starting H MatlabFunction')
H=matlabFunction(int(h));
display('H MatlabFunction Done !')
display('Starting MaxStrain Calculation')
Maxstrain=Fstrain(TI);
display('MaxStrain Calculation Done !')
```

```
display('Starting MinStrain Calculation')
Minstrain=Fstrain(Tcg);
display('MinStrain Calculation Done !')
display('Starting MaxH Calculation')
MaxH=H(Tl);
display('MaxH Calculation Done !')
display('Starting MinH Calculation')
MinH=H(Tcg);
display('MinH Calculation Done !')
display('Starting Totalstrain Calculation')
Totalstrain=Maxstrain-Minstrain;
display('Totalstrain Calculation Done !')
display('Starting TotalH Calculation')
TotalH=MaxH-MinH;
display('TotalH Calculation Done !')
%Having calculated the contributions of each integral seperately the
%equation is brought together for the total Pressure drop
display('Starting Pc Calculation')
Pc=PreA*(Totalstrain)+PreB*(TotalH);
display('Pc Calculation Done !')
% Once Pc has been calculated we can calculate the max strain before hot
% cracks occur

% The parameters for the equaiton have been combined for easier design
display('Starting PreC Calculation')
PreC = (G/((1+sf)*u))*((Ltwo^2)/180);
display('PreC Calculation Done !')
display('Starting PreD Calculation')
PreD = VT*(sf/(1+sf));
display('PreD Calculation Done !')
display('Starting FstrainMax Calculation')
FStrainmax = (PreC*Pc) - (PreD*TotalH);
display('FstrainMax Calculation Done !')
% The hot tearing susceptabilty is inversaly proportional to The Max strain
% before hot tearing forms
display('Starting HTS Calculation')
HTS =1/FStrainmax;
display('HTS Calculation Done !')
```

```
HCS(i,1)=HTS;
HCS(i,2)=Pc
end
% NormalHTS=HTS/max(HTS);
%  scatter(EVGValues(:,1),HTS)
%  xlabel('Normalised Energy')
%  ylabel('Normalised HTS')
```